

A Thesis Submitted for the Degree of PhD at the University of Warwick

Permanent WRAP URL:

<http://wrap.warwick.ac.uk/98779/>

Copyright and reuse:

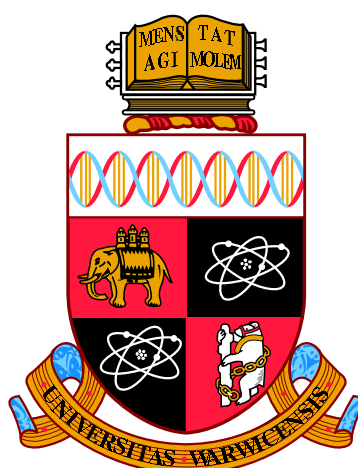
This thesis is made available online and is protected by original copyright.

Please scroll down to view the document itself.

Please refer to the repository record for this item for information to help you to cite it.

Our policy information is available from the repository home page.

For more information, please contact the WRAP Team at: wrap@warwick.ac.uk



**Magnetic Properties of Frustrated
Shastry-Sutherland Magnets; Rare Earth
Tetraborides**

by

Daniel C. Brunt

Thesis

Submitted to the University of Warwick

for the degree of

Doctor of Philosophy

Physics

October 2017



Contents

List of Tables	iv
List of Figures	v
Acknowledgments	xv
Declarations	xvi
Abstract	xviii
Chapter 1 Introduction	1
Chapter 2 Magnetism, Frustration and the Shastry-Sutherland Lat- tice	3
2.1 Introduction to Magnetism	3
2.1.1 Magnetic Moment	3
2.1.2 Magnetic Moment in an applied Magnetic Field	5
2.1.3 Crystal Electric Fields	7
2.1.4 Magnetic Interaction	8
2.1.5 Magnetic Order	9
2.1.6 Excitations	12
2.2 Frustration	13
2.3 Shastry-Sutherland Lattice	16
2.3.1 Rare-Earth Tetraborides	18
Chapter 3 Scattering Theory	21
3.1 Crystal and Magnetic Structures	21
3.2 Diffraction	23
3.3 Neutron Scattering	24
3.3.1 Neutron Production	24

3.3.2	Neutron Diffraction	25
3.3.3	Magnetic Scattering	27
3.3.4	Polarised Neutron Diffraction	28
3.3.5	Inelastic Neutron Scattering	30
Chapter 4	Experimental Techniques	32
4.1	Sample Preparation and Characterisation	32
4.1.1	Polycrystalline Preparation	32
4.1.2	Single Crystal Growth	33
4.1.3	Powder X-ray Diffraction	34
4.1.4	Least-Squares Structure Refinement	34
4.1.5	Laue Diffraction	36
4.2	Bulk Property Measurements	36
4.2.1	Magnetic Susceptibility and Magnetisation	36
4.2.2	Resistivity	38
4.2.3	Heat Capacity	38
4.3	Neutron Diffraction	40
4.3.1	D10, Single Crystal Diffractometer, ILL	40
4.3.2	D7, Polarised Neutron Diffractometer, ILL	41
4.4	Neutron Spectroscopy	42
4.4.1	MARI, ISIS	43
4.4.2	IN4C, ILL	44
4.4.3	IN5, ILL	45
Chapter 5	Magnetic Properties of HoB₄	47
5.1	Bulk Characterisation	48
5.1.1	Magnetic Susceptibility	49
5.1.2	Magnetisation	51
5.1.3	Low Temperature (³ He) Measurements	54
5.1.4	High Field Magnetisation	56
5.1.5	Heat Capacity	58
5.1.6	Resistivity	61
5.2	Single Crystal Neutron Diffraction	62
5.2.1	Polarised Neutron Diffraction	62
5.2.2	Neutron Diffraction In Applied Magnetic Field	66
5.2.3	Magnetic Phase Diagrams	75
5.3	Inelastic Neutron Scattering	79
5.3.1	Polycrystalline Samples	79

5.3.2	Single Crystal Samples	84
5.4	Summary	88
Chapter 6 Magnetic Properties of NdB₄		94
6.1	Bulk Characterisation	96
6.1.1	Magnetic Susceptibility	97
6.1.2	Magnetisation	100
6.1.3	Low Temperature (³ He) Measurements	101
6.1.4	High Field Magnetisation	104
6.1.5	Heat Capacity	104
6.1.6	Resistivity	108
6.2	Single Crystal Neutron Diffraction	112
6.2.1	Polarised Neutron Diffraction	112
6.2.2	Zero Field Measurements	116
6.2.3	Zero Field Magnetic Structure Determination	119
6.2.4	In Applied Magnetic Field	126
6.2.5	Magnetic Phase Diagrams	129
6.3	Inelastic Neutron Scattering	133
6.3.1	$E_i = 12$ meV	133
6.3.2	$E_i = 24$ meV	137
6.3.3	$E_i = 110$ meV	137
6.4	Summary	142
Chapter 7 Conclusion		144

List of Tables

2.1	The quantum numbers, Landé g value, the effective moment for select rare earth ions.	6
5.1	Fractional coordinates and Wyckoff Positions for each site in HoB_4 determined from powder x-ray diffraction measurements.	49
5.2	Fractional coordinates and Wyckoff Positions for each site in HoB_4 , determined from single crystal neutron diffraction measurements on D10.	74
6.1	Fractional coordinates and Wyckoff Positions for each site in NdB_4 , determined through the Rietveld refinement of NdB_4 powder x-ray diffraction pattern.	96
6.2	The magnetic transitions temperatures for both $H \parallel c$ and $H \perp c$ found from the magnetic susceptibility, including the effective moment, μ_{eff} , and Curie-Weiss constant, θ_{CW} calculated from the inverse magnetic susceptibility.	99
6.3	Fractional coordinates and Wyckoff Positions for each site in NdB_4 , determined through the magnetic refinement of NdB_4 single crystal neutron diffraction pattern.	120

List of Figures

2.1	Various spin arrangements in ordered states (a) ferromagnetic, (b) antiferromagnetic, (c) ferrimagnetic and (d) helimagnetic order. . . .	9
2.2	Inverse magnetic susceptibility curves for paramagnets, ferromagnet and antiferromagnets.	10
2.3	A spin wave on a line of spins, (a) a perspective view and (b) a view from above.	12
2.4	Frustrated plaquettes	13
2.5	A selection of two and three dimensional frustration lattices (a) Triangular, (b) Kagomé, (c) face centred cubic and (d) pyrochlore lattices.	16
2.6	(a) The Shastry-Sutherland Lattice, (b) demonstration of the frustration occurring in the SSL when J_2 is an antiferromagnetic exchange and (c) zoomed in view of the exchange interactions observed in the Shastry-Sutherland lattice.	17
2.7	(a) Section of RB_4 lattice to illustrate the B6 octahedra forming chains, as well as the rings above and below the R^{3+} ions. (b) ab plane of RB_4 to illustrate how the SSL mapped to the network of squares and triangles formed by the R^{3+} ions.	19
3.1	Schematic of the diffraction process where beams of radiation are scattering by parallel planes of atoms.	23
3.2	(a) Vector diagram showing elastic scattering (b) Simple geometry of a scattering experiment.	26
4.1	Illustration of the floating zone method. A polycrystalline feed and seed rod are brought together in the focal point of light from four Xe lamps to create a molten region between the two. The molten region between the two rods is pulled through the hot zone, crystallising as it cools.	33

4.2	Schematic of the SQUID magnetometer. The magnetic sample is moved through a set of detection coils inducing a current, which is then converted into a measure of the magnetic moment.	37
4.3	A Schematic of 4 probe measurement. Current is applied across the two outer wire, while the voltage is measured across a pair of silver wires.	38
4.4	A schematic of the experimental set up for making specific heat measurements using the relaxation technique. The sample is adhered to to a platform with Apiezon grease, a heater in the platform briefly heats the sample and the thermometer measures the pulse and subsequent cooling of the sample.	39
4.5	Schematic of the single crystal neutron diffractometer, D10 at the ILL. (b) Illustration of the Eulerian cradle.	40
4.6	Schematic of the single crystal polarised neutron diffractometer, D7 at the ILL.	41
4.7	Distance-time plot to illustrate the principle of time of flight for a direct geometry chopper spectrometer.	43
4.8	A schematic of the time of flight direct geometry spectrometer, MARI at ISIS. The instrument was used to investigate the crystal field excitations on polycrystalline samples of RB_4	44
4.9	A schematic of the time of flight direct geometry spectrometer, IN4 at the ILL. The instrument was used to investigate the crystal field excitations on polycrystalline samples of HoB_4	45
4.10	A schematic of the time of flight direct geometry spectrometer, IN5 at the ILL. The instrument was used to investigate the low energy excitations on single crystal samples of HoB_4	46
5.1	Powder x-ray diffractogram of HoB_4 . The red line corresponds to the fit from the Rietveld refinement, while the blue line corresponds to the difference between the observed and calculated intensity. The green dashes correspond to the expected positions for nuclear Bragg reflections.	48
5.2	Single crystal Laue diffraction photographs of HoB_4 showing (a) the [100] direction compared to the simulated pattern of the [100] direction and (b) the [001] directions compared to simulated pattern for the [001] direction.	50

5.3	Temperature dependent magnetic susceptibility of HoB_4 in a magnetic field of 0.1 kOe for $H \parallel c$ and $H \perp c$. The inset shows the inverse susceptibility between 40 and 300 K.	50
5.4	Temperature dependent magnetic susceptibility in a range of magnetic fields from 0.1 to 40 kOe for (a) $H \parallel c$ and (b) $H \perp c$	52
5.5	Field dependent magnetisation measurements for $H \parallel c$ for two separate crystal growths. The D10 crystal was found to have a small HoB_2 impurity and there are two slightly different orientations of the D7 crystal. Each curve is subsequently offset by $0.75\mu_{\text{B}}/\text{Ho}$ ion. (b) Shows the derivative of the magnetisation curves. Each curve is subsequently offset by $1\mu_{\text{B}}/\text{Ho}$ ion kOe. All magnetisation curves correspond to the field ramping up.	52
5.6	Field dependent magnetisation measurements for $H \parallel c$ and $H \perp c$ at temperatures of (a) 2 K, (b) 4 K and (c) 6 K. The solid curves correspond to the field ramping up, while dash-dot curves are the field ramping down. The dotted curves correspond to the derivative, dH/dM of the curve corresponding to the field being ramped up (right axis).	53
5.7	(a) Field dependent magnetisation measurements using ^3He to achieve temperatures below $T \leq 1$ K. (b) The derivative, dM/dH , of the magnetisation curves. Scans made by ramping up the field. (c) Temperature dependent susceptibility measurements at 24.6, 25.4 and 27 kOe between the temperatures of 0.5-10 K. Filled symbols correspond to measurements made with the ^3He inset, while open symbols were made using ^4He	55
5.8	Field dependent magnetisation measurements made on HoB_4 at $T = 1.5$ K with a pulsed magnetic field up to 500 kOe. The inset shows a lower field range to highlight the fractional magnetisation plateaux. The derivative dM/dH is shown as the dashed curve. Only curves where the field was ramped up are shown.	56
5.9	Temperature dependent heat capacity measurements of HoB_4 in different magnetic fields made for the field directions of (a) $H \parallel c$ and (b) $H \perp c$. For both directions the curves are subsequently offset by 7 J/mol K.	57

5.10	The magnetic contribution of the heat capacity for the two crystal geometries (a) $H \parallel c$ and (b) $H \perp c$. This was determined by subtracting the heat capacity of the non-magnetic LuB_4 reference compound from the total heat capacity of HoB_4 . A comparison of the total heat capacity for both compounds is shown in the inset.	58
5.11	C_{mag}/T (filled squares) curve for HoB_4 for (a) $H \parallel c$ and (b) $H \perp c$. The open circles corresponds to C_{mag}/T where the nuclear Schottky anomaly (dashed line) has been subtracted. C_{mag}/T has been integrated with respect to T giving the magnetic entropy (red curve).	59
5.12	Temperature dependent resistivity measurements for (a) $H \parallel c$ and (b) $H \perp c$ each curve is subsequently offset by $2 \mu\Omega - \text{cm}$. Field dependent resistivity measurements for (c) $H \parallel c$ and (d) $H \perp c$, each curve is subsequently offset by $3 \mu\Omega - \text{cm}$	61
5.13	Single crystal neutron diffraction maps of $(h0l)$ plane for HoB_4 using the D7 diffractometer. The non spin-flip (left column) and spin-flip (right column) channels at different temperature (a) 10 K, (b) 6.5 K and (c) 1.5 K are shown.	63
5.14	Line cuts of the z -polarisation intensity maps at 10, 6.5 and 1.5 K for the incommensurate reflections in the (a) $[0 \ 0 \ L]$ and (b) $[H \ 0 \ 0.43]$ directions.	65
5.15	Evolution of (top panel) fractional and (middle panel) integer (hkl) reflections intensities with magnetic field compared to (bottom panel) the magnetisation curve for the magnetic field ramping up at $T = 2 \text{ K}$. There are four <i>stationary</i> magnetic structures, coloured in grey and labelled as Phases I, II, III and IV, in which magnetisation remains almost constant, while the white regions are <i>transitory</i> structures in which magnetisation is rapidly changing. The dashed line corresponds to a narrow transitory state between phases II and III.	67
5.16	(a) Field dependence of the intensity of the incommensurate $(2.02 \ 1.02 \ 0.43)$ reflection at different temperatures. Filled symbols correspond to the field ramping up, while empty symbols the field ramping down. Each curve is sequentially by 1500 counts. (b) Temperature dependence of the intensity incommensurate reflection $(2.02 \ 1.02 \ 0.43)$ in different fields. A stabilisation of the incommensurate phase is observed at 20 kOe, while a decrease of the low temperature intensity with increasing field. Each curve is sequentially offset by 1100 counts.	68

5.17	Field dependence of the intensity of $(2\ 1\ \frac{1}{3})$ reflection at different temperatures. Filled symbols correspond ramping the field up, empty symbols correspond to ramping the field down. The temperature increase between $T = 1.8$ to 4 K causes a visible shift of the magnetic phase corresponding to $\frac{1}{3}$ -magnetisation plateau to lower fields. . . .	70
5.18	Field dependence of the intensity of the (a) (100) and (b) (210) reflection at different temperatures. Filled symbols correspond ramping the field up, empty symbols correspond to ramping the field down. .	71
5.19	Comparison of the calculated and observed intensity for (a) the incommensurate phase re-established at $T = 2$ K in a field of 17.5 kOe and for (b) Phase II, corresponding to the $\frac{1}{3}$ -magnetisation plateau. The inset in both pictures corresponds to the found magnetic structure.	73
5.20	The lattice distortion (left column) applied to (a) the Ho ions and the B atoms in the (b) B2 site and (c) B3 site. (Right column) The intensity as a function of size of displacement.	76
5.21	Magnetic phase diagram of HoB_4 constructed from neutron diffraction data for different reflections (squares, filled circles, triangles and diamonds) and magnetisation (empty circles) measurements. All field dependent measurements were made by ramping the field up. The labelling of different magnetic structures is consistent with the one used in Fig. 5.15 for $T = 2$ K, however, with the increased temperature the magnetic phases tend to overlap. The separation between the stationary and transitionary phases also becomes less obvious on heating, with the <i>transitionary</i> Phases II+IT and II+III occupying large portions of the phase diagram.	77
5.22	Magnetic phase diagram of HoB_4 constructed from magnetisation (squares), resistivity (circles) and heat capacity (triangles) measurements. All field dependent measurements were made by ramping the field up. The magnetic phases are the paramagnetic regime (PM), the intermediate temperature (IT), a non-collinear antiferromagnetic phase I and a field induced phase II.	78
5.23	$S(Q, \omega)$ for $\lambda = 3.06$ Å at several temperatures. The low energy excitations become dispersive in the intermediate temperature phase and further new features appear as crystal field levels become thermally populated.	81
5.24	Dynamic susceptibility of HoB_4 for (a) temperatures between 1.6 – 14 K and (b) 8 – 80 K with an incident wavelength of $\lambda = 3.06$ Å. . .	82

5.25	Gaussian fits of $S(Q, \omega)$ of HoB_4 in a range of temperatures with an incident wavelength of $\lambda = 3.06 \text{ \AA}$. Blue peaks correspond to crystal field levels, while green peaks correspond to secondary transitions from thermally populated energy levels.	83
5.26	$S(Q, \omega)$ for $\lambda = 1.61 \text{ \AA}$ at several temperatures. The low energy excitations become dispersive in the intermediate temperature phase and further new features appear as crystal field levels become thermally populated.	85
5.27	Dynamic susceptibility of HoB_4 for (a) temperatures between 1.6–20 K and (b) 20–160 K with an incident wavelength of $\lambda = 1.61 \text{ \AA}$. .	86
5.28	Gaussian fits of $S(Q, \omega)$ of HoB_4 in a range of temperatures with an incident wavelength of $\lambda = 3.06 \text{ \AA}$. Blue peaks correspond to crystal field levels, while green peaks correspond to secondary transitions from thermally populated energy levels.	87
5.29	Energy spectrum of (left column) $[\text{H } 0 \text{ } 0.6]$ and (right column) $[2 \text{ } 0 \text{ } \text{L}]$ at different temperatures (a) 1.6 K, (b) 6 K and (c) 10 K using an incident wavelength of 3.5 \AA	89
5.30	Energy spectrum of the $[0 \text{ } 0 \text{ } \text{L}]$ direction at different temperatures (a) 35 K, (b) 20 K, (c) 10 K and (d) 6 K using an incident wavelength of 5 \AA	90
6.1	Rietveld refinement of the powder x-ray diffractogram of NdB_4 to determine structural parameters. data points and Rietveld fit are shown in the upper curve, while the lowest curve is the difference between the observed and calculated intensity. The set of vertical dashes correspond to the expected nuclear Bragg positions of NdB_4	95
6.2	Single crystal Laue diffraction photographs of NdB_4 of (a) the $[100]$ and (b) the $[001]$ directions compared to simulated patterns from the OrientExpress software.	97
6.3	Temperature dependent magnetic susceptibility of NdB_4 in a field of $H = 1 \text{ kOe}$ for (a) $H \parallel c$ and (b) $H \perp c$, shading indicates the different magnetic phase and the inset shows the inverse susceptibility, χ^{-1} . .	98
6.4	The temperature dependent magnetic susceptibility curves of NdB_4 in different magnetic field for (a) $H \parallel c$ and (b) $H \perp c$. Each curve in (b) is subsequently offset by 0.002 emu/mol-Oe	99

6.5	Field dependent magnetisation measurements of NdB ₄ for $H \parallel c$ (black) and $H \perp c$ (red) taken in each of the three magnetic phases at temperatures of (a) 2 K, (b) 6 K and (c) 10 K. Solid curves correspond to the field being ramped up, while dash-dot curves are the field ramping down.	100
6.6	The evolution of the field dependent magnetisation measurements in temperatures between 0.5 and 10 K for $H \parallel c$	101
6.7	Temperature dependent magnetic susceptibility at $H = 10, 15$ and 20 kOe. Filled symbols correspond to measurements made using ³ He, while empty symbols correspond to ⁴ He measurements. Each curve is subsequently offset by 0.03 emu/mol-Oe.	103
6.8	Field dependent magnetisation measurements for $H \parallel c$ and $H \perp c$, made using a pulsed magnetic field up to 500 kOe for two temperatures, (a) $T = 1.5$ K and (b) $T = 8$ K.	105
6.9	Temperature dependent specific heat measurements for (a) $H \parallel c$ and (b) $H \perp c$ in increasing fields. Each curve is subsequently offset by 7 J/mol K.	106
6.10	Field dependent specific heat measurements of NdB ₄ for $H \parallel c$ at $T = 1.9$ K.	107
6.11	Temperature dependence of the magnetic contribution of the specific heat measurements for (a) $H \parallel c$ and (b) $H \perp c$. The inset shows the total heat capacity at high temperatures for NdB ₄ and the non-magnetic LuB ₄	108
6.12	Temperature dependence of the magnetic contribution of the heat capacity divided by the temperature. The red curve shows the magnetic entropy, which was determined by integrating the C_{mag}/T with respect to T	109
6.13	Temperature dependent resistivity measurements of NdB ₄ made for (a) $H \parallel c$ and (b) $H \perp c$. Each curve is subsequently offset by 2 and 3 $\mu\Omega - \text{cm}$ respectively. Field dependent resistivity measurements made for (c) $H \parallel c$ and (d) $H \perp c$. Each curve is subsequently offset by 2.5 $\mu\Omega - \text{cm}$	110
6.14	Single crystal neutron diffraction maps of ($h0l$) plane for NdB ₄ using the D7 diffractometer. Full xyz polarisation analysis was used to separate the intensity maps into (a) total scattering, (b) nuclear coherent, (c) nuclear spin incoherent scattering and (d) magnetic scattering. .	111

6.15	Single crystal neutron diffraction maps of ($h0l$) plane for NdB ₄ using the D7 diffractometer. The non spin-flip (left column) and spin-flip (Right column) channels at different temperatures (a) 30 K (b) 12 K, (c) 6 K and (d) 1.5 K are shown.	114
6.16	(a) line cuts in the spin flip channel for the [1.4 0 L] and [1.8 0 L] direction and (b) line cuts along the [1.8 0 L] for the non-spin-flip (NSF) and spin-flip (SF) channel.	115
6.17	Temperature dependence of the intensity of the Bragg reflections allowed by the nuclear symmetry of NdB ₄ (a) (210) and (b) (001) and the antiferromagnetic reflections (c) (100) and (d) (101). Shading indicates the separate magnetic phases.	116
6.18	Temperature dependence of the intensity of a selection of incommensurate reflections from NdB ₄ . Fill symbols corresponding to the temperature ramping and continuously measuring the intensity, while empty symbol correspond to stabilising and measuring the intensity at a particular temperature.	118
6.19	Line cuts from along the [1 0 L] direction for NdB ₄ taken using the D7 polarised neutron diffractometer. Measurements were made for three temperatures, 1.5, 6 and 12 K using the two channels (a) non-spin-flip and (b) spin-flip.	120
6.20	The irreducible representations of a $k = 0$ commensurate structure. .	121
6.21	Magnetic refinements of 3 separate magnetic structures corresponding to a mixture of two irreducible representations (a) D+E, (b) C+E and (c) D+A. The inset shows the resultant magnetic structure.	122
6.22	psi scans between psi=-90 and 90° at $T = 25$ K for the (a) (010) and (b) (050) reflections. Smaller psi-scans between -90 and -70° were taken for the (010) reflection at (c) 25 K and (d) 2 K.	124
6.23	Comparison of the observed and calculated intensity for the magnetic refinement of the intermediate temperature phase. (a) is a direct comparison between the two intensity, while (b) plots the intensity of the reflections as a function of $\sin \theta / \lambda$	125
6.24	Comparison of the observe and calculated magnetic intensities at $T = 2$ K.	126
6.25	Comparison of the observe and calculated magnetic intensities at $T = 2$ K and the incommensurate magnetic structure.	127

6.26	Temperature dependence of the intensity of (a) the antiferromagnetic (010) reflection each curve is subsequently offset by 1500 and (b) the Bragg (210) reflection in increasing fields each curve offset subsequently by 1000.	128
6.27	(a) Temperature dependence of the intensity of incommensurate (-1.85 0.15 0.4) reflection present in the intermediate temperature phase. (b) Field dependence of the intensity of incommensurate reflections in the low temperature phase.	130
6.28	Magnetic phase diagram of NdB ₄ for $H \parallel c$ constructed from neutron diffraction data for different reflections (inverted triangles and pentagons), and magnetisation (circles and triangles), resistivity (diamonds) and heat capacity (squares) measurements. All field dependent measurements were made by ramping the field up. The different magnetic structures is denoted with roman numerals.	131
6.29	Magnetic phase diagram of NdB ₄ for $H \perp c$ constructed from magnetisation (circles and triangles), resistivity (diamonds) and heat capacity (squares) measurements. All field dependent measurements were made by ramping the field up. The different magnetic structures is denoted with roman numerals.	132
6.30	Colour intensity plots from inelastic neutron measurements on NdB ₄ . Each measurement was taken in a different magnetic phase (a) IT at 5 K, (b) HT at 10 K and (c) the paramagnetic regime at 20 K using an incident energy of 12 meV.	134
6.31	Dynamic susceptibility of NdB ₄ taken at temperatures between 5–20 K using an incident energy of 12 meV.	135
6.32	Gaussian fits of $S(Q, \omega)$ of NdB ₄ in a range of temperatures with an incident energy of 12 meV. Blue peaks correspond to crystal field levels, while green peaks correspond to secondary transitions from thermally populated energy levels.	136
6.33	Colour intensity plots from inelastic neutron measurements on NdB ₄ . Each measurement was taken in a different magnetic phase (a) IT at 5 K, (b) HT at 10 K and the paramagnetic regime at (c) 20 K, (d) 50 K, (e) 100 K and (f) 150 K using an incident energy of 24 meV.	138
6.34	Dynamic susceptibility of NdB ₄ for temperatures between 20–150 K using an incident energy of 24 meV.	139

6.35	Gaussian fits of $S(Q, \omega)$ of NdB_4 in a range of temperatures with an incident energy of 12 meV. Blue peaks correspond to crystal field levels, while green peaks correspond to secondary transitions from thermally populated energy levels.	140
6.36	Colour intensity plots from inelastic neutron measurements on NdB_4 . Each measurement was taken in a different magnetic phases (a) IT at 5 K and (b) the paramagnetic regime at 20 K using an incident energy of 110 meV.	141

Acknowledgments

First and foremost I would like to thank my supervisor Oleg Petrenko for his guidance and support throughout my project. My thanks also go to Geetha Balakrishnan for help and supervision with crystal growth. Martin Lees for help with lab-based measurements and proof reading posters, papers, etc. As well as the other members of the superconductivity and magnetism group. Particularly my fellow Ph.D students for providing interesting discussions on all things and making my time at Warwick an enjoyable one. My particular thanks to Monica Ciomaga Hatnean for our frequent tea breaks and discussions.

I would like to thank all the instruments scientists at ISIS, Robert Brewley, David Veneshon and Tatiana Guidi and at the ILL, Björn Fåk, Hanna Mutka, Jacques Ollivier, Andrew Wildes, Bachir Ouladdiaf for help throughout the experiments and making beam time enjoyable. My particular heartfelt thanks to Navid Qureshi for his patience with my numerous FullProf questions and general help during the project.

Finally I would like to thank Rebecca Keeling for her continuing love and support, I would not be where I am today without her.

Declarations

The experimental work presented in this thesis was carried out between October 2013 and March 2017 at the University of Warwick's Physics department, the ISIS neutron facility at the Rutherford Appleton Laboratory (RAL) in Oxford and the Institut Laue Langevin (ILL) in Grenoble. All Rietveld and magnetic refinements were performed by myself with the advice of Navid Qureshi. Applied Field measurements on D10, ILL and the initial polarised neutron measurements on D7, ILL were performed by Oleg Petrenko in September 2011, however all data analysis was performed by myself. High field measurements on NdB_4 and HoB_4 were performed by Oleg Petrenko and Daniel Mayoh in September 2016, but all data analysis was performed by myself.

The thesis has been composed by myself and no part has been submitted for examination at any other institute. Parts of the work described in this thesis have been published as follows:

- D. Brunt, G. Balakrishnan, A. R. Wildes, B. Ouladdiaf, N. Qureshi, and O. A. Petrenko Physical Review B **95** (2017) 024410
- D. Brunt, G. Balakrishnan, D. Mayoh, M. R. Lees, D. Gorbunov, N. Qureshi, and O. A. Petrenko Scientific Reports (Submitted)
- D. Brunt, N. Qureshi, G. Balakrishnan, A. R. Wildes, B. Ouladdiaf, and O. A. Petrenko Physical Review B (Under preparation)

Additional work that will not be discussed further in this thesis have been published as follows:

- O. A. Petrenko, O. Young, D. Brunt, G. Balakrishnan, P. Manuel, D. D. Khalyavin, and C. Ritter Physical Review B **95** (2017) 104442

This work was also presented at the following conferences as a poster presentation:

- Highly Frustrated Magnetism (HFM) "*Characterisation and Crystal Growth of Rare-Earth Tetraborides*", Cambridge (2014)
- Frontiers of Unconventional Superconductivity and Magnetism (FUSM) "*Magnetic Properties of Frustrated Shastry-Sutherland Magnets, the Rare Earth Tetraboride*" Bristol (2015)
- European Conference for Neutron Scattering (ECNS) "*Magnetic Structure of Frustrated Shastry-Sutherland Magnets, Neodymium Tetraboride*" Zaragoza (2015)

and in the form of oral presentations:

- 2nd ISIS Student Meeting "*Magnetic Excitation in the Rare Earth Tetraborides*" Abingdon (2015)
- Magnetism "*Field Induced Incommensurate Magnetic Structure in Holmium Tetraboride*" Sheffield (2016)
- Theoretical and Experimental Magnetism Meeting (TEMM) "*Magnetic Structure of the frustrated Shastry-Sutherland magnet, neodymium tetraboride*" Abingdon (2017)

Abstract

Geometrically frustrated magnetism arises when the competing interactions are incompatible with the geometry of the lattice. This leads to a large ground state degeneracy and the system typically has difficulty establishing a unique ground state, often giving rise to complex intermediate magnetic phases and other unusual phenomena. Recently the rare-earth tetraborides, RB_4 , family of compounds has garnered attention as it is a rare experimental realisation of the frustrated Shastry-Sutherland lattice. Here the R^{3+} ions form a network of squares and triangles which is topologically equivalent to the Shastry-Sutherland lattice. The competing interactions lead to a rich variety of magnetic phase in the RB_4 family in both zero and applied magnetic field.

An investigation into two members of the RB_4 family, HoB_4 and NdB_4 is presented in this thesis. Both compounds show successive magnetic phase transitions, where HoB_4 orders with an incommensurate magnetic state at 7.1 K and orders with a non-collinear antiferromagnetic structure at 5.7 K, as well as magnetisation plateaux with fractional values of the saturation magnetisation of $\frac{1}{6}$, $\frac{1}{3}$ and $\frac{3}{5}$. NdB_4 orders at 17 K with a non-collinear antiferromagnetic structure followed by two distinct incommensurate structures at 7 K and 4.9 K. NdB_4 shows a single magnetisation plateau at $\frac{1}{5}$ the saturation magnetisation. Bulk property measurements of magnetisation, magnetic susceptibility, resistivity and heat capacity were used to map out and construct the complex phase diagrams of HoB_4 and NdB_4 with measurements down to 0.5 K and magnetic fields up to 500 kOe. HoB_4 shows six distinct magnetic phases, while NdB_4 has five. The stabilised magnetic phases were determined in zero field using single crystal neutron diffraction measurements utilising both polarised and un-polarised measurements. While the un-polarised neutron measurements were extended to investigate the magnetic structures of the field-induced magnetic structure in both HoB_4 and NdB_4 . Finally inelastic neutron scattering measurements on polycrystalline samples were used to map out the crystal field scheme in HoB_4 and NdB_4 . Single crystal samples were used to investigate the low temperature magnetic excitations in HoB_4 . The initial analysis of the inelastic neutron studies is presented.

Overall, both HoB_4 and NdB_4 exhibit a variety of magnetic phenomena, and their magnetic properties contribute to the understanding of the physics of the RB_4 family of compounds.

Chapter 1

Introduction

The first recorded discovery of a magnetic material was by the Greeks in the 6th century BC in regards to magnetite (Fe_2O_3) which was found on the island of Magnesia. However the first utilisation of magnetic materials is credited to the Chinese with the invention of the compass, which found its way to Europe in the 12th century. The study of magnetism then flourished in the 19th with the work by Oersted, Ampère, Faraday and Maxwell and the development of quantum mechanics in the 20th century laid the foundation of our understanding of magnetism and magnetic materials [1]. Magnetism and magnetic materials now permeate almost all parts of modern day life from computers to electrical power generation.

Magnetic moments acting in a cooperative way can give rise to behaviour quite different to that expected from isolated moments. This, coupled with the diversity of magnetic interactions present in many real systems leads to a rich variety of phenomena. One of which is magnetic frustration. Frustration occurs in a magnetic system when the spins are unable to orientate themselves to satisfy all the competing interactions. This results in the system being unable to find a unique ground state, often leading to many interesting and unexpected behaviour to arise. One particular set are geometrically frustrated materials where the frustration is arising due to the crystal symmetry.

What makes geometrically frustrated magnets of great interest is the wealth of different behaviour they display. For example, the pyrochlore system shows spin ice behaviour, where the moments have a “2-in-2-out” arrangement, reminiscent to the position of hydrogen in ice [2]. It is also possible to excite one of the spins to change its direction creating a “magnetic charge”, which act independently of one another and are analogues to magnetic monopoles [3]. The range of physics these materials provide gives us unrivalled insight. These magnets have also been shown

to exhibit analogues of solids, glassy and liquid phases. This diversity of phenomena, coupled with the multitude of experimental probes available for magnets makes them the obvious choice for investigation.

Many of the basic structures that gives rise to frustration have been extensively studied and now more complicated structures with further interactions are gaining a lot of attention in the search for unusual physics and to further our understanding. One set of compounds are the rare-earth tetraborides, a rare experimental realisation of the frustrated, square Shastry-Sutherland lattice. The interplay between the magnetic frustration, antiferromagnetic exchange and quadrupolar interactions has lead to a rich and diverse phase diagram in relatively low magnetic fields.

The magnetic properties of two rare-earth antiferromagnets, NdB_4 and HoB_4 , have been investigated and the results are presented in this thesis. The thesis is broadly comprised of two parts, initially a brief theoretical introduction is given in chapters 2 and 3, while the experimental techniques used and the results for NdB_4 and HoB_4 are presented in chapters 4 to 7. The first theoretical chapter is concerned with the discussion of magnetism, its origin, magnetic order, magnetic interactions among other topics are outlined and further magnetic frustration is introduced as well as giving a broad introduction to the magnetic properties of the RB_4 family. The crystal structure and magnetic structure are introduced in chapter 3, where the theory behind diffraction techniques are also introduced. This chapter primarily focuses on neutron scattering techniques, which form the foundation for numerous measurements presented in this thesis.

The bulk of the thesis is concerned with the magnetic properties of HoB_4 and NdB_4 . The sample preparation, crystal growth, methods and the equipment used for bulk characterisation measurements, as well as introducing the neutron instruments from large scale facilities (ISIS and the ILL) used are described in Chapter 4. The results for HoB_4 and NdB_4 are presented in chapters 5 and 6 respectively. They both follow a similar structure beginning with characterisation through compositional analysis with x-ray diffraction and then bulk magnetic properties using magnetic susceptibility, magnetisation, heat capacity and resistivity measurements. The chapters then focus on single crystal neutron diffraction, first with polarised neutrons and then using un-polarised neutrons in both zero and applied magnetic field. The initial analysis of the inelastic neutron scattering data is presented before summarising the chapter. Finally the main results of the investigations into both HoB_4 and NdB_4 are reviewed in chapter 7, along with current work and suggestions for possible future experimental and theoretical work on these compounds.

Chapter 2

Magnetism, Frustration and the Shastry-Sutherland Lattice

In this chapter a brief introduction to magnetism is presented. It is by no means an exhaustive review of the physics involved and will primarily focus on the relevant parts for the work presented in this thesis. A more complete description of the theory can be found in texts such as Ref. [4–6]. The chapter is split into three main parts, the first outlines more conventional magnetism, the second gives an introduction to frustration and frustrated lattices and the final part focuses on the frustrated Shastry-Sutherland lattice and gives a broad introduction to the properties of the RB_4 family.

2.1 Introduction to Magnetism

2.1.1 Magnetic Moment

The most fundamental object in solid-state magnetism is the magnetic moment, $\boldsymbol{\mu}$. Classically this can be equated to a current loop, where an electron orbiting a nucleus can be approximated as a current, I . A generalised formula for the magnetic moment moving, in plane, around a loop of arbitrary size can be given by [4]:

$$\boldsymbol{\mu} = \frac{1}{2} \int \mathbf{r} \times \mathbf{j}(\mathbf{r}) d^3r, \quad (2.1)$$

where $\mathbf{j}(\mathbf{r})$ is current per unit area at a point \mathbf{r} and is typically referred to as the current density. Considering an irregular loop, the current element can be rewritten $I dl = j \partial V$, thus giving:

$$\boldsymbol{\mu} = \frac{1}{2} \int \mathbf{r} \times \mathbf{j}(\mathbf{r}) d^3r = \frac{1}{2} \oint \mathbf{r} \times \mathbf{I} d\mathbf{l} = I \int d\mathbf{A}. \quad (2.2)$$

Consider a circular orbit, the current can be re-written in terms of velocity $I = qv/2\pi r$, substituting this into equation (2.2) gives:

$$\boldsymbol{\mu} = \frac{q}{4\pi r} \oint \mathbf{r} \times \mathbf{v} d\mathbf{l} = \frac{q}{4m\pi r} \int \mathbf{L} d\mathbf{l}, \quad (2.3)$$

where \mathbf{L} is the orbital angular momentum defined as $\mathbf{L} = \mathbf{r} \times m\mathbf{v}$. For the simple case of a circle, the integral equates to the circumference and the relationship between the magnetic moment and the angular moment is given by:

$$\boldsymbol{\mu} = \frac{q}{2m} \mathbf{L} = \gamma \mathbf{L} \quad (2.4)$$

where γ is the gyromagnetic ratio. A measure of the size of the magnetic moment can be determined from the simplest case of a single electron orbiting a hydrogen nucleus. This quantity is referred to as the Bohr magneton, μ_B :

$$\mu_B = \frac{e\hbar}{2m_e} = 9.274 \times 10^{-24} \text{Am}^2 \quad (2.5)$$

However a classical approach is not sufficient to describe the full theory of magnetism in solid-state materials and quantum mechanics is required for a fuller description. The orbital angular momentum, \mathbf{L} , is given by $\hbar\sqrt{l(l+1)}$, where l is orbital quantum number ($l = 0, 1, 2, \dots$) and \hbar is the reduced Planck constant and has a value of 1.055×10^{-34} Js. The electron also possesses an intrinsic angular momentum referred to as spin, \mathbf{S} . Similar to the orbital momentum the magnitude of the spin is given by $\hbar\sqrt{s(s+1)}$, where s is spin quantum number ($s = \frac{1}{2}$).

Atomic states can be described by the total angular momentum \mathbf{J} , which is the sum of the orbital angular momentum and the spin angular momentum given by:

$$\mathbf{J} = \mathbf{L} + \mathbf{S} \quad (2.6)$$

The combination of angular momentum quantum number can be used to estimate the ground state energy using Hund's rules. These three empirical rules are listed below in order of decreasing importance [7]:

- (1) Maximise S - Pauli exclusion principle prohibits two electron states from occupying the same quantum state simultaneously. To minimise the electronic repulsion, the orbitals are filled with the same spin state before occupying

them with the other.

- (2) Maximize L - Also reduces electron repulsion because if all electron precess around the nucleus in the same sense, it minimised the chance an electron will meet its neighbour.
- (3) Finally the value of J is found using $J = |L - S|$ if the energy shell is half filled, while $J = |L + S|$ if it is more than half full. This is linked with the spin-orbit coupling.

Hund's rules assume that only the ground state of the atom is populated and cannot be applied to excited states of atoms. The third rule arises from minimising the spin orbit coupling in the system. This, however, is only really applicable to $4f$ electron systems. For $3d$ electron systems crystal field effects are typically more important than the spin orbit coupling and orbital quenching is normally observed in these systems. Here the orbital angular momentum does not effect the size of the magnetic moment and only spin is important. This means that S is the important quantum number for transition metals, while J is the important quantum number for rare earth metals.

2.1.2 Magnetic Moment in an applied Magnetic Field

Magnetic materials contains vast amount of atoms and if there are unpaired electrons, magnetic moments as well. The magnetisation, \mathbf{M} , is defined as the magnetic moment per unit volume. The magnetisation depends on the size of the applied magnetic field, \mathbf{H} , and the magnetic flux density according to the following expression:

$$\mathbf{B} = \mu_0(\mathbf{H} + \mathbf{M}) \quad (2.7)$$

where \mathbf{B} is the magnetic flux density and is a scaled version of the magnetic field according to $\mathbf{B} = \mu_0\mathbf{H}$. In special cases, the magnetisation is linearly related to the applied field:

$$\mathbf{M} = \chi\mathbf{H} \quad (2.8)$$

where χ is a dimensionless quantity called the magnetic susceptibility. In this special case there is still a linear relation between \mathbf{B} and \mathbf{H} , namely:

$$\mathbf{B} = \mu_0(1 + \chi)\mathbf{H} = \mu_0\mu_r\mathbf{H}, \quad (2.9)$$

Ion	Shell	S	L	J	g_J	$\mu_{\text{eff}}(\mu_B)$
Nd ³⁺	4f ³	$\frac{3}{2}$	6	$\frac{9}{2}$	0.727	3.62
Ho ³⁺	4f ¹⁰	2	6	8	1.25	10.60

Table 2.1: The quantum numbers, Landé g value, the effective moment for select rare earth ions.

where μ_r is the relative permeability. Materials can be categorised based on the temperature dependent magnetic susceptibility, $\chi(T)$. If $\chi < 0$ the material is referred to as diamagnetic. For a diamagnetic substance, a magnetic field induces a magnetic moment which opposes the applied magnetic field that caused it. The diamagnetic susceptibility is given by:

$$\chi_{\text{dia}} = -\frac{N}{V} \frac{e^2 \mu_0}{6m_e} \sum_{i=1}^Z \langle r^2 \rangle. \quad (2.10)$$

where N is the number of ions (each with Z electrons) and r is the radius of the atom. In the case of a positive susceptibility ($\chi > 0$) there are a few possibilities, the first is a paramagnetic state. Here the magnetic moments are randomly oriented due to the temperature of the system. Application of the field tends to align the moments. The susceptibility is given by the following expression:

$$\chi_{\text{para}} = \frac{n \mu_0 \mu_{\text{eff}}^2}{3k_B T} \quad (2.11)$$

where n is the number of moments per unit volume and μ_{eff} is the effective magnetic moment of the system and can be calculated according to the L , S and J values of the system:

$$\mu_{\text{eff}} = g_J \mu_B \sqrt{J(J+1)} \quad (2.12)$$

where g_J is a constant known as the Landé g-value is determined by:

$$g_J = \frac{3}{2} + \frac{S(S+1) - L(L+1)}{2J(J+1)} \quad (2.13)$$

The values for quantum numbers as well as g_L and μ_{eff} are shown in Table 2.1.

The other options are ordered states such as ferromagnetism and antiferromagnetism, which are discussed further in section 2.1.5. The trend of the moments to align with the magnetic field can be seen by considering the energy of the magnetic moment in field given by:

$$E = -\boldsymbol{\mu} \cdot \mathbf{B}, \quad (2.14)$$

as can be seen the energy is minimised when the magnetic moments are aligned parallel to the field. When all the moments are aligned with the magnetic field the system is said to have saturated. The saturation magnetisation is given by:

$$M_{\text{sat}} = ng_j\mu_B J = n\mu_{\text{sat}} \quad (2.15)$$

where μ_{sat} is the saturated magnetic moment and is smaller than the effective moment.

2.1.3 Crystal Electric Fields

In condensed matter, crystalline materials are an assembly of ions and are bound together by long range electrostatic forces. The electrostatic interactions set-up an internal electric field referred to as the crystalline electric field (CEF). The size and nature of the crystal field effects depends crucially on the local environment. This can be analyzed using the method of Stevens operators [8, 9]:

$$\mathcal{H}_{\text{CEF}} = \sum_{n,m} B_m^n \mathcal{O}_m^n \quad (2.16)$$

where B_m^n are the crystal field parameters and \mathcal{O}_m^n are the Steven's operators. For many systems the number of crystal field parameters depends greatly on the symmetry of the system. To determine these parameters it is typical to perform inelastic neutron scattering to find the position of the crystal field levels. Once these are known, the experimental data is fitted and the crystal field scheme of the material can be found. The Wigner-Eckart theorem considers the J - J coupling in a system and allows the Steven's operators to be written in terms of J . Thus the crystal field levels in rare earth compounds depends on the quantum number, J and the number of levels can be estimated with $2J + 1$. For ions with a half integer J values, there are an even number of crystal field levels which pair up and forms Kramer doublets. However for integer values of J the crystal field can have anywhere up to $2J + 1$ singlet levels, this can lead to large degeneracies at low temperatures and with the onset of magnetic order, lead to a spontaneous symmetry breaking of the crystal structure and is referred to as the Jahn-Teller effect. This typically manifests as a lattice distortion with the typical example being a distortion of the octahedra, but is not limited to such cases [10]. This thesis presents one of each case, Neodymium, where $J = \frac{9}{2}$, which is a Kramer ion and thus we expect five

doublets, while Holmium has $J = 8$ and can have up to 17 singlet states and thus susceptible to the Jahn-Teller effect.

2.1.4 Magnetic Interaction

When a collection of magnetic moments are arranged in close proximity to one another, they are able to exert an influence on the neighbouring moments and this gives rise to the plethora interesting magnetic phenomena that is observed in magnetic materials. The first step to describing the magnetic interaction is to considering the Hamiltonian, \mathcal{H} . The Hamiltonian of the Heisenberg model is given by [11]:

$$\mathcal{H} = - \sum_{i,j} J_{ij} \mathbf{S}_i \cdot \mathbf{S}_j \quad (2.17)$$

where J_{ij} is the exchange constant between the i^{th} and j^{th} spins. The exchange falls into a number of different categories. If the electrons on neighbouring magnetic atoms interact via an exchange interaction, this is known as direct exchange. While direct exchange is generally present, it is often not a very important mechanism, particularly in materials involving rare earth ions. A fuller description needs to takes account for both the localised and band character of the electrons. This means that it is necessary to consider indirect exchange interactions in many magnetic materials.

In metals the exchange interaction between the magnetic ions can be mediated by the conduction electrons. A localised magnetic moment spin-polarises the conduction electrons and in turn this polarisation couples to a neighbouring localised magnetic moment a distance r away. This is known as the RKKY (Ruderman, Kittel, Kasuya and Yosida) interaction. The coupling takes the form of an r -dependent exchange $J_{\text{RKKY}}(r)$ given by [4]:

$$J_{\text{RKKY}}(r) \propto \frac{\cos(2k_{\text{F}}r)}{r^3} \quad (2.18)$$

where k_{F} is the Fermi wave vector and at large r the interaction is long range and has an oscillatory dependence on the distance between the magnetic moments. Depending on the size of the separation it may be either ferromagnetic or antiferromagnetic [11].

In addition another example of a magnetic interaction that can be considered is the magnetic dipolar interaction. Two magnetic dipoles μ_1 and μ_2 separated by \mathbf{r} have an energy equal to [4]

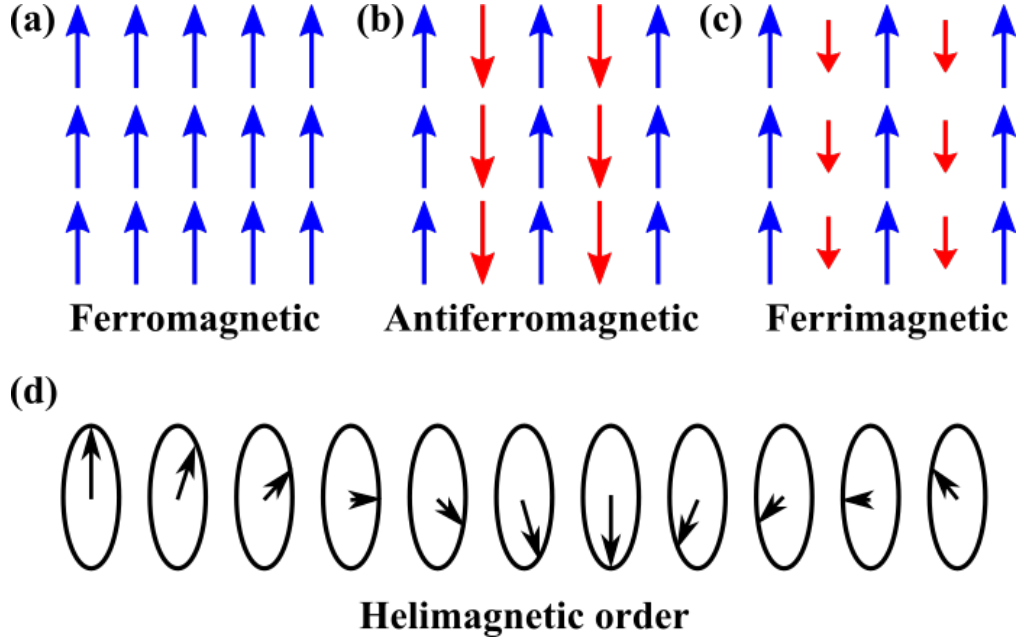


Figure 2.1: Various spin arrangements in ordered states (a) ferromagnetic, (b) antiferromagnetic, (c) ferrimagnetic and (d) helimagnetic order.

$$E = \frac{\mu_0}{4\pi r^3} \left[\boldsymbol{\mu}_1 \cdot \boldsymbol{\mu}_2 - \frac{3}{r^2} (\boldsymbol{\mu}_1 \cdot \mathbf{r})(\boldsymbol{\mu}_2 \cdot \mathbf{r}) \right] \quad (2.19)$$

which depends on the separation and their degree of mutual alignment.

2.1.5 Magnetic Order

In some magnetic materials there is a spontaneous magnetisation in the absence of an applied magnetic field. This is arising due to the interactions between the magnetic atoms (as discussed in the previous section). The spontaneous magnetic order depends on the temperature of the system with order occurring at low temperatures. At high temperatures the thermal fluctuations are large enough to overcome the exchange interactions and the magnetic moments are considered to exist independently of one another. This is the paramagnetic regime and the system possesses no order and the moments are randomly aligned (as was briefly discussed in section 2.1.2).

This gives rise to a characteristic ordering temperature, below which the magnetic interactions start to dominate and the system orders. The order comes from minimising the Hamiltonian in equation (2.17). The favoured alignment of the neighbouring moments depends on the sign of exchange constant, J_{ij} . When $J_{ij} > 0$

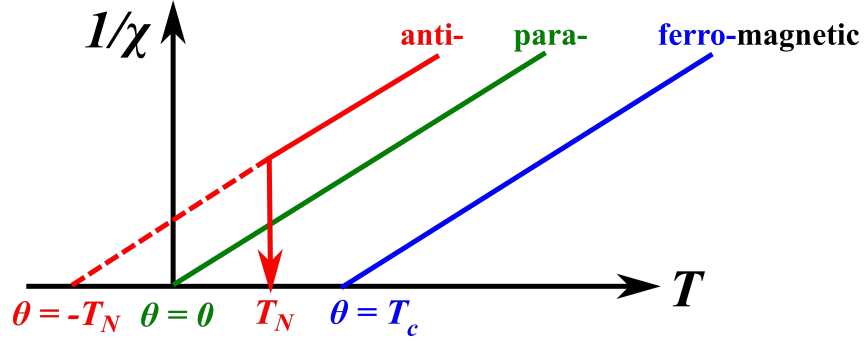


Figure 2.2: Inverse magnetic susceptibility curves for paramagnets, ferromagnet and antiferromagnets.

the energy is minimised when there is a parallel alignment of the spins, while for $J_{ij} < 0$ an anti-parallel alignment is favoured. When all magnetic moments have the same magnitude these exchanges lead to two forms of magnetic order; ferromagnetic ordering and antiferromagnetic ordering respectively. These two types of magnetic order are represented in Fig. 2.1(a) and (b).

Depending on the exchange interaction the ferromagnetic and antiferromagnetic ordering will be of different strengths with an associated temperature at which the magnetic moments will possess sufficient thermal energy to overcome the exchange interactions. Above this temperature the moments become disordered. This temperature can be quantified via the Curie-Weiss law:

$$\chi = \frac{C}{T - \theta_{CW}}, \quad (2.20)$$

where the Curie-Weiss temperature, θ_{CW} gives an indication of the magnetic ordering. A positive value indicates ferromagnetism, while a negative value indicates antiferromagnetism. The ordering temperatures are referred to as the Curie and Néel temperatures for a ferromagnet and antiferromagnet respectively. C is the Curie constant, where $C = n\mu_0 g_J^2 J(J+1)/3k_B$. In low applied fields and at high temperatures some magnetic materials will tend to behave like paramagnets, so the effective moment can be calculated from the Curie constant by using:

$$\mu_{\text{eff}} = \left[\frac{3k_B}{\mu_0 N_A \mu_B^2} \right]^{\frac{1}{2}} \sqrt{\chi_m T} \quad (2.21)$$

which reduces to $\mu_{\text{eff}} = 2.827 \sqrt{\chi_m^{\text{cgs}}}$ when the molar susceptibility is in the cgs system of units. The Curie-Weiss temperature and Curie constant can be determined

from the inverse susceptibility curves, the characteristic curves for a ferromagnet, antiferromagnet and a paramagnetic are shown in Fig. 2.2.

One of the ways to treat antiferromagnetic order assumes that there are two interpenetrating sublattices, one of which has the moments pointing up, while the other points down with equal magnitude. However situations due to the crystal structure can arise where the two sublattices are not equivalent. This can be due to ions being in different oxidation states. As different oxidation states have differing number of electrons, the magnetic moment can then vary between the oxidation states. Thus the spontaneous magnetisation of the two sublattices may not be equal and opposite and therefore will not necessarily cancel out. The material will have a net magnetisation and this phenomenon is known as ferrimagnetism (Fig 2.1(c)). The sublattices do not necessarily have to have the same temperature dependences either and thus can have different ordering temperatures.

The above structures can generally be considered as commensurate with the crystal structure, that is it can be represented with an integral number of crystallographic unit cells. In some systems, incommensurate order can also be achieved. These structures are normally complicated, and act as an intermediate magnetic phase before long range order is achieved. An example of this is helical order. The crystal structure is such that the atoms lie in layers. One of the situations there are layers of magnetic moments, where there is a ferromagnetic alignment of moments within the layers. There are then interactions between the layers, which can be described by a nearest-neighbour interaction, J_1 and next nearest neighbour exchange constant J_2 . If the angle between the magnetic moments in successive basal planes is θ , then the energy of the system can be written as:

$$E = -2NS^2(J_1 \cos \theta + J_2 \cos 2\theta) \quad (2.22)$$

the energy is minimised when $\partial E / \partial \theta = 0$, which gives:

$$(J_1 + 4J_2 \cos \theta) \sin \theta = 0 \quad (2.23)$$

This means solutions are either $\sin \theta = 0$, that is $\theta = 0$ or $\theta = \pi$ (ferromagnetism or antiferromagnetism) or:

$$\cos \theta = -\frac{J_1}{4J_2}. \quad (2.24)$$

This last solution corresponds to helical order and is favoured over either ferromagnetism or antiferromagnetism when $J_2 < 0$ and $|J_1| < 4|J_2|$. The exchange interaction in helical magnets are generally long range such as the indirect RKKY

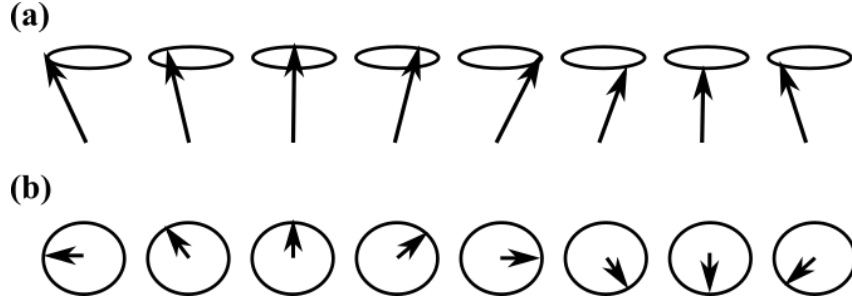


Figure 2.3: A spin wave on a line of spins, (a) a perspective view and (b) a view from above.

interaction, mediated by the conduction electrons.

2.1.6 Excitations

There are a diverse range of excitations possible in solid state systems. In magnetic systems the most common collective excitations are phonons and magnons. At any finite temperature the atoms in a lattice undergo thermal vibration. These vibrations are quantised into discrete packets referred to as phonons. Phonons are then characterised by a dispersion relation, which relates the angular frequency $\omega(k)$ as a function of wavevector k . The dispersion relation for 1D phonons is given by:

$$\omega(k) = \sqrt{\frac{2K}{m} (1 - \cos(ka))} \quad (2.25)$$

where a is the size of the box the oscillator is in and K is the spring constant, which represents the bonds between atoms. This dispersion relation is one of multiple branches and is referred to as the acoustic, the other being the optical branches. Acoustic phonons have a relation, where $\omega \propto k$. In particular, at $k = 0$ their energy is zero and it increases with increasing k . This shape is characteristic of phonons and will be observed in the inelastic neutron scattering as an increase in intensity with increasing k . The optical phonons, on the other hand have non-zero energy at $k = 0$ and tend to be flatter modes.

In complete analogy to phonons, long-range ordered magnetic systems will have quantised fluctuations of the spins, called magnons and are typically characterised by spin waves propagating through the system. The fluctuation can arise due to a perturbation from the neutron. This can also be thought of in terms of quantum mechanics, with the neutron causes the spin to fluctuate between spin up and down (imagine a plucked string), which creates a spin wave [12]. Magnons also

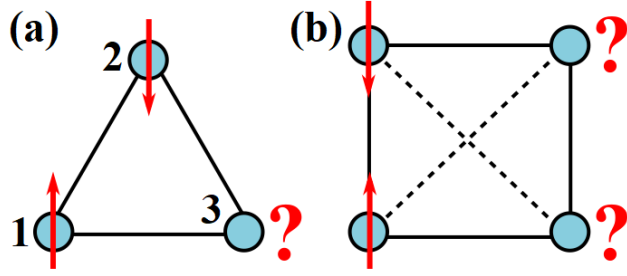


Figure 2.4: Frustrated plaquettes

have a well defined characteristic dispersion relation, which are different depending on the type of magnetic order present in the system. For example the dispersion relation for a one-dimensional chain of spins is given by [4]

$$\omega(k) = \frac{4JS}{\hbar}(1 - \cos(ka)) \quad (2.26)$$

where the spin wave for this is shown in Fig. 2.3.

2.2 Frustration

It was assumed throughout the previous section that the material was able to minimise their energy and an ordered state is achieved. However, for some systems this is not always the case and there is an inability for the system to satisfy all the competing interactions. This leads to a large ground state degeneracy, which normally suppresses long range order [5]. In some cases this can prevent long range order down to the lowest achievable temperatures [13–15]. The suppression of long range order leads some systems to exhibit unusual properties and magnetic structures. This suppression of magnetic order has lead to an empirical measure of the frustration, by comparison of the Curie-Weiss and Néel temperature [16]:

$$f = \frac{\theta_{\text{CW}}}{T_{\text{N}}} \quad (2.27)$$

where for $f > 1$ corresponds to frustrated system. While this serves as an indicator, care must be taken when applying this rule as thermal fluctuations can influence this ratio and thus $f \neq 1$ can arise in systems with no frustration which is often true for antiferromagnets. To be sure of frustration the crystal lattice, symmetries and interactions should be considered.

Magnetic frustration can manifest in numerous ways and can generally be

divided into two broad categories; spin glasses and geometric frustration [16]. In spin glass systems, due to a degree of disorder in the magnetic sites a conflict between magnetic ions arises, suppressing any conventional long-range order to be established. However these systems display a distinct magnetic phase below a characteristic “freezing temperature” in which the spins are aligned in random directions [17]. The second type of frustration is termed geometrical frustration and is arising due to the lattice itself [16]. Here the structure of the crystal lattice leads the clashing of the magnetic interaction. This is illustrated by the simplest situation in which geometric frustration is observed. Considering a triangular arrangement of magnetic moments coupled by antiferromagnetic nearest neighbour interaction (Fig 2.4(a)). Atoms 1 and 2 minimise the energy when the moments are aligned anti-parallel to one another. However, the third moment cannot be anti-aligned to the other moments simultaneously leading to frustration [18]. The triangular lattices gives rise to geometric frustration, however the type and range of interactions, among other factors that can give rise to frustration in lattices that would otherwise not show it [16]. This can be demonstrated by considering the moments arranged on a square plaquette (Fig 2.4(b)). Although the system is not frustrated when only nearest neighbour interactions are important, when next nearest neighbour interactions become important it begins to display frustration [19].

These plaquettes can be extended to form lattices which appear in many real systems [19]. Typically the geometrically frustrated lattices are based on corner- or edge-sharing triangles or tetrahedra. The materials based on corner-sharing are typically more susceptible to frustration and this can be seen by considering the degeneracy of the system. To understand this, consider the classical nearest neighbour antiferromagnetic Hamiltonian observed in equation (2.17), where the sum is taken over nearest neighbour bonds only. The spins can be represented in two ways: the discrete Ising spins that point in one of two directions (up or down) or the Heisenberg vector spins ($S = (S_x, S_y, S_z)$) of fixed length and point in any direction. Considering the latter, the degeneracy can be seen using simple counting arguments, similar to those used by Maxwell in 1864 [20]. The size of the degeneracy is given by the number of degrees of freedom in the ground state [20]:

$$F = D - K, \tag{2.28}$$

where D is the total number of degrees of freedom and K is the number of constraints placed upon the system. These arguments are best applied when considering clusters of q mutually interacting spins. Rewriting the Hamiltonian [21]:

$$H = \sum_{i,j} J_{ij} S_i \cdot S_j = \frac{J}{2} L_{\text{sum}}^2, \quad (2.29)$$

where $L_{\text{sum}} \equiv \sum_{i=1}^q S_i$ is the total spin of the unit. The energy is clearly minimised when L_{sum} vanishes, corresponding to the ground state. This places the constraint that $L_x = L_y = L_z = 0$. As the length of the vectors are fixed the only free parameter is the direction the vector points. This can be described with two parameters (e.g. Longitude and Latitude). This means there are two degrees of freedom associated with the spins. This leads to $D - K = 2q - 3$. Three of these correspond to global rotation, meaning $2q - 6$ remain [20]. These counting arguments can be generalised to treat lattices rather than isolated clusters of spins. Minimising the number of constraints will maximise the ground-state degeneracy and this is seen in vertex sharing clusters. This means that lattices in which the moments are shared between more triangles will be less frustrated. For example in the triangular lattice with edge sharing triangles each moment is shared between 6 triangles, where as in the corner sharing lattice each moment is only shared between two making it more frustrated [20].

The large ground state degeneracy raises the question of whether the system can freely move between ground states or whether there is an energy barrier separating them. In each of the ground states the internal energy is identical, this is not the case for the free energy. Where the internal energy is the quantity that is normally minimised at low temperature this becomes the free energy. This gives different entropic weighting to each ground state and if the fluctuations are very small, a situation can arise where the system effectively spends all of its time fluctuating around a special state [22]. Thus, this is known as order-by-disorder, as order is induced by thermal fluctuations which are normally associated with disorder in a system [22].

In general the nearest neighbour Heisenberg Hamiltonian, \mathcal{H} is only an approximation. A more accurate way to represent different models is to apply a perturbation such that the Hamiltonian looks like $\mathcal{H}_{\text{tot}} = \mathcal{H} + \mathcal{H}_P$, where \mathcal{H}_P is one of many possible perturbations. These perturbations could take many forms, such as further neighbour exchange, single-ion anisotropy, magnetic dipolar interactions, etc. [21].

There are a large number of frustrated systems in both two and three dimensions and some of these are illustrated in Fig. 2.5. The two dimensional structures include the simple edge-sharing triangular lattice, and corner-sharing triangular networks such as the kagomé lattice [23, 24] as well as the honeycomb lattice [25].

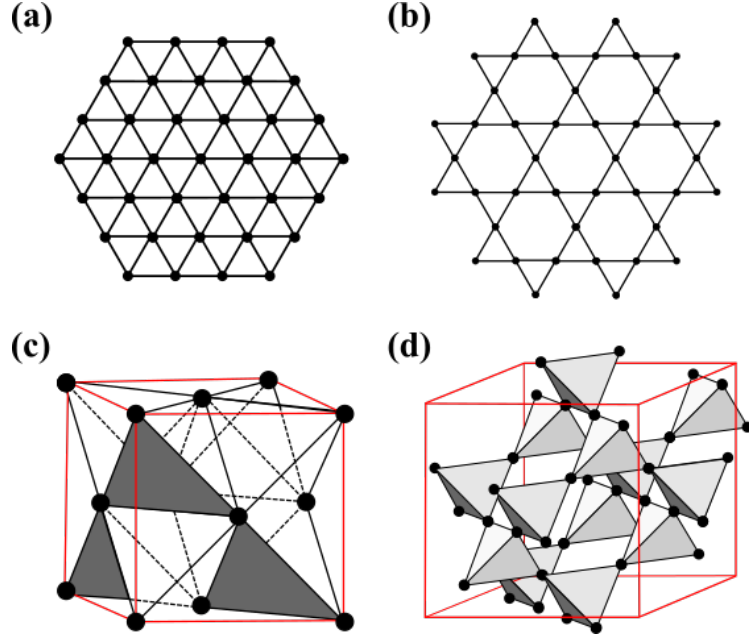


Figure 2.5: A selection of two and three dimensional frustration lattices (a) Triangular, (b) Kagomé, (c) face centred cubic and (d) pyrochlore lattices.

Figure 2.5(c) and (d) shows the three dimensional analogues of the triangular and kagomé lattice respectively. The face centred cubic structure is frustrated cubic lattice, a notable example of this is the double perovskites [26, 27], while the pyrochlore lattice is highly frustrated example of corner sharing tetrahedra [28, 29]. Other corner sharing arrangements in three-dimensions include the garnets [30, 31] and kagomé staircase [32] compounds. This is just a very narrow cross section of the frustrated lattices realised in nature showing the depth and the diversity of the field.

2.3 Shastry-Sutherland Lattice

The Shastry Sutherland lattice (SSL) is a frustrated lattice that can be described as a square lattice with antiferromagnetic couplings J_1 and additional diagonal antiferromagnetic couplings J_2 every other square (Fig. 2.6(a)). The Hamiltonian for such a system is given by [33]:

$$\mathcal{H} = J_1 \sum_{\text{edges}}^N \mathbf{S}_i \cdot \mathbf{S}_j + J_2 \sum_{\text{diagonal}}^N \mathbf{S}_i \cdot \mathbf{S}_j. \quad (2.30)$$

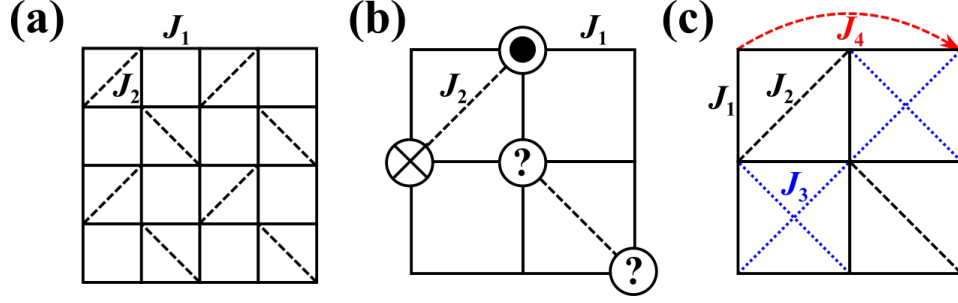


Figure 2.6: (a) The Shastry-Sutherland Lattice, (b) demonstration of the frustration occurring in the SSL when J_2 is an antiferromagnetic exchange and (c) zoomed in view of the exchange interactions observed in the Shastry-Sutherland lattice.

The Hamiltonian can be modified to include an applied magnetic field, B [34]

$$\mathcal{H} = J_1 \sum_{\text{edges}} \mathbf{S}_i \cdot \mathbf{S}_j + J_2 \sum_{\text{diagonal}} \mathbf{S}_i \cdot \mathbf{S}_j - B \sum_i S_i^z. \quad (2.31)$$

The lattice has been studied extensively with a number of different models, such as the Heisenberg, Ising and XXZ model. Each have a number of different regimes that can be investigated. For example consider the quantum limit of the Heisenberg model. This gives a solution to equation (2.30) as [35]:

$$|\psi_G\rangle = \prod_{\alpha} |S\rangle_{\alpha}, \quad (2.32)$$

where α denotes nearest neighbour J_1 interaction and $|S\rangle_{\alpha}$ represents a singlet state [35]. It has been shown that the nature of this ground state correlations in $|\psi_G\rangle$ is seen to be liquid like, and thus referred to as the quantum spin liquid phase [36].

For the Ising case, consider $J_x = J_y = 0$ and $B = 0$ for spin 1/2. For the case $J_1/J_2 > 1$, the ground state entropy is $\mathcal{O}(1)$, while for $J_1/J_2 < 1$ the entropy is $\mathcal{O}(N)$. The case where $J_1/J_2 = 1$ is much more complex, since more configurations are allowed. Shastry and Sutherland found it could be mapped to a 10 vertex model containing $N/2$ sites with two sublattices [36]. The Ising case is where frustration arises which is demonstrated in Fig. 2.6(b). Here magnetic moments sit at the vertices of the squares, as the diagonal exchange is antiferromagnetic, the two spins will align anti-parallel to one another. When additional diagonal bonds are considered, regardless of the type of nearest neighbour interaction the system is unable to satisfy the competing interactions, leading to frustration.

The final case is the classical limit for the Heisenberg model, this is applicable

for the when $S \rightarrow \infty$. Due to the large angular momentum of R ions, this case is the most relevant for the RB_4 . In zero magnetic field the lowest energy configuration is for the spins to be coplanar. For the case when $J_1/J_2 > 1$, a Neel ordered state is formed, otherwise a spiral state with an angle $\phi = \pi \pm \arccos(J'/J)$ between nearest neighbour spins [33]. Similar to the helical order outlined in section 2.1.5. While the lattice only considers nearest and next nearest neighbour interaction a small perturbation to the Hamiltonian is to include further neighbour interactions, which are depicted in Fig 2.6(c), where J_3 corresponding to a diagonal across the square and J_4 corresponds to an exchange interaction across every other atom. Considering these further neighbour interactions is incorporated into simple models such as the anisotropic next nearest neighbour interaction (ANNNI) model. This model has been important in describing compounds with complex phase diagram such as CeSb [37]. Despite its relative simplicity it is able to exhibit complex phase diagrams, which include commensurate, incommensurate phases as well as field induced features [38].

There have been a few experimental realisation of the Shastry-Sutherland lattice, however the most notable being $\text{SrCu}_2(\text{BO}_3)_2$, where the Cu ions form a sublattice that is equivalent to the Shastry-Sutherland lattice. $\text{SrCu}_2(\text{BO}_3)_2$ drew a lot of attention due to its interesting magnetic properties including fractional magnetisation plateau at $\frac{1}{8}$, $\frac{1}{4}$ and $\frac{1}{3}$ of the saturated magnetisation [39, 40]. Recently it was found that the RB_4 family was an experimental realisation of the Shastry-Sutherland lattice.

2.3.1 Rare-Earth Tetraborides

The rare earth tetraborides crystallise into a tetragonal structure with space group $P4/mbm$. The lattice can be separated into two parts; a boron and a rare earth sublattice. The boron sublattice can be described as chains of B6 octahedra that extend along the c -axis, these octahedra are bonded by pairs of B2 in the ab -plane. This forms rings between the octahedra (Fig. 2.7(a)) [41].

The rare earth ions sit above and below the boron rings that are between the octahedral [41]. They form a network consisting of squares and triangles that is topologically equivalent to the Shastry Sutherland lattice [42], highlighted by the the solid and dashed lines (Fig. 2.7(b)).

Many metal borides are known to be electron deficient (i.e. the number of conduction electrons are reduced compared to the number of valence electrons available). This is due to the strong participation of electrons in the B-B bonds [43]. However, these materials are metallic and this could suggest there is a strong

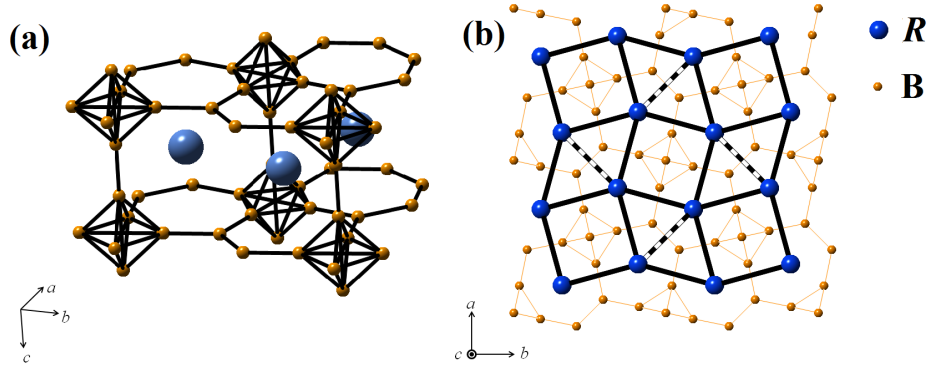


Figure 2.7: (a) Section of RB_4 lattice to illustrate the B_6 octahedra forming chains, as well as the rings above and below the R^{3+} ions. (b) ab plane of RB_4 to illustrate how the SSL mapped to the network of squares and triangles formed by the R^{3+} ions.

variation in the physical principles within the family of compounds [43]. Due to the metallic nature of the family, the RKKY interaction is believed to be important, but previous studies have also suggested the quadrupolar interaction also plays a part [44–46].

The magnetic properties of the RB_4 family of compounds were investigated by Buschow *et al.* [47]. Here the magnetic susceptibility on polycrystalline samples was reported. The predominant ordering is antiferromagnetic with a disparity between θ_{CW} and T_N suggesting that frustration could play a role in this family of compounds [47]. Quite striking is PrB_4 , which is the exception to the rest of the RB_4 family and orders ferromagnetically at 15 K [48]. Magnetisation studies have shown Ising like anisotropy appears to be common among the RB_4 compounds. The classical and Ising-like spins further suggests the possibility of frustration [36].

Since the work of Buschow, the members have been studied in detail. Single crystals have been grown in a variety of methods [49–51]. A review of the early work was given by Etourneau, however significant insight into the RB_4 compounds have been obtained since the review paper [52]. In particular ErB_4 , GdB_4 , DyB_4 , TbB_4 and TmB_4 have been studied in depth. ErB_4 and GdB_4 both order antiferromagnetically at 15.4 K [53] and 42 K [54] respectively. Neutron diffraction experiments on ErB_4 revealed the magnetic structure is a collinear arrangement of the spins pointing along the c -axis [55]. The magnetic structure of GdB_4 was more controversial with debate between a collinear and non-collinear ordering in the ab -plane [56–58], however spherical neutron polarimetry settled the debate indicating non-collinear

antiferromagnetic order in GdB_4 [59]. DyB_4 , TbB_4 and TmB_4 all show successive phase transitions. DyB_4 shows two transitions at 20.3 K and 13 K [45, 60], the magnetic structure was determined to order (upon cooling) with a collinear antiferromagnetic structure, while the low temperature phase was found to have static order with short range correlations forming due to the frustration [55, 61]. TbB_4 orders at 44 K [62] with a non-collinear antiferromagnetic with the moments in the ab -plane [63, 64]. There is a further transition to an incommensurate phase at 23 K, the structure of which remains undetermined. TmB_4 on the other hand shows three magnetic phase transitions, two at 11.7 K and 10.4 K to incommensurate phases [65] and then to antiferromagnetically with a non-collinear structure in the ab -plane [66]. Across these studies, the typical ordering within the RB_4 family was found to be antiferromagnetic with a non-collinear structure in the ab -plane.

One of the most striking features of the RB_4 family are the presence of magnetisation plateaux at fractional values of the saturation magnetisation, which will be referred to as fractional magnetisation plateaux throughout this thesis. These fractional magnetisation plateaux are indicative of a magnetic state and are a common feature to the RB_4 family. A $\frac{1}{2}$ -plateau is observed in ErB_4 [67], DyB_4 [60], TbB_4 [68] and TmB_4 [69]. TbB_4 and TmB_4 also displaying further fractional magnetisation plateau at $\frac{1}{3}$ and $\frac{1}{8}$ respectively. The field induce magnetic states in the RB_4 family show a diverse range of structures, these range from a simple ferrimagnetic structure in ErB_4 [70]. TmB_4 shows two sets of striped structures, for the $\frac{1}{2}$ plateau, there are strips of antiferromagnetic spins separated by equally sized strips of ferromagnetic spins. There is a similar structure on the $\frac{1}{8}$ -plateau, but the antiferromagnetic region spans 7 units cells, separated by a single unit cell of ferromagnetic spins [71]. Finally TbB_4 has an expansion of the unit cell in the ab -plane, where half the cell orders in plane and the other half has a ferromagnetic component, again making a stripe like structure. The nature of the $\frac{1}{2}$ magnetisation plateau state in DyB_4 still remains undetermined.

The final members of the RB_4 to be studied are HoB_4 , NdB_4 and SmB_4 , but literature is lacking for the latter two. For SmB_4 all that is known is that it has successive phase transitions at 25 and 7 K and orders antiferromagnetic [72]. The main focus of this thesis is on HoB_4 and NdB_4 and a description of the previous work done on both these compounds is presented in chapters 5 and 6 respectively.

Chapter 3

Scattering Theory

Diffraction of radiation, whether x-ray photons, neutrons or electrons, is an invaluable technique in the investigation of crystal (and magnetic) structures. This chapter serves as a brief overview to the theory of scattering, with a particular focus on neutron scattering. It is by no means an exhaustive review of the subject, but will focus on the relevant parts for the work presented in this thesis. A more complete coverage of the theory can be found in texts such as [73–76]. The chapter will begin with a brief description of the crystal and magnetic structures. The chapter will then move on to scattering theory beginning with x-ray diffraction, highlighting the diffraction condition, Bragg’s Law. Neutron scattering will then be considered starting with neutron production followed by sections on nuclear, magnetic, polarised and inelastic neutron scattering.

3.1 Crystal and Magnetic Structures

Within solid state materials the crystal structure can be described by the crystal lattice. The crystal lattice is an infinite set of points, with a periodic structure and is defined by three basis vector; \mathbf{a} , \mathbf{b} , and \mathbf{c} . Due to the periodic nature any point in the crystal lattice can be found using the following vector:

$$\mathbf{R} = U\mathbf{a} + V\mathbf{b} + W\mathbf{c} \tag{3.1}$$

where U, V , and W are constants with integer values. The lattice can then be convolved with atomic basis to create the crystal. In the simplest case this would be a single element, but can range up to complicated compounds. The structure can then be described by its base building blocks referred to as the unit cell. The dimensions are usually denoted with a , b and c in accordance with the basis vectors

and the angles between them are α , β and γ . The position on the atom in the unit cell can be described by:

$$\mathbf{r} = x\mathbf{a} + y\mathbf{b} + z\mathbf{c} \quad (3.2)$$

where xyz are fractional coordinates in the unit cell. Thus any point in the crystal structure can be described by a translation of the unit cell by combining equations (3.1) and (3.2) to give:

$$\mathbf{T} = \mathbf{R} + \mathbf{r} \quad (3.3)$$

There are six types of three dimensional unit cell; triclinic, monoclinic, orthorhombic, tetragonal, hexagonal and cubic. Depending on the number and position of lattice points, these six types can be classed as either primitive, face-, body or side-centred unit cells giving rise to the 14 Bravais Lattices. The position of atoms in the unit cell can then be described by a set of symmetry operations which further sub divides the 14 Bravais lattices into 230 space groups, which are most commonly used for the description of the crystal structure.

For diffraction experiments the reciprocal lattice is more useful as it facilitates the interpretation of the diffraction data. This forms a new set of basis vectors using the real lattice vectors. These are given by:

$$\mathbf{a}^* = 2\pi \frac{\mathbf{b} \times \mathbf{c}}{\mathbf{a} \cdot (\mathbf{b} \times \mathbf{c})}, \quad \mathbf{b}^* = 2\pi \frac{\mathbf{c} \times \mathbf{a}}{\mathbf{a} \cdot (\mathbf{b} \times \mathbf{c})}, \quad \mathbf{c}^* = 2\pi \frac{\mathbf{a} \times \mathbf{b}}{\mathbf{a} \cdot (\mathbf{b} \times \mathbf{c})} \quad (3.4)$$

Similarly to the real space any point in the reciprocal lattice can be described with the following vector:

$$\mathbf{G} = h\mathbf{a}^* + k\mathbf{b}^* + l\mathbf{c}^* \quad (3.5)$$

where hkl are Miller indices and define sets of lattice planes. A full description of both the crystal and reciprocal lattices can be found in Ref. [74, 77].

In a similar manner to the crystal structure, the magnetic structure can be described by the periodic repetition of a magnetic unit cell. For simplicity we use a description based on the nuclear unit cell and a *propagation vector*, \mathbf{k} , that describes the relations between moment orientations of equivalent magnetic atoms in different nuclear unit cells [78]. In a commensurate magnetic structure where the magnetic and crystallographic unit cell are identical giving rise to a propagation vector of $\mathbf{k} = (0, 0, 0) \equiv 0$. The magnetic unit cell can also be larger than

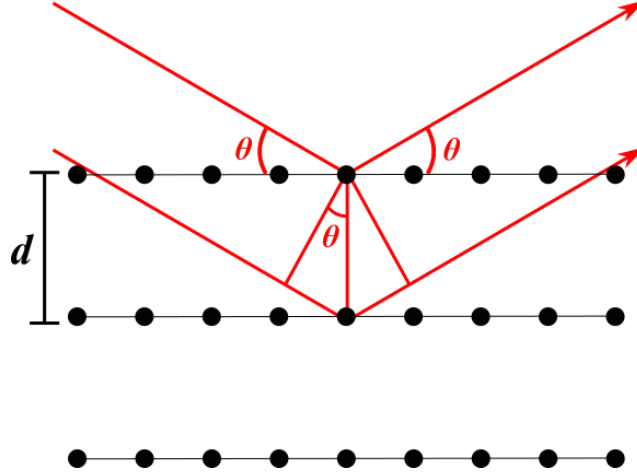


Figure 3.1: Schematic of the diffraction process where beams of radiation are scattering by parallel planes of atoms.

the crystallographic unit cell due to a reduction of symmetry. This is the case in a simple antiferromagnetic structure, where the magnetic unit cell doubles in size. For example if the antiferromagnetic order propagates along the c -axis, the propagation vector is given by $\mathbf{k} = (0, 0 \frac{1}{2})$. Additionally there is a situation, where there is no simple relation between the structural and magnetic cells. This implies a spin density wave propagating through the lattice in the direction of the incommensuration and at least one term in the propagation vector would be non-integer.

3.2 Diffraction

The basic diffraction condition can be illustrated using Fig. 3.1. The incoming beams of radiation are scattered by parallel planes of atoms separated by a distance, d . A coherent superposition of the waves is achieved when the path difference between beams scattering from adjacent planes is equal to an integral number of wavelengths, λ , leading to [74]:

$$n\lambda = 2d \sin \theta, \quad (3.6)$$

where θ is the angle between the wave and the plane. This is Bragg's law and is a consequence of the periodicity of the crystal lattice. This however gives no information on the spatial arrangement of atoms in the unit cell only whether or not diffraction occurs. To determine the position of atoms in the unit cell the intensity needs to be found from the amplitude and phase of the scattered waves

and is quantified by the structure factor, F_{hkl} [74]:

$$F_{hkl} = \sum_j f_j(Q) \exp(2\pi i(hx_j + ky_j + lz_j)) \quad (3.7)$$

where $f_j(Q)$ is the form factor and is a measure of the scattering power of the j^{th} atom in the unit cell [74]. The form this takes on depends on the type of radiation used. In the case of x-rays, the scattering comes from the distribution of electrons in the system and generally scales with the atomic number, Z , of the atoms. If we take the electron density as ρ_{el} , the the form factor is given by [75]:

$$f(\mathbf{Q}) = \int \rho_{\text{el}}(\mathbf{r}) \exp(i\mathbf{Q} \cdot \mathbf{r}) \, d\mathbf{r} \quad (3.8)$$

In the limit of $\mathbf{Q} \rightarrow 0$, the form factor is given by $f(\mathbf{Q} = 0) = Z$. In most diffraction experiments the intensity of the beams is measured such that $I_{hkl} \propto |F_{hkl}|^2$. The structure can then be determined through a trial and error method by comparison of measured and calculated intensities, more detail on this process can be found in Section 4.1.4.

3.3 Neutron Scattering

The neutron is an uncharged particle that has a number of properties that make it an invaluable probe in the investigation of numerous physical systems. Unlike surface specific techniques, such as x-rays and electrons, the neutron interacts weakly with the atoms meaning the neutron can travel further into the sample allowing investigation into the interiors of materials. The typical energies of neutrons are a similar magnitude to crystalline and magnetic excitation in many systems, making it an ideal tool for the investigation of excitation schemes. The deBroglie wavelength is a similar order to the atomic spacing allowing diffraction by the crystal structure. Finally and arguably the most useful property for the present work is the neutron is a spin- $\frac{1}{2}$ particle, making the neutron well suited to the study of microscopic magnetism and sensitive to the magnetic structures in a system

3.3.1 Neutron Production

Neutrons used in scattering experiments are produced by two mechanisms. The first is utilised by research nuclear reactors, such as the Institut Laue Langevin (ILL) Grenoble, France. While the second is used at spallation sources such as that employed by ISIS at the Rutherford Appleton Laboratory, UK.

Reactor sources produce neutrons through the fission of ^{235}U nuclei. Some of the neutrons from this process are used to sustain the fission reaction, while the excess are used for the neutron flux. The neutrons are then moderated to define the energy of the beam. They undergo inelastic collisions with the nuclei in the moderator so the neutrons are in thermal equilibrium with the moderator. Typically moderation by water at 300 K produces “thermal” neutrons, although moderation by deuterium at 25 K and graphite at 2000 K is used to produce low energy (“cold”) and high energy (“hot”) neutrons respectively. This process produces a distribution of wavelengths so it is necessary to monochromate the beam before the instrument in order to select a narrow wavelength range for the experiment [79]. The exception to this are time of flight instruments as well as the neutron Laue technique, which utilises the distribution of wavelengths.

Spallation sources produce neutrons by accelerating protons with a synchrotron and colliding them with a heavy metallic target (for example tantalum, uranium or tungsten). The spallation process is a violent interaction between the proton and the target nuclei, which results primarily in the emission of neutrons and light nuclear fragments. The neutrons emerging from the target are moderated to slow the neutrons. Accelerator sources, such as those used for spallation sources, typically use pulses of protons and thus produce pulses of neutrons. This lends itself to time of flight techniques, which eliminates the need for monochromators for selection of wavelength, however they are still utilised as analysers [79].

3.3.2 Neutron Diffraction

This section details the basics behind nuclear neutron scattering. The scattering of radiation is characterised by the change in momentum, \mathbf{P} and energy, E .

$$\mathbf{P} = \hbar(\mathbf{k}_i - \mathbf{k}_f) = \hbar\mathbf{Q}, \quad (3.9)$$

where Q is the scattering vector. If there is no change in energy between the incident and scattered beam, we have elastic scattering. The vector diagram for an elastic scattering event is shown in Fig. 3.2(a). Applying some elementary trigonometry leads to the following result:

$$Q = \frac{4\pi \sin \theta}{\lambda} \quad (3.10)$$

where $Q = |\mathbf{Q}|$ is the magnitude of the scattering vector. When the scattering vector is equivalent to a reciprocal space vector, \mathbf{G} :

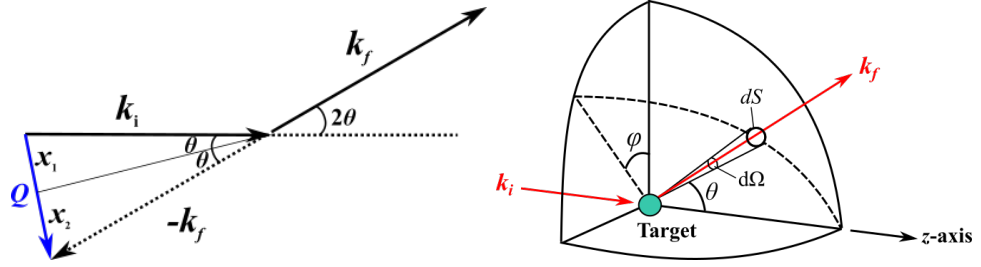


Figure 3.2: (a) Vector diagram showing elastic scattering (b) Simple geometry of a scattering experiment.

$$\mathbf{Q} = \mathbf{k}_i - \mathbf{k}_f = \mathbf{G}, \quad (3.11)$$

we have diffraction. This is referred to as the Laue condition and indicates when the beam is diffracted. Using the relationship $G = 2\pi/d$ and substituting it into equation (3.10) gives Bragg's law, indicating that the Laue and Bragg condition are equivalent. Fig. 3.2(b) shows the geometry of a simple scattering experiment. A wave of neutrons incident on a nucleus can be represented by the wave-function $\psi_i = \exp(ikz)$. The scattered wave will be spherically symmetrical and can be represented by $\psi_{sc} = -\frac{b}{r} \exp(ikr)$. Here b is the scattering length and represents the scattering power of the nucleus. The quantity b is complex, the imaginary component is only important for nuclei that strongly absorb neutrons (such as ^{103}Rh , ^{113}Cd , ^{157}Gd , and ^{176}Lu). However, the majority nuclei are real and unlike the form factor used in x-ray diffraction, there is no nuclear theory for the scattering length. The value can vary dramatically between isotopes and the values have to be experimentally determined [76]. The scattering cross-section of the nucleus can be defined by [73]:

$$\sigma = \frac{\text{outgoing current of scattered neutrons}}{\text{incident neutron flux}} = 4\pi b^2 \quad (3.12)$$

The cross section is the effective area of the nucleus “seen” by the incident neutron and gives an indication to the probability of a scattering event occurring. However in a real experiment only a small area dS is measured and this is referred to as the partial differential cross section defined by:

$$\begin{aligned}
\frac{d\sigma}{d\Omega} &= N^2 \left| \sum_n b_n \exp(2\pi i \mathbf{Q} \cdot \mathbf{r}_n) \right|^2 \\
&= N^2 \left| \sum_n b_n \exp(2\pi i (hx_n + ky_n + lz_n)) \right|^2 \\
&= N^2 |F_{hkl}|^2
\end{aligned} \tag{3.13}$$

where N is the number of unit cells.

The nucleus has a spin, I , which can combine with the neutron of spin- $\frac{1}{2}$ giving combined spins of $I + \frac{1}{2}$ and $I - \frac{1}{2}$. This gives rise to two components of the scattering cross-section:

$$\sigma = \sigma_{\text{coh}} + \sigma_{\text{incoh}} \tag{3.14}$$

where σ_{coh} and σ_{incoh} is the cross sections for coherent and incoherent scattering respectively. These are giving by:

$$\sigma_{\text{coh}} = 4\pi(\bar{b})^2 \quad \text{and} \quad \sigma_{\text{incoh}} = 4\pi\{\overline{b^2} - (\bar{b})^2\} \tag{3.15}$$

The coherent scattering tells us about the correlations between nuclei and gives an indication to the nuclear structure. While the incoherent scattering has no information on structure and gives rise to background scattering.

3.3.3 Magnetic Scattering

While in general the scattering of the neutron is a nuclear process, there is an exception for magnetic ions, where there is additional scattering arising from the interaction between the neutron's magnetic moment and the magnetic moment of the atom. As the scattering is due to the electrons the magnetic form factor is similar to that of the x-ray form factor, however the drop off with scattering vector Q is more dramatic. The magnetic form factor is given by the following equation:

$$f_{\text{mag}} = \int \rho(r) \exp(i\mathbf{k}r) dr, \tag{3.16}$$

where $\rho(r)$ is the density of magnetic atoms. The atoms may be regarded as having a magnetic scattering amplitude, p :

$$p = \mathbf{S} \left(\frac{e^2 \mu_N}{m_e c^2} \right) f_{\text{mag}} \tag{3.17}$$

where μ_N is the nuclear magneton and \mathbf{S} is the spin value of the neutron. This scattering amplitude is the counterpart of the nuclear scattering amplitude b . The magnitude of which is comparable allowing simultaneous measurement of both the nuclear and magnetic contribution of a system. Similarly to the nuclear scattering, the structure factor is given by [73]:

$$F_{\text{mag}} = \sum_n \mathbf{q}_n p_n \exp\{2\pi i(hx_n + ky_n + lz_n)\} \quad (3.18)$$

where \mathbf{q} is the magnetic interaction vector defined by:

$$\mathbf{q} = \epsilon(\epsilon \cdot \mathbf{K}) - \mathbf{K} \quad (3.19)$$

where ϵ is the unit vector in the direction perpendicular to the scattering vector and \mathbf{K} is a unit vector in the direction of the atomic magnetic moment. This equation shows that for an atom to make a magnetic contribution to the scattered intensity there must be a component of the magnetic moment perpendicular to the scattering vector.

Equation (3.13) and (3.18) can be used to find the total intensity of the structure factor, F_{hkl} for a particular (hkl) reflection is given by:

$$|F_{hkl}|^2 = |F_{\text{nuc}}|^2 + |F_{\text{mag}}|^2 \quad (3.20)$$

3.3.4 Polarised Neutron Diffraction

Uniaxial neutron polarisation

To perform a uniaxial neutron experiment the neutron beam needs to be polarised. Applying a magnetic field the neutron spin then quantized into its two Zeeman states, either parallel or anti-parallel to the quantization axis giving by the external magnetic field. The degree of polarisation can be quantified with [80]:

$$P = \frac{N_+ - N_-}{N_+ + N_-}, \quad (3.21)$$

where N_+ and N_- are the numbers of neutrons in the parallel and anti-parallel Zeeman states respectively. For an unpolarised beam, the two states are equal (i.e. $N_+ = N_-$), leading to $P = 0$, where as if N_+ or $N_- = 0$, the beam is fully polarised and gives $P = \pm 1$. Therefore the polarisation of the neutron beam will vary between $0 \leq |P| \leq 1$. The neutron interacts with the magnetic moment according to the magnetic scattering potential, V_m . Within the scattering process

the the neutron spin state can change. We therefore arrive at the magnetic scattering amplitudes [80]:

$$\begin{aligned}
U_m^{++} &= \langle + | V_m(\mathbf{Q}) | + \rangle = M_{\perp,z}(\mathbf{Q}) \\
U_m^{--} &= \langle - | V_m(\mathbf{Q}) | - \rangle = -M_{\perp,z}(\mathbf{Q}) \\
U_m^{+-} &= \langle + | V_m(\mathbf{Q}) | - \rangle = M_{\perp,x}(\mathbf{Q}) + iM_{\perp,y}(\mathbf{Q}) \\
U_m^{-+} &= \langle - | V_m(\mathbf{Q}) | + \rangle = M_{\perp,x}(\mathbf{Q}) - iM_{\perp,y}(\mathbf{Q})
\end{aligned} \tag{3.22}$$

where $\mathbf{M}_{\perp}(\mathbf{Q})$ is the magnetic interaction vector defined by [80]:

$$\mathbf{M}_{\perp} = \hat{\mathbf{Q}} \times (\mathbf{M} \times \hat{\mathbf{Q}}) \tag{3.23}$$

which is the Fourier transform of the magnetisation perpendicular to the scattering vector. The first two amplitudes do not change the neutron spin state and are referred to as non spin-flip (NSF) amplitudes, while the latter two involve a change in spin state and are called spin-flip (SF) amplitudes. These amplitudes lead to the rule of thumb:

- (i) The non spin-flip amplitude is sensitive only to components of the sample magnetisation, which are parallel to the neutron spin.
- (ii) The spin-flip amplitude is sensitive only to components of the sample magnetisation, which are perpendicular to the neutron spin.

xyz-polarisation

In order to get full separation of the magnetic, nuclear and spin-incoherent cross sections analysis of the x , y , and z polarisation measurements must be made. In this experiment the x and y polarisation are fixed in the experimental set-up while the angle, α , between the x -axis and the scattering vector Q is referred to as the Schärpf angle. The magnetic cross section can be calculated in two ways [81]

$$\begin{aligned}
\left(\frac{d\sigma}{d\Omega}\right)_{\text{mag}} &= 2 \left(\frac{d\sigma}{d\Omega}\right)_{\text{SF}}^x + 2 \left(\frac{d\sigma}{d\Omega}\right)_{\text{SF}}^y - 4 \left(\frac{d\sigma}{d\Omega}\right)_{\text{SF}}^z \\
\left(\frac{d\sigma}{d\Omega}\right)_{\text{mag}} &= 4 \left(\frac{d\sigma}{d\Omega}\right)_{\text{NSF}}^z + 2 \left(\frac{d\sigma}{d\Omega}\right)_{\text{NSF}}^x + 2 \left(\frac{d\sigma}{d\Omega}\right)_{\text{NSF}}^y
\end{aligned} \tag{3.24}$$

while the nuclear and the spin-incoherent cross are given by [81]:

$$\left(\frac{d\sigma}{d\Omega}\right)_{\text{nuc}} = \frac{1}{6} \left[2 \left(\frac{d\sigma}{d\Omega}\right)_{\text{TNSF}} - \left(\frac{d\sigma}{d\Omega}\right)_{\text{TSF}} \right] \tag{3.25}$$

$$\left(\frac{d\sigma}{d\Omega}\right)_{\text{si}} = \frac{1}{2} \left(\frac{d\sigma}{d\Omega}\right)_{\text{TNSF}} - \left(\frac{d\sigma}{d\Omega}\right)_{\text{mag}} \quad (3.26)$$

where the subscripts TNSF and TSF refer to the total non spin-flip and total spin-flip cross sections respectively.

3.3.5 Inelastic Neutron Scattering

For inelastic scattering, there is a transfer of energy between the sample and the neutrons. This means the magnitude of wave vectors are no longer equal, $|k_i| \neq |k_f|$, this gives the energy transfer as:

$$\hbar\omega = E_i - E_f = \frac{\hbar^2}{2m}(k_i^2 - k_f^2) \quad (3.27)$$

The scattering function is related to the total differential cross-section according to the following equation:

$$\begin{aligned} \frac{d^2\sigma}{d\Omega dE_f} &= \frac{k_f}{k_i} S(\mathbf{Q}, \omega) \\ &= \left| \sum_t \sum_n b_n \exp(i\mathbf{Q} \cdot \mathbf{r}_n - \omega t) \right|^2 \end{aligned} \quad (3.28)$$

where $S(\mathbf{Q}, \omega)$ is the scattering function. We can see that in the case of elastic scattering (i.e. $\omega = 0$) we obtain the results from equation (3.13). The scattering function can also be related to the dynamic susceptibility $\chi''(\mathbf{Q}, \omega)$ [82]:

$$S(\mathbf{Q}, \omega) = \frac{\chi''(\mathbf{Q}, \omega)}{1 - \exp(-\hbar\omega/k_B T)} \quad (3.29)$$

where $\chi''(\mathbf{Q})$ is an odd function. Neutrons are capable of exciting transitions between the energy levels split by the crystal fields. This is due to the neutron scattering from the magnetic field associated with the unpaired f -electrons flipping the neutron's spin from $+\frac{1}{2}$ to $-\frac{1}{2}$. In order to conserve angular moments the ionic state must change by $\Delta m_J = \pm 1$, which corresponds to the crystal field level transition selection rules. Thus the measured spectrum will give rise to a series of peaks in energy transfer representing transitions between crystal field levels, phonons and magnetic excitations. The phonon and magnetic excitations are usually easily distinguished due to their Q dependence. Intensity from phonons increases with increasing Q , while the intensity arising from magnetic excitation drops off with Q , according to

the magnetic form factor. The intensity of the crystal field level generally decreases with increasing Q , the decrease corresponding to the neutron's form factor. Typically the energy loss of the neutron is only investigated, However some information can be gained from the energy gain of the neutron. The relationship between the energy gain and loss of the neutron is given by:

$$\underbrace{S(\mathbf{Q}, -\omega)}_{\text{EnergyGain}} = \exp(-\hbar\omega/k_{\mathbf{B}}T) \underbrace{S(\mathbf{Q}, \omega)}_{\text{EnergyLoss}} \quad (3.30)$$

It can be seen that peaks are only observed in the energy gain part of the spectrum when the temperature is significant and is usually a similar order to the temperatures required to thermally populated crystal field levels. Thus, the energy levels can give an indication to transitions in the spectrum arising due to thermal population of crystal field levels.

Chapter 4

Experimental Techniques

4.1 Sample Preparation and Characterisation

4.1.1 Polycrystalline Preparation

Polycrystalline samples were prepared using the Centorr tri-arc furnace. Ingots of rare earth metal, R , were placed in a water cooled copper hearth with powdered boron. The equation for the reaction is [41]:



where a 5% excess of boron was added to account for loss during the melting. Isotopically enriched boron, ^{11}B (99%) was used to reduce neutron absorption. The reaction chamber was evacuated and flushed with argon several times before melting under a flow of argon. An arc of current is struck between the copper hearth and a tungsten electrode, the arc is brought over the sample and used to melt it. Before preceding, a small piece of titanium was melted, to check for and remove any presence of air in the reaction chamber. If the titanium is clean, there is no air in the argon atmosphere and the melt can precede. After each melt the sample was flipped and re-melted to improve homogeneity. Some member of the RB_4 ($R = \text{La, Ce, Pr, Nd, Sm or Yb}$) family decompose at high temperatures according to [41]:



Care was taken with these compounds by melting for shorter periods of time and using a smaller current to minimise the presence of impurities.

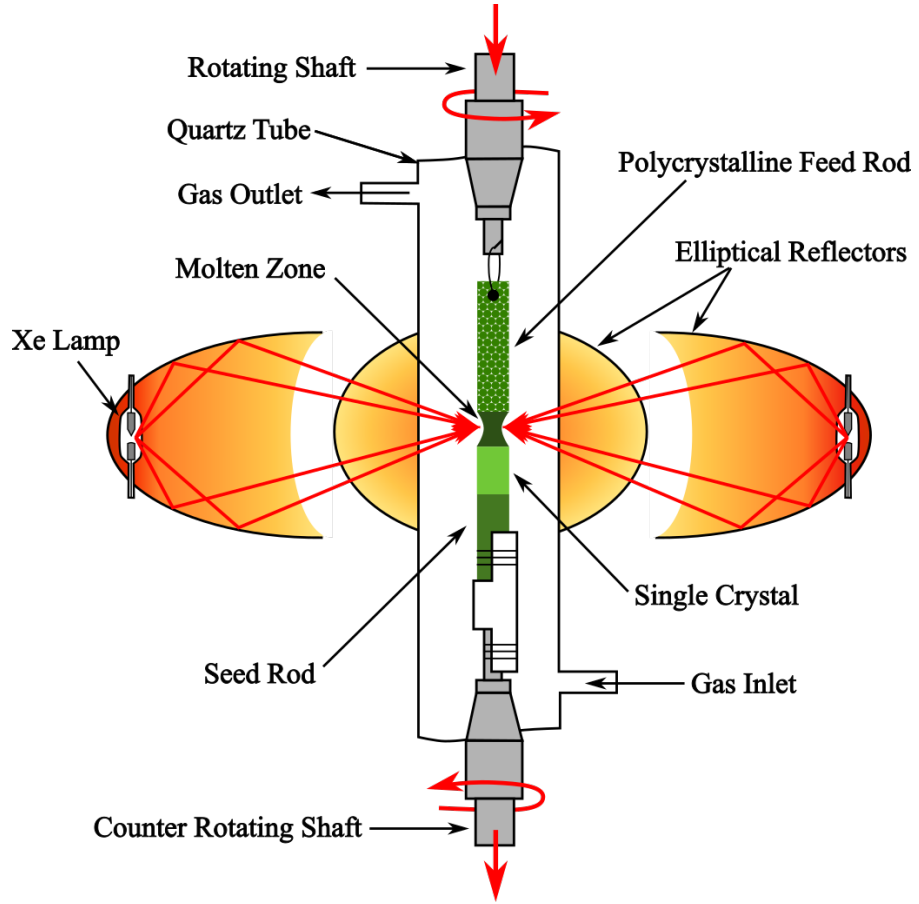


Figure 4.1: Illustration of the floating zone method. A polycrystalline feed and seed rod are brought together in the focal point of light from four Xe lamps to create a molten region between the two. The molten region between the two rods is pulled through the hot zone, crystallising as it cools.

4.1.2 Single Crystal Growth

The floating zone technique was utilized for the RB_4 crystal growth. It is a crucible free method and allows the growth of high quality crystals of congruently and incongruently melting materials. The principle of the technique is illustrated in Fig. 4.1. The light from four xenon arc lamps is focused to a central hot zone by four elliptical mirrors. A polycrystalline feed rod is suspended to a rotating shaft above the hot zone, while a preferably crystalline seed rod is fixed to a shaft below [83, 84]. The feed and seed rods were made by arc melting the polycrystalline samples into a rod shape ranging between 35 to 70 mm in length with a diameter of 4 mm. The first crystal growth used a polycrystalline seed rod, while subsequent growths used

a crystalline sample.

A high temperature optical image furnace (Crystal Systems Inc. Optical Floating Zone Furnace Model FZT-12000-X-VI-VP) was used and the rods were fixed within a quartz tube. The chamber was evacuated and flushed several times with argon and then filled with argon up to a pressure of 5 bars. The tips of the two rods are brought together establishing a liquid bridge between the two referred to as the *floating zone*. The shafts are counter-rotated, this ensuring an even distribution of heat throughout the molten region as well as ensuring homogeneity of the composition [83, 84]. The molten region was moved through the hot zone at a rate of 18 mm h⁻¹, crystallising as the melt cools.

4.1.3 Powder X-ray Diffraction

Composition analysis of the samples was carried out using powder x-ray diffraction on a Panalytical X-Pert Pro MPD diffractometer. A monochromated Cu K α 1 ($\lambda = 1.54056$ Å) source with a standard Bragg-Brentano geometry was used to produce the diffractograms. When the Bragg condition is satisfied a peak is observed arising from the coherent scattering of the x-rays from the crystalline planes. The diffractograms produced depend on the symmetry and lattice parameters of the compound. The diffractogram is thus unique for each compound and can be used to identify the sample as well as any impurity phases. The presence of impurities was checked by performing Rietveld refinements using the Fullprof program [85].

4.1.4 Least-Squares Structure Refinement

The least-squared refinement methods fall into two main categories for checking a crystal and magnetic structure of a compound. The first is the Rietveld method which is used for the analysis of powder samples. The method works by minimising the weighted squared difference between the observed y_i^{obs} and calculated y_i^{calc} intensity at a point, i [86, 87]:

$$X^2 = \sum_{i=1}^n w_i \{y_i^{\text{obs}} - y_i^{\text{calc}}\}^2, \quad (4.3)$$

where w_i is the statistical weight. The profile of the calculated intensity is made up of several parameters and can be calculated according to:

$$y_i^{\text{calc}} = s \sum_{hkl} L_{hkl} P_{hkl} A |F_{hkl}|^2 \Omega(\theta) + b_i \quad (4.4)$$

where s is the scale factor such that $y_i^{\text{calc}} = sy_i^{\text{obs}}$, L_{hkl} is a correction term which encompasses Lorentz, polarisation and multiplicity factors, P_{hkl} is a preferred orientation function and A is an absorption correction. $\Omega(\theta)$ is a peak shape function which models both instrumental and sample effects (typically a Gaussian, Lorentzian or Pseudo-Voigt function is used), while b_i is the background intensity. More information on the Rietveld method can be found in reference [88].

The second method compares a list of observed structure factors $|F_{hkl}|_{\text{obs}}^2$ to the calculated structure factors $|F_{hkl}|_{\text{calc}}^2$ for a particular structural model. In a similar way to the Rietveld refinements, structural parameters, correction factors, etc. are refined to minimise the difference between $|F_{hkl}|_{\text{obs}}^2$ and $|F_{hkl}|_{\text{calc}}^2$. This method can be used for both single crystal and powder analysis.

The magnetic structure refinement can be done by using either method. For a magnetic phase $|F_{hkl}|^2$ is calculated using the general formula [89]:

$$F_{hkl}^2 \propto |\mathbf{F}_{\perp}(\mathbf{Q})|^2 = |\mathbf{F}_m(\mathbf{Q})|^2 - \left[\frac{\mathbf{Q} \cdot \mathbf{F}_m(\mathbf{Q})}{|\mathbf{Q}|} \right]^2 \quad (4.5)$$

where $\mathbf{F}_m(\mathbf{Q})$ is the magnetic structure factor and \mathbf{Q} is the scattering vector. The scattering vector can be written as $\mathbf{Q} = \mathbf{G} + \mathbf{k}$, where \mathbf{G} is the reciprocal lattice vector and \mathbf{k} is the propagation vector. For a given magnetic structure, the distribution of the magnetic moments can be expanded as a Fourier series:

$$\mathbf{m}_{lj} = \sum_{\mathbf{k}} \mathbf{S}_{\mathbf{k}j} \exp\{-2\pi i \mathbf{k} \cdot \mathbf{R}_l\} \quad (4.6)$$

where \mathbf{m}_{lj} is the magnetic moment vector of the j^{th} atom in the l^{th} unit cell. The Fourier term, $\mathbf{S}_{\mathbf{k}j}$ is a complex vector and obeys the condition, $\mathbf{S}_{-\mathbf{k}j} = \mathbf{S}_{\mathbf{k}j}^*$, to ensure the magnetic moment is real. In such a case the magnetic structure factor is given by:

$$\mathbf{F}_m(\mathbf{Q}) = pf_j(\mathbf{Q}) \sum_j \mathbf{S}_{\mathbf{k}j} \exp\{2\pi i \mathbf{Q} \cdot \mathbf{r}_j\} \quad (4.7)$$

$f_j(\mathbf{Q})$ is the magnetic form factor and $p = (r_c\gamma/2)$.

The quality of the fit is accessed using the R -factors. The R -factors quoted through the thesis are R_{WP} , R_{Bragg} [88]

$$R_{\text{WP}} = 100 \times \left[\frac{\sum_{i=1}^n w_i \{y_i^{\text{obs}} - y_i^{\text{calc}}\}^2}{\sum_{i=1}^n w_i \{y_i^{\text{obs}}\}^2} \right]^{\frac{1}{2}} \quad (4.8)$$

$$R_{\text{Bragg}} = 100 \times \left[\frac{n - p}{\sum_{i=1}^n w_i \{y_i^{\text{obs}}\}^2} \right]^{\frac{1}{2}} \quad (4.9)$$

$$\chi_{\nu}^2 = \left[\frac{R_{\text{WP}}}{R_{\text{exp}}} \right]^2 \quad (4.10)$$

4.1.5 Laue Diffraction

Before bulk property and neutron measurements could be made single crystal need to be aligned along a principal axis. A polychromic source of x-rays passes through a small hole in a CCD (charged-coupled device) plate and is incident on the sample. The wide range of wavelength means the Bragg condition is satisfied for different lattice planes and is backscattered by the sample onto the CCD plate. The image produced reflects the symmetry of the crystal structure and the position of the crystal. The sample is attached to a 3 axis goniometer and allows rotation to find highly symmetry directions which coincide with a principal axis.

To identify the different crystal orientations, the Laue images were compared with simulated patterns generated using OrientExpress, which simulates the x-ray Laue images using the space group, lattice parameters and positions of the atoms in the unit cell. Once the desired axis was identified, the sample was glued to an aluminium plate and faces perpendicular to the axis were cut with a low speed diamond saw to define the principal axis.

4.2 Bulk Property Measurements

4.2.1 Magnetic Susceptibility and Magnetisation

Temperature dependent magnetisation measurements were made using a Quantum Design Magnetic Property Measurement System (MPMS), in a temperature range of 1.8-300 K in fields upto 70 kOe [90]. Fig. 4.2 shows a schematic of the measurement system. It is comprised of three main components; a superconducting magnet, a superconducting detection coil, which are in a second-order gradiometer configuration and a superconducting quantum interference device (SQUID).

The sample is attached to a non-magnetic sample holder, connected to a rigid sample rod, which is brought down vertically into the center of the detection coils. The superconducting magnet supplies a static vertical magnetic field across the sample. During the measurements the sample is moved through the coils in a series of discreet steps and a current is induced in the coils via electromagnetic induction. The SQUID acts as a highly sensitive current to voltage converter and the output

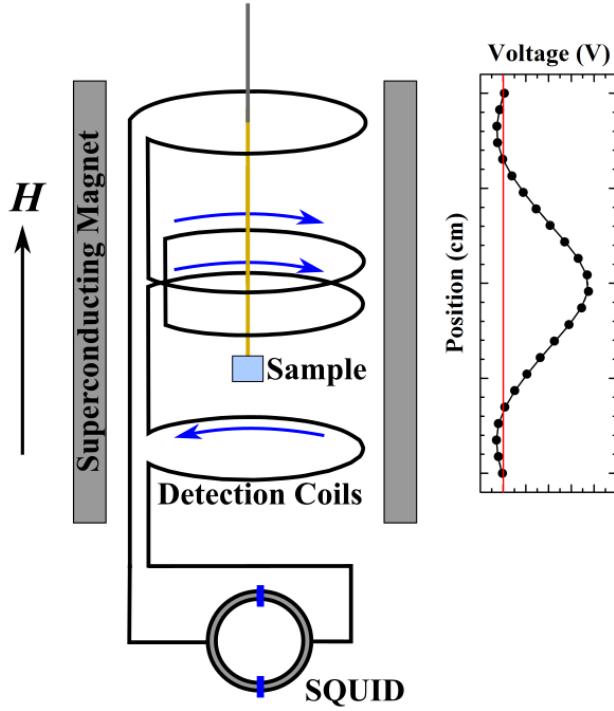


Figure 4.2: Schematic of the SQUID magnetometer. The magnetic sample is moved through a set of detection coils inducing a current, which is then converted into a measure of the magnetic moment.

voltage is measured as a function of position (See Fig. 4.2). Calibration with a reference sample of known magnetic susceptibility, then allows the magnetisation of an unknown sample to be determined from fitting the output voltage with a model based on the response of a magnetic dipole through a second-order gradiometer. The temperature ranges were extended down to 0.5 K using an iQuantum ^3He low temperature insert [91].

Field dependent magnetisation measurements were made using an Oxford Instruments vibrating sample magnetometer (VSM). The sample is attached to a non-magnetic sample stick and brought to the centre of set of stationary pick-up coils. A pair of mechanically coupled transducers (similar to loudspeaker) are driven by a set of coils. This causes the sample rod to vibrate with an amplitude of 1.5 mm at a frequency of 55 Hz [92]. A static magnetic field supplied by a superconducting magnet is applied vertically to magnetise the sample. The oscillating sample induces an AC signal in the pick-up coils and the resulting voltage is measured with a lock-in amplifier. Calibrating with a sample of known magnetic moment allows the

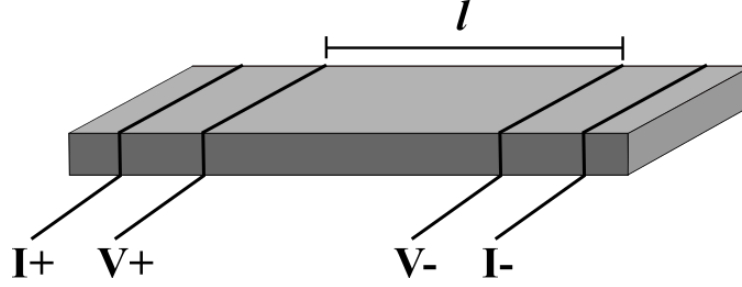


Figure 4.3: A Schematic of 4 probe measurement. Current is applied across the two outer wire, while the voltage is measured across a pair of silver wires.

magnetisation of the sample to be determined [92]. High field magnetisation measurements were made using a pulsed magnetic field up to 580 kOe at the Dresden High Magnetic Field Laboratory (HLD), Germany. Pulse magnets work by supplying a fast pulse of current through a small coil of wire, producing a high magnetic field. The measurements were carried out on small (typically less than 10 mg) plate-like samples aligned along a principal axis, such that the field was parallel to the plate face to minimise the demagnetising factor.

4.2.2 Resistivity

Resistivity measurements were made using a Quantum Design Physical Properties Measurements System (PPMS). The four probe method was used to measure the resistivity down to temperatures of 1.8 K and in fields up to 90 kOe. Fine silver wire (0.05 mm diameter) were attached to the sample using silver paste as illustrated in Fig. 4.3. An alternating current is passed through the outer wires, while the voltage is measured across the two inner wires separated by a distance, l . The resistivity is calculated according to,

$$\rho = \frac{RA}{l}, \quad (4.11)$$

where R is the resistance and A is the cross sectional area. A current of 10 mA and a frequency of 113 Hz was used for all measurements.

4.2.3 Heat Capacity

Heat capacity measurements were made using a Quantum Design PPMS in a temperature range of 1.8 and 300 K and in fields of up to 90 kOe. The sample was prepared by polishing at least one side and mounting it to a platform using Apiezon

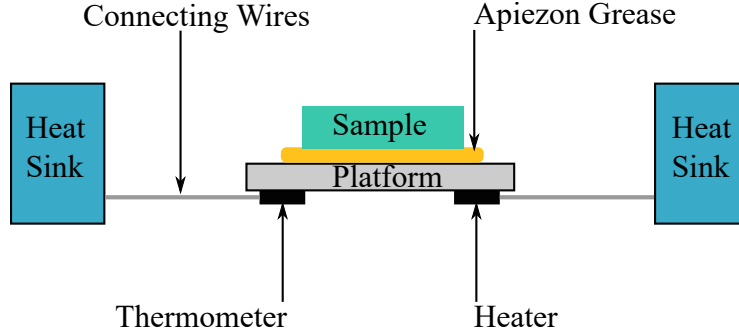


Figure 4.4: A schematic of the experimental set up for making specific heat measurements using the relaxation technique. The sample is adhered to a platform with Apiezon grease, a heater in the platform briefly heats the sample and the thermometer measures the pulse and subsequent cooling of the sample. Figure adapted from Ref. [95]

N grease for both temperature and field dependent heat capacity measurements. The grease acts as an adhesive as well as providing good thermal contact between the sample and the platform. The platform is suspended by eight thin wires, which also act as electrical leads to the heater and thermometer. They also provide a thermal link between the sample platform and heat sink, which is kept at a constant temperature. A schematic of the experimental set-up is shown in Fig. 4.4

The measurements utilize the relaxation method, which consists of several stages. The temperature of heat sink and stage is stabilised before power is applied to the heater for a predetermined time. The heater is then switched off and the temperature of the sample and stage is allowed to relax towards the initial temperature of the heat sink. The sample temperature is measured for the entire duration of heating and cooling. The temperature rise and decay curve is then fitted by the PPMS software using either a single or a pair of exponential functions. The latter is referred to as the two-tau model, which assumes the sample is not in good thermal contact with the platform. In this case two time constants are used to fit the data; τ_1 represents the relaxation time of the sample platform and the puck and τ_2 is the relaxation time of the sample platform and sample itself. More information on the two-tau method is given in [93, 94].

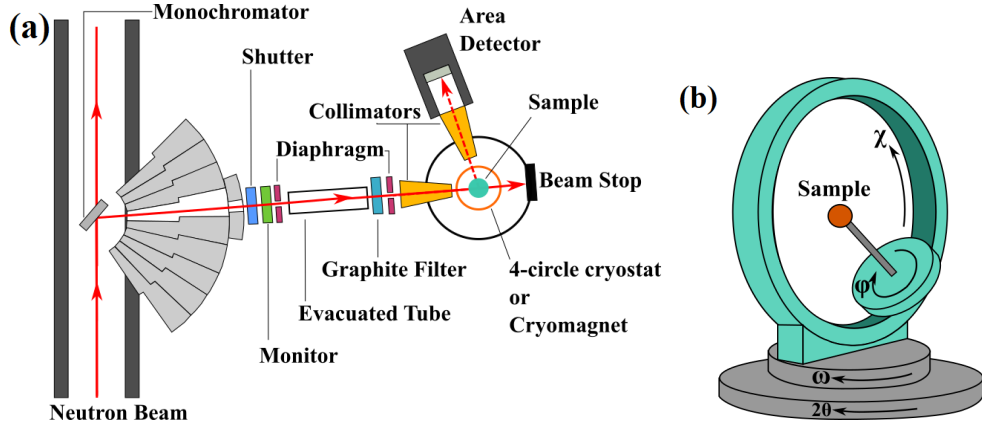


Figure 4.5: (a) Schematic of the single crystal neutron diffractometer, D10 at the ILL. (b) Illustration of the Eulerian cradle. This figure was adapted from Ref. [96].

4.3 Neutron Diffraction

4.3.1 D10, Single Crystal Diffractometer, ILL

D10 is a high flux single crystal diffractometer [96]. Its good momentum resolution and low intrinsic background make it well suited for investigating nuclear and magnetic structures. A schematic of the experimental set-up on D10 is shown in Fig. 4.5. Thermal neutrons are monochromated by either a pyrolytic graphite (PG) or Cu(200) monochromator to produce a neutron beam with an incident wavelength of 2.36 \AA and 1.26 \AA respectively. The beam then passes through a PG filter to reduce the half-lambda contamination. The HoB_4 (0.33 g) and NdB_4 (0.18 g) samples were fixed to separate aluminium pins with Kwik Fill two part resin and fitted into the sample environment.

Two configurations were used for D10, the first is a four-circle set-up used for zero field measurements. The sample was placed inside a helium flow cryostat, able to obtain temperatures between 1.6 and 300 K, and mounted to an Eulerian cradle. The Eulerian cradle has three axes of rotation (ω , ϕ and χ) for the sample and is shown Fig. 4.5(b). Using an orientation (UB) matrix any (hkl) value in the reciprocal lattice can be found. There are a number of scan available, first of all there are ω scans where the sample is rotated around a small range in ω in a discrete number of steps. For each step the intensity is measured and the ω scans creates an intensity peak. The second scan used were ϕ -scans. Again the sample is rotated around ϕ in a number of steps, with the intensity measured at each step. In this geometry, the reflection will not move in the two dimensional detector

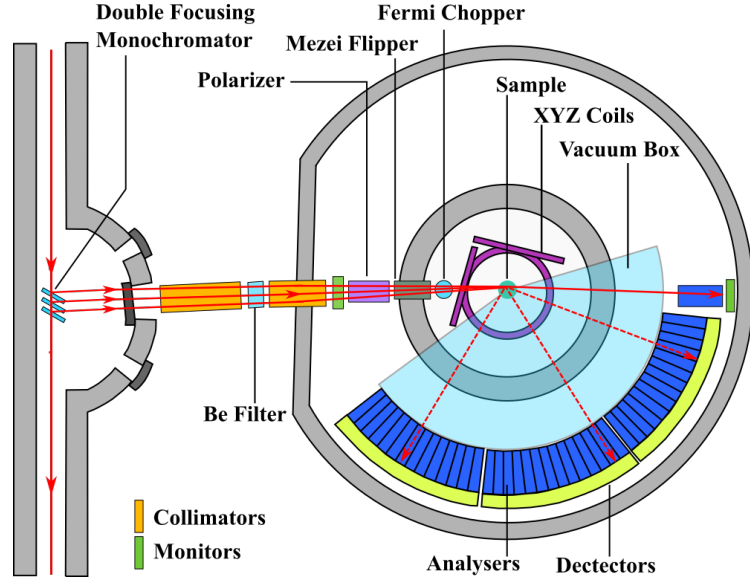


Figure 4.6: Schematic of the single crystal polarised neutron diffractometer, D7 at the ILL. This figure was adapted from Ref. [96].

so the intensity is expected to be constant unless there are other effects such as multiple scattering. The detector is placed at a value of 2θ which satisfies the Bragg condition for a particular (hkl) value. A two-axis configuration was used for measurements in an applied field. The sample was placed in a standard cryomagnet capable of supplying a vertical magnetic field of up to 60 kOe. For both NdB_4 and HoB_4 the magnetic field was applied along the c -axis defining the horizontal $(hk0)$ scattering plane. Out of plane coverage can be achieved by inclining the detector by up to 30° .

A two dimensional $80 \times 80 \text{ mm}^2$ area detector was used for both configurations. To track magnetic phase transitions, the temperature and field dependence of the intensity of different (hkl) reflections was measured. This was performed by either ramping the field or temperature continuously and summing up the counts in a small area of the detector or by performing an ω scan at various fixed temperatures and fields.

4.3.2 D7, Polarised Neutron Diffractometer, ILL

D7 is a cold neutron diffractometer with full XYZ polarisation analysis [80, 96]. A schematic of the D7 diffractometer is shown in Fig. 4.6. A vertically and horizontally focusing PG monochromator selects a wavelength of either 3.1, 4.8 or 5.8 Å. A

beryllium filter is used to suppress higher order contamination. Polarisation of the neutron beam is achieved by first polarising the beam with a high efficiency in the vertical Z direction using a Co/Ti Schärpf bender-type supermirror. A guide field of approximately 20 G is present across the entire instrument to ensure the polarisation efficiency remains intact. A Mexei-type flipper is then used to manipulated the neutron spins to rotate π radians with respect to the guide field. A set of orthogonal xyz coils situated around the sample environment, rotate the incoming beam in each of the \mathbf{x} , \mathbf{y} and \mathbf{z} directions. The \mathbf{x} , \mathbf{y} and \mathbf{z} directions are fixed with respect to the instrument and only the \mathbf{z} direction is parallel and perpendicular to the scattering vector Q . The diffractometer has 3 banks of 44 ^3He detectors, covering an angular range of approximately 132° . Two independent channels were measured, here called the non spin-flip (NSF) and the spin-flip (SF) channel. The NSF channel is sensitive to nuclear scattering and scatter from a component of the magnetic moment parallel to the polarisation, while the SF channel is only sensitive to the component of the magnetic moment in the scattering plane and perpendicular to the scattering vector. Hence, the sum of the NSF and SF channels gives the total intensity that would be observed in an unpolarised neutron experiment.

The NdB_4 (2.79 g) was attached to a thin Al strip and tied in place with Al wire. The strip was connected to a goniometer to allow fine adjustment to the sample orientation. The HoB_4 sample (1.60 g) was glued to an Al sample holder using Kwik fill two part resin. For both cases, the crystal was aligned such that the b -axis was vertical defining a horizontal ($h0l$) scattering plane. The sample sits in an standard orange cryostat capable of reaching temperatures down to 1.5 K. Scans were made by rotating the sample around the vertical access with 1° step size. Calibration measurements were run on vanadium, quartz and an empty sample holder. Vanadium was used to normalised the detector efficiency, quartz to normalised the polarisation efficiency, while the empty sample holder determined the background. In addition, there is a small degree of “leakage” between the NSF and SF channels, arising from imperfect polarisation of the neutron beam. Although this is corrected for by the quartz normalisation, the correction does not work well for high-intensity Bragg peaks. This gives rise to small features corresponding to the exact positions of nuclear Bragg peaks in the spin-flip channel.

4.4 Neutron Spectroscopy

To perform an inelastic neutron scattering measurement it is necessary to have knowledge of the incident and scattered energies of the neutron. There are a variety

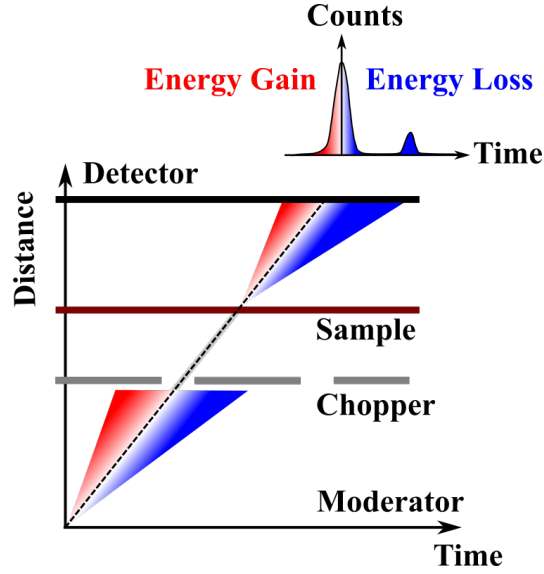


Figure 4.7: Distance-time plot to illustrate the principle of time of flight for a direct geometry chopper spectrometer.

of different techniques to achieve this including the use triple-axis and time-of-flight (TOF) spectrometers. TOF spectrometers can be split into two broad classes; direct geometry, where the incident energy is selected and the final energy is calculated from the total TOF and indirect geometry, where the final energy is selected. For the work presented here only direct geometry TOF spectrometers were used.

Fig. 4.7 shows a TOF diagram illustrating how a direct geometry spectrometer works. First of all a polychromatic neutron beam is monochromated through use of either a crystal or a chopper. The monochromated neutron beam scatters from the sample inelastically, changing the energy and direction of the neutron. The final energy of the neutron can be calculated from the TOF between the moderator and the detector. The neutron also transfers momentum to the sample enabling the neutron to map out the scattering function $S(Q, \omega)$. The resolution of direct geometry instruments depends predominately on two factors. The first is the width of the pulse from the moderator, which is generally fixed by the properties of the moderator used. While the second is the opening time of the chopper which depends on the size of the aperture and rotation speed of the chopper.

4.4.1 MARI, ISIS

MARI (Multi-Angle Rotor Instrument) is a direct geometry chopper spectrometer (See Fig. 4.8) [97]. A Fermi chopper is magnetically suspended in a vacuum and

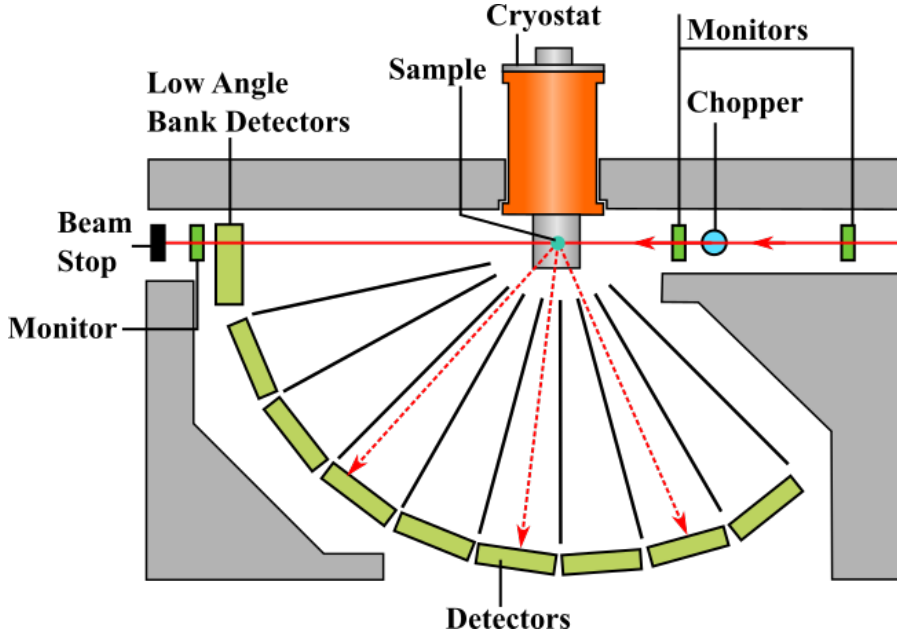


Figure 4.8: A schematic of the time of flight direct geometry spectrometer, MARI at ISIS. The instrument was used to investigate the crystal field excitations on polycrystalline samples of RB_4 . The figure was adapted from Ref. [97].

rotated up to frequencies of 600 Hz. There are four choppers available for use on MARI, which have a variety of E ranges and resolutions. However, during the experiment the “S-Chopper” was solely used. This is capable of producing incident energies between 7-1000 meV and has an energy resolution of $\Delta E/E_i = 3$ -8%. Polycrystalline samples of NdB_4 (4.27 g) and ErB_4 (4.00 g) were spread out in an aluminium envelope, flatted and wrapped around a vanadium cylinder and placed in a CCR (closed cycle refrigerator), which was able to cool the samples down to 5 K. MARI has a bank of ^3He detectors situated in the vertical scattering plane, which covers an angular range of 12-135°. The wide angular coverage, wide energy coverage and good resolution make it ideal for the study crystalline field excitations in magnetic materials.

4.4.2 IN4C, ILL

IN4C is a spectrometer at the ILL and is shown in Fig. 4.9. The incident neutron beam passes through two rapidly pulsating background choppers [96, 98]. These act as low bandpass filters, eliminating gamma rays and fast neutrons, which contribute to the background noise of the spectra. A curved monochromator consisting of an

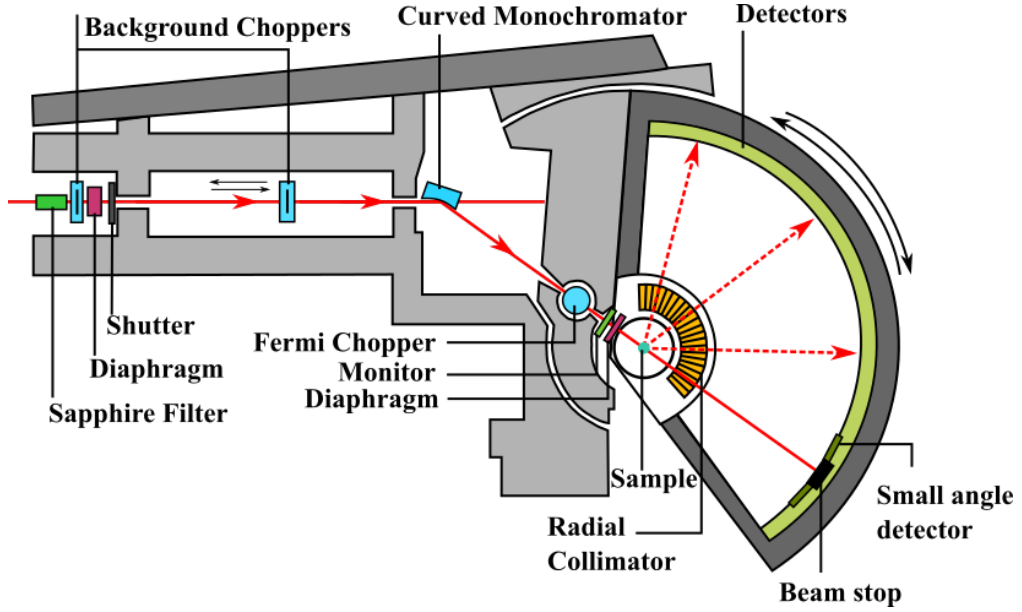


Figure 4.9: A schematic of the time of flight direct geometry spectrometer, IN4 at the ILL. The instrument was used to investigate the crystal field excitations on polycrystalline samples of HoB_4 . The figure was adapted from Ref. [96].

assembly of 55 crystal pieces focuses the divergent beam onto a small area at the sample position. The monochromator assembly allows for four separate crystals, PG(002), PG(004), Cu(220) and Cu(111). For our experiment only the PG(002) and PG(004) were used to produce a wavelength of 3.06 and 1.61 Å respectively. A Fermi chopper is used to pulse the incident beam, which is required for the time of flight technique.

The powdered HoB_4 (3.38 g) sample was spread out in an aluminium envelope, flattened and held in a sample holder creating a square window approximately $40 \times 40 \text{ mm}^2$. The sample was placed in a standard orange cryostat capable of reaching temperatures down to 1.5 K. A radial collimator was used to minimise scattering from the equipment. The scattered neutrons are detected by a bank of ^3He detectors covering an angular range of 120° .

4.4.3 IN5, ILL

IN5 is a direct geometry spectrometer, located at the ILL. A schematic of the instrument is shown in Fig. 4.10 [96, 99]. A continuous, polychromatic neutron beam becomes pulsed by the first set of pulsing choppers. Here two counter rotating choppers remove frame overlap of different pulses and reduced the background. The

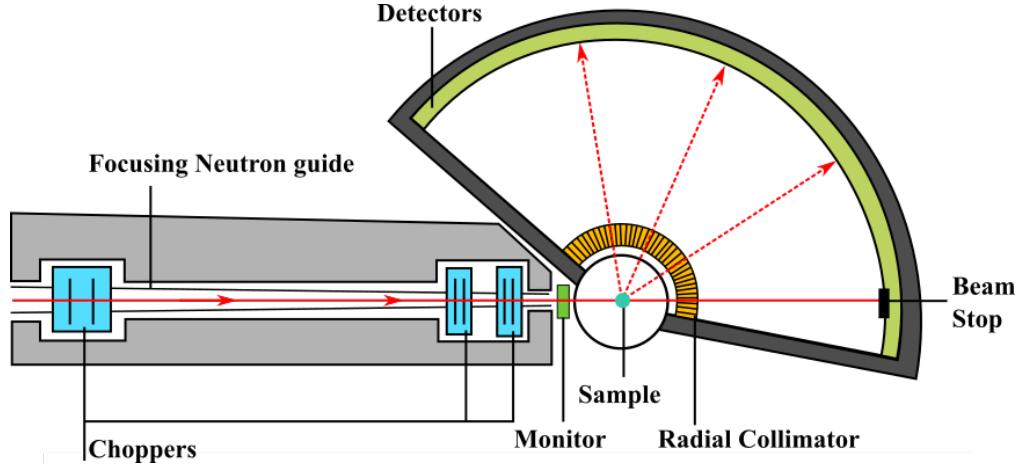


Figure 4.10: A schematic of the time of flight direct geometry spectrometer, IN5 at the ILL. The instrument was used to investigate the low energy excitations on single crystal samples of HoB_4 . The figure was adapted from Ref. [96].

pulses are then monochromated by a second set of choppers. Two incident wavelengths of $\lambda = 3.5$ and 5 \AA were used throughout the experiment. The single crystal HoB_4 (1.6 g) sample was attached to an aluminium sample holder with Kwik Fill two part resin and orientated so that an b -axis was vertical, defining the horizontal ($h0l$) scattering plane. The scattered neutrons are detected by an array of position sensitive ^3He detectors, which cover an angular range of 150° and a vertical angular range of $\pm 20.55^\circ$.

Chapter 5

Magnetic Properties of HoB_4

This chapter is devoted to the study of the magnetic properties of the frustrated antiferromagnet HoB_4 . The investigation into the magnetic properties of HoB_4 presented in this thesis begins by checking the quality of the crystals grown by performing x-ray measurements as well as characterising single crystal samples with lab based measurements such as magnetic susceptibility [47, 100], magnetisation [42, 101], heat capacity [100] and resistivity [102]. We then expanded upon these measurements by performing magnetisation measurements down to lower temperatures of 0.5 K as well as going to higher magnetic fields of 500 kOe. HoB_4 shows successive phase transitions, the first is second order at $T_{\text{N1}} = 7.1$ K, while the latter is first order at $T_{\text{N2}} = 5.7$ K. The field dependent magnetisation measurements have shown the existence of metastable phases at fractional values of the saturation magnetisation, M_{sat} , where $M/M_{\text{sat}} = \frac{1}{3}$, $\frac{4}{9}$ and $\frac{3}{5}$.

The main focus of the chapter is on the neutron scattering measurements. Previous measurements on polycrystalline samples have revealed the presence of an incommensurate magnetic phase with a propagation vector $(\delta, \delta, \delta')$, where $\delta = 0.022$ and $\delta' = 0.43$ in the intermediate temperature phase as well as a non-collinear antiferromagnetic phase with a $\mathbf{k} = 0$ commensurate structure in the low temperature phase. The investigation also revealed the presence of diffuse scattering in the paramagnetic and incommensurate phases using polarised neutron measurements. We have performed zero field measurements with both polarised and un-polarised neutrons using single crystals. We also expanded upon the zero-field measurements by performing neutron diffraction experiments in fields up to 50 kOe to investigate the magnetic structures of the fractional magnetisation plateaux observed in HoB_4 .

To better understand the unusual behaviour of HoB_4 , further inelastic neutron measurements were made on polycrystalline samples to investigate the crys-

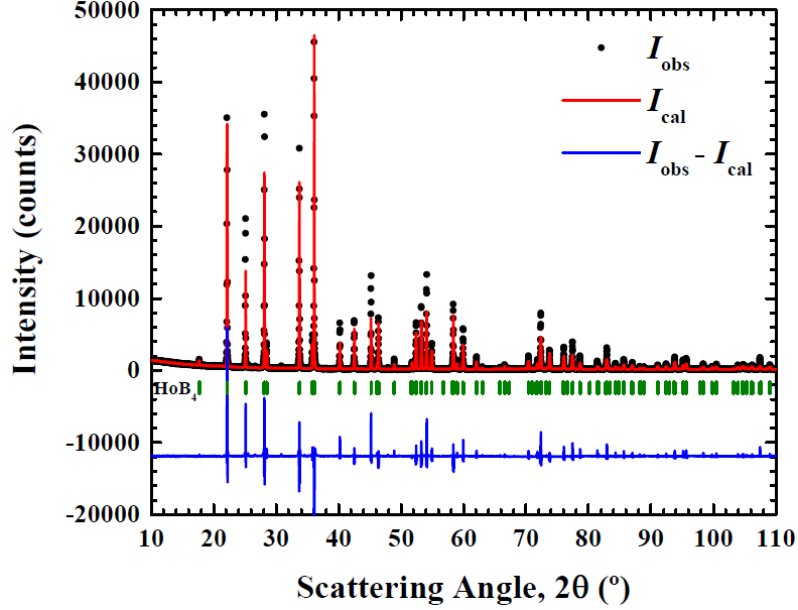


Figure 5.1: Powder x-ray diffractogram of HoB_4 . The red line corresponds to the fit from the Rietveld refinement, while the blue line corresponds to the difference between the observed and calculated intensity. The green dashes correspond to the expected positions for nuclear Bragg reflections.

talline electric field. Inelastic neutron measurements on single crystal were also made in order to investigate the low energy magnetic excitations. The initial analysis is presented, however the fitting the crystal fields is quite challenging and is still an on-going project. The final section of the chapter is devoted to the conclusions and a careful comparison of the magnetic properties of HoB_4 with that of the other members of the RB_4 family.

5.1 Bulk Characterisation

The single crystals were grown as described in section 4.1. It was found that the single crystals had a higher purity compared to the initial polycrystalline rods formed. Thus for polycrystalline samples, part of the single crystal were powdered. The composition of the sample was determined by Rietveld refinement of the powder x-ray diffractogram which is shown in Fig. 5.1. The main phase is HoB_4 , and there is no significant presence of an impurity phase. The red line shows the fit, while the blue curve is the difference between the observed and calculated intensity. The peaks observed in the difference curve are arising due to the fit not estimating the peak shape

Space Group: $P4/mbm$			
Lattice Parameters: $a = b = 7.08 \text{ \AA}$, $c = 4.01 \text{ \AA}$			
Ion	Wyckoff Position	Positions	Fractional Coordinates
Ho	$4g$	$(x, x + \frac{1}{2}, 0)$	$x = 0.318$
B1	$4e$	$(0, 0, z)$	$z = 0.196$
B2	$8j$	$(x, y, \frac{1}{2})$	$x = 0.172, y = 0.0506$
B3	$4h$	$(x, x + \frac{1}{2}, \frac{1}{2})$	$x = 0.0880$

Table 5.1: Fractional coordinates and Wyckoff Positions for each site in HoB_4 determined from powder x-ray diffraction measurements.

accurately due to the asymmetrical shape of the peak. The structural parameters have been determined from the refinement and are shown in Table 5.1. While the determined parameters are in agreement with previous investigations [46, 103], the fractional x, y, z value depend on the intensity of the peaks, so there should be some caution with the exact value and the value determined from neutron diffraction are more reliable (Section 5.2.2).

The quality of the single crystal was checked using the a backscattering Laue camera (as described in section 4.1.5). Fig. 5.2 shows the Laue photographs of the $[001]$ and $[100]$ -directions compared to the simulated pattern made using the OrientExpress software [104]. As can be seen there is good agreement between the two patterns. During scanning along the crystal it was found there are some positions where there was doubling up of points or shifting of the Laue pattern. This was caused by grain boundaries and have multiple grains. However, the grain were large and allowed good single crystal samples to be isolated.

5.1.1 Magnetic Susceptibility

Fig. 5.3 shows the temperature dependence of the magnetic susceptibility for both $H \parallel c$ and $H \perp c$ in an applied magnetic field of $H = 0.1 \text{ kOe}$. For $H \parallel c$ HoB_4 shows successive magnetic phase transitions in $\chi(T)$, observed as a broad maximum at approximately $T_{N1} = 7.1 \text{ K}$ and a discontinuous drop at $T_{N2} = 5.4 \text{ K}$. These transitions define three phases, referred to in this chapter as the high temperature paramagnetic regime ($T > T_{N1}$), the intermediate temperature (IT) phase ($T_{N2} < T < T_{N1}$) and the low temperature (LT) antiferromagnetic phase ($T < T_{N2}$). The transitions are also observed for $H \perp c$, although the maximum at T_{N1} is less pronounced compared to that observed for $H \parallel c$.

The inverse magnetic susceptibility is shown in the inset of Fig. 5.3. For $H \parallel c$, HoB_4 exhibits Curie-Weiss behaviour between 50-300 K and was fitted in

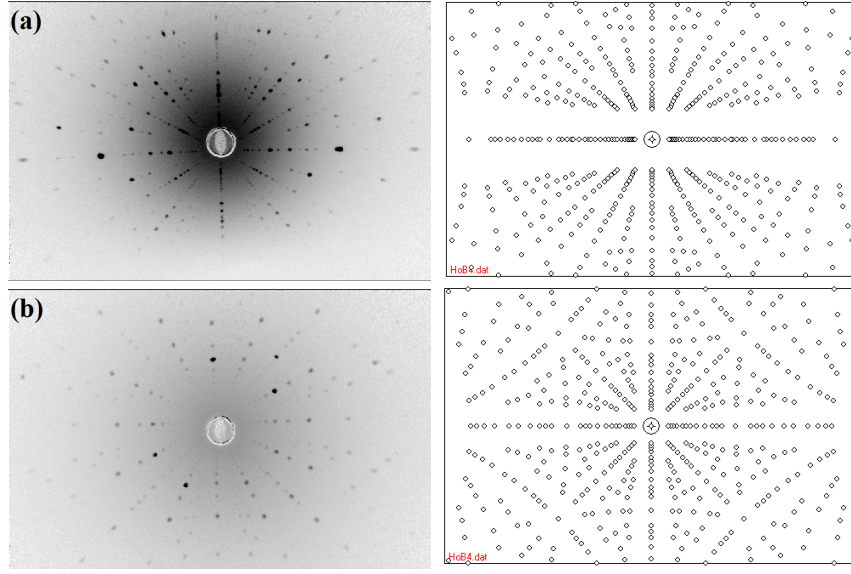


Figure 5.2: Single crystal Laue diffraction photographs of HoB_4 showing (a) the $[100]$ direction compared to the simulated pattern of the $[100]$ direction and (b) the $[001]$ directions compared to simulated pattern for the $[001]$ direction.

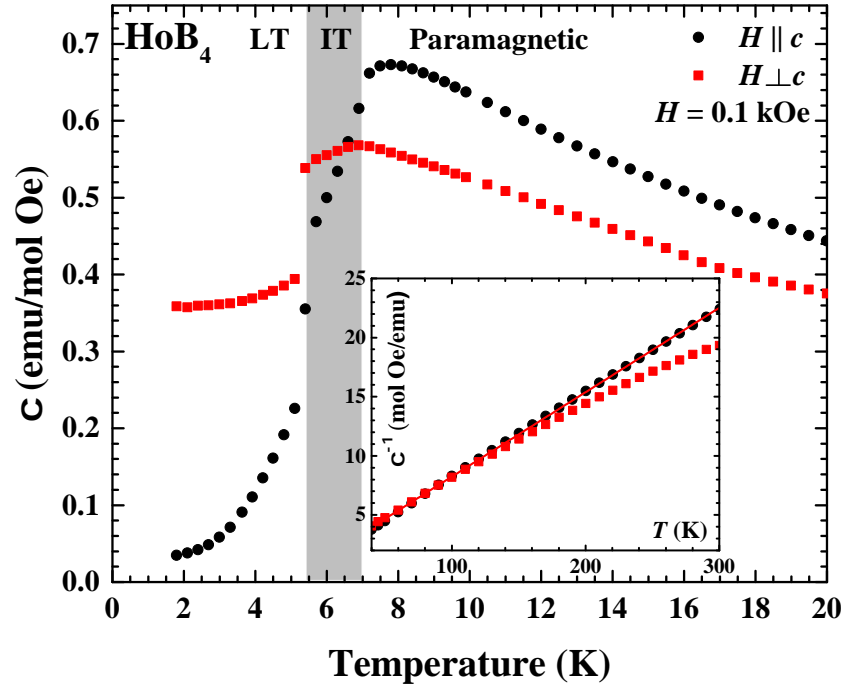


Figure 5.3: Temperature dependent magnetic susceptibility of HoB_4 in a magnetic field of 0.1 kOe for $H \parallel c$ and $H \perp c$. The inset shows the inverse susceptibility between 40 and 300 K.

this range with a least squares linear regression fit [105]. The Curie-Weiss constant is $\theta_{\text{CW}} = -14$ K, the negative Curie-Weiss temperature indicates the antiferromagnetic nature of the magnetic structure. The effective magnetic moment, μ_{eff} was determined to be $\mu_{\text{eff}} = 10.6\mu_{\text{B}}$, which is in agreement with the value of $10.6\mu_{\text{B}}$ calculated using Hund's rules as described in section 2.1.1 as well as previously published works [47, 67, 100, 102]. The inverse susceptibility for $H \perp c$, however does not show Curie-Weiss behaviour at high temperatures and is linear between 50-100 K before curving away. Fig. 5.4 shows how of the temperature dependent magnetic susceptibility curves evolve in different magnetic fields. For $H \parallel c$ both ordering temperatures are suppressed by an increasing magnetic field; $T_{\text{N}2}$ is no longer present above 20 kOe, while $T_{\text{N}1}$ persists up to at least 25 kOe. The value of the magnetic susceptibility has a similar value for both 20 and 25 kOe suggesting a stable, field induced magnetic state is formed. For $H > 30$ kOe the magnetic susceptibility increases and levels off where the system appears to have reached saturation.

Fig. 5.4(b) shows the temperature dependent magnetic susceptibility curves in different magnetic fields for $H \perp c$. Similarly to $H \parallel c$, the ordering temperature is suppressed. $T_{\text{N}1}$ can no longer be distinguished above 100 Oe, while $T_{\text{N}2}$ is present up to at least 20 kOe.

5.1.2 Magnetisation

The samples used were plate-like and arranged to reduce the demagnetisation factor. The demagnetisation factor did not exceed 0.22, therefore the correction for an effective field does not exceed 1%. The demagnetisation factor was calculated by followed the method outline in ref [106]. Fig. 5.5(a) shows the magnetisation curves for two separate samples at $T = 2$ K. The first crystal was used for neutron diffraction measurements on D10 and was found to contain a small HoB_2 impurity, while the second crystal was used for polarised neutron diffraction measurements on D7 and contains no significant impurity. These will be referred to as D10 and D7 crystal respectively. The D10 crystal magnetisation curve shows a large plateau at $M/M_{\text{sat}} = \frac{1}{3}$ with a very small feature occurring at $M/M_{\text{sat}} \approx \frac{1}{6}$, while there is a slightly more pronounced feature at $M/M_{\text{sat}} \approx \frac{3}{5}$. The derivative (see Fig. 5.5(b)), dM/dH indicates these features more clearly. These have been observed in previously published results [42, 102] except for the feature at $M/M_{\text{sat}} \approx \frac{1}{6}$, which is not observed in either work. The D7 crystal measurements were taken at two slightly different tilt angles away from the c -axis. Comparing the D10 crystal magnetisation curve to the two curves shown for the D7 crystal it can be seen that the $\frac{1}{3}$ magnetisa-

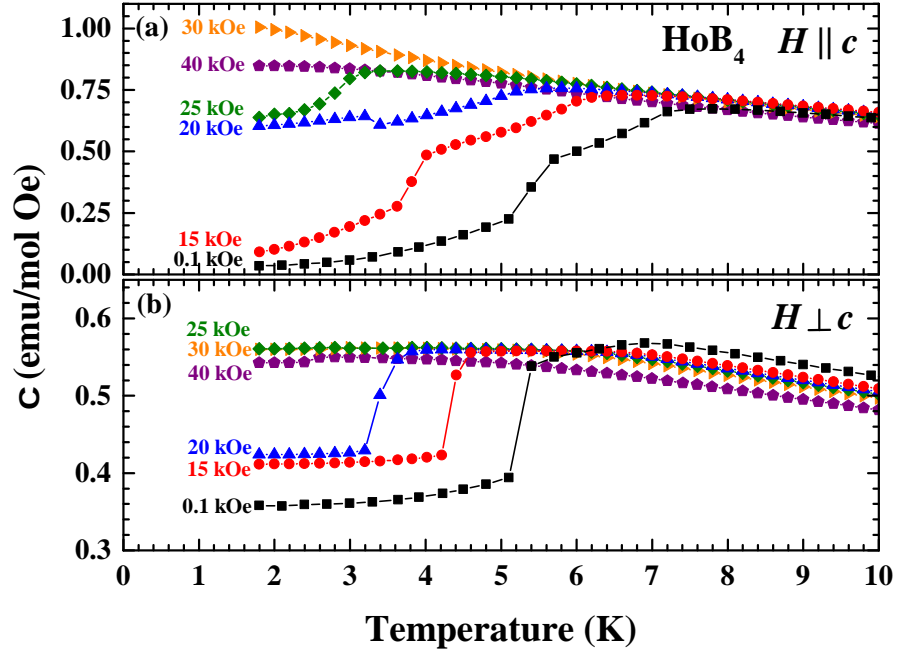


Figure 5.4: Temperature dependent magnetic susceptibility in a range of magnetic fields from 0.1 to 40 kOe for (a) $H \parallel c$ and (b) $H \perp c$.

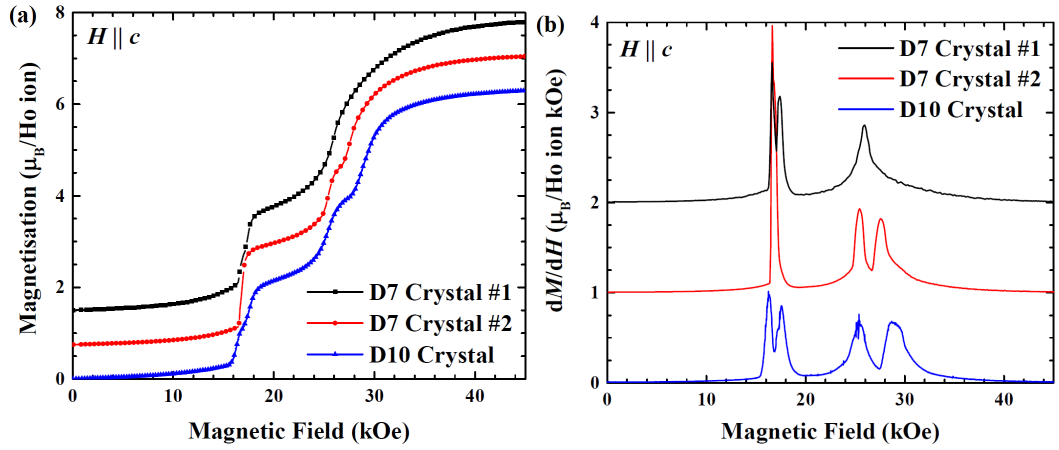


Figure 5.5: Field dependent magnetisation measurements for $H \parallel c$ for two separate crystal growths. The D10 crystal was found to have a small HoB_2 impurity and there are two slightly different orientations of the D7 crystal. Each curve is subsequently offset by $0.75\mu_B/\text{Ho ion}$. (b) Shows the derivative of the magnetisation curves. Each curve is subsequently offset by $1\mu_B/\text{Ho ion kOe}$. All magnetisation curves correspond to the field ramping up.

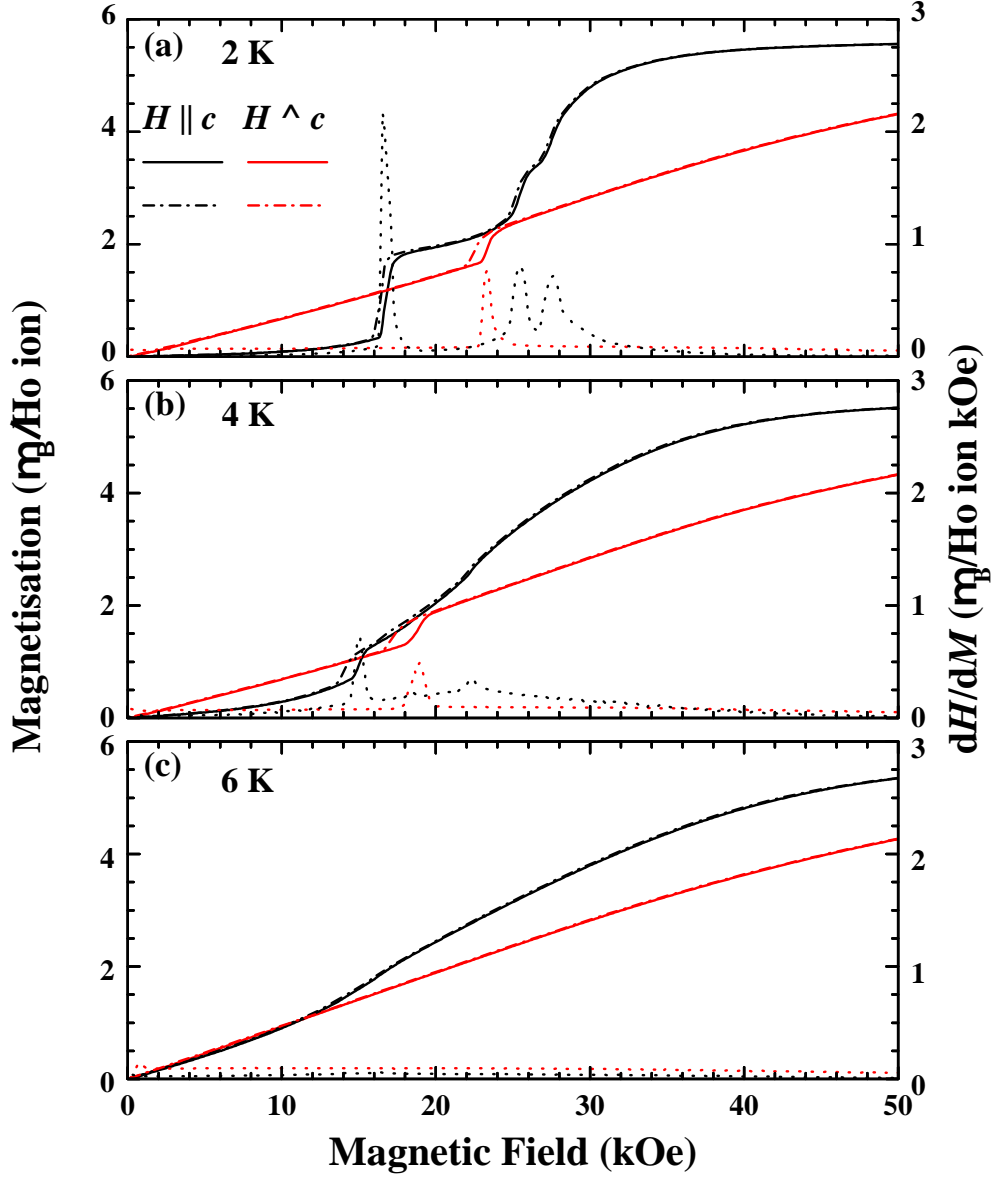


Figure 5.6: Field dependent magnetisation measurements for $H \parallel c$ and $H \perp c$ at temperatures of (a) 2 K, (b) 4 K and (c) 6 K. The solid curves correspond to the field ramping up, while dash-dot curves are the field ramping down. The dotted curves correspond to the derivative, dH/dM of the curve corresponding to the field being ramped up (right axis).

tion and one of the two small features is observed in each curve. This suggests that the appearance of the small features above and below the $\frac{1}{3}$ magnetisation plateau depends heavily on the orientation of the c -axis and the field. Where possible the tilt away from the field is quoted. The magnetisation curves saturate at approximately $6.5\mu_B$ per Ho ion, which is significantly smaller than the effective moment, $\mu_{\text{eff}} = 10.6\mu_B$, found from $\chi^{-1}(T)$ measurements as well as the saturation moment for a Ho ion, predicted to be $gJ\mu_B = 10\mu_B$. For the remainder of this section the D7 crystal has been used.

Fig. 5.6 shows the field dependent magnetisation curves at different temperatures for both $H \parallel c$ and $H \perp c$. Fig. 5.6(a) shows the magnetisation curves at $T = 2$ K for $H \parallel c$ and $H \perp c$. The measurements for $H \parallel c$ are in agreement with those in Fig. 5.5, while $H \perp c$ shows a single transition at 23.5 kOe, which is highlighted by the derivative, dH/dM . There is no indication of saturation up to 100 kOe for the curve taken where $H \perp c$. There is a large anisotropy between the two directions favouring the c -axis, the large difference suggesting an Ising characteristic to the spins in the LT phase. The field ramping down is shown as a dashed line. Both curves show hysteresis around each transition. Increasing the temperature to $T = 4$ K (Fig. 5.6(b)), the $\frac{1}{3}$ -magnetisation plateau becomes significantly less defined, similarly for the $\frac{3}{5}$ -magnetisation feature, both transitions shifting to lower magnetic fields. The transitions for $H \perp c$ are still present, but shift to a lower magnetic field of 19 kOe. Again the field ramping down is shown with a dashed line, there is still hysteresis for both field directions, but it is only pronounced around the main field induced transition. Increasing the temperature further to $T = 6$ K (Fig. 5.6(c)), the $H \parallel c$ curve shows a broad transition, beginning at 15 kOe, while there is no obvious transition for the $H \perp c$ curve. For both field directions there are no obvious hysteresis effects.

5.1.3 Low Temperature (^3He) Measurements

Fig. 5.7 shows the field dependent magnetisation measurements at $T = 0.5, 0.8$ and 1 K. The transition to the $\frac{1}{3}$ -magnetisation plateau shifts to larger fields with increasing temperatures, while the feature at $M/M_{\text{sat}} \approx \frac{3}{5}$ becomes more pronounced at lower temperatures compared to the magnetisation curve at $T = 2$ K shown in Fig. 5.6. At $T = 0.5$ K an additional feature appears at a 25.4 kOe corresponding to $M/M_{\text{sat}} \approx \frac{1}{2}$. This is highlighted by a local minimum in the derivative, dM/dH shown in Fig. 5.7(b). To investigate this new field-induced state, the temperature dependent magnetic susceptibility measurements were made in a magnetic field of 25.4 kOe corresponding to the local minimum between two magnetisation jumps

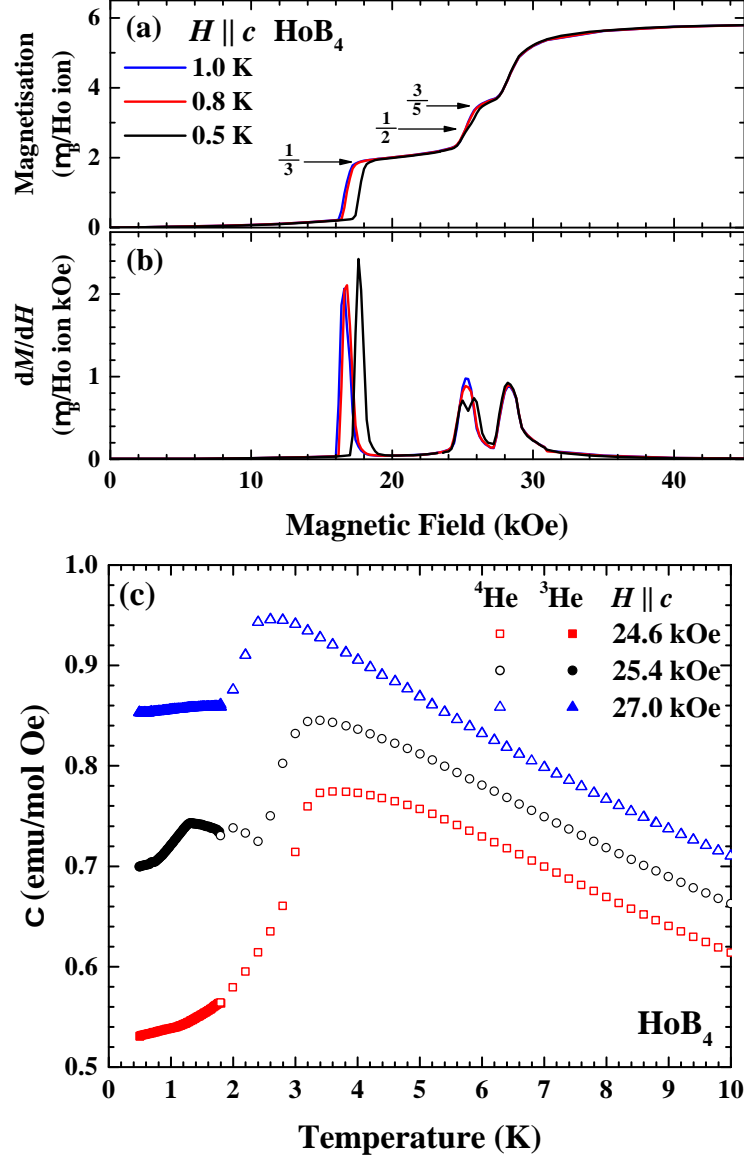


Figure 5.7: (a) Field dependent magnetisation measurements using ^3He to achieve temperatures below $T \leq 1$ K. (b) The derivative, dM/dH , of the magnetisation curves. Scans made by ramping up the field. (c) Temperature dependent susceptibility measurements at 24.6, 25.4 and 27 kOe between the temperatures of 0.5-10 K. Filled symbols correspond to measurements made with the ^3He inset, while open symbols were made using ^4He .

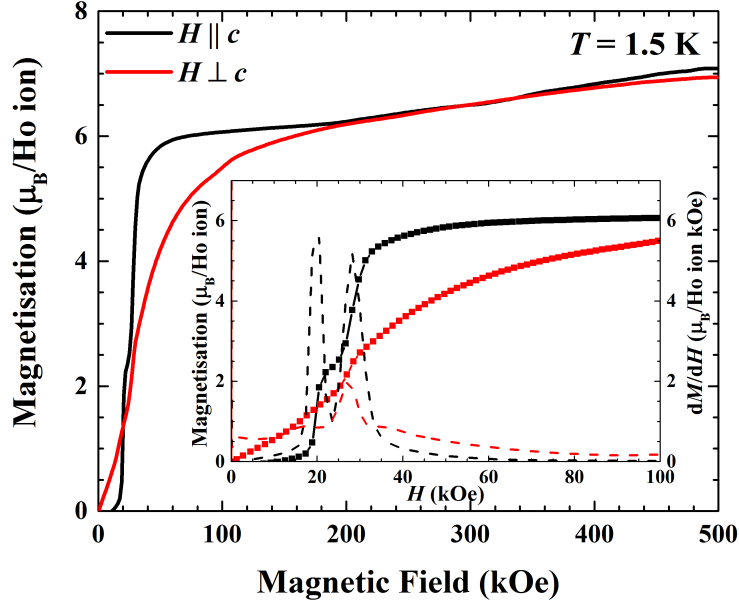


Figure 5.8: Field dependent magnetisation measurements made on HoB_4 at $T = 1.5$ K with a pulsed magnetic field up to 500 kOe. The inset shows a lower field range to highlight the fractional magnetisation plateaux. The derivative dM/dH is shown as the dashed curve. Only curves where the field was ramped up are shown.

in the dM/dH for $T = 0.5$ K, as well as in fields just above and below it (see Fig. 5.7(c)). All three susceptibility curves show a broad maximum at around 3.7 K, which is suppressed to lower temperatures with an increasing magnetic field. At $H = 25.4$ kOe, a clear extra feature is observed in $\chi(T)$ at $T \approx 1$ K, which is not seen at either $H = 24.6$ kOe or $H = 27.0$ kOe. This observation provides additional support to the claim that $M/M_{\text{sat}} = \frac{1}{2}$ might be stabilised in HoB_4 in a narrow field interval at a sufficiently low temperature.

5.1.4 High Field Magnetisation

Field dependent magnetisation measurements in fields up to 500 kOe are shown in Fig. 5.8. For $H \parallel c$, at low fields, we observe the $\frac{1}{3}$ -magnetisation plateau as expected. The magnetisation curve levels off at approximately 40 kOe, before upturning at approximately 200 kOe, and gradually increasing. This suggests that the magnetic moments are tilting towards the field direction with increasing field. Similarly for $H \perp c$ we observe the expected transition at $H = 30$ kOe, while the magnetisation gradually increases, before levelling off at approximately 200 kOe and then gradually increasing again, reaching $7\mu_B$ per Ho ion at 500 kOe. During the

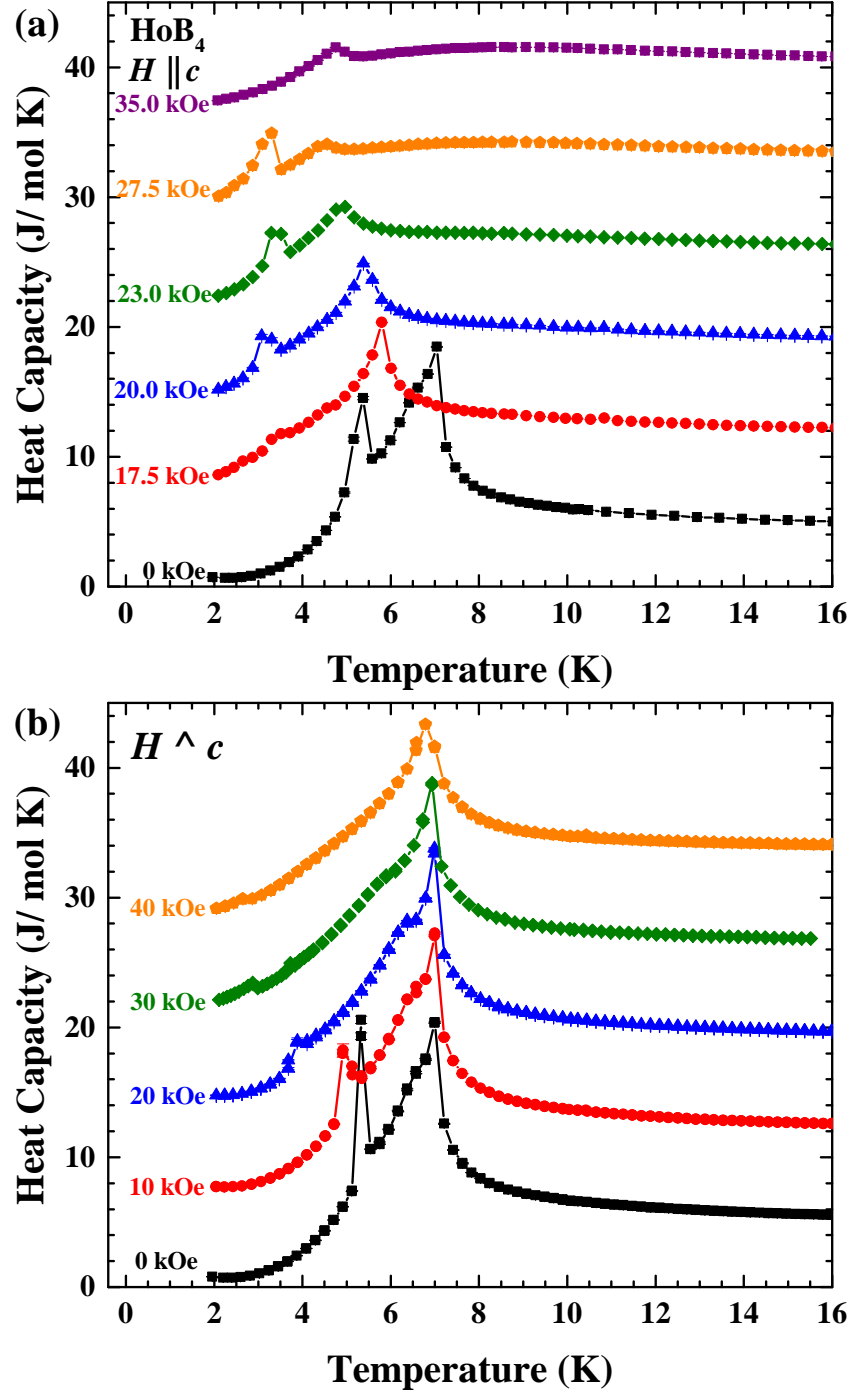


Figure 5.9: Temperature dependent heat capacity measurements of HoB_4 in different magnetic fields made for the field directions of (a) $H \parallel c$ and (b) $H \perp c$. For both directions the curves are subsequently offset by 7 J/mol K.

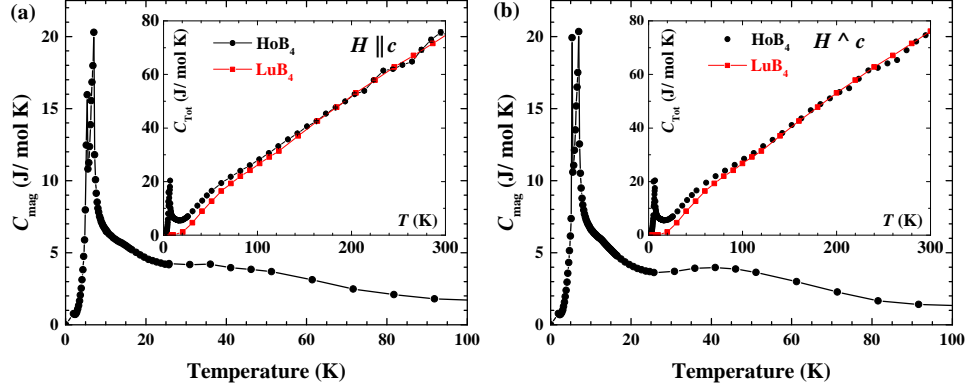


Figure 5.10: The magnetic contribution of the heat capacity for the two crystal geometries (a) $H \parallel c$ and (b) $H \perp c$. This was determined by subtracting the heat capacity of the non-magnetic LuB_4 reference compound from the total heat capacity of HoB_4 . A comparison of the total heat capacity for both compounds is shown in the inset.

experiment we have found that upon application of the magnetic field the sample experienced significant torque and had a tendency to deviate away from the $H \parallel c$ and $H \perp c$ geometries unless firmly attached to a sample holder. These observations as well as the magnetisation curves suggest that the a or c -axis may not be the easy magnetisation direction in HoB_4 in higher applied fields and that it may lay somewhere in between.

5.1.5 Heat Capacity

Figure 5.9 shows the evolution of the temperature dependent heat capacity in different magnetic fields for both $H \parallel c$ and $H \perp c$. Fig. 5.9(a) corresponds to heat capacity measurements where $H \parallel c$. In zero field there is a lambda-type anomaly at approximately $T_{N1} = 7$ K indicating the second order nature of the transition. While a sharp spike observed at $T_{N2} = 5.7$ K is a first order transition. The sharp spike arises as the relaxation method used to collect the data is better suited to detecting second order phase transitions. Increasing the field, T_{N1} is suppressed to 4.2 K at $H = 27.5$ kOe. In a field of 35 kOe T_{N1} is increased to 4.3 K. T_{N2} is suppressed to 2.7 and 2.6 K at 17.5 and 20 kOe respectively. This transition is then increased to 2.8 K in a field of 23 and 27.5 kOe and is no longer visible at 35 kOe.

Figure 5.9(b) shows the heat capacity measurements for $H \perp c$. As expected it displays two transitions; a second order phase transition at 7.1 K and a first order phase transition at 5.7 K. Increasing the field we see that the second order transition

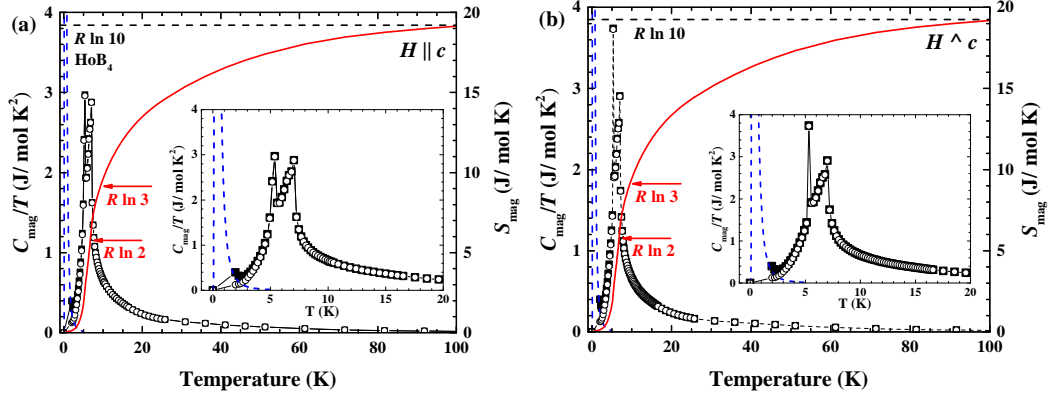


Figure 5.11: C_{mag}/T (filled squares) curve for HoB_4 for (a) $H \parallel c$ and (b) $H \perp c$. The open circles corresponds to C_{mag}/T where the nuclear Schottky anomaly (dashed line) has been subtracted. C_{mag}/T has been integrated with respect to T giving the magnetic entropy (red curve).

remains broadly unchanged, while the first order phase transition is suppressed from 5.7 K in zero field to 2.5 K in a field of 40 kOe.

The heat capacity shown in Fig. 5.9 is the total heat capacity and is comprised of lattice, electronic and magnetic contributions. The lattice and electronic contributions of the heat capacity can then be estimated through use of a non-magnetic isostructural compound (LuB_4 is used in this case, the data for which was taken from Ref. [107]). The magnetic contribution to the heat capacity can then be determined by subtracting the heat capacity of the reference compound from the total heat capacity of the magnetic compound, however the differences in molecular masses must be accounted for. This can be done by determination of the ratio $r = \theta'/\theta$, where θ' and θ are the Debye temperatures of the reference compound and the magnetic compound respectively. This ratio can be estimated with [108, 109]:

$$r \approx \sqrt{\frac{M(\text{HoB}_4)}{M(\text{LuB}_4)}} \quad (5.1)$$

The re-normalisation ratio can then be used to estimate the lattice contribution by multiplying the ratio with the temperature values of the non magnetic reference compound, fitted and the subtracted. This procedure was performed for HoB_4 and the ratio was found to be $r = 0.978$ and the magnetic heat capacity is shown in Fig. 5.10 for both $H \parallel c$ and $H \perp c$. The inset in both cases shows a comparison between the total heat capacity of LuB_4 and HoB_4 at high temperatures. As both curves are in zero field we expect the results to be identical and the labels $H \parallel$

c and $H \perp c$ are merely used to indicate the differing geometry of the crystals used. The insets in Fig. 5.10 show a comparison between the heat capacity of HoB_4 and LuB_4 , in both case the temperature dependence is approximately linear at high temperatures. This temperature dependence has also been observed in ErB_4 , GdB_4 , TbB_4 and DyB_4 , which is to be expected [110–113]. It was put forward by ref. [113], that this linear dependence was arising due to differences between the Debye temperatures of the rare earth and boron sublattices. The LuB_4 curves was fitted with a 7th order polynomial and the resulting curve was subtracted from HoB_4 total heat capacity. As can be seen for both directions, we observe the two magnetic phase transitions, however we also observe two Schottky anomalies at approximately 15 and 33 K. To estimate the energy gap giving rise to the Schottky anomaly we used the following [114]:

$$C_{\text{sh}} = R \left(\frac{\delta}{T} \right) \frac{g_0}{g_1} \frac{\exp(\delta/T)}{[1 + (g_0/g_1) \exp(\delta/T)]^2} \quad (5.2)$$

where R is the ideal gas constant, δ is the energy separation in Kelvin. g_0 and g_1 is the degeneracy in the ground and first excited state. The Schottky anomalies are most likely arising from the population of low energy crystal field levels and Equation (5.2) suggests that the energy separations giving rise to these anomalies are approximately 33 and 72 K.

We then determined the magnetic entropy by integrating C_{mag}/T with respect to T , which is shown in Fig. 5.11. Holmium ions are unusual in that there is a large hyperfine coupling between the nuclear spins and the electronic spins. This hyperfine interaction leads to a nuclear Schottky anomaly, which is observed as a peak at low temperatures, the upturn of which is seen in Fig. 5.11. The anomaly was estimated from measurements on $\text{Ho}_2\text{GaSbO}_7$ and has been successful in estimating the anomaly in other Ho compounds such as $\text{Ho}_2\text{Ti}_2\text{O}_7$ [2, 115]. The estimation of the anomaly is shown by the dotted line. This was subtracted from the solid points and the resulting curve is shown as the open symbols.

The entropy reaches 3.21 J/mol K at $T_{\text{N}2}$ and 7.11 J/mol K at $T_{\text{N}1}$. At high temperatures the entropy levels off to a value of 19.07 J/mol K, which corresponds to a value of $R \ln 10$. The maximum entropy of a magnetic subsystem is defined as $R \ln(2J + 1)$, where J is the quantum number of the electron angular momentum in a paramagnetic ion. This means the maximum entropy of Ho ions is $R \ln 17$ ($J=8$). This implies that the crystal field splitting in Ho can be upto 17 singlet levels. The entropy we observe at $T_{\text{N}1}$ is very close to $R \ln 2$, where the entropy reaches $R \ln 2$ between $T_{\text{N}2}$ and $T_{\text{N}1}$ at $T = 6.7$ K. The entropy reaches $R \ln 3$ at 9.2 K. This is in

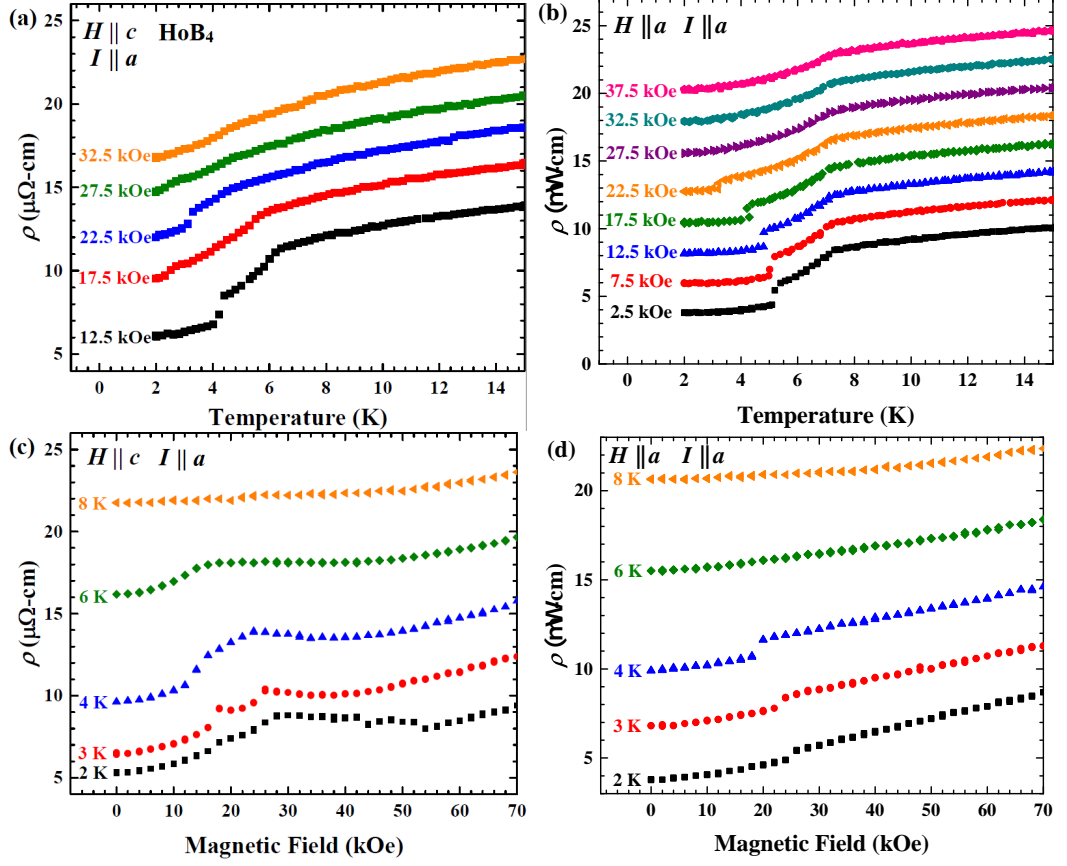


Figure 5.12: Temperature dependent resistivity measurements for (a) $H \parallel c$ and (b) $H \perp c$ each curve is subsequently offset by $2 \mu\Omega - \text{cm}$. Field dependent resistivity measurements for (c) $H \parallel c$ and (d) $H \perp c$, each curve is subsequently offset by $3 \mu\Omega - \text{cm}$.

agreement with previous measurements [113]. The difference between the maximum allowed entropy and the value of $R \ln 10$ imply large splitting between the crystal field and that there are relatively high energy crystal field levels.

5.1.6 Resistivity

Fig. 5.12(a) and (b) shows the temperature dependent resistivity measurements for HoB_4 for $H \parallel c$ and $H \perp c$ respectively. In zero field the resistivity displays a linear relationship from high temperatures (not shown) down to the magnetic phase transition, T_{N1} indicating the metallic nature of HoB_4 , consistent with other members of the RB_4 family. For both field arrangements, HoB_4 shows two transitions; there is a drop in the resistivity at $T_{N1} = 6.9 \text{ K}$ and a further discontinuous drop at resistivity

at $T_{N2} = 5.4$ K in low magnetic fields. The sudden slope change could be due to the loss of spin disorder scattering at the antiferromagnetic transition temperature, which has been suggested for the other members of the RB_4 family [62, 72]. For $H \parallel c$, both transition temperatures are suppressed with increasing field with T_{N1} no longer visible above at least 22.5 kOe and T_{N2} no longer visible above 27.5 kOe. For $H \perp c$, T_{N1} remains broadly unchanged, while T_{N2} is suppressed from 5.4 K at 2.5 kOe to 3.4 K at 22.5 kOe and is no longer visible above this field.

The field dependent resistivity curves for $H \parallel c$ and $H \perp c$ are shown respectively in Fig 5.12(c) and (d). At $T = 2$ K, there is a change of gradient at 18 kOe, which is consistent with the $\frac{1}{3}$ -magnetisation plateau. The resistivity levels off at approximately 30 kOe, before increasing again at 55 kOe. A similar magnetoresistance is was observed in other Ising-type RB_4 family memebers such as ErB_4 and was explained due to conventional orbital magnetiresistance with additional scattering due to magnetic disorder and spin excitations as the plateau state evolves in magnetic field [116]. The feature is observable up to 4 K, but shifts to lower magnetic fields. There is a feature at 6 K, which is consistent with the magnetisation curve in Fig.5.6(c). For $H \perp c$ (Fig. 5.12(d)) the resistivity curves at 2, 3 and 4 K show a single transition which shifts to lower fields with increasing temperature. The magnetoresistance increases with decreasing temperature is a maximum at $T = 2$ K with a value of 1.7% and 1.3%. This is significantly smaller than the previously published results of 4000% [102]. While the transition temperature and fields are all consistent with previously published results and characterisation, the values for the resistivity are larger. This could indicate the presence of cracks, grain boundaries or impurity in the sample.

5.2 Single Crystal Neutron Diffraction

5.2.1 Polarised Neutron Diffraction

Fig. 5.13 shows the zero-field intensity maps of the $(h0l)$ scattering plane of HoB_4 . Using a z -polarisation (parallel to the $[010]$ -direction) the non spin-flip (NSF) and spin-flip (SF) channels were measured for $T = 10, 6.5$ and 1.5 K. The paramagnetic phase at $T = 10$ K, close to the first magnetic transition is shown in Fig. 5.13(a). The nuclear Bragg reflections are observed in the NSF channel, while weak features are also observed corresponding to Bragg positions are observed in the SF channel. These features are arising due to “leakage” as described in section 4.3.2. A comparison of the intensity shows these features are approximately 1% of the intensity of the NSF counterparts and are easily distinguished from real features. Broad magnetic

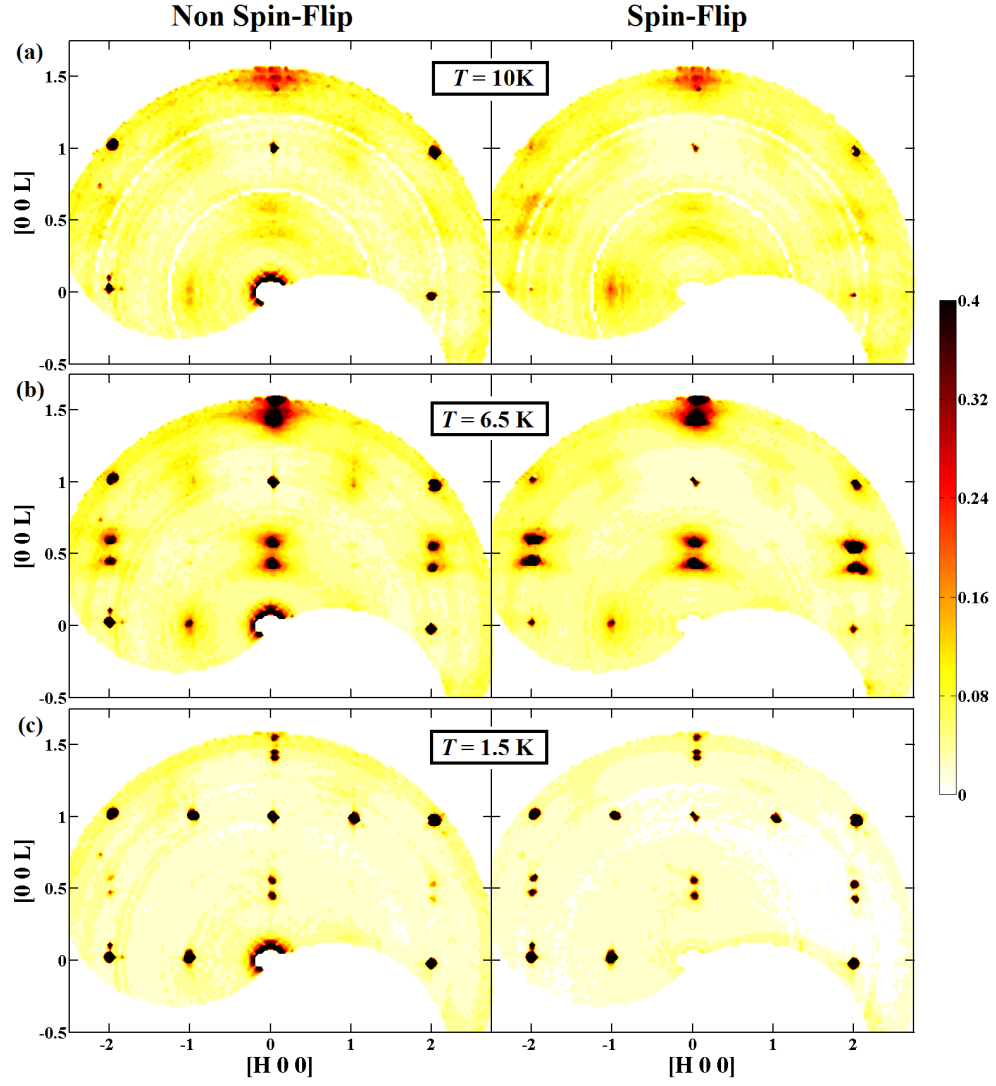


Figure 5.13: Single crystal neutron diffraction maps of $(h0l)$ plane for HoB_4 using the D7 diffractometer. The non spin-flip (left column) and spin-flip (right column) channels at different temperature (a) 10 K, (b) 6.5 K and (c) 1.5 K are shown.

features are observed at positions $(0\ 0\ 0.43)$, $(0\ 0\ 1.43)$, $(\bar{2}\ 0\ 0.43)$ and $(2\ 0\ 0.43)$ corresponding to the incommensurate reflection positions. The first transition occurs at $T_{N1} = 7.1$ K indicating these broad features are diffuse scattering arising from the formation of short range correlations above ordering. There are additional diffuse magnetic features observed at $(\bar{1}00)$, (100) , $(\bar{1}01)$ and (101) , again arising due to short-range correlations forming before the onset of long range antiferromagnetic order in the LT phase.

Fig 5.13(b) shows the intermediate temperature phase, with an incommensurate propagation vector of $(\delta, \delta, \delta')$, where $\delta = 0.02$ and $\delta' = 0.43$. D7 is unable to resolve $\pm\delta$ separately, however measurements on the D10 diffractometer has allowed us to determine the propagation vector. There is a dramatic increase in the intensity of the broad features at the incommensurate positions in both the NSF and SF channels. This suggests that there is a component of the magnetic moment in the horizontal ($h0l$) scattering plane as well as one parallel to $[010]$ direction and is consistent with the proposed incommensurate magnetic structure [46]. There is also an increase in the intensity of broad features observed at $(\bar{1}00)$, (100) , $(\bar{1}01)$ and (101) .

The low temperature phase (Fig. 5.13(c)) shows an increase in the intensity of the commensurate reflection as well as a dramatic increase in the intensity of the (100) reflection indicating the onset of long range antiferromagnetic order with a propagation vector of $\mathbf{k} = 0$. Surprisingly we still observe remnants of the incommensurate reflections down to 1.5 K in both the NSF and SF channels, although with significantly reduced intensity.

We have taken line cuts through the reciprocal space maps along the $[H\ 0\ L]$ direction for the NSF and SF channels, where $L = 0.43 \pm 0.10$ and to illustrate the temperature evolution of the scattering patterns. Fig. 5.14(a) shows the cuts along $[0\ 0\ L]$ focusing on the $(0\ 0\ 0.4)$ and $(0\ 0\ 0.6)$ reflections. At $T = 10$ K there is diffuse scattering heralding the onset of the incommensurate magnetic phase. It can be seen that the incommensurate reflections persist down to 1.5 K.

This behaviour is mirrored in fig. 5.14(b) which shows the line cut $[H\ 0\ 0.43]$, centred on $H = 0$. A broad diffuse scattering feature centred on $(0\ 0\ 0.43)$ is clearly seen at 10 K. At 6.5 K we see a well defined peak form on top of the diffuse scattering. This two component aspect of the peak suggests there is some disorder associated with the incommensurate phase, which is consistent with previous measurements [46]. However we observe at 1.5 K the peaks persisting, with reduced intensity and the diffuse scattering has disappeared. This can also be seen in the intensity maps (Fig. 5.13) where the broad features are well defined on cooling from

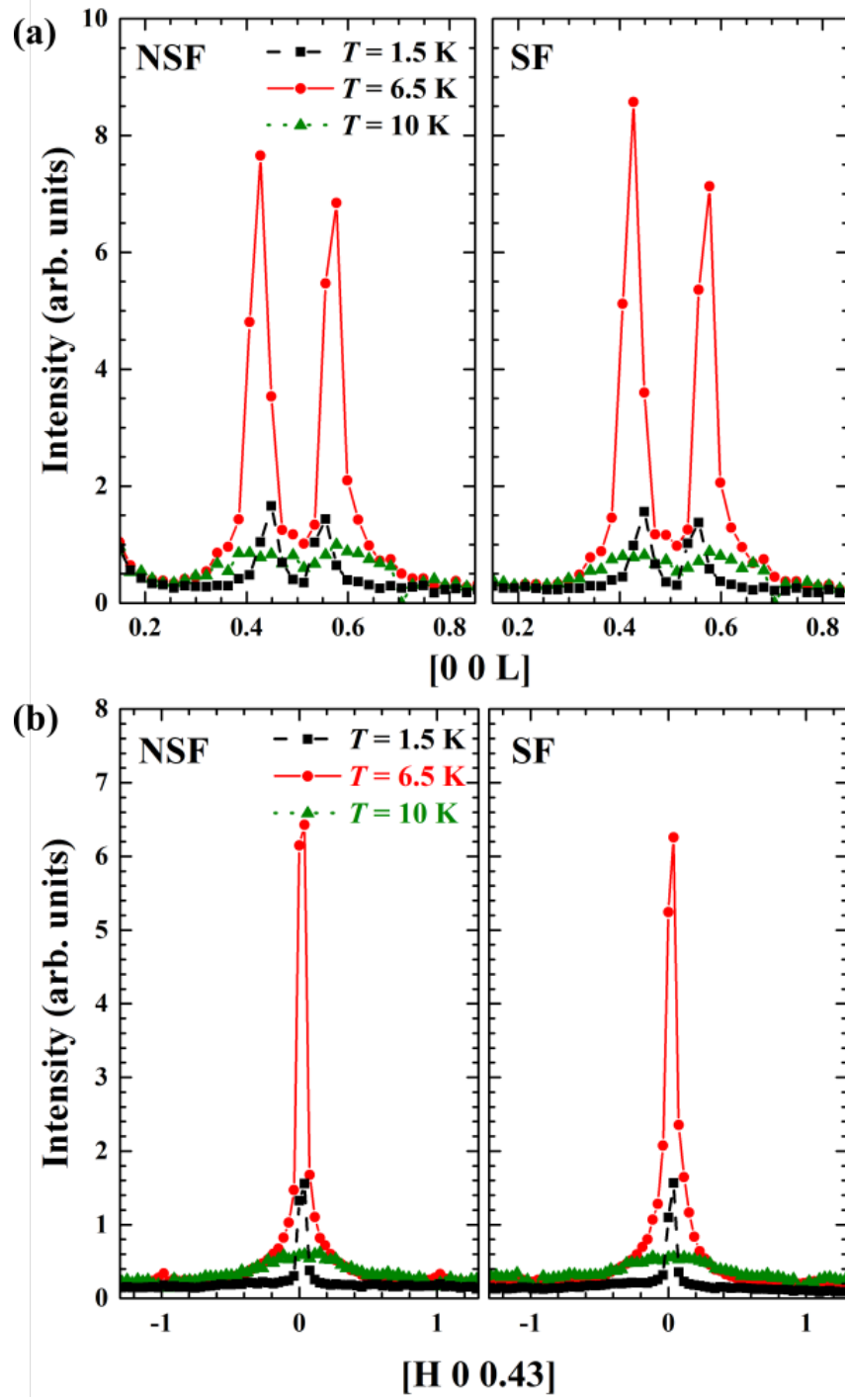


Figure 5.14: Line cuts of the z -polarisation intensity maps at 10, 6.5 and 1.5 K for the incommensurate reflections in the (a) $[0\ 0\ L]$ and (b) $[H\ 0\ 0.43]$ directions.

6.5 to 1.5 K in both the NSF and SF channels. We therefore suggest that the remnant intensity arises due to the incommensurate magnetic structure becoming “frozen” at low temperatures.

5.2.2 Neutron Diffraction In Applied Magnetic Field

Applied Field Scans

Single crystal neutron diffraction measurements were made using the D10 diffractometer at the ILL. The experimental set-up is described in section 4.3.1. Fig. 5.15 compares the intensity of the incommensurate $(2.02\ 1.02\ 0.43)$, fractional $(hk\frac{1}{3})$ and integer $(hk0)$ reflections with the field dependent magnetisation curve at $T = 2$ K. It is split into 4 stationary phases (grey shading), where the magnetisation remains approximately constant, separated by mixed transitional phases (white shading), where the magnetisation is changing rapidly. The dashed line also represents a very narrow transitional state between phases III and IV.

Phase I has intensity in both the (210) and (100) reflection, the latter is forbidden by the symmetry of the crystal structure, further indicating the antiferromagnetic nature of the phase. The zero field neutron diffraction experiment has indicated phase I corresponds to a long range, non-collinear antiferromagnetic order. There is a sharp decrease in the intensity of the (100) reflection at 16 kOe, which is mirrored in the field dependence of the intensity of the (210) reflection. The incommensurate $(2.02\ 1.02\ 0.43)$ is the antithesis of the (100) reflection and there is a dramatic increase in the intensity, as well as a gradual increase in the intensity of the $(h\ k\ \frac{1}{3})$ -type reflections. Here the zero field incommensurate phase is re-established as the dominant phase for a narrow field range ($16 < H < 18$ kOe), mixed with the ferrimagnetic phase II. The $(2\ 1\ \frac{1}{3})$ reflection reaches a maximum in Phase II at 21 kOe, coinciding with the $\frac{1}{3}$ -magnetisation plateau. Although with reduced intensity the incommensurate reflections persist into phase II as well. Phase III sees the onset of antiferromagnetic order with an increase in the intensity of the (100) , suppressing the incommensurate reflections. There is a transitional state where the intensity of the (100) decreases and the intensity of the (210) and $(2.02\ 1.02\ 0.43)$ reflection increases where both level off in Phase IV. With the gradual decrease of the intensity of the incommensurate reflection, the levelling off of the intensity of the (210) reflection and coupled with the high field measurements suggest phase IV is a polarised phase with the incommensurate phase “frozen-in”. Here the moments are tilting towards the field direction and the “frozen-in” phase steadily shrinks.

Fig. 5.16(a) shows the field dependence of the intensity of the $(2.02\ 1.02\ 0.43)$

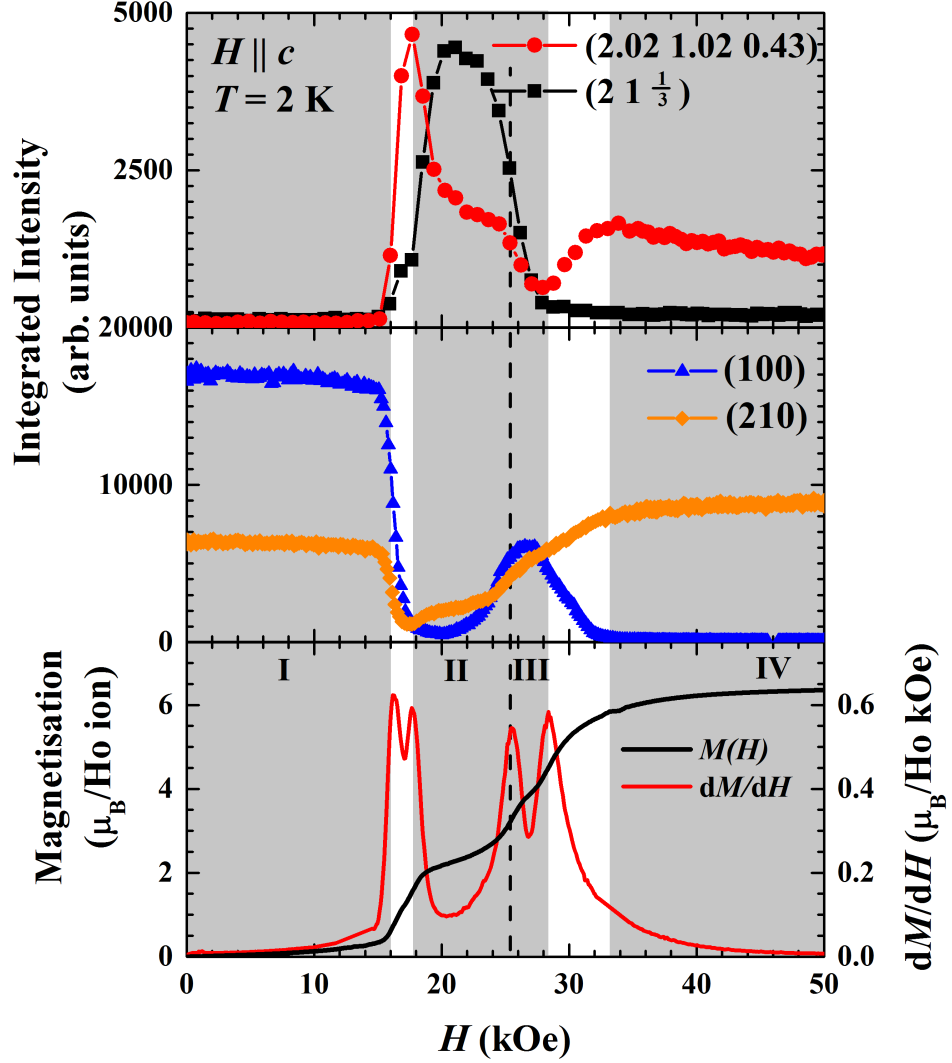


Figure 5.15: Evolution of (top panel) fractional and (middle panel) integer (hkl) reflections intensities with magnetic field compared to (bottom panel) the magnetisation curve for the magnetic field ramping up at $T = 2$ K. There are four *stationary* magnetic structures, coloured in grey and labelled as Phases I, II, III and IV, in which magnetisation remains almost constant, while the white regions are *transitional* structures in which magnetisation is rapidly changing. The dashed line corresponds to a narrow transitional state between phases II and III.

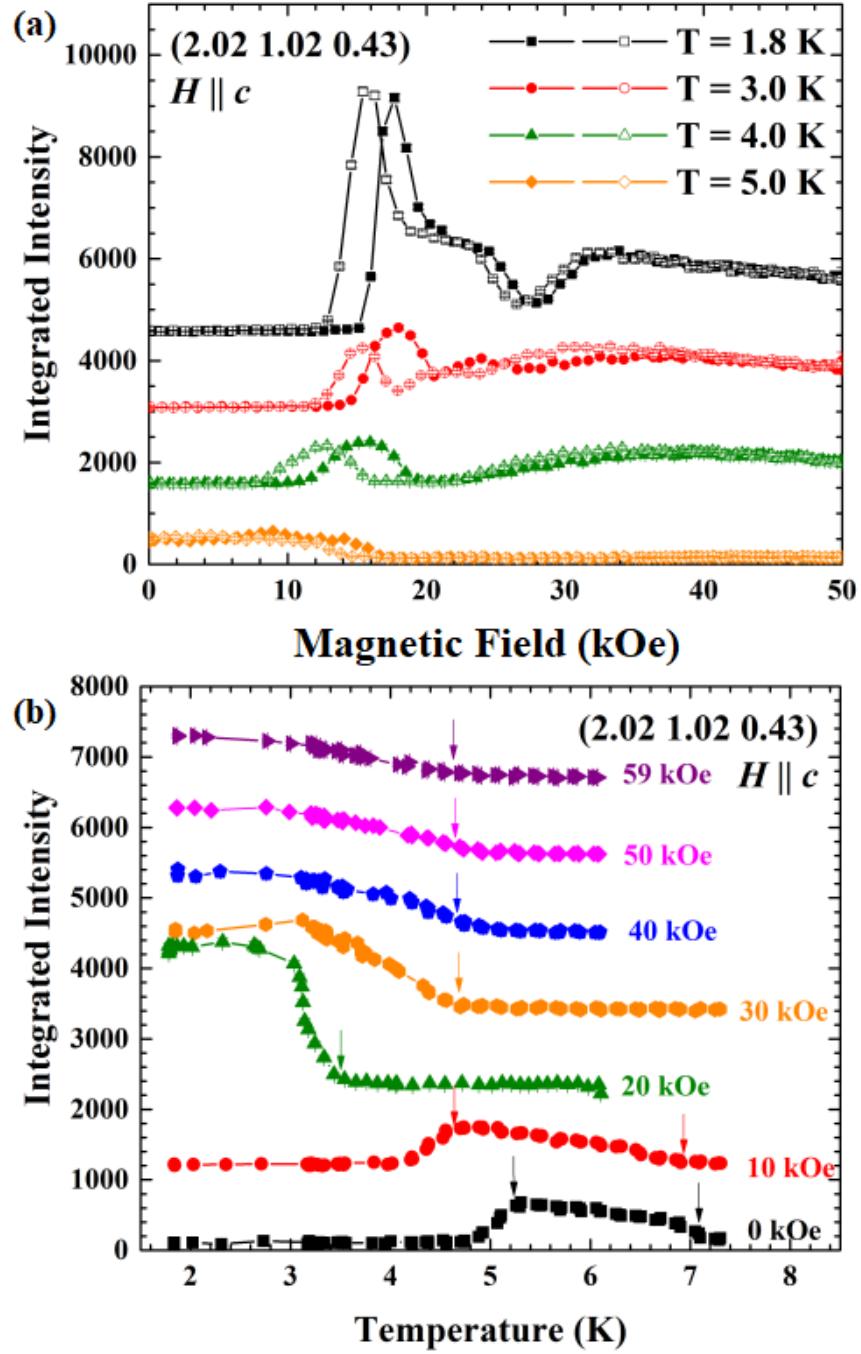


Figure 5.16: (a) Field dependence of the intensity of the incommensurate (2.02 1.02 0.43) reflection at different temperatures. Filled symbols correspond to the field ramping up, while empty symbols the field ramping down. Each curve is sequentially by 1500 counts. (b) Temperature dependence of the intensity incommensurate reflection (2.02 1.02 0.43) in different fields. A stabilisation of the incommensurate phase is observed at 20 kOe, while a decrease of the low temperature intensity with increasing field. Each curve is sequentially offset by 1100 counts.

reflection at different temperatures. The scan at $T = 2$ K (shown also in Fig. 5.15) shows the re-establishment of the zero-field incommensurate phase between 16–18 kOe and suppressed at between 26–33 kOe with the onset of antiferromagnetic order. Increasing the temperature to $T = 3$ K, again we see the re-established incommensurate phase between 16–18 kOe, however with a lower intensity. The intensity of the $(2.02\ 1.02\ 0.43)$ is suppressed at 26 kOe although it is significantly less pronounced compared to the base temperature. At $T = 4$ K, the incommensurate phase appears in a lower field range of 12–19 kOe, the reflections are no longer suppressed at 26 kOe, suggesting the antiferromagnetic order in Phase IV is not present above $T = 3$ K. For temperatures, $T \leq 4$ K the incommensurate reflections persist up to 50 kOe. Finally the $T = 5$ K corresponds to the overlapping region of the non-collinear antiferromagnetic order and the incommensurate state. The incommensurate state is present up to approximately 17 kOe, disappearing in the paramagnetic regime.

The temperature dependence of the intensity of the $(2.02\ 1.02\ 0.43)$ reflection in different fields is shown in Fig. 5.16(b). The zero field data shows the appearance of the $(2.02\ 1.02\ 0.43)$ reflection between $T_{N2} < T < T_{N1}$ corresponding to the expected incommensurate phase. The transitions are denoted using arrows. On increasing the field to 10 kOe, the region shifts to lower temperatures. Increasing further to 20 kOe, which is on the tail-end of the re-established phase we see a sharp transition with the appearance of the $(2.02\ 1.02\ 0.43)$ reflection at 3.5 K. Increasing the field further to 59 kOe we see the transition becomes much more gradual, starting at 4.8 K, with the intensity levelling off at approximately 3.2 K. The levelled off intensity at low temperature then decreases with increasing magnetic field.

Fig. 5.17 shows the field dependence of the intensity of the $(2\ 1\ \frac{1}{3})$ reflection at different temperatures. As can be seen, with increasing temperature, the intensity dramatically falls and on increasing the temperature further there is a shift of the peaks to a lower field ranges of 15–27 kOe and 11–19 kOe for $T = 3$ and 4 K respectively. Interestingly the field range at 4 K overlaps exactly with the incommensurate phase observed at $T = 4$ K creating the mixed IT+II transitional state.

The field dependence of the intensity of the integer (100) and (210) reflections at different temperatures is shown in Fig. 5.18(a) and (b) respectively. The low temperature ($T = 1.8$ K) is described above in regards to Fig. 5.15. Warming to 3 K, there is little change in the transitions from the non-collinear antiferromagnetic order for both reflections, however the newly established antiferromagnetic phase at 26 kOe is significantly less pronounced. The non-collinear antiferromagnetic phase

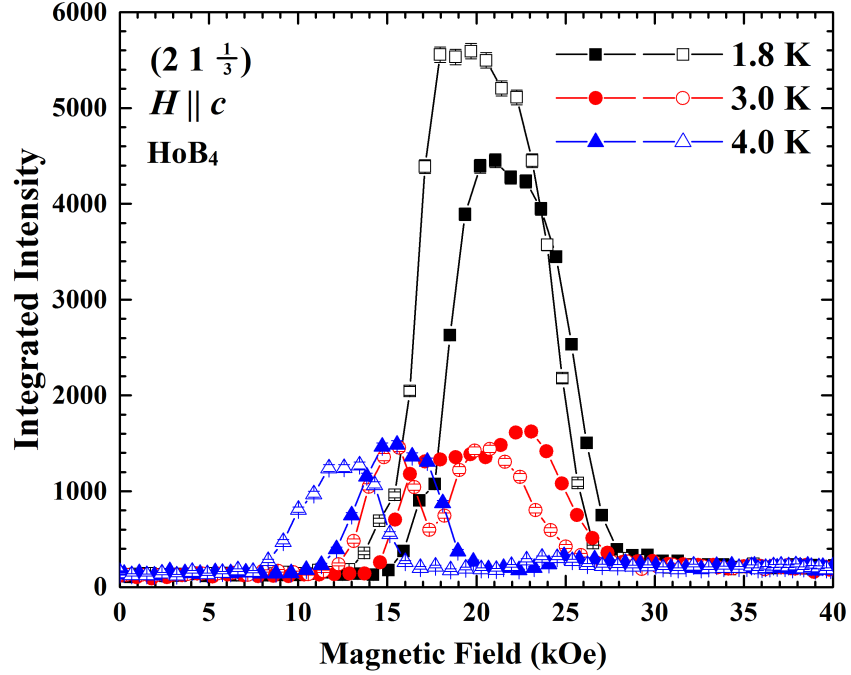


Figure 5.17: Field dependence of the intensity of $(2\ 1\ \frac{1}{3})$ reflection at different temperatures. Filled symbols correspond ramping the field up, empty symbols correspond to ramping the field down. The temperature increase between $T = 1.8$ to 4 K causes a visible shift of the magnetic phase corresponding to $\frac{1}{3}$ -magnetisation plateau to lower fields.

persists up to 5 K the transition field shifting to 12 and 5 kOe for $T = 4$ and 5 K respectively. As expected the ferromagnetic (210) reflection levels off at higher fields with the field value increasing with increasing temperature supporting a polarised component to the magnetic moment.

Magnetic Structure Determination

In the transitionary state between Phases I and II at $H = 17.5$ kOe we have collected the integrated intensities of a set of 120 incommensurate reflections and performed a magnetic refinements using the model for the zero field incommensurate structure [46]. The fit ($R_{\text{Bragg}} = 15.84\%$) is shown in Fig. 5.19(a). We confirmed there was a component of the magnetic moment in the ab plane as well as along the c -axis. The moments are tilted from the c -axis by approximately 23° compared to 25° degrees reported by Okuyama *et al.* [46] for zero field and the ab plane component points along the $[110]$ direction (see inset Fig. 5.19(a)). There is an amplitude modu-

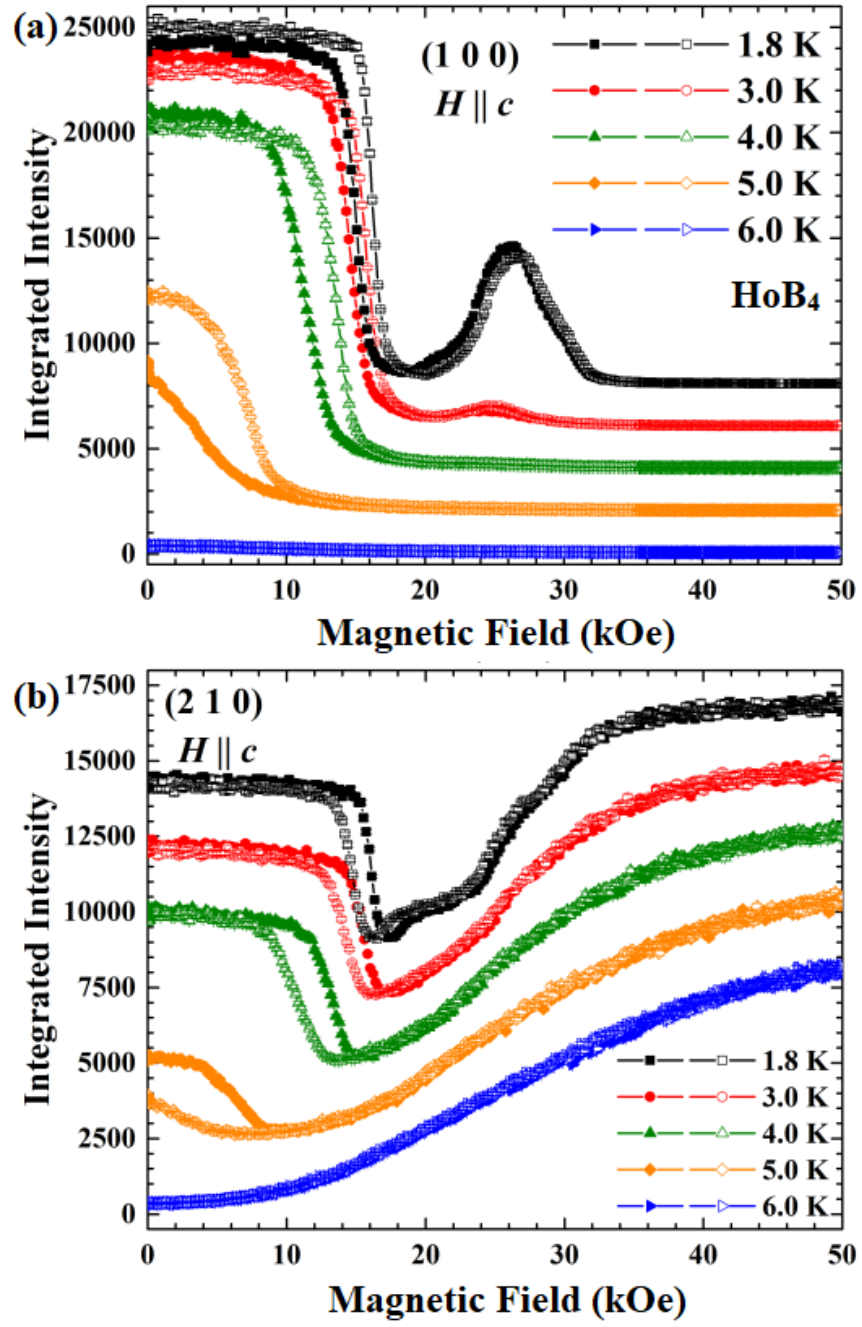


Figure 5.18: Field dependence of the intensity of the (a) (100) and (b) (210) reflection at different temperatures. Filled symbols correspond ramping the field up, empty symbols correspond to ramping the field down.

lation, which is most prominent along the c -axis as a consequence of the propagation vector $(\delta, \delta, \delta')$ being close to commensurate position in the ab -plane.

In order to determine the magnetic structure of Phase II we derived the irreducible representations for a propagation vector of $(0, 0, \frac{1}{3})$. Using a collection of 127 $(h k \frac{1}{3})$ -type reflections, we found the best fit for Phase II arises from a basis vector with the moments aligned parallel to c -axis. The moments form ferromagnetic layers in the ab -plane, which stack in an *up-up-down* arrangement, expanding the crystallographic unit cell along the c -axis by a factor of three. All the moments have equal magnitude with one plane pointing in the anti-parallel relative to the other two layers, thus there is a net magnetisation along the c -axis, which is $\frac{1}{3}$ compared to the magnetisation of a fully polarised state. The comparison of the observed and calculated intensity for this fit ($R_{\text{Bragg}} = 15.21\%$) is shown in Fig. 5.19(b), while the inset shows a schematic of the magnetic structure. The refinements gave a z -component of the magnetic moment to $1.95\mu_{\text{B}}$ per Ho ion, which is in agreement with the value observed in field dependent magnetisation data (Fig. 5.15). This however does not preclude the presence of a significant ab -plane component. For both fits, there is a slight spread of intensity around the expected intensity line. This spread is due to extinction from the sample.

We have attempted a magnetic structure determination of the re-established antiferromagnetic phase (Phase III). In order to achieve purely magnetic intensity of the integer position we subtracted the high temperature (30 K), zero-field intensity of a full collection of integer (hkl) reflections from those at 27 kOe. The intensity of some reflections, such as the (140) and (330) and their Friedel pairs, had decreased on cooling down to base temperature, therefore the subtraction returned negative intensity. The decrease was significant and could not be explained as random error around a zero value where there was no change to the intensity. As we have a net magnetisation along the c -axis we would expect the intensity of the (140) and (330) to either remain constant or for there to be an increase. The most likely explanation for this decrease in intensity is a structural phase transition.

In order to try and account for the decrease in the intensities on the (140) and (330) reflections we applied different distortions to the atoms in the unit cell. We have estimated the intensities for the nuclear reflection using the following equation:

$$I_{\text{nuc}} = \left| \sum_{\rho} b_{\rho} \exp\{2\pi i(hx + ky + lz)\} \right|^2, \quad (5.3)$$

where x, y, z refers to the fractional position of the atoms in the unit cell, h, k and l are the Miller indices and b_{ρ} is the scattering length for a particular element. The

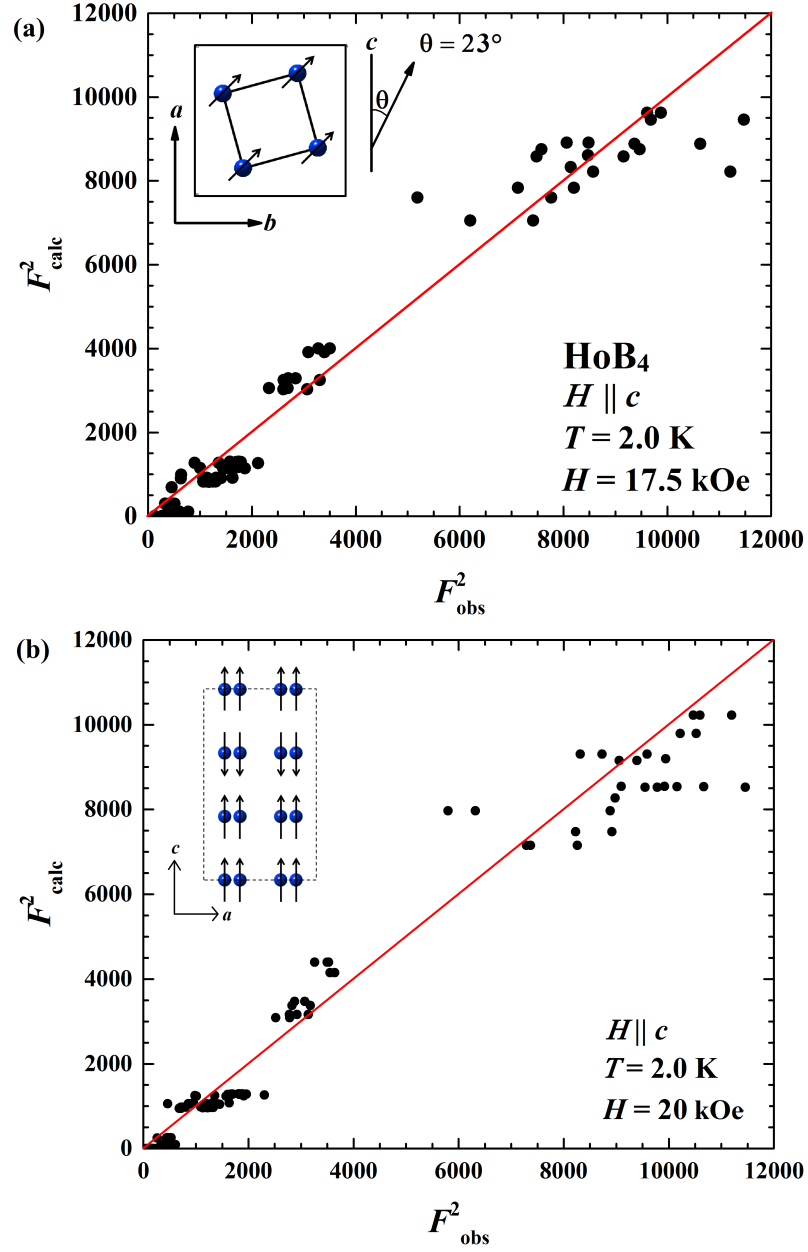


Figure 5.19: Comparison of the calculated and observed intensity for (a) the incommensurate phase re-established at $T = 2$ K in a field of 17.5 kOe and for (b) Phase II, corresponding to the $\frac{1}{3}$ -magnetisation plateau. The inset in both pictures corresponds to the found magnetic structure.

Space Group: $P4/mbm$			
Lattice Parameters: $a = b = 7.08 \text{ \AA}$, $c = 4.00 \text{ \AA}$			
Ion	Wyckoff Position	Positions	Fractional Coordinates
Ho	$4g$	$(x, x + \frac{1}{2}, 0)$	$x = 0.319$
B1	$4e$	$(0, 0, z)$	$z = 0.202$
B2	$8j$	$(x, y, \frac{1}{2})$	$x = 0.177, y = 0.039$
B3	$4h$	$(x, x + \frac{1}{2}, \frac{1}{2})$	$x = 0.087$

Table 5.2: Fractional coordinates and Wyckoff Positions for each site in HoB_4 , determined from single crystal neutron diffraction measurements on D10.

unit cell has a single Ho site and three B sites, denoted B1, B2 and B3 and the positions for each atom is shown in Table 5.2. The x , y and z values were determined from structural refinement of the single crystal neutron diffraction measurements at $T = 30 \text{ K}$. It was assumed the space group ($P4/mbm$) and symmetries for each site remained the same and applied a displacement to the x , y or z values. As there was a negative intensity after subtraction for both the (140) and (330) reflections a distortion that resulted in a decrease in the intensity for both reflection simultaneously was looked for.

To begin we displaced the Ho ions by applying a small change to the Ho x value. That is x became $x + \epsilon$, where $\epsilon = nx$ and n is a constant which can vary between 0 and 1, although large displacements ($n > 0.1$) are likely to be unphysical. This displacement corresponds to a slight rotation and expansion of the square formed by the Ho ions. Fig. 5.20(a) shows how the nuclear intensity evolves with the displacement. As can be seen this results in a decrease in both the (140) and (330) reflection after approximately a 10% change in Ho's x value. While the intensity does decrease for both reflections, the large displacement to achieve this suggests this distortion is unlikely to be the cause.

We tried distorting the B octahedra formed by the B2 site atoms. This was done by applying a $x + \epsilon$ and $y + \eta$, where $\eta = -ny$ for an expansion, while $x - \epsilon$ and $y - \eta$ correspond to compression. Fig. 5.20(b) shows the evolution of the nuclear intensity with change in n . As can be seen again the distortion results in a simultaneous decrease in the intensity of both reflections.

A small change in the x value of the B3 site such that x became $x + \epsilon$. The distortion for this is shown in Fig. 5.20(c) along with the change in nuclear intensity. Although this results in a decrease in the (330) reflection, there is a gradual increase in the (140) intensity, suggesting a change solely to the B3 site atoms is not sufficient to describe the present data.

Although further investigation is needed to confirmed the true nature of the lattice distortion, a distortion in the Ho ions or a compression/expansion of the B2 octahedra can account for the decrease in nuclear intensity. Previous measurements have revealed the presence of a small monoclinic distortion upon cooling into the LT phase [46]. There is a change of γ by 0.02° . Although in this phase there is no noticeable discrepancy in the intensity of the (140) and (330) reflection. Thus the distortion becoming more pronounced could also serve as an alternative explanation.

5.2.3 Magnetic Phase Diagrams

We have constructed the magnetic phase diagram for $H \parallel c$ using temperature and field dependence of the intensity of different reflections from the single crystal neutron experiment as well as from the magnetic susceptibility, magnetisation and heat capacity measurements. The phase diagram is shown in Fig. 5.21. As can be seen, besides the paramagnetic regime, there are six distinct magnetic phases separated by mixed transtionary phases. In zero-field there are two transitions at T_{N1} and T_{N2} leading to an incommensurate magnetic state (IT) and a non-collinear antiferromagnetic phase (Phase I) respectively. Application of a magnetic field suppresses both T_{N1} and T_{N2} , while for a narrow field range ($16 < H < 18$ kOe) at low temperatures, Phase II+IT acts as an intermediary phase between non-collinear antiferromagnetic phase and the ferrimagnetic *up-up-down* structure formed in Phase II. The magnetic structure of Phase III remains undetermined, however the presence of the (100) reflection in the single crystal neutron data indicated that it is antiferromagnetic in nature. In phase V there is an increase in the ferromagnetic type reflections, suggesting the moments are tilting towards the magnetic field direction, while the incommensurate reflections persist up to 59 kOe indicating a polarised phase with a “frozen-in” phase. Phase IV appears over a small field range below $T < 1$ K corresponding to a $\frac{1}{2}$ -magnetisation plateau, the nature of this phase is unknown.

Figure 5.22 shows the phase diagram for $H \perp c$. There are four clearly defined phases; The paramagnetic (PM), intermediate temperature (IT), an antiferromagnetic phase I and the field induced phase II. The paramagnetic regime is present above 7 K, below this we have the incommensurate phase observed as expected, the transition remaining broadly unchanged with increasing magnetic field. Below approximately 5.5 K we see the onset of a non-collinear antiferromagnetic ordering. Interestingly there is only one field induced transition, leading to the magnetic state denoted as Phase II, this is consistent with the transition to ferrimagnetic ordered phase observed for $H \parallel c$. However with the present evidence we cannot be sure

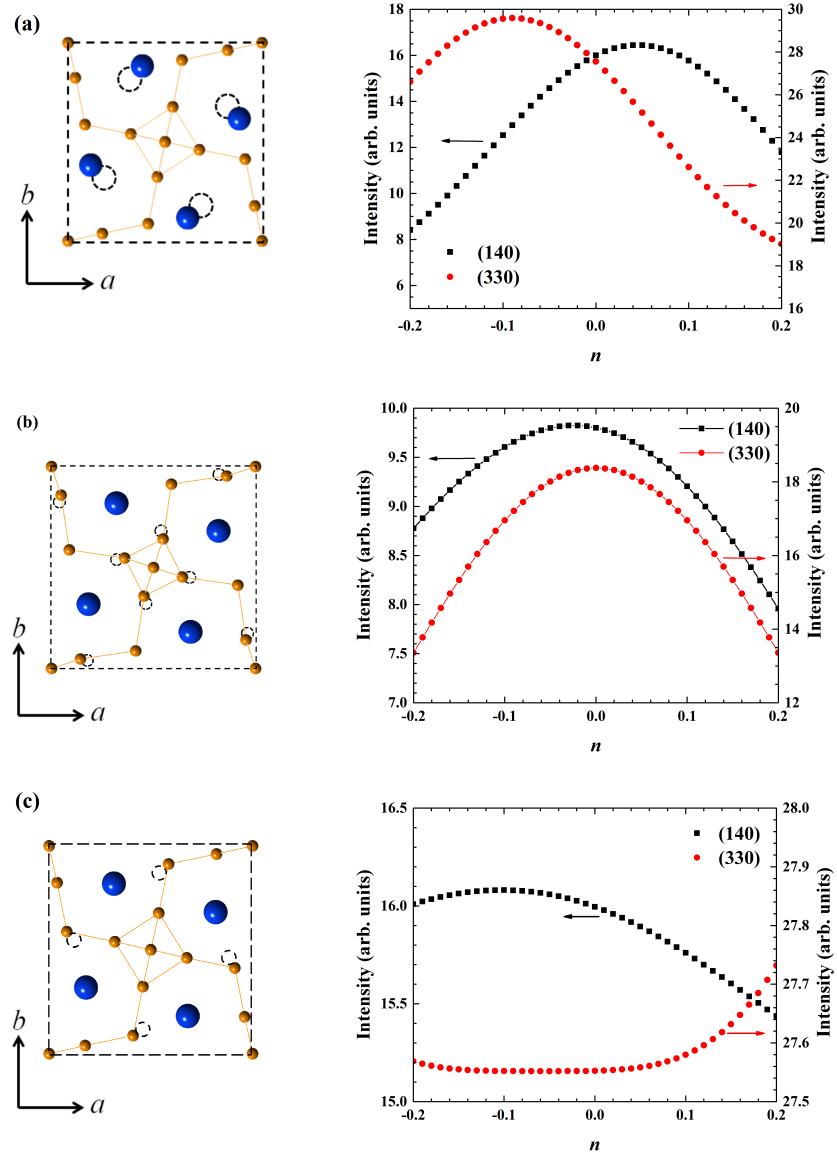


Figure 5.20: The lattice distortion (left column) applied to (a) the Ho ions and the B atoms in the (b) B2 site and (c) B3 site. (Right column) The intensity as a function of size of displacement.

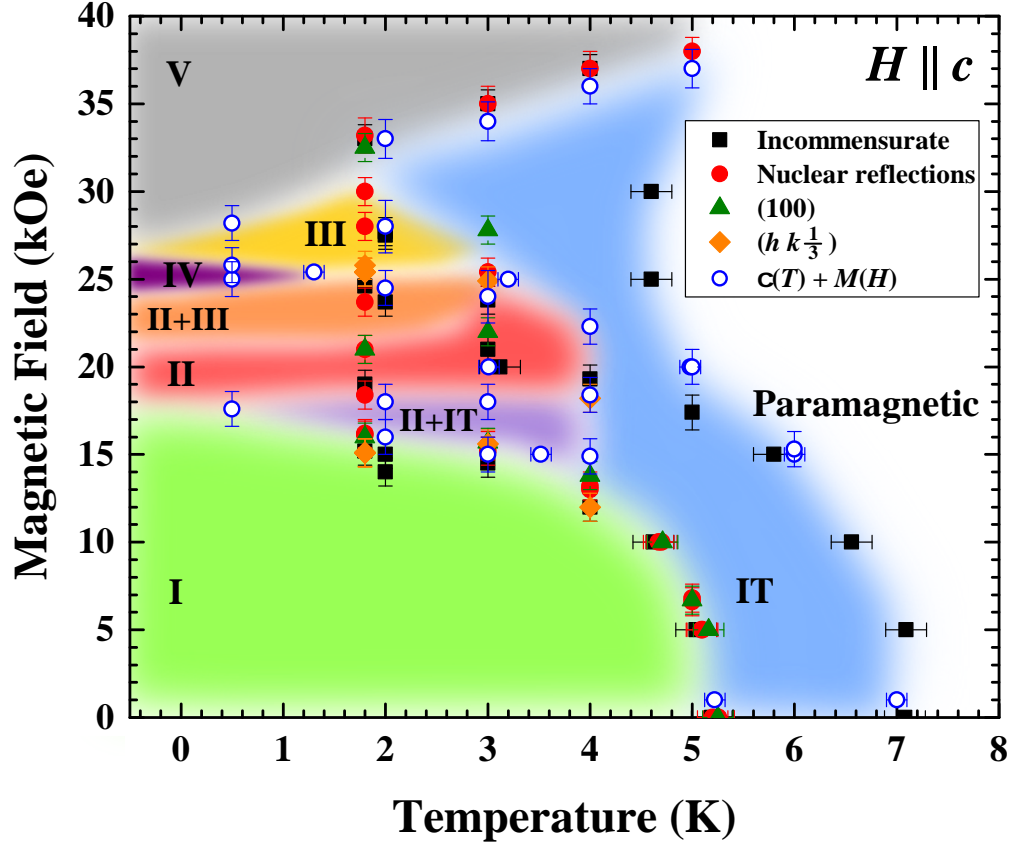


Figure 5.21: Magnetic phase diagram of HoB_4 constructed from neutron diffraction data for different reflections (squares, filled circles, triangles and diamonds) and magnetisation (empty circles) measurements. All field dependent measurements were made by ramping the field up. The labelling of different magnetic structures is consistent with the one used in Fig. 5.15 for $T = 2$ K, however, with the increased temperature the magnetic phases tend to overlap. The separation between the stationary and transitional phases also becomes less obvious on heating, with the *transitional* Phases II+IT and II+III occupying large portions of the phase diagram.

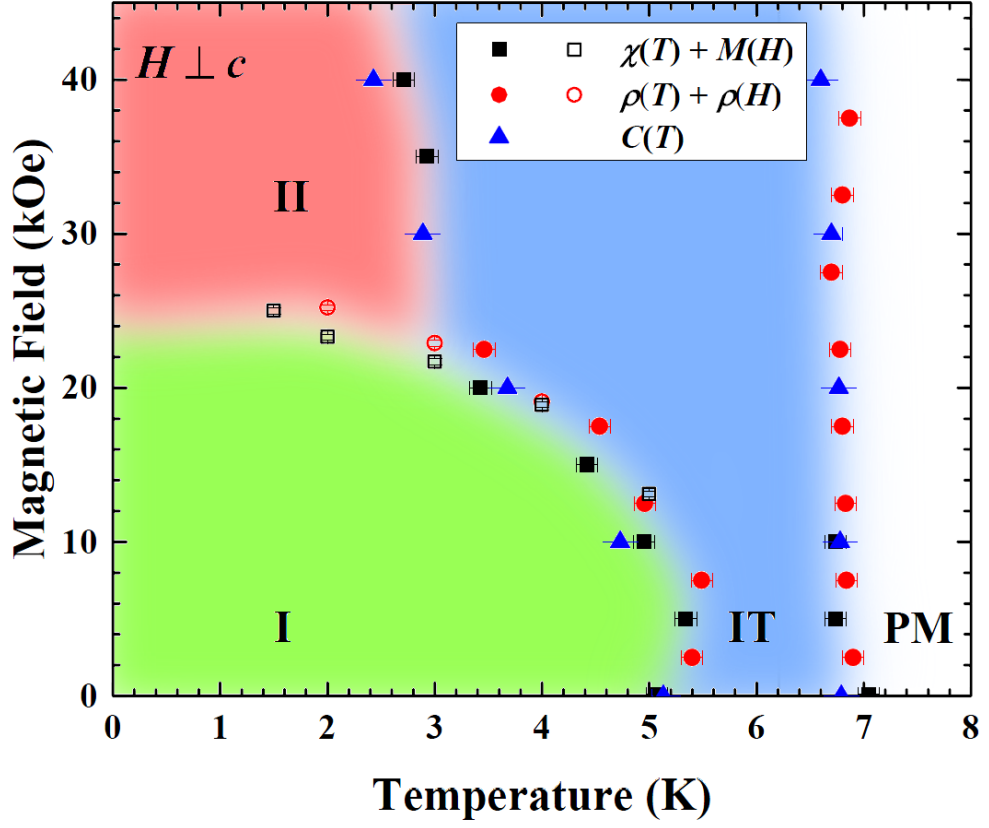


Figure 5.22: Magnetic phase diagram of HoB_4 constructed from magnetisation (squares), resistivity (circles) and heat capacity (triangles) measurements. All field dependent measurements were made by ramping the field up. The magnetic phases are the paramagnetic regime (PM), the intermediate temperature (IT), a non-collinear antiferromagnetic phase I and a field induced phase II.

whether there is ordering within the *ab*-plane giving rise to transition or whether it is arising from a tilt of the moments towards the field direction when the ferrimagnetic order is established. Finally from the high field magnetisation measurements, we see that we have entered a partially polarised at around 150 kOe.

5.3 Inelastic Neutron Scattering

5.3.1 Polycrystalline Samples

$$\lambda = 3.06 \text{ \AA} \quad (E_i = 8.7 \text{ meV})$$

We have carried out inelastic neutron scattering on polycrystalline samples of HoB₄ using IN4 to investigate the crystal field scheme. Fig. 5.23 shows the colour intensity plots for an incident wavelength of $\lambda = 3.06 \text{ \AA}$ in a range of temperatures between 1.6 and 80 K. The data in Fig. 5.23(a) and (b) corresponds to the LT phase. The general features of the plot are the elastic line around $E = 0$ corresponding to elastic scattering and is where the Bragg reflections are located. There are then three main lines located approximately at 2.3, 2.7 and 5.2 meV. The intensity of all three lines decreases with increasing Q , strongly suggesting they are crystal field levels. The excitations are also gapped suggesting we have an Ising-like system, which is in agreement with earlier measurements. These features are also present at 4 K.

The intermediate phase is shown in Fig. 5.23(c), the crystal field level at 5.2 meV has disappeared. There are a couple possibilities for this, the first is that the peak is arising from a degenerate energy levels which is splitting in the ordered phase. Alternatively the magnetic order reduces the symmetry and can make crystal field levels, which the neutron is not sensitive to. The lower energy crystal field levels are still present, the energy level at 2.7 meV remains stationary, but the lower energy level have shifted position to approximately 1.3 meV. The lower of the two crystal field levels becomes more dispersive and the energy level is no longer gapped, where the excitation comes down to the reflections corresponding to the low Q incommensurate reflections. The crystal field levels in the magnetic phases have a modulated intensity, this is most likely arising from the influence of magnetic order.

The paramagnetic phase in a range of temperatures is shown in Fig. 5.23(d)-(h). In the colour plots, the detail is difficult to make out, but there is a general increase in the intensity around all the excitations and new features appearing at around 4, 5.2 7.5 meV. These are most arising due to secondary transitions from crystal field levels becoming thermally populated.

To more accurately determine the position of the excitations and track their temperature dependence we took line cuts at $Q = 1.5 \pm 0.5 \text{ \AA}^{-1}$ for all temperatures, which are shown in Fig. 5.24. To determine the positions the peaks were fitted with a Gaussian, with fitted peaks at lower temperatures being used as a starting point for fitting the spectrum at higher temperatures. The fits are shown in Fig. 5.25.

In the low temperature phase, there are two well defined peaks at 2.2 and 2.9 meV as well as a significantly smaller peak observed at 5.5 meV. Warming into the intermediate phase, we see that the low energy level at 2.2 meV shifts to 1.7 meV, while the feature at 5.5 meV is no longer visible. Warming further into the paramagnetic phase, there is a shift in energy by approximately 0.2 meV to lower energies for both peaks. This is most likely due to a structural phase transitions, which has been previously observed in neutron diffraction measurements [46]. The energy levels at 1.5 and 2.7 meV are most likely crystal field levels. This is further supported by the heat capacity measurements where Schottky anomalies (See Fig. 5.10), which correspond to energies of approximately 2.8 and 6.2 meV. The energy level at 2.8 meV would corresponds to crystal field level in the energy spectrum. While the 6.2 meV is not observed in the energy spectrum, it could be arising due to a crystal field level, which is not neutron sensitive or it could be arising due to a transitions between a populated low energy level to a higher energy level. With increasing temperature we see a feature begins to appear at approximately 4 meV, this is most like arising from the first crystal field level becoming thermally populated and then a transition occurring from there. This would indicate there is a crystal field level at 5.5 meV, which is observed in the LT phase.

$\lambda = 1.61 \text{ \AA} (E_i = 31.6 \text{ meV})$

Fig. 5.26 shows the colour intensity plots for an incident wavelength of 1.61 \AA in a range of temperatures between 1.6 and 160 K. Figure 5.26 (a) and (b) correspond to the low temperature and intermediate temperature phases. They broadly show the same features. Two lines where, again, the intensity increases with increasing Q at approximately 10 and 18 meV, which most likely correspond to crystal field levels. There is then a low intensity feature at approximately 12 meV, where the intensity increases with Q , which is characteristic of phonons. Finally the elastic line is broader at low Q , which is made up of many of the features observed with $\lambda = 3.06 \text{ \AA}$, the features are just not resolvable using an incident wavelength of 1.61 \AA . The features at 10 meV and around the elastic have a greater intensity in the low temperature phase compared to intermediate temperature phase.

Fig. 5.26(c)-(h) are all in the paramagnetic phase with each subsequent pic-

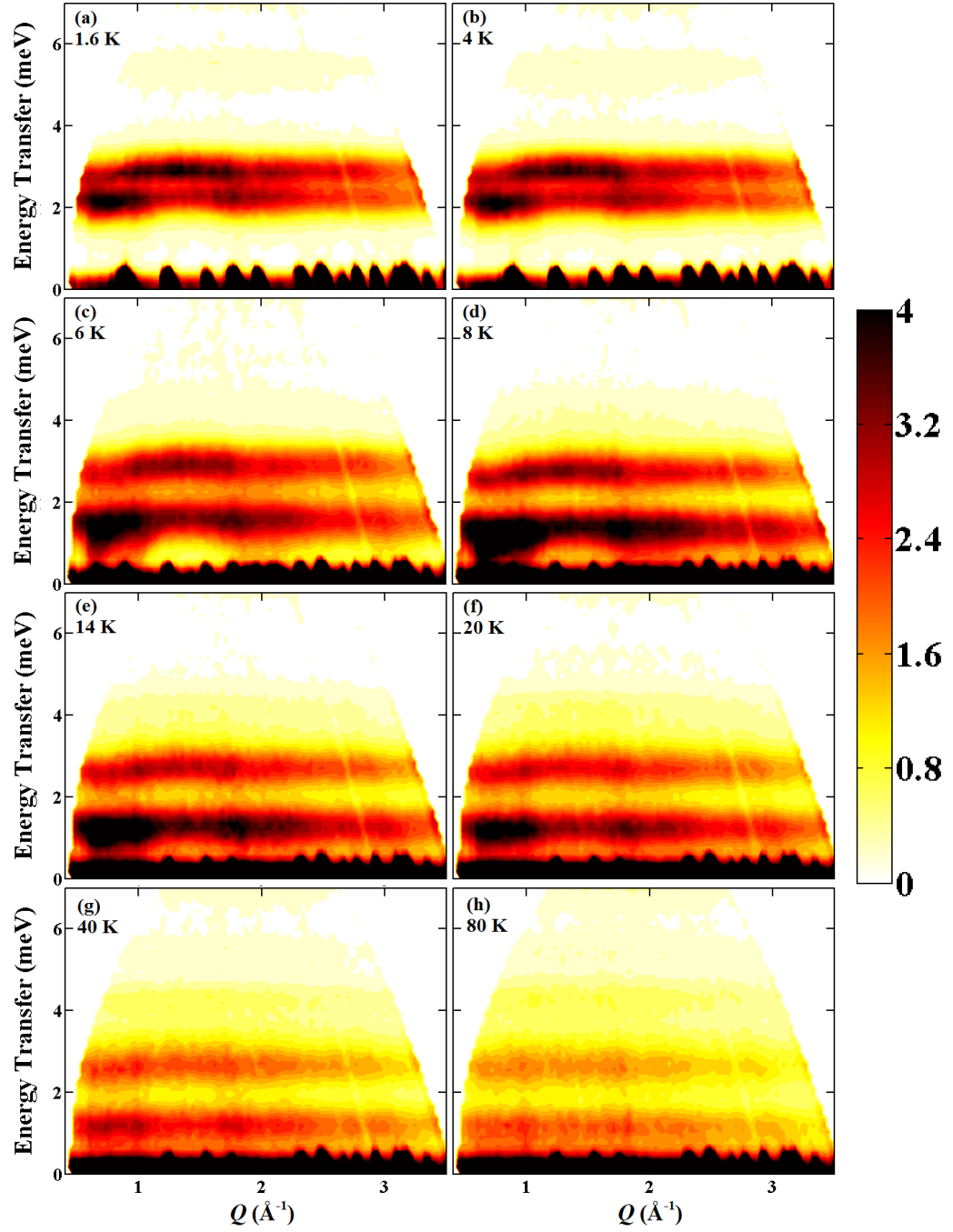


Figure 5.23: $S(Q, \omega)$ for $\lambda = 3.06 \text{ \AA}$ at several temperatures. The low energy excitations become dispersive in the intermediate temperature phase and further new features appear as crystal field levels become thermally populated.

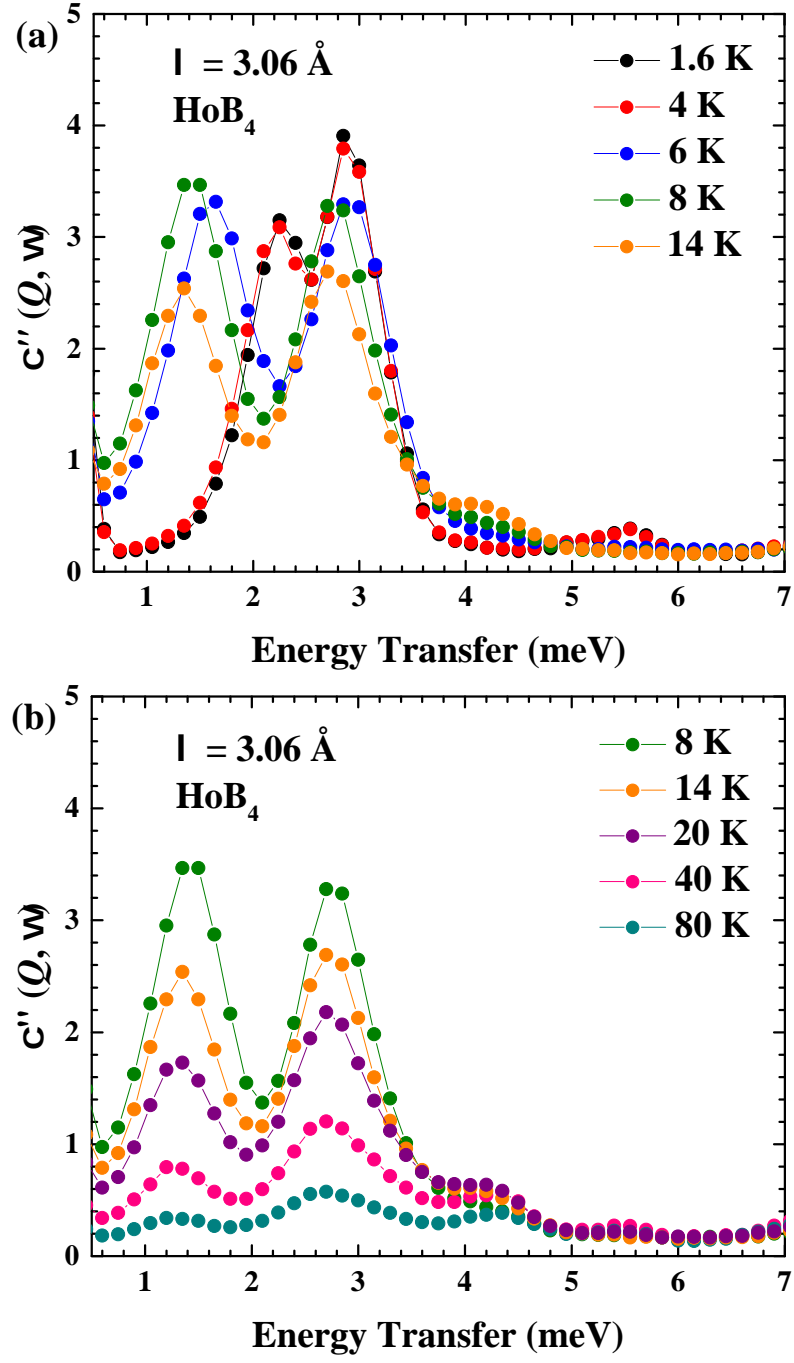


Figure 5.24: Dynamic susceptibility of HoB_4 for (a) temperatures between 1.6–14 K and (b) 8–80 K with an incident wavelength of $\lambda = 3.06 \text{ \AA}$.

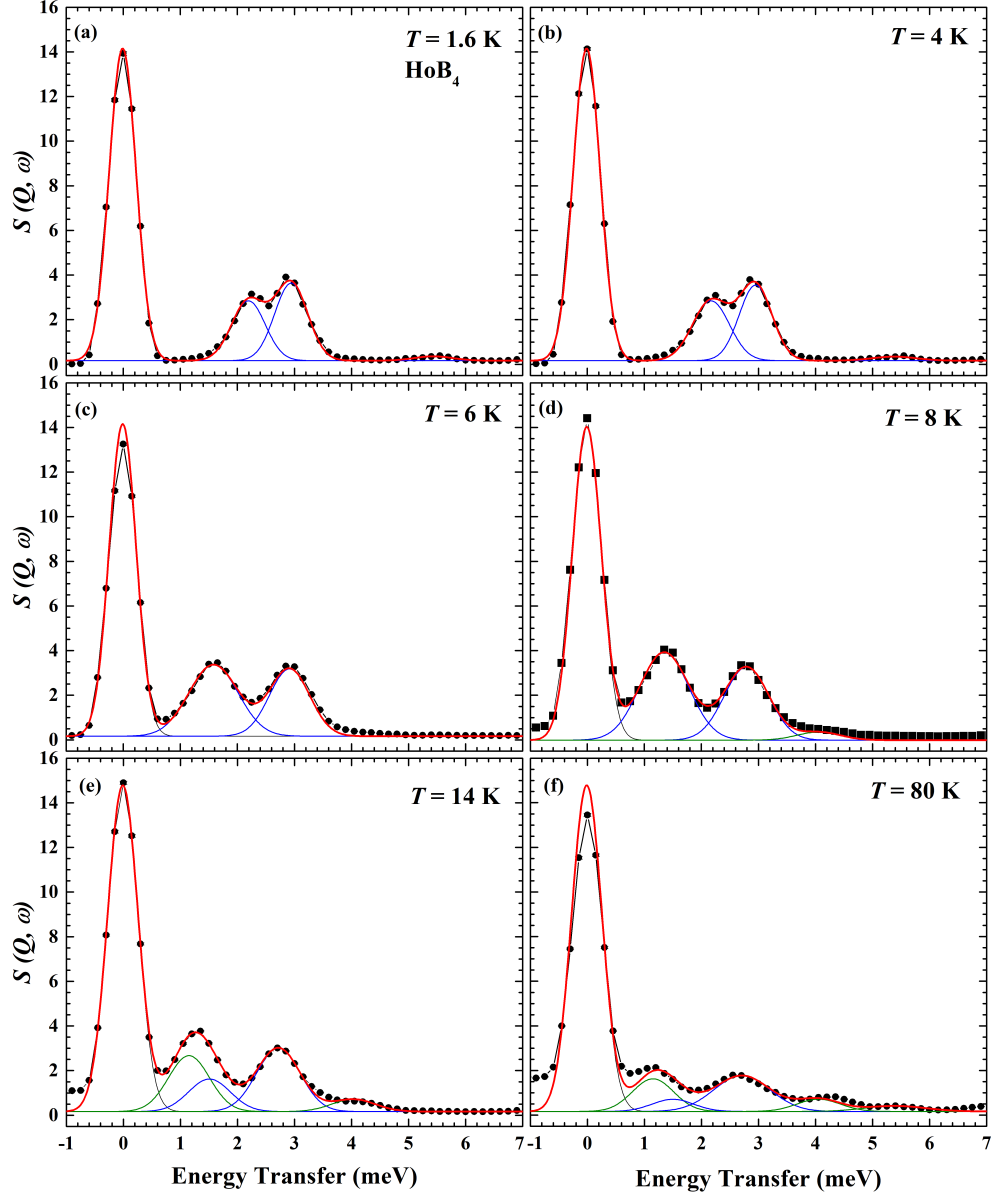


Figure 5.25: Gaussian fits of $S(Q, \omega)$ of HoB_4 in a range of temperatures with an incident wavelength of $\lambda = 3.06 \text{ \AA}$. Blue peaks correspond to crystal field levels, while green peaks correspond to secondary transitions from thermally populated energy levels.

ture increasing in temperature from 8 K upto 160 K. The feature at 10 meV, broadens and the intensity increases with increases with temperature, with the maximum centred on around 7 meV. There appears to be a subtle increase in the intensity between 10 and 18 meV. Again this is most likely due to secondary transitions arising from crystal field becoming populated with the increasing temperature. The intensity of the crystal field level at 18 meV decreases with increasing temperature.

To investigate these more thoroughly we performed line cuts at $Q = 2 \pm 0.5 \text{ \AA}^{-1}$ at each temperature. The resultant curves are shown in Fig. 5.27. The fits have revealed the presence of two crystal field levels in the LT term 10 meV and 17.7 meV, warming into the IT phase there is a shift in the higher energy crystal field level from 17.7 to 17.0 meV. As with the 3.06 \AA data in the paramagnetic phase the crystal field levels shift to lower energy, with crystal field levels at 9.5 and 17 meV. Warming in the paramagnetic phase peaks appear at 7.5 meV as well as 12.05 meV.

Combining the measurements from 1.61 and 3.06 \AA . We have crystal field levels at 1.4, 2.9, 5.3, 9.5 and 17 meV. From the peaks appearing from the crystal field levels becoming thermally populated we can estimate that there are further crystal field levels at 10.8 meV, which is not neutron sensitive. From the maximum entropy we are expecting a maximum of 17 singlet state. While this gives an upper bound on the energy levels, it makes determine the crystal field scheme challenging. We have found five energy levels, that could be singlets, doublets, etc. that we are unable to resolve. Further refinements and modelling of the crystal field levels is needed before we can definitively state the crystal field scheme.

5.3.2 Single Crystal Samples

We have carried out single crystal neutron scattering experiment on IN5 in order to investigate any low lying magnetic excitations in HoB_4 . The crystal was aligned and glued such that the $[0K0]$ direction was vertical defining the horizontal ($h0l$) scattering plane. Two incident wavelength of 5 and 3.5 \AA energies ($E_i = 3.3$ and 6.8 meV), were used throughout the experiment. Fig. 5.29 shows the energy spectrum along the $[H 0 0.6]$ and $[2 0 L]$ directions at 10, 6 and 1.6 K with an incident wavelength of $\lambda = 3.5 \text{ \AA}$. As can be seen there are two dispersive bands of excitations. The higher energy band a low lying crystal field which is observed in Fig. 5.24. The low energy band in $[H 0 0.6]$ has a parabolic shape while there is a distinctive “pronged” structure, which go down to the incommensurate reflections. There is a slight increase in intensity of the low energy band cooling from 10 to 6 K. Interestingly cooling down to 1.6 K we seen the excitation becomes gapped, again

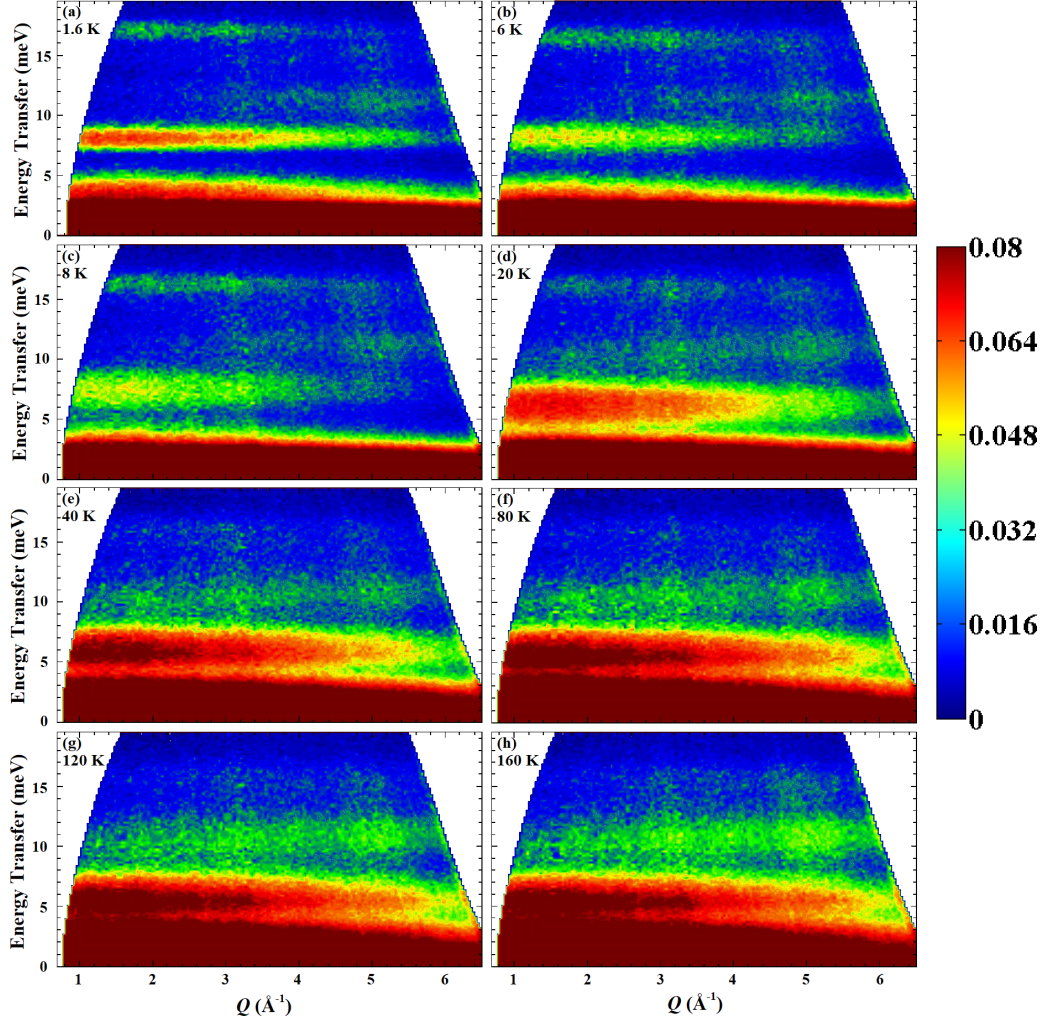


Figure 5.26: $S(Q, \omega)$ for $\lambda = 1.61 \text{ \AA}$ at several temperatures. The low energy excitations become dispersive in the intermediate temperature phase and further new features appear as crystal field levels become thermally populated.

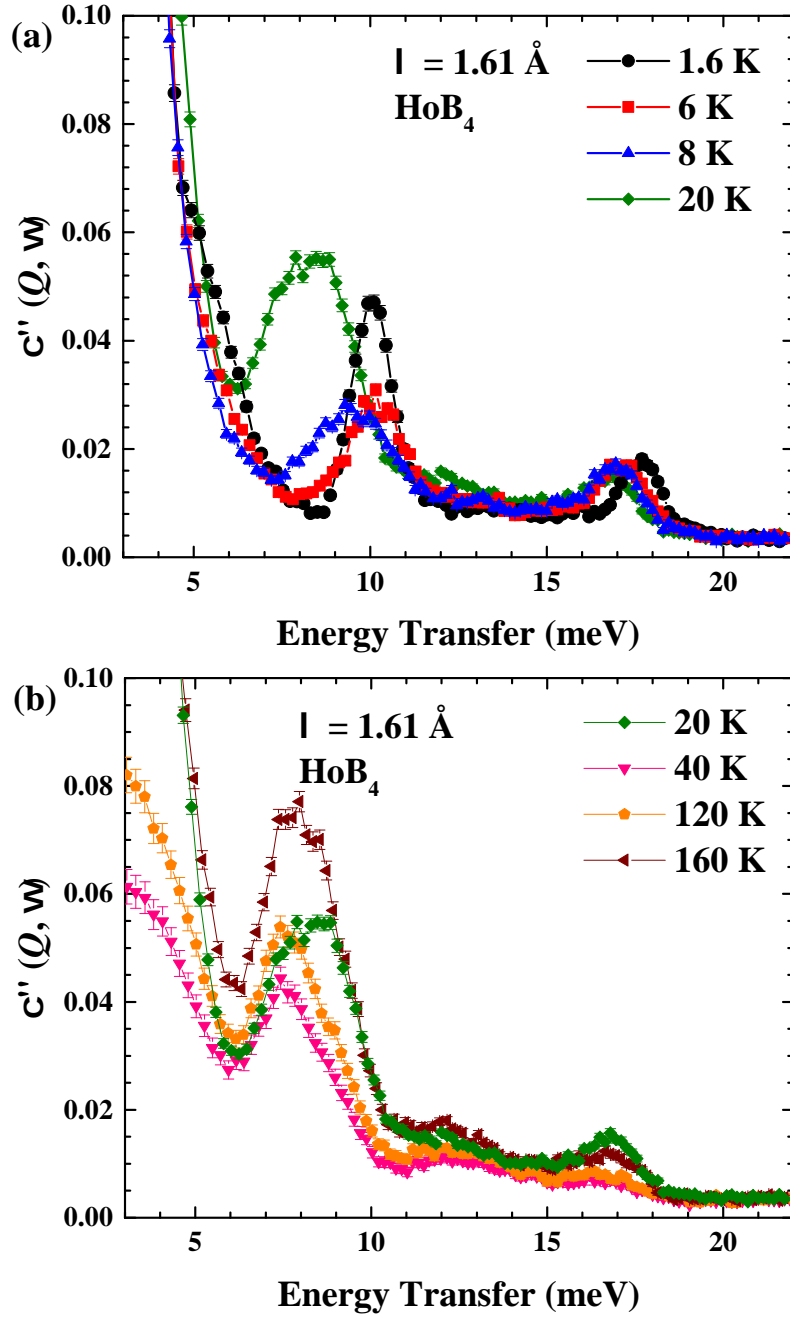


Figure 5.27: Dynamic susceptibility of HoB_4 for (a) temperatures between 1.6–20 K and (b) 20–160 K with an incident wavelength of $\lambda = 1.61 \text{ \AA}$.

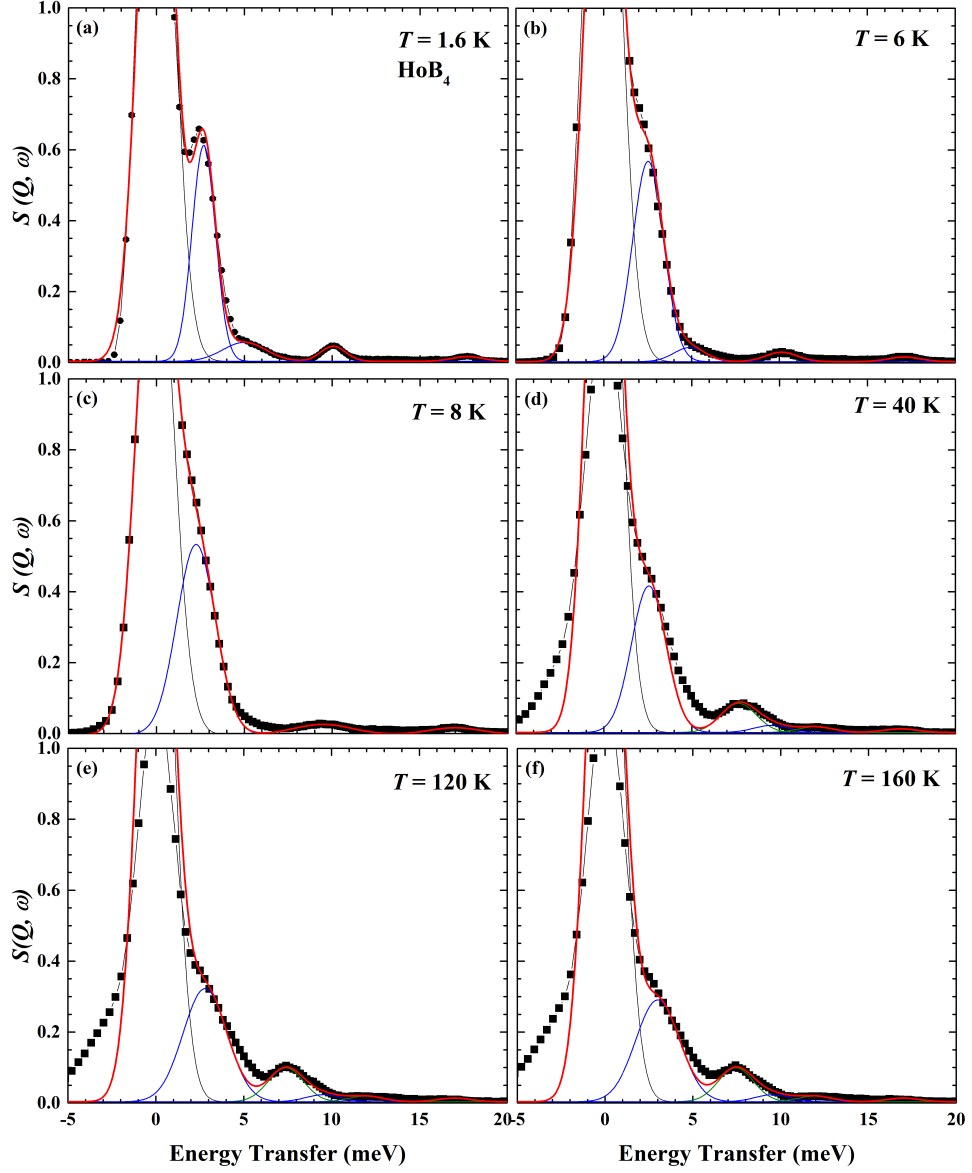


Figure 5.28: Gaussian fits of $S(Q, \omega)$ of HoB_4 in a range of temperatures with an incident wavelength of $\lambda = 3.06 \text{ \AA}$. Blue peaks correspond to crystal field levels, while green peaks correspond to secondary transitions from thermally populated energy levels.

indicating Ising anisotropy. The parabolic shape observed in the intermediate and low temperature phases are characteristic of spin-waves. In the high temperature phase we can observe the two low energy levels observed at 1.5 and 2.9 meV in the inelastic neutron scattering from IN4. The level at 1.4 meV is quite dispersive and has a sinusoidal shape, which is not typical for a crystal field level while the slightly higher crystal field level is flatter, which suggests that it is a crystal field level. We are able to get an estimate between the exchange interactions along the $[H\ 0\ 0]$ and $[0\ 0\ L]$ directions by finding the ratio of the amplitude of the spin waves in both directions. As can be seen from section 2.1.6 the dispersion relation of the spin waves depends on the exchange interaction, J and by comparing the two amplitudes we can compare the strength between the in-plane Ho ions and between the planes of Ho ions. Comparing the amplitude we find the ratio to be approximately $J_{[00L]}/J_{[H00]} = 0.94$, suggesting the interaction strength is comparable and the system has to be considered as three dimensional and not two dimensional like the SSL. This is a rough estimate and to fully describe the dynamics a multi-spin level model will need to be considered.

In order to investigate the low energy excitation we used a smaller incident energy ($\lambda = 5\ \text{\AA}$) and looked at the energy spectrum along the $[00L]$ direction. As can be seen in Fig. 5.30, the excitation is gapless in the incommensurate phase and the “pronged” structure which comes down to the incommensurate reflections in the elastic line is clearly observed here. Increasing the temperature from 6 to 35 K, we see the excitation becomes gapped and the intensity decreases. The “prongs” are no longer visible from 20 K. The crystal field level becomes less dispersive from 10 K to 20 K, although dispersive behaviour is still visible even at 20 K and 35 K, the intensity decreases upon warming. This is very unusual for a crystalline electric field and suggests there are strong correlations even in the paramagnetic regime.

5.4 Summary

An investigation into the magnetic properties of the frustrated antiferromagnet, HoB_4 have been presented in this chapter. The magnetic susceptibility and magnetisation measurements made using ^4He are in agreement with those presented in Ref. [102] and shows successive magnetic phase transitions at 7.0 and 5.6 K. Curie-Weiss behaviour is observed for $H \parallel c$ giving an effective moment of $10.6\mu_B$ and the Curie Weiss temperature of -14 K indicates the presence of an antiferromagnetic exchange. Single crystal neutron diffraction measurements have shown the appearance of incommensurate reflections corresponding to a propagation vector of

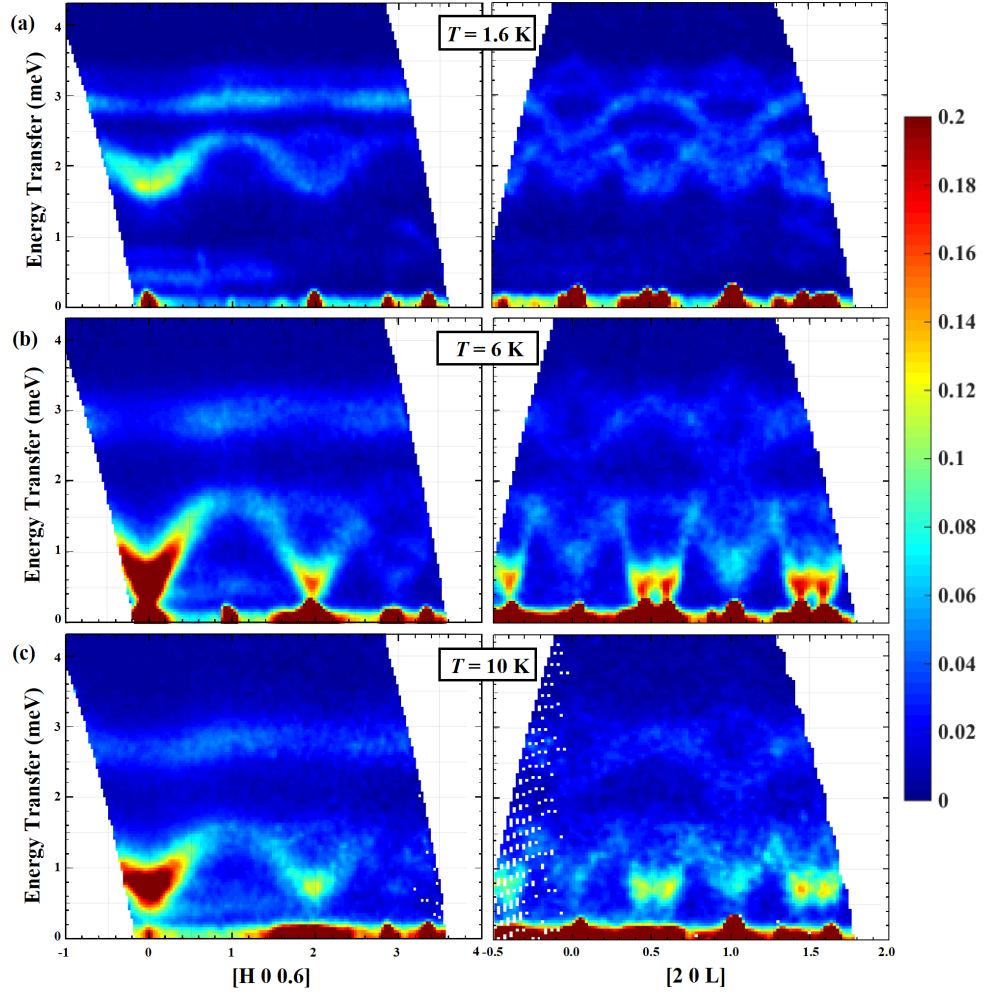


Figure 5.29: Energy spectrum of (left column) $[H\ 0\ 0.6]$ and (right column) $[2\ 0\ L]$ at different temperatures (a) 1.6 K, (b) 6 K and (c) 10 K using an incident wavelength of $3.5\ \text{\AA}$.

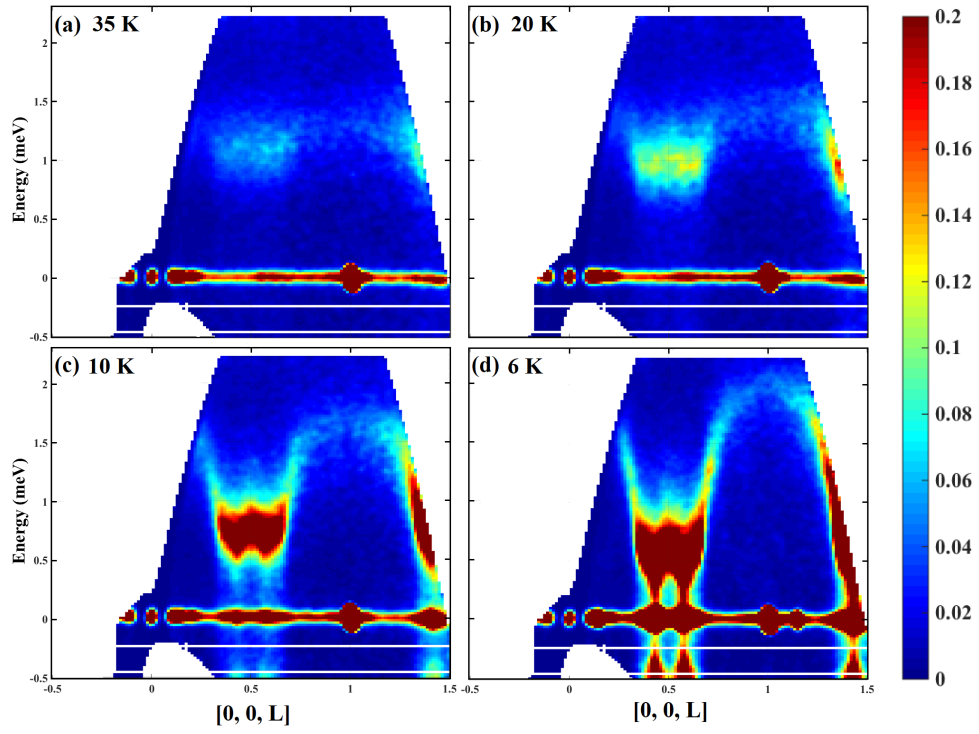


Figure 5.30: Energy spectrum of the $[0\ 0\ L]$ direction at different temperatures (a) 35 K, (b) 20 K, (c) 10 K and (d) 6 K using an incident wavelength of 5 Å.

$(\delta, \delta, \delta')$ where $\delta = 0.022$ and $\delta' = 0.43$, polarised neutron measurements have shown the presence of diffuse scattering around these reflections. The peaks themselves are resolution limited situated on a top of a diffuse background. This two component aspect is indicative of some sort of disorder in the system. Single crystal magnetic refinements using intensities from the incommensurate magnetic phase obtain with the D10 diffractometer have shown that the moments are tilted away from the c -axis by 43° , with the component of the magnetic moment in the basal plane pointing parallel to the $[110]$ direction. There is then an amplitude modulation along the c -axis and a much broader modulation along the $[110]$ direction. In the low temperature phase single crystal neutron diffraction measurements have shown the appearance of the antiferromagnetic (100) reflection below 5.6 K, magnetic refinement finding the structure to be a non-collinear antiferromagnet with a $\mathbf{k} = 0$ propagation vector. Here the ordering can be completely described by a single unit cell suggesting that only the exchange interactions between the in plane moments (i.e. J_1 and J_2 in Fig. 2.6(b) in section. 2.3) are the important interactions at low temperatures, implying that the Shastry-Sutherland lattice is applicable to this low temperature, zero field magnetic phase. Polarised neutron measurements on the D7 diffractometer in the low temperature phase show that the incommensurate reflection persists down to 1.5 K, although with a significantly reduced intensity suggesting it is “frozen-in” at low temperatures. This incommensurate phase is re-established with the application of a magnetic field over a narrow field range (16-18 kOe) and is observed in the field dependent magnetisation as a small feature occurring at $\frac{1}{6}$ the saturation magnetisation. The incommensurate phase itself does not have a net magnetisation, however in this field range reflection of the type $(hk\frac{1}{3})$ are also observed. This implies that in this transitional phase region order with the ferrimagnetic phase (Phase II), while parts are order with the re-established incommensurate structure.

The magnetisation curve for $H \parallel c$ shows a main fractional plateau of $\frac{1}{3}$ the saturation magnetisation and two smaller features at $\frac{1}{6}$ and $\frac{3}{5}$, which depends on the orientation of the magnetic field with the c -axis. There is a large difference between the magnetisation curves for $H \parallel c$ and $H \perp c$ at low temperatures and a large magnetic field is required to bring the magnetisation curves to a similar magnitude suggesting an Ising anisotropy. Neutron diffraction measurements using D10 have revealed that the $\frac{1}{3}$ -magnetisation plateau has a propagation vector of $(0, 0, \frac{1}{3})$, while magnetic refinements have shown that HoB_4 orders in the $\frac{1}{3}$ -magnetisation plateau by forming ferromagnetic sheets in an up-up-down arrangement. This is at odds with many of the predicted structures for the $\frac{1}{3}$ -plateau state from modelling the SSL. These structures order in plane and have a variety of structures such as

the “umbrella” structure where the moments are rotated 120° to each other, tilted towards the vertical axis to form a spiral-like structure, which propagates through the lattice [117], however in most cases the favoured structure is an up-up-down structure, in which each triangle has a collinear arrangement of the spins/moments with two of them pointing along the magnetic field and one opposite to it [33]. Unlike the low temperature zero field magnetic phase, inter-plane interactions are now important and it appears the SSL is not well suited to describing the physics of this field induced phase. The magnetic structure of the $\frac{3}{5}$ feature currently remains undetermined due to a structural phase transition, neutron diffraction measurements have shown that over the field range the feature is present, the intensity of the (100) increases strongly suggesting the onset of antiferromagnetic order with a $\mathbf{k} = 0$ commensurate structure. As the magnetic structure remains undetermined the applicability of the SSL is unknown at present. Field induced lattice distortion has been observed in ErB_4 as well [118]. It would be interesting to perform x-ray diffraction measurements in an applied field to determine the nature of the structural phase transition and factor it into the magnetic refinement so that magnetic structure can be determined.

The low temperature magnetic susceptibility and magnetisation measurements have revealed the presence of a new field induced magnetic phase transition in a field of $H = 25.4$ kOe, below 1 K. This corresponds to a fractional magnetisation plateau of $\frac{1}{2}$ the saturation magnetisation. The $\frac{1}{2}$ plateau is quite common in the RB_4 family, observed in ErB_4 and TmB_4 arising from a ferrimagnetic [70] and striped structure respectively [71]. DyB_4 also displays a $\frac{1}{2}$ -plateau, but the magnetic structure remains undetermined [60]. The nature of the $\frac{1}{2}$ plateau phase remains unknown in HoB_4 and it would be interesting to perform single crystal neutron diffraction measurements on it to determine the magnetic structure. A number of theoretical works have been done into the RB_4 lattice by considering the SSL. There are some notable examples which include both a $\frac{1}{3}$ and $\frac{1}{2}$ plateau. The presence of both the $\frac{1}{3}$ and $\frac{1}{2}$ plateau generally arises when considering further interactions. These include the RKKY interaction, dipolar interaction and long range interaction, J_3 and J_4 (see Fig. 2.6 in section 2.3). With the inclusion of the RKKY interaction both plateaux are observed at relatively high temperatures and cooling suggests the appearance of a $\frac{1}{4}$ -plateau [119]. Considering dipolar interactions, simulations predict the $\frac{1}{3}$ plateau for a small contribution, however when the dipolar interaction becomes more significant the $\frac{1}{2}$ appears [120]. This behaviour is mirrored for the long range interactions, where when J_3 and J_4 become important, the $\frac{1}{2}$ plateau appears [121]. The only other member of the RB_4 family that

displays both the $\frac{1}{2}$ and $\frac{1}{3}$ plateau is TbB_4 , similarly to HoB_4 , TbB_4 orders with a non-collinear antiferromagnetic structure in plane [64]. High field magnetisation revealed the presence of the $\frac{1}{2}$ and $\frac{1}{3}$ as well as other values [68, 122], which neutron diffraction studies revealed that the plateau has an in plane magnetic structure [123]. Thus HoB_4 contrasts the other members of the RB_4 family by having inter-planer interactions.

Finally we have looked into the energy level scheme of HoB_4 using heat capacity and inelastic neutron scattering. The magnetic entropy reaches a value of $R \ln 10$, less than the maximum entropy allowed of $R \ln(2J + 1) = R \ln 17$. The difference is due to large scale splitting in the crystal field scheme. The inelastic neutron scattering measurements on polycrystalline samples revealed the presence of crystal field levels at 1.4, 2.9, 5.3, 9.5, 10.8 and 17 meV and the missing crystal fields likely are not neutron sensitive. Further refinements and modelling of the crystal field scheme is needed, it would be beneficial to consider the crystal field parameters of other RB_4 family members to build up a coherent model of the family and accurately predict the location of the crystal fields. The single crystal inelastic neutron scattering measurements revealed that the low energy crystal field levels are dispersive implying it is not a simple crystal field level and dispersion is significant up to 35 K, where strong magnetic correlations persist into the paramagnetic regime. The intermediate temperature shows clear spin waves allowed a comparison of the exchange interactions between the a - and c - axis indicated they have an almost identical strength. This means it can not be considered a two dimensional system and adds further opposition to the use of the SSL in HoB_4 . Fitting the spin waves and dispersion will allow the exchange parameters to be determined and can perhaps understand the ordering in HoB_4 .

Chapter 6

Magnetic Properties of NdB_4

Despite the plethora of interesting and unusual behaviour observed in the other members of the RB_4 family, NdB_4 has been relatively neglected with dedicated investigation having only recently been performed. Structural analysis using single crystal x-ray diffraction [124] determined it has a tetragonal crystal structure ($P4/mbm$). Characterisation with magnetic susceptibility and heat capacity measurements on polycrystalline and single crystal [44, 47] have revealed successive phase transitions at $T_{\text{N1}} = 17.0$, $T_{\text{N2}} = 6.2$ and $T_{\text{N3}} = 4.9$ K, defining three magnetic phases. It was originally suggested that the first transition at T_{N1} arose due to quadrupolar ordering. However recent single crystal neutron diffraction experiment [125] have revealed it orders antiferromagnetically with a $\mathbf{k} = 0$ commensurate structure. It has been determined to have an “all-in/all-out” order where the moments on four Nd ions in the unit cell are in the ab -plane and point into the square formed by the Nd ions, cooling causes the the moments to rotate in the ab -plane slightly. While on the other hand the subsequent phases below T_{N2} and T_{N3} were found to be incommensurate with a propagation vector of $(\delta, \delta, \delta')$ and $(\delta'', 0, \delta')$ respectively where $\delta = 0.14$, $\delta' = 0.4$ and $\delta'' = 0.2$. However the magnetic structure for these phases remains undetermined [125].

In this chapter we report the results of a comprehensive investigation into NdB_4 with both polycrystalline and single crystal samples. First of all we have characterised the sample performing magnetic susceptibility, heat capacity, resistivity and magnetisation measurements, the latter revealing a field induced magnetic phase, which has a fractional value of $\frac{1}{5}$ the saturation magnetisation. We have extended these measurements down to temperatures of 0.5 K and in fields up to 500 kOe, revealing an unusual non-monotonic temperature dependence the transition to the field induced magnetic state, where we observe a re-entrant phase transition

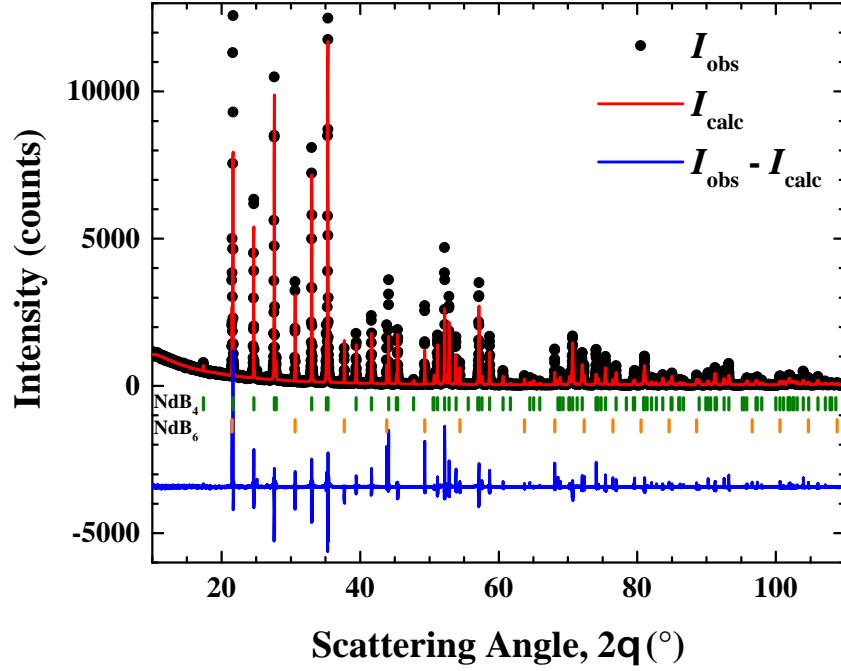


Figure 6.1: Rietveld refinement of the powder x-ray diffractogram of NdB_4 to determine structural parameters. data points and Rietveld fit are shown in the upper curve, while the lowest curve is the difference between the observed and calculated intensity. The set of vertical dashes correspond to the expected nuclear Bragg positions of NdB_4 .

where the field induced state returns to the zero field antiferromagnetic order upon cooling.

We have also performed single crystal neutron diffraction experiments in order to determine the zero field magnetic structures of each phase, which was then expanded to include the use of polarised neutrons, where the diffuse scattering was also investigated. Neutron diffraction experiments in field were then performed in order to determine the structure of the field induced phase on the magnetisation plateau observed.

Finally we have performed inelastic neutron measurements on polycrystalline samples to investigate the crystal field levels. Determining the crystal field scheme is currently under way and the initial analysis is presented.

Space Group: $P4/mbm$			
Lattice Parameters: $a = b = 7.21 \text{ \AA}$, $c = 4.10 \text{ \AA}$			
Ion	Wyckoff Position	Positions	Fractional Coordinates
Nd	$4g$	$(x, x + \frac{1}{2}, 0)$	$x = 0.186$
B1	$4e$	$(0, 0, z)$	$z = 0.112$
B2	$8j$	$(x, y, \frac{1}{2})$	$x = 0.0453, y = 0.155$
B3	$4h$	$(x + \frac{1}{2}, x, \frac{1}{2})$	$x = 0.089$

Table 6.1: Fractional coordinates and Wyckoff Positions for each site in NdB₄, determined through the Rietveld refinement of NdB₄ powder x-ray diffraction pattern.

6.1 Bulk Characterisation

Polycrystalline and single crystal samples of NdB₄ were made as detailed in section 4.1.1. Similarly to HoB₄ polycrystalline samples were made by powdering single crystals. The composition of the sample was checked using powder x-ray diffraction. The diffractogram and the Rietveld refinement (red line) is shown in Fig. 6.1. The difference curve (blue line) shows a number of peaks around the Bragg reflections where the fit is not predicting the intensity well. The diffractogram shows the presence of a few small impurity peaks arising from the decomposition of NdB₄ to NdB₆. The structural parameters from the Rietveld refinement are shown in Table 6.1 and are in agreement with previous measurements [124]. Similarly to HoB₄, while the fractional xyz values are in agreement with previous literature, the discrepancies in the intensities mean we should be cautious in the value and the values from the neutron diffraction study in section 6.2.2 are more accurate. The grown crystals had patches of blue, which is arising due to NdB₆ [126] and was confirmed to be NdB₆ using EDAX (energy-dispersive x-ray spectroscopy). The NdB₆ formed a polycrystalline coating on the crystal as well as clusters within the crystal which were easily isolated for the single crystal and thus we expect the NdB₆ impurity to be small in the single crystal samples. Fig. 6.2 shows Laue photographs along the principal axis of NdB₄ compared to simulated patterns. The simulated patterns were created using the OrientExpress software [104] As can be seen there is good agreement between the observed and simulated patterns, however scanning along the rod gave indications that the rod was made up of a few similarly aligned crystals, similar to HoB₄. The grains were large enough to isolate to give reasonably sized crystals for neutron experiments.

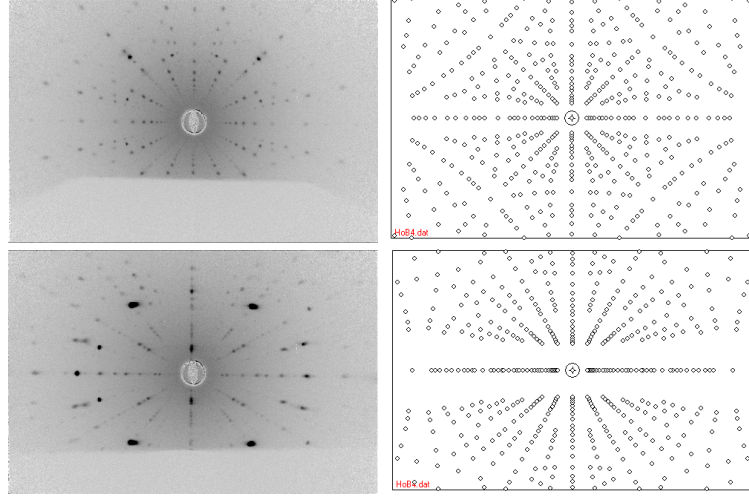


Figure 6.2: Single crystal Laue diffraction photographs of NdB_4 of (a) the $[100]$ and (b) the $[001]$ directions compared to simulated patterns from the OrientExpress software.

6.1.1 Magnetic Susceptibility

The temperature dependent magnetic susceptibility of NdB_4 is shown in Fig. 6.3. For $H \parallel c$ NdB_4 shows two magnetic phase transitions, seen as a broad maximum at approximately $T_{N2} = 7$ K, followed by a small discontinuous drop at $T_{N3} = 4.2$ K. Both transitions are also observed for $H \perp c$, while an additional transition is seen at $T_{N1} = 17$ K. This defines three magnetic phases; the high temperature ($T_{N2} < T < T_{N1}$), the intermediate temperature ($T_{N3} < T < T_{N2}$) and the low temperature ($T < T_{N1}$) phases, which are denoted HT, IT and LT respectively.

The insets on Fig. 6.3 shows the inverse magnetic susceptibility. Curie-Weiss behaviour is observed for both $H \parallel c$ and $H \perp c$ and the data was fitted between (50–300 K) with a least squares linear regression fit [105]. The effective moment and the Curie-Weiss temperatures were determined from the fit and are shown in Table 6.2. The effective moment is in agreement with the value predicted by Hund’s rules, while the negative Curie-Weiss temperature indicates the antiferromagnetic nature of NdB_4 ’s phase transitions. The determined values are in agreement with previously published results [44, 47].

Fig. 6.4 shows the temperature dependent magnetic susceptibility curves and how they evolve in increasing magnetic fields. For $H \parallel c$ the broad maximum at $T_{N2} = 7$ K is suppressed with increasing field and is no longer obvious above 30 kOe. The second transition observed is a discontinuous drop at $T_{N3} = 4.2$, as

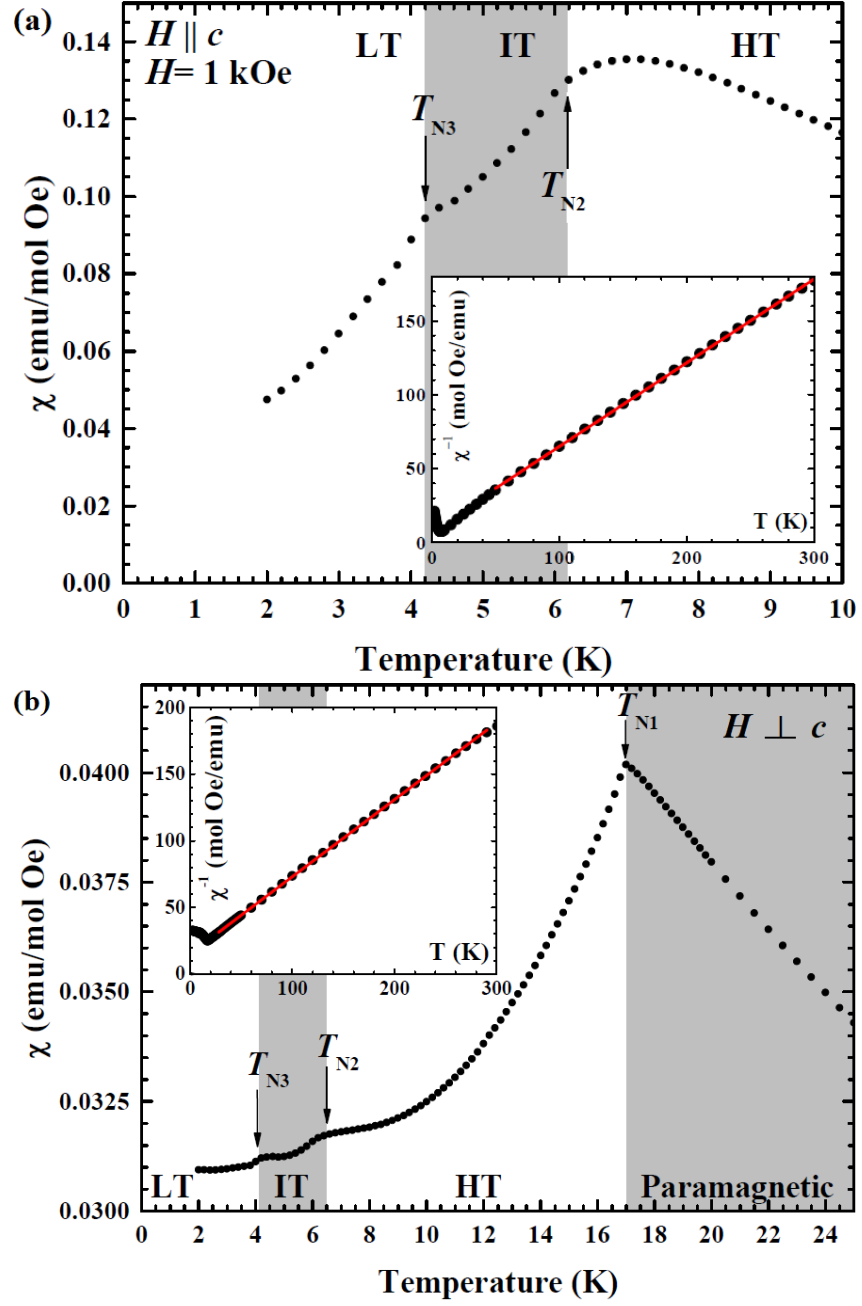


Figure 6.3: Temperature dependent magnetic susceptibility of NdB_4 in a field of $H = 1 \text{ kOe}$ for (a) $H \parallel c$ and (b) $H \perp c$, shading indicates the different magnetic phase and the inset shows the inverse susceptibility, χ^{-1} .

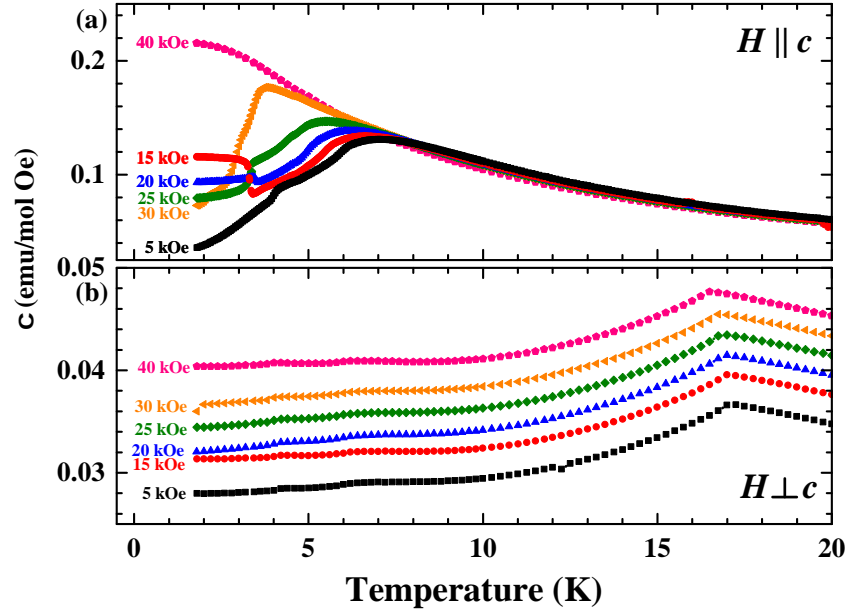


Figure 6.4: The temperature dependent magnetic susceptibility curves of NdB_4 in different magnetic field for (a) $H \parallel c$ and (b) $H \perp c$. Each curve in (b) is subsequently offset by 0.002 emu/mol-Oe.

was the case for $H = 1$ kOe (see Fig. 6.3). At $H = 15$ kOe, the transition is heralded by a significant increase in the magnetic susceptibility, most likely arising due to a field induced magnetic phase. The transition at T_{N3} to the field induced state, remains broadly unchanged up to 25 kOe, before being further suppressed at $H = 30$ kOe to $T = 2.9$ K and is no longer present at $H = 40$ kOe. For $H \perp c$, T_{N2} and T_{N3} are both suppressed, but not to the same extent as that of $H \parallel c$, with both transitions visible up to 40 kOe and the temperatures changing by only 0.2 and 0.4 K respectively between 5 and 40 kOe. T_{N1} remained broadly unchanged with increasing the field with the transition being suppressed to 15.7 K at 40 kOe.

	T_{N1} (K)	T_{N2} (K)	T_{N3} (K)	μ_{eff} (μ_B)	θ_{CW} (K)
$H \parallel c$	-	7	4.2	3.76	-15.9
$H \perp c$	17	6.5	4.2	3.73	-27.4

Table 6.2: The magnetic transitions temperatures for both $H \parallel c$ and $H \perp c$ found from the magnetic susceptibility, including the effective moment, μ_{eff} , and Curie-Weiss constant, θ_{CW} calculated from the inverse magnetic susceptibility.

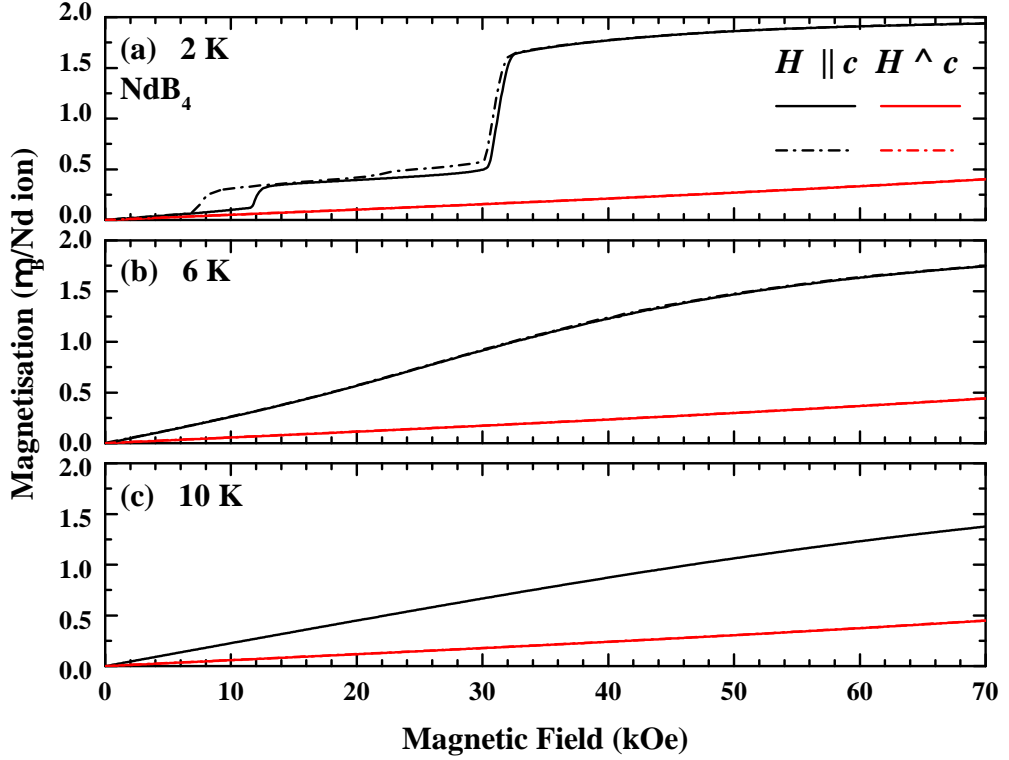


Figure 6.5: Field dependent magnetisation measurements of NdB_4 for $H \parallel c$ (black) and $H \perp c$ (red) taken in each of the three magnetic phases at temperatures of (a) 2 K, (b) 6 K and (c) 10 K. Solid curves correspond to the field being ramped up, while dash-dot curves are the field ramping down.

6.1.2 Magnetisation

The samples used were plate-like and arranged to reduce the demagnetisation factor. The demagnetisation factor did not exceed 0.2, therefore the correction for an effective field does not exceed 1%. The demagnetisation factor was calculated by following the method outline in ref [106]. We have performed field dependent magnetisation measurements for $H \parallel c$ and $H \perp c$. Both are shown in Fig. 6.5. The low temperature phase at $T = 2$ K for $H \parallel c$ shows a magnetisation plateau occurring at a fractional value of the saturation magnetisation, $M/M_{\text{sat}} = \frac{1}{5}$ and the curve appears to have reached saturation at $2\mu_B/\text{Nd ion}$, which is smaller than the saturated moment predicted by $g_J\mu_B J = 3.27\mu_B$ and the value obtain from the magnetic susceptibility. This difference could be due to strong crystalline electric fields. The curve shows hysteresis upon ramping the field down, first of all it appears to reach a meta-stable state ramping down from saturation and then a further hysteresis effect

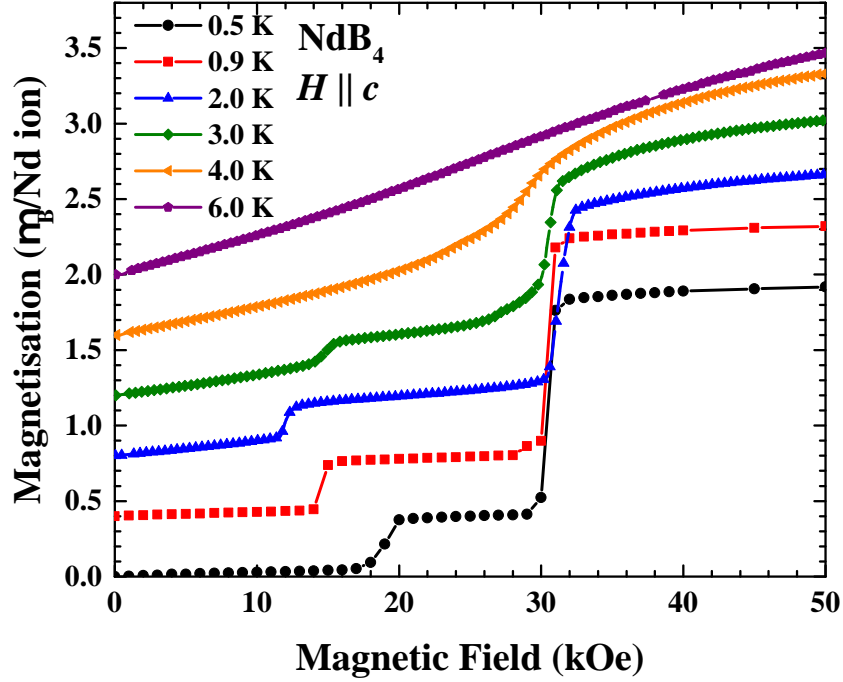


Figure 6.6: The evolution of the field dependent magnetisation measurements in temperatures between 0.5 and 10 K for $H \parallel c$.

from the $\frac{1}{5}$ -plateau. Tracking the evolution of the field dependent magnetisation curves with temperature, we can see that the $\frac{1}{5}$ -magnetisation is present only in the low temperature phase and is no longer present at 6 K (IT phase), where we see a broad upturn and then levelling off at $1.75\mu_B$. The curve at $T = 10$ K increases linearly reaching $1.4\mu_B$ at 70 kOe. There is no obvious hysteresis upon ramping down the field for either curve at 6 K and 10 K. For $H \perp c$ there is a general curve upwards for all temperatures below T_{N1} and the curve has not reached saturation by 100 kOe. Comparing the magnetisation between $H \parallel c$ and $H \perp c$ suggests the easy axis in small magnetic fields is the c -axis. The large difference between the magnetisation of the two directions is characteristic of Ising-type anisotropy, which seems to be a common trait amongst the rare earth tetraborides, being seen in HoB_4 as well as ErB_4 . There are no obvious signs of hysteresis for any of the curves, where $H \perp c$.

6.1.3 Low Temperature (^3He) Measurements

The magnetisation measurements were extended to low temperatures, which can be seen in Fig. 6.6. The curve shows a single magnetisation plateau at $M/M_{\text{sat}} = \frac{1}{5}$,

consistent with the higher temperature measurements. Interestingly, the field in which the transition occurs increases with decreasing temperature, which is the same for increasing temperatures as well, suggesting that at low temperature the field induced magnetic state is returning to the zero field antiferromagnetic phase. While the temperature dependence of the latter transitions remains broadly unchanged, the temperature dependence of the critical field of the transition to the plateau appears to be non-monotonic. The value of the transitions decreases to 14 and to 12 kOe for 0.9 and 2 K respectively before increasing to 15 kOe at 3 K, with the plateau becoming less defined. While the transition to saturation begins with a gradual up turn at approximately $H = 26$ kOe before a more significant jump at approximately 29 kOe. Increasing the temperature further to $T = 4$ K, the magnetisation plateau becomes significantly less pronounced and differentiating the magnetisation curve (not shown) reveals the two transitions. The first transition shifts to 24 kOe, while the latter transition remains at approximately 30 kOe. In all the low temperature phase curves there is a further, smaller transition located at approximately $M/M_{\text{sat}} = 0.24$. The magnetisation curve at $T = 6$ K (in the intermediate temperature phase) shows no discernible transition, linearly increasing towards saturation. The exact nature of the plateau phases is still an open question, however single crystal neutron diffraction on D10 has revealed a structure that propagates along the c -axis, similar to HoB_4 [127] and will be discussed in more detail in Section 6.2.4.

To investigate this unusual temperature dependence of the field induced phase, magnetic susceptibility measurements at 10, 15 and 20 kOe were made, as shown in Fig. 6.7. The susceptibility curve at $H = 10$ kOe shows a broad maximum at $T = 6.8$ K and a discontinuous drop at $T = 4.2$ K. These correspond to transitions to the incommensurate intermediate and low temperature phases. Increasing the field to 15 kOe the broad maximum is suppressed to $T = 6.7$ K, while there is now a discontinuous jump at $T = 3.3$ K, which is the magnetisation plateau state. Cooling further reveals a discontinuous drop in the susceptibility at $T = 1.5$ K. Temperature dependent susceptibility at lower fields shows no indication of a new phase, suggesting the transition at $T = 1.5$ K in Fig. 6.7 goes from the field induced state back to the zero field antiferromagnetic state. Increasing the field to 20 kOe, $T_{\text{N}2}$ is further suppressed to 6.2 K, while $T_{\text{N}3}$ increases to 3.6 K. It can also be seen that the lower, novel transition is suppressed with the transition beginning at $T \approx 0.5$ K, but we are unable to achieve temperatures to see the entire transition.

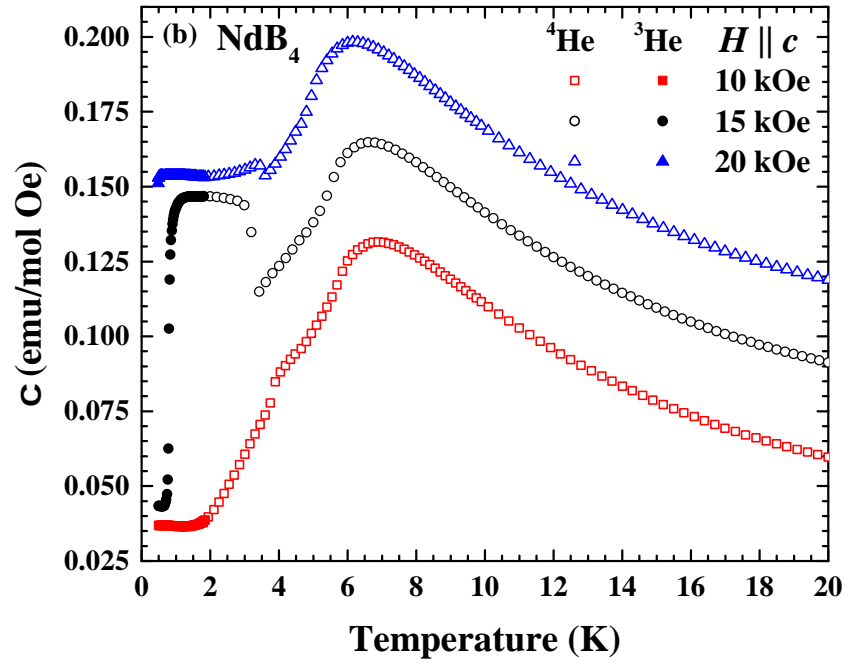


Figure 6.7: Temperature dependent magnetic susceptibility at $H = 10, 15$ and 20 kOe. Filled symbols correspond to measurements made using ^3He , while empty symbols correspond to ^4He measurements. Each curve is subsequently offset by 0.03 emu/mol-Oe.

6.1.4 High Field Magnetisation

Figure 6.8 shows the field dependent magnetisation measurements up to 500 kOe and $T = 1.5$ K for $H \parallel c$ and $H \perp c$ using a pulsed magnetic field. For $H \parallel c$, we observe the expected $\frac{1}{5}$ -magnetisation plateau at 14 kOe and then the transition to saturation at 30 kOe. The magnetisation then remains approximately constant at $2\mu_B$ per Nd ion up to 500 kOe. The difference between the saturated moment and expected moment could be arising due to strong crystalline electric field effects. For $H \perp c$ on the other hand, the magnetisation is linear up to approximately 70 kOe, with a gradual up turn in the value showing a distinct change in gradient at approximately 150 kOe. Above the transition the magnetisation increases, surpassing the magnetisation of $H \parallel c$ at 350 kOe, the magnetisation continues to increase with no suggestion of saturation, achieving $2.6\mu_B$ per Nd ion by 500 kOe. There is no clear indication to the direction of the easy axis, this suggests that the easy axis could be off-axis and not along one of the principal axes.

High field measurements were also made in the HT phase at 8 K. For $H \parallel c$, we see a gradually increase and saturating at approximately $1.85\mu_B$. For $H \perp c$, we see a similar behaviour to that of 1.5 K, There is a general increase and a kink at a lower field at approximately 130 kOe. As with the low temperature curve, the nature of this phase transition is currently unknown.

6.1.5 Heat Capacity

The temperature dependent heat capacity in different magnetic fields for both $H \parallel c$ and $H \perp c$ is shown in Fig. 6.9. For $H \parallel c$ (Fig. 6.9(a)) three transitions are observed; $T_{N1} = 17$ K, $T_{N2} = 6.2$ K and $T_{N3} = 4.8$ K, all of which were also seen in the magnetic susceptibility. The transitions at T_{N1} and T_{N2} are second-order phase transitions, while T_{N3} is a first order phase transition. The curves for $H \parallel c$ and $H \perp c$ in a field of $H = 0$ kOe (Fig. 6.9(b)) is expected to be identical. However, we see that T_{N1} is different, this is because the PPMS used has difficulty measuring first order phase transitions as was also the case for HoB_4 (Sec. 5.1.5). Upon increasing the field for $H \parallel c$, T_{N1} remains broadly unchanged up to 35 kOe, while both T_{N2} and T_{N3} are suppressed. There is a broad transition at $T = 5$ K for $H = 35$ kOe, which correspond to the system tending towards a polarised state.

Figure 6.9(b) shows the heat capacity for $H \perp c$. Again, three transitions are observed, two lambda-like anomalies at T_{N1} and T_{N2} and a sharp peak at T_{N3} . Unlike for $H \parallel c$ the transitions remain at approximately the same temperature upon increasing field with T_{N1} only being slightly suppressed from 17 K to 15.9 K

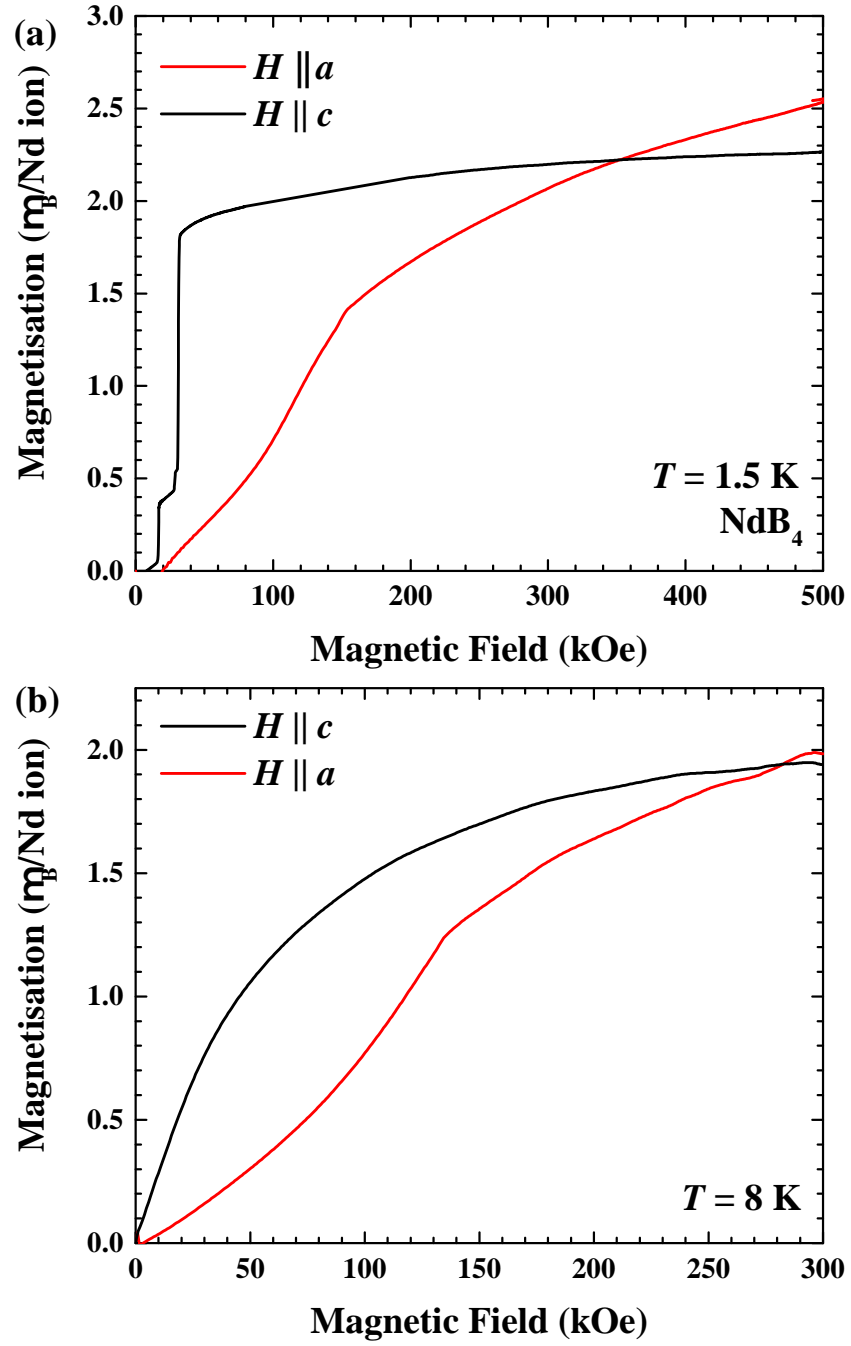


Figure 6.8: Field dependent magnetisation measurements for $H \parallel c$ and $H \perp c$, made using a pulsed magnetic field up to 500 kOe for two temperatures, (a) $T = 1.5 \text{ K}$ and (b) $T = 8 \text{ K}$.

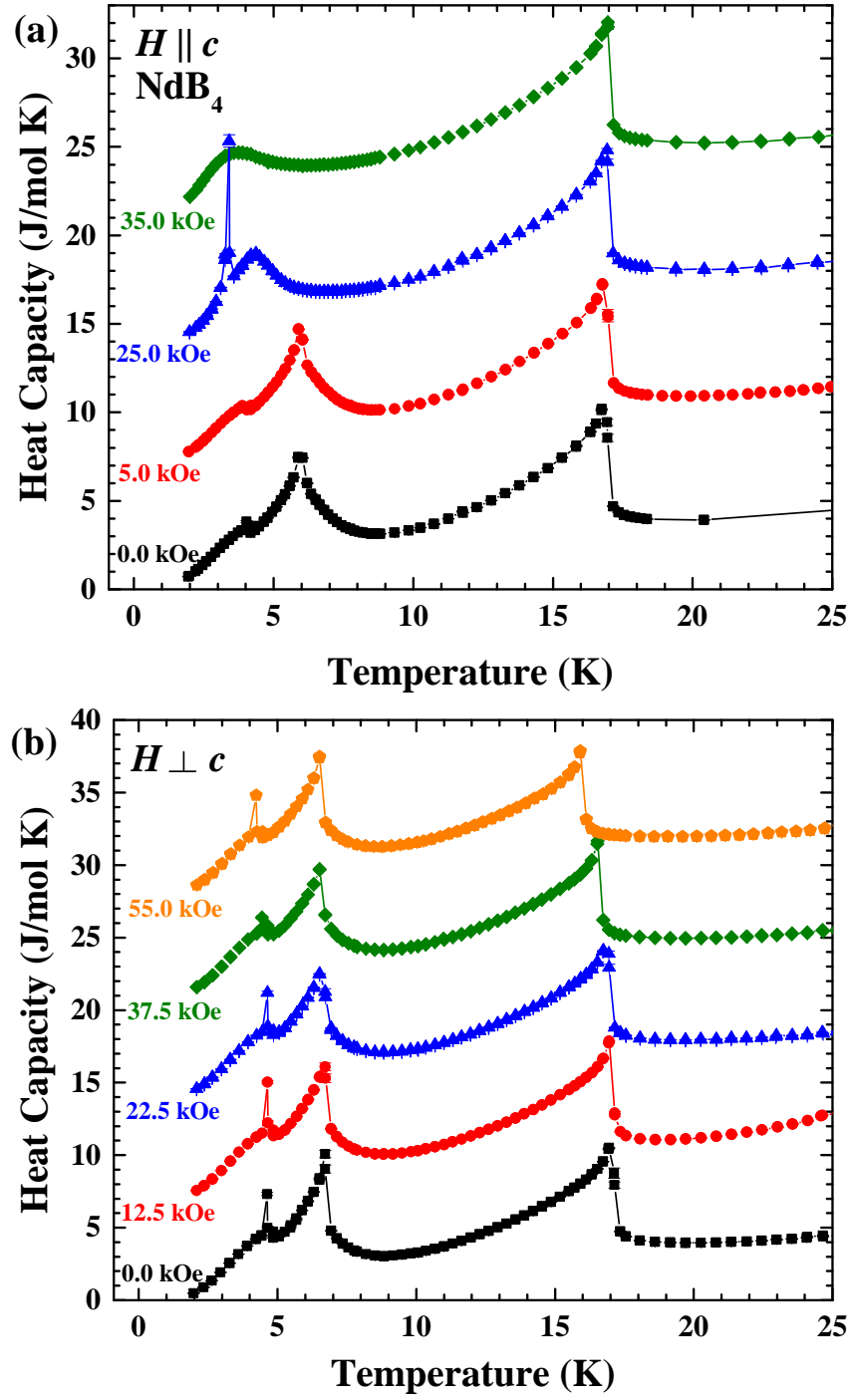


Figure 6.9: Temperature dependent specific heat measurements for (a) $H \parallel c$ and (b) $H \perp c$ in increasing fields. Each curve is subsequently offset by 7 J/mol K.

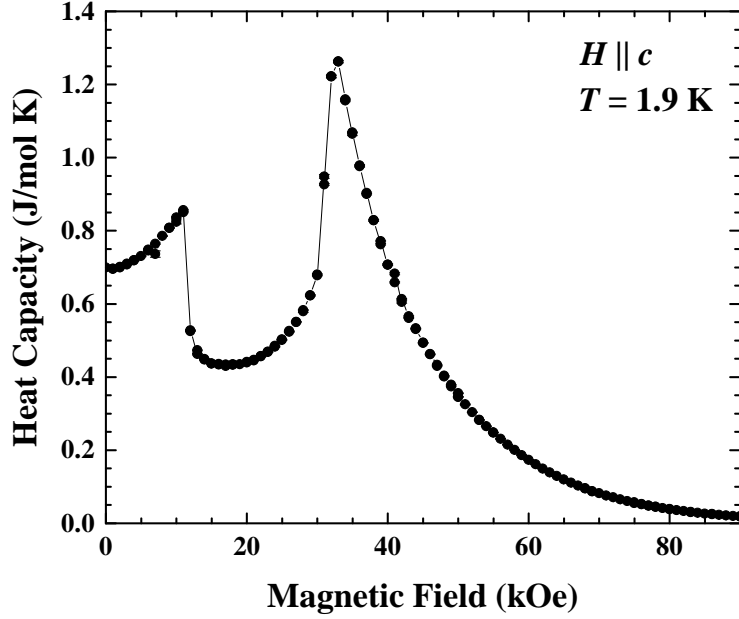


Figure 6.10: Field dependent specific heat measurements of NdB_4 for $H \parallel c$ at $T = 1.9 \text{ K}$.

at 55 kOe.

Figure 6.10 shows the field dependent heat capacity for $H \parallel c$ at $T = 1.9 \text{ K}$. It shows two transitions at approximately 11 and 33 kOe, which is consistent with the $\frac{1}{5}$ -magnetisation plateau phase observed in Fig. 6.6. The heat capacity then gradually decreases down to zero with increasing magnetic field. This behaviour is expected at low temperatures, states with low energy become more probable, the degree of alignment of the magnetic moments parallel to an applied magnetic field increases and the entropy falls. At low temperatures and sufficiently high field all the magnetic moments will align with the magnetic field to save energy. In this case there is only one way of arranging the moments, so the entropy is zero and thus, heat capacity is also zero [4].

Figure 6.11 shows the magnetic contribution of the heat capacity of NdB_4 . This was determined by subtracting the total heat capacity of the non-magnetic LuB_4 using the same process that was used for HoB_4 outlined in Sec. 5.1.5. The normalisation ratio, r for NdB_4 and LuB_4 was determined to be $r = 0.863$. As both curves are in zero field we expect the results to be identical and the labels $H \parallel c$ and $H \perp c$ are merely used to indicate the differing geometry and the crystals used. The insets in Fig. 6.11 shows the total heat capacity of NdB_4 and LuB_4 , as expected from HoB_4 and a variety of other RB_4 members [110–113] the heat capacity is linear

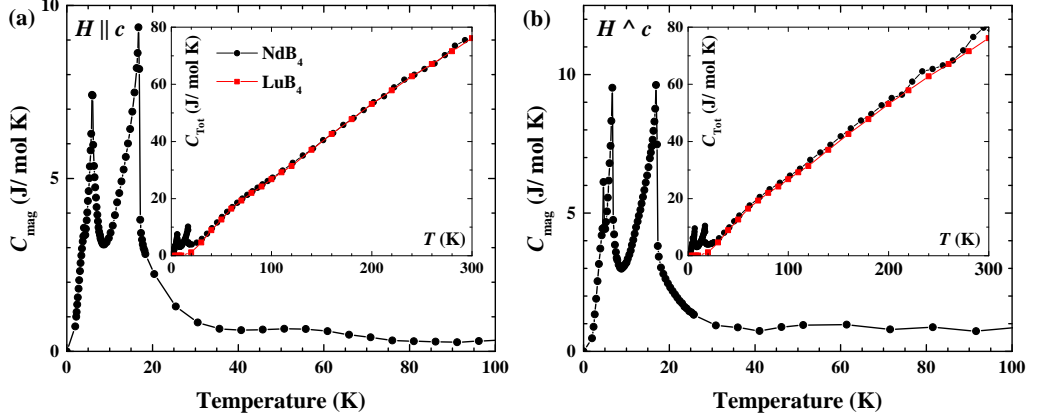


Figure 6.11: Temperature dependence of the magnetic contribution of the specific heat measurements for (a) $H \parallel c$ and (b) $H \perp c$. The inset shows the total heat capacity at high temperatures for NdB_4 and the non-magnetic LuB_4 .

down to low temperatures.

For both plots, we observe the three expected transitions, additionally we observe a Schottky anomaly at approximately 55 K, again using Equation (5.2) we estimated the energy gap and found the Schottky anomaly would correspond to an energy gap of approximately 120 K. The insets show a comparison between the total heat capacity of NdB_4 to the total heat capacity of LuB_4 at high temperatures.

We then determined the magnetic entropy by numerically integrating C_{mag}/T with respect to T , which is shown in Fig. 6.12. The red curve shows the entropy, there are a number of kinks in the curve correspond to each of the three transition temperatures. The entropy reaches 1.83 J/mol K at $T_{\text{N}3}$, 3.50 J/mol K at $T_{\text{N}2}$ and 8.47 J/mol K at $T_{\text{N}1}$. At high temperatures the entropy levels off to a value of 10.0 J/mol K. The maximum allowed entropy for Nd ions in RB_4 is $R \ln(2J + 1) = R \ln 10$ ($J = \frac{9}{2}$). As $2J + 1$ gives an even value, Nd is a Kramer ion meaning that we are expecting the crystal field scheme to be made up for five doublets. The entropy reaches $R \ln 2$ by 10.5 K and just surpasses $R \ln 3$ at 21.5 K before levelling out. The difference between the maximum entropy and the maximum we observe is arising due to a large splitting of the crystal field levels.

6.1.6 Resistivity

Temperature dependent resistivity measurements are shown in Fig. 6.13 for both $H \parallel c$ and $H \perp c$. NdB_4 has a high residual resistance ratio value (RRR; $\rho(300 \text{ K})/\rho(2 \text{ K}) = 100$) re-enforcing the high quality of the sample. For both field directions the re-

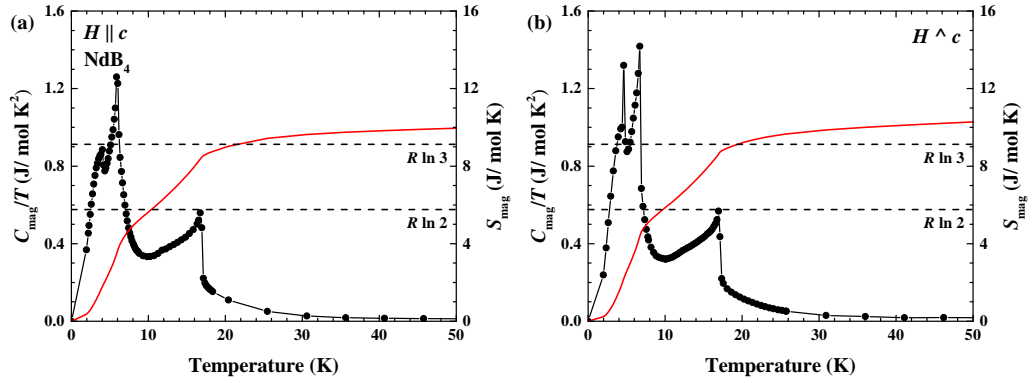


Figure 6.12: Temperature dependence of the magnetic contribution of the heat capacity divided by the temperature. The red curve shows the magnetic entropy, which was determined by integrating the C_{mag}/T with respect to T .

sistivity curves are linear down (not shown) to the first transition, $T_{\text{N}1}$, indicating the metallic nature of NdB_4 which is the case in the other RB_4 family members. There is a sudden drop at $T_{\text{N}1} = 17$ K, with two further features at $T_{\text{N}2} = 6.8$ K and $T_{\text{N}3} = 4.9$ K. The sudden slope change could be due to the loss of spin disorder scattering at the antiferromagnetic transition temperature, which has been suggested for other members of the RB_4 family [62, 72]. The evolution of the temperature dependence in field for $H \parallel c$ is shown in Fig. 6.13(a). Similarly to the magnetic susceptibility and heat capacity, the transitions at $T_{\text{N}2}$ and $T_{\text{N}3}$ are suppressed with increasing field, while $T_{\text{N}1}$ remains unchanged. $T_{\text{N}3}$ becomes significantly more pronounced for $H = 17.5, 22.5$ and 27.5 kOe, which corresponds to the transitions into the $\frac{1}{5}$ -magnetisation plateau phase observed in Fig. 6.6. The transition becomes very broad above 27.5 kOe as the system tends towards a polarised state. The measurements for $H \perp c$ are shown in fig. 6.13(b). As expected from the previous characterisation, we observe the three transitions at $T_{\text{N}1}$, $T_{\text{N}2}$ and $T_{\text{N}3}$, which do not change significantly between $0 \leq H \leq 37.5$ kOe.

The field dependent resistivity measurements for $H \parallel c$ is shown in Fig. 6.13(c). As can be seen there is magnetoresistance at all temperatures, the magnetoresistance (defined by $\text{MR}(H, T) = [\rho(H, T) - \rho(0, T)]/\rho(0, T)$) gradually increases from 50% to 71% from 20 K to 8 K. It further increases to 130% in the intermediate temperature phase (6 K), before dramatically increasing in the low temperature phase to 414%, 766% and 1200% for 4, 3 and 2 K respectively. Large magnetoresistances have also been observed in HoB_4 [102] and GdB_4 [54]. The curves at $T = 2$ and 3 K show features which mirror the plateau observed in the magnetisation mea-

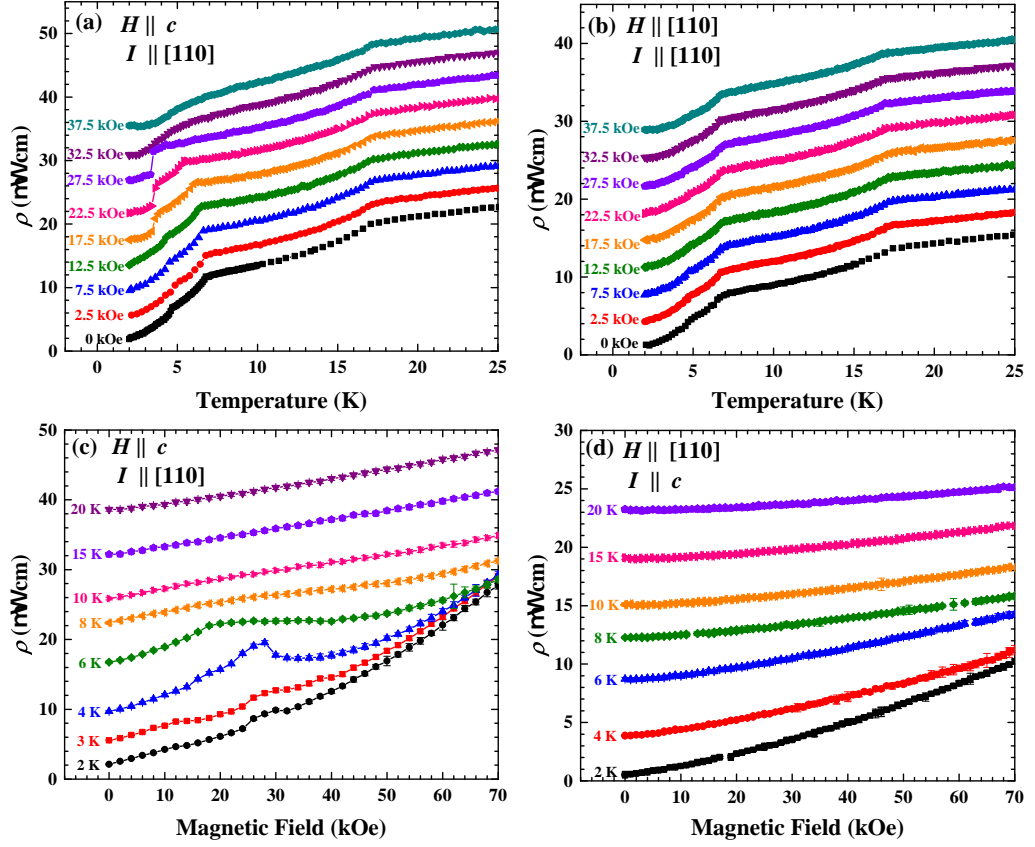


Figure 6.13: Temperature dependent resistivity measurements of NdB_4 made for (a) $H \parallel c$ and (b) $H \perp c$. Each curve is subsequently offset by 2 and 3 $\mu\Omega - \text{cm}$ respectively. Field dependent resistivity measurements made for (c) $H \parallel c$ and (d) $H \perp c$. Each curve is subsequently offset by 2.5 $\mu\Omega - \text{cm}$.

measurements shown in Fig. 6.6. A plateau is also observed at $T = 6$ K, the constant resistivity most likely arising as the system goes from the intermediate to the high temperature phase.

The field dependent resistivity curves for $H \perp c$ are shown in Fig. 6.13(d), as can be seen there are no noticeable features at any temperature, consistent with the magnetisation measurements. Similarly to $H \parallel c$ there is a magnetoresistance, which gradually increases from 22% to 73% upon cooling from 20 to 8 K. There is an increase to 212% at 6 K and further increases in the low temperature to 549% and 2140% at 4 K and 2 K respectively.

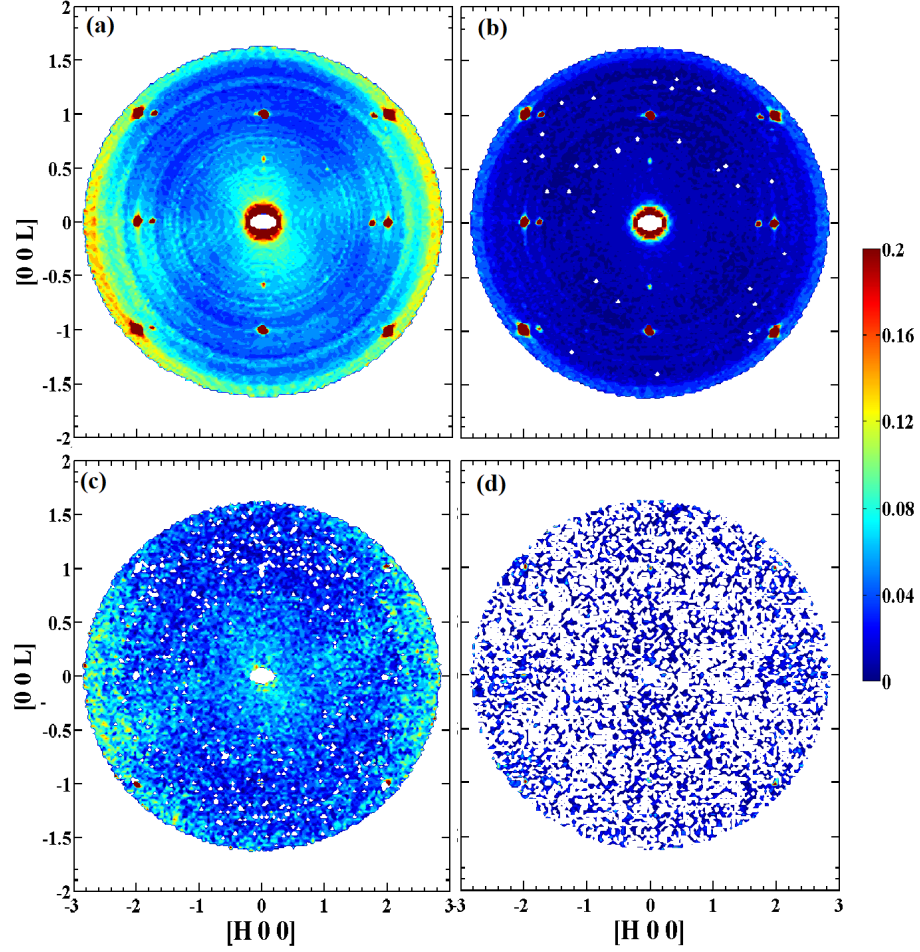


Figure 6.14: Single crystal neutron diffraction maps of $(h0l)$ plane for NdB_4 using the D7 diffractometer. Full xyz polarisation analysis was used to separate the intensity maps into (a) total scattering, (b) nuclear coherent, (c) nuclear spin incoherent scattering and (d) magnetic scattering.

6.2 Single Crystal Neutron Diffraction

6.2.1 Polarised Neutron Diffraction

Figure 6.14 shows the zero-field intensity maps of the $(h0l)$ scattering plane of NdB_4 in the paramagnetic regime at $T = 30$ K. Full xyz -polarisation analysis was used to separate the total intensity map (a) into nuclear coherent scattering (b), nuclear incoherent scattering (c) and the magnetic scattering (d). As can be seen there are Bragg reflections at $(\bar{2}0\bar{1})$, $(\bar{2}00)$, $(\bar{2}01)$, (001) , $(00\bar{1})$, $(20\bar{1})$ and (201) . These are all expected by the crystal symmetry of NdB_4 , however there are additional features appearing only in the nuclear coherent scattering at $(\frac{3}{4} 0 1)$, $(\frac{3}{4} 0 \bar{1})$, $(\frac{3}{4} 0 1)$ and $(\frac{3}{4} 0 \bar{1})$ as well as $(0 0 \frac{1}{2})$ and $(0 0 \frac{1}{2})$. It is suspected that these are arising due to a small NdB_6 impurity. Although the well defined positions would suggest the presence of a co-aligned NdB_6 crystal, which is quite unusual.

In addition it can be seen that there is structure to the background, which can be observed in all the intensity maps and is most prominent in the nuclear incoherent scattering map (Fig. 6.14(c)). This structure is arising due to shape of the sample. The sample was a rod shape, so when making the intensity maps by rotating the sample, there are angles where the beam is hitting the cross section, while there will also be geometries where it is hitting along the rod. This means the amount of crystal a neutron travels through depends on the rotation of the sample. Therefore there is a higher chance of secondary events like multiple scattering, etc. which will increase the background for certain angles. This gives rise to an angular dependence of the intensity. To try and account for this we used a box smoothing algorithm on the total scattering intensity maps. The algorithm works by taking a detector element and then averaging 10 detector elements either side of the chosen element for each theta. The algorithm then moves along one element and repeats the process, producing a smoothed map. We performed the smoothing algorithm at a sufficiently high temperature (30 K) to ensure we were in the paramagnetic regime and were not going to observe any magnetic signal. This smoothed map was then used to account for the shape in the intensity, by dividing the maps in the magnetic phases, which should eliminate the shape and should reveal any diffuse signal that is hidden within the signal.

Figure 6.15 shows the intensity maps of the $(h0l)$ scattering plane using only a z -polarisation (parallel to the $[010]$ -direction). The NSF and SF channels were measured at $T = 30, 12, 6$ and 1.5 K. Figure 6.15(a) shows the z -polarisation reciprocal space map for $T = 30$ K, this is the paramagnetic regime and we expect to only see nuclear Bragg peaks, which is what we observed. Much like for HoB_4 in

section 5.2.1 “leakage” from the Bragg peaks in the NSF channel is observed in the SF channel. The leakage features are 3% of the intensity.

The HT magnetic phase at $T = 12$ K is shown in Fig. 6.15(b). There is the appearance of the (100), (101) and $(10\bar{1})$ reflections, which are not allowed by the crystal symmetry suggests the onset of antiferromagnetic order. The (100) reflection is only present in the spin-flip channel, implying that there is a significant c -axis component to the antiferromagnetic phase. This is because the SF channel would be sensitive to a component to the magnetic moment along the a and/or c -axis, as NdB_4 has a tetragonal crystal structure, if the magnetic moment was along the a -axis, we would also expect to see intensity on the (100) in the NSF channel as well. This finding is at odds with the structure suggested in ref. [125], which put forward that the moments sit only in the ab -plane. Diffuse scattering is also observed around $(20\frac{1}{2})$ and $(20\frac{1}{2})$ is most likely arising due to short range correlation forming, heralding the on-set of the magnetic structure in the intermediate temperature phase.

The IT phase at $T = 6$ K is shown in Fig. 6.15(c). We observe the appearance of some incommensurate reflections at $(1.85\ 0\ 0.4)$, $(2.15\ 0\ 0.4)$, $(1.85\ 0\ 0.6)$ and $(2.15\ 0\ 0.6)$ as well as those at the equivalent negative L values. While these appear at $K = 0$, D7 detectors can detect a small out of plane component and further measurements on D10 (see section 6.2.2) reveal that these reflection actually correspond to a propagation vector of $(\delta, \delta, \delta')$, where $\delta = 0.15$ and $\delta' = 0.4$. Again these incommensurate reflections are only observed in the spin-flip channel suggesting there is a significant c -axis component to the magnetic phase. Diffuse scattering can still be observed around the incommensurate reflections.

The LT phase at 1.5 K is shown in Fig. 6.15(d). First of all the intermediate temperature phase incommensurate reflections shift positions to $(1.8\ 0\ 0.4)$, $(2.2\ 0\ 0.4)$, $(1.8\ 0\ 0.6)$ and $(2.2\ 0\ 0.6)$. While there is the appearance of additional reflections appearing at $(0.4\ 0\ 0.2)$, $(0.4\ 0\ \bar{0.2})$, $(0.6\ 0\ 0.2)$ and $(0.6\ 0\ \bar{0.2})$ as well as equivalent reflections appearing for $L = \pm 1$. The diffuse scattering observed in the high and intermediate phases is no longer present suggesting the low temperature phase is ordered.

Figure 6.16(a) shows the line cuts along $[1.4\ 0\ L]$ and $[1.8\ 0\ L]$ in the SF channel. It illustrates the positions of the incommensurate reflections suggesting two propagation vectors of $(\delta', 0, \delta'')$ and $(\delta'', 0, \delta')$, where $\delta'' = 0.2$ and $\delta' = 0.4$. Diffuse scattering can be observed in 12 K line cut around the incommensurate reflection. This is most likely arising due to short range correlation forming before the onset of the intermediate temperature phase. Although small, diffuse scattering

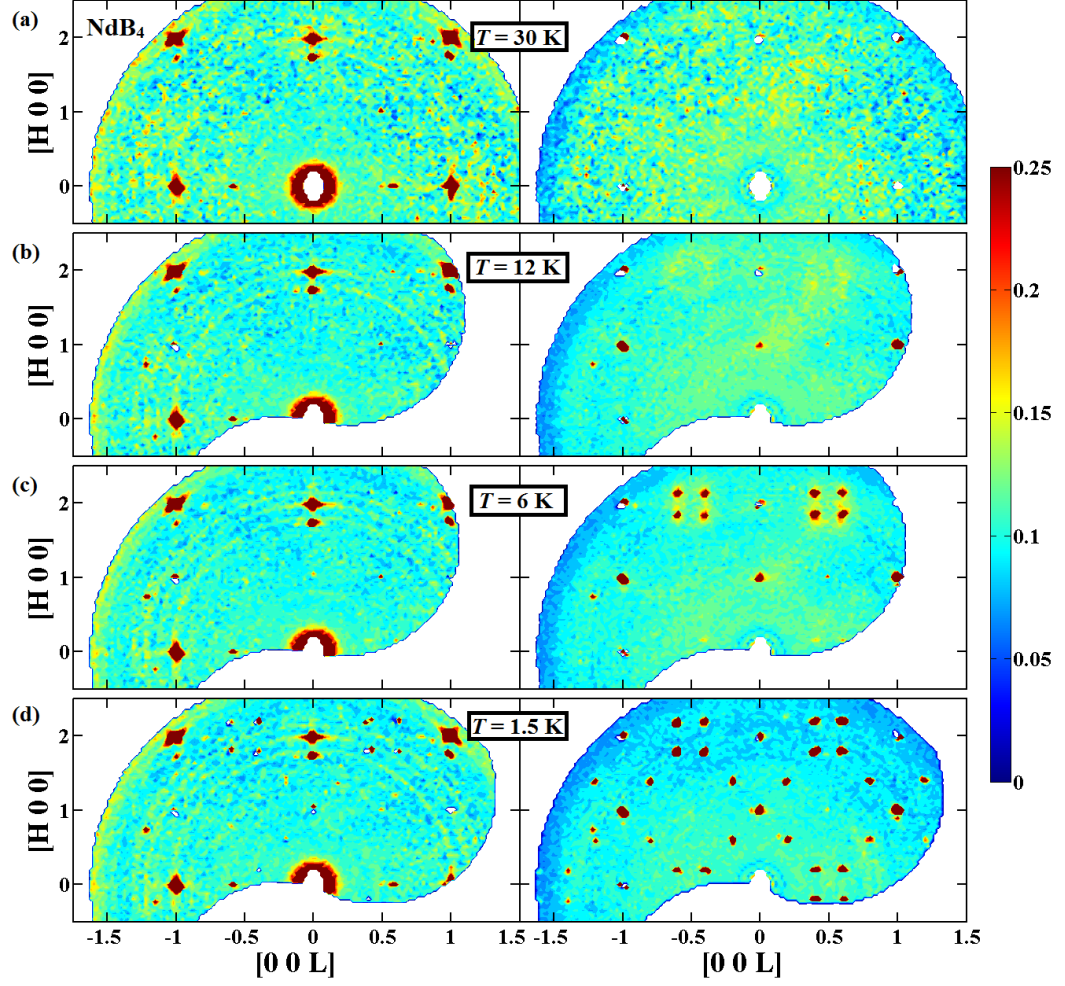


Figure 6.15: Single crystal neutron diffraction maps of $(h0l)$ plane for NdB_4 using the D7 diffractometer. The non spin-flip (left column) and spin-flip (Right column) channels at different temperatures (a) 30 K (b) 12 K, (c) 6 K and (d) 1.5 K are shown.

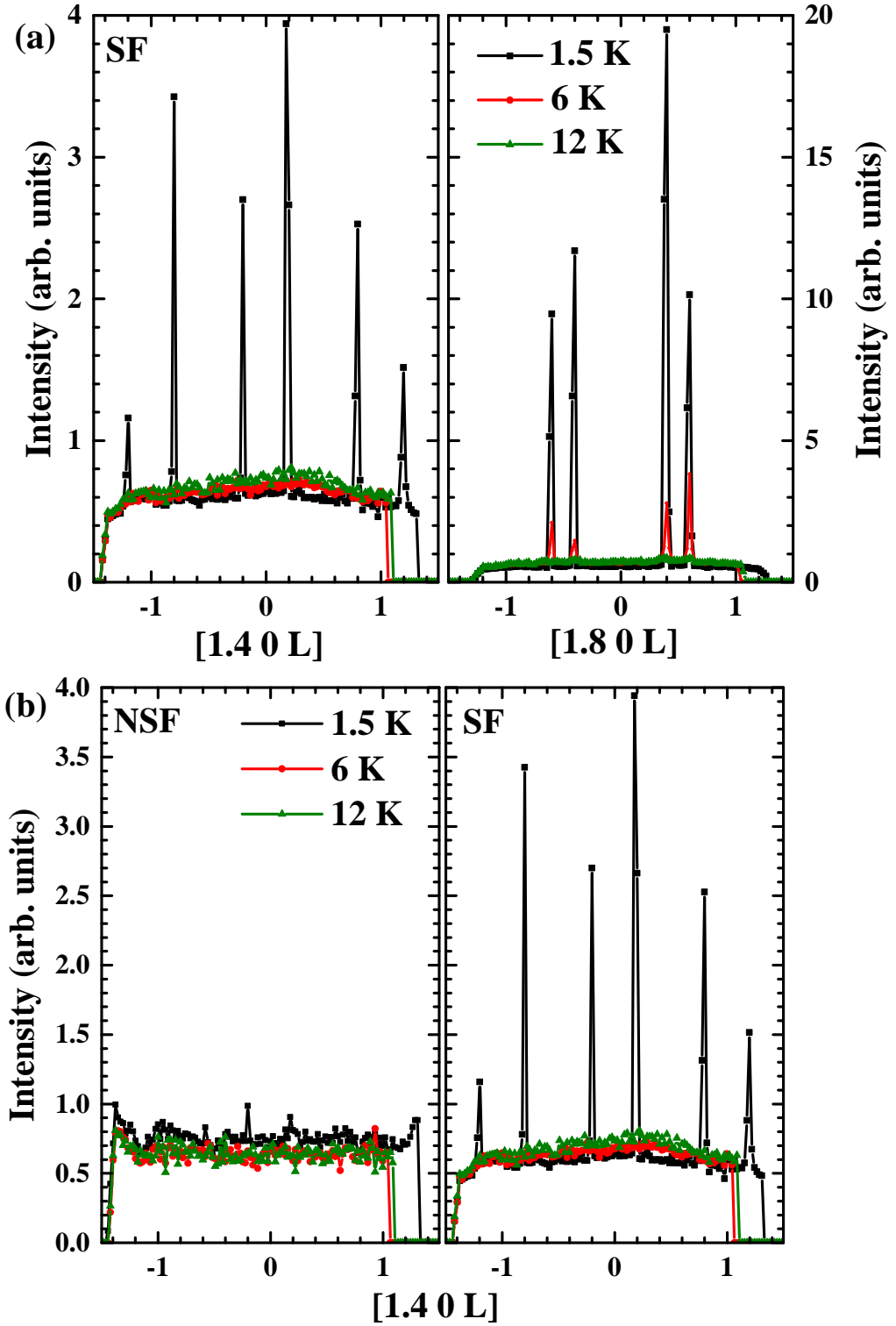


Figure 6.16: (a) line cuts in the spin flip channel for the $[1.4\ 0\ L]$ and $[1.8\ 0\ L]$ direction and (b) line cuts along the $[1.8\ 0\ L]$ for the non-spin-flip (NSF) and spin-flip (SF) channel.

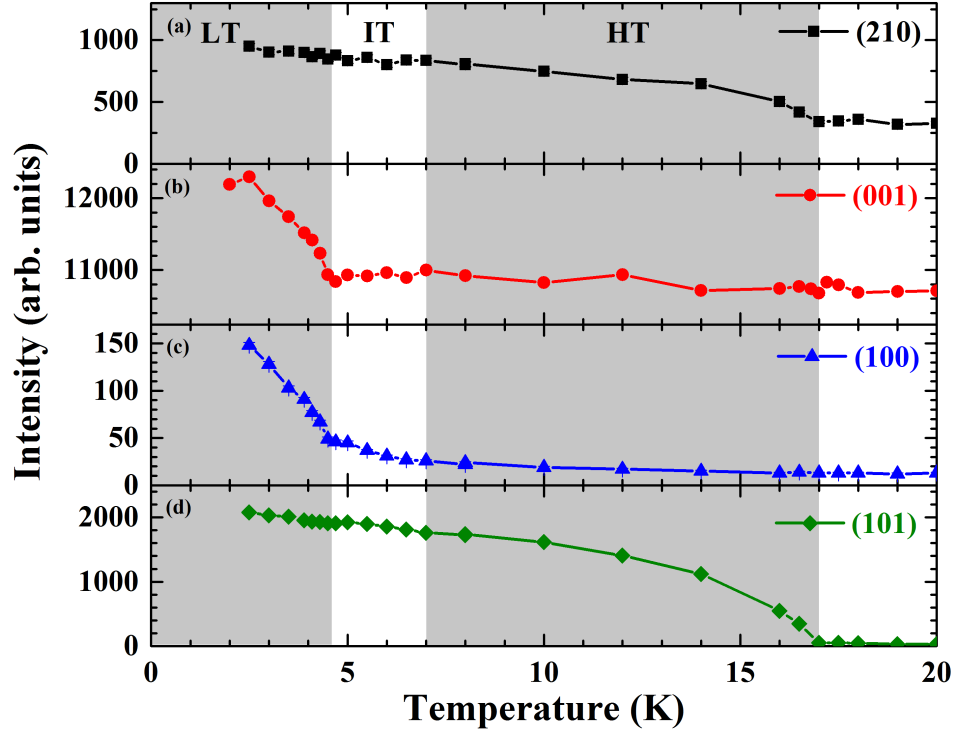


Figure 6.17: Temperature dependence of the intensity of the Bragg reflections allowed by the nuclear symmetry of NdB_4 (a) (210) and (b) (001) and the anti-ferromagnetic reflections (c) (100) and (d) (101). Shading indicates the separate magnetic phases.

can also be observed at 6 K, where the incommensurate peaks are not resolution limited, suggesting that we have short range order. This diffuse scattering has disappeared in the low temperature phase and only the incommensurate reflections remain suggesting there is long range order.

6.2.2 Zero Field Measurements

Integer (hkl) reflection scans

Fig. 6.17 shows the temperature dependence of the intensity of a selection of integer (hkl) reflections. (210) is allowed by the symmetry of the crystal. As can be seen the intensity of the (210) reflection at $T_{N1} = 17$ K, starts to gradually increasing until it levels off in the IT phase. (001) is also allowed by the nuclear symmetry, the intensity remains approximately unchanged throughout the HT and IT phase, while there is a significant increase in the intensity in the LT phase. Interestingly, magnetic intensity on this reflection can only be attributed to a ferromagnetic component in

the ab -plane, however polarised neutron experiments on this sample using the D7 diffractometer, showed no depolarisation of the beam, typical of a ferromagnetic signal as well as no magnetic contribution in the spin-flip channel. This suggests that there is a structural phase transition occurring in the LT phase. (100) and (101) are both purely magnetic reflections, (100) suggests the ordering is antiferromagnetic, in agreement with previous measurements [125]. We can see there is a gradual increase in the HT, with more of an upturn in IT, with an obvious transition into the LT phase. While the (101) reflection intensity, shows a transition into the HT, which increases and levels off into the IT and LT phases. There are a few possibilities for this sudden increase, the first is a structural phase transition to a tetragonal system with a reduced symmetry where the (100) is allowed by the crystal structure. The second possibility is that there is a rearrangement of the magnetic moment, either to different commensurate structure or for the moments to further tilt towards the c -axis. The final option is that both are occurring. The polarised neutron on D7 shows an increase in the intensity of the (100) reflection, showing that there is a magnetic contribution to this increase, ruling out a increase due to purely a structural change.

Incommensurate reflection scans

The temperature dependence of the intensity of a selection of incommensurate reflection is shown in Fig. 6.18. As can be seen (1.85 0.15 0.4) is part of only one set of incommensurate reflections in the intermediate temperature phase. This corresponds to a propagation vector of $(\delta, \delta, \delta')$, where $\delta = 0.15$ and $\delta' = 0.4$. This propagation vector is in agreement to that observed in Ref. [125], where they found $\delta = 0.14$ and $\delta' = 0.4$ instead. In the low temperature phase we observe the appearance of the incommensurate reflections, (0.2 0 0.4), (0.6 0 0.2), (0 0.6 0.4) and (-2 0.18 0.4) these correspond to propagation vector of $q_1 = (\delta', 0, \delta'')$, $q_2 = (\delta'', 0, \delta')$, $q_3 = (0, \delta', \delta'')$, $q_4 = (0, \delta'', \delta')$, where $\delta'' = 0.2$. Due to the tetragonal symmetry of the unit cell, we would expect q_3 and q_4 from q_1 and q_2 respectively as we do not expect there to be a preferred direction between the a and b -axis. However, it is interesting that between q_1 and q_2 we see a swap in δ' and δ'' , as there should be no relation between the a and c -axis. This can be overcome if one set of incommensurate reflections are harmonics of the other set. Looking at intensity maps at 1.5 K (Fig. 6.15(d)), a clearer picture can be seen of the layout of the incommensurate reflections. If the propagation vector is described as $(100) \pm (\delta'', 0, \delta')$, then the reflections that correspond to $(\delta', 0, \delta'')$ can be described as second order harmonics and so forth. This gives us two possibilities:

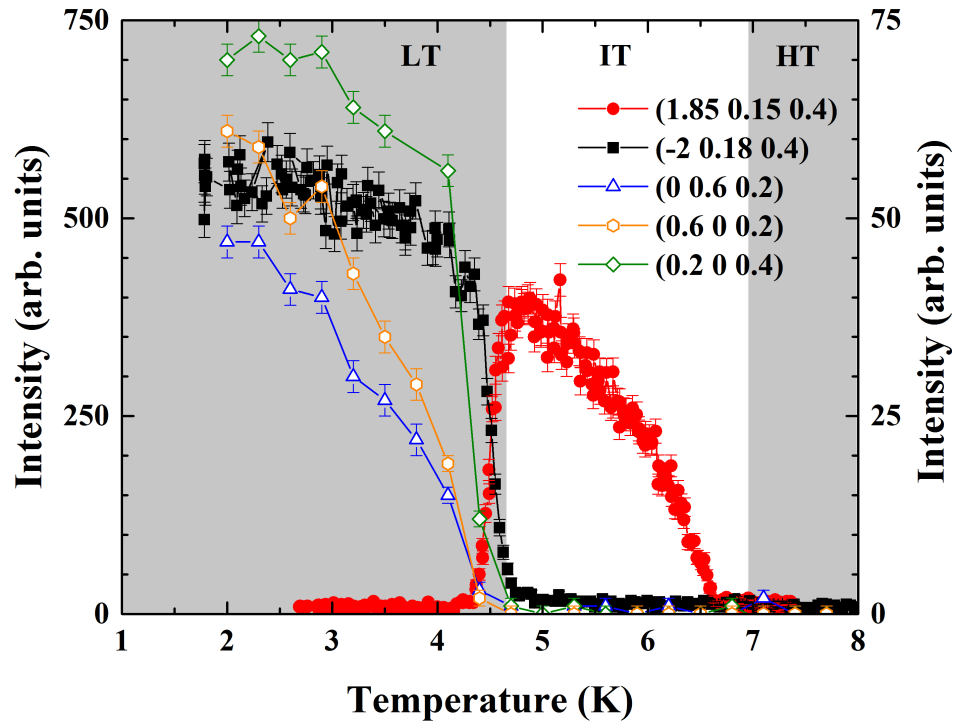


Figure 6.18: Temperature dependence of the intensity of a selection of incommensurate reflections from NdB_4 . Fill symbols corresponding to the temperature ramping and continuously measuring the intensity, while empty symbol correspond to stabilising and measuring the intensity at a particular temperature.

- (1) The (100) is a forbidden nuclear reflection in the LT phase and we have a multi- k magnetic structure formed of q_1 and q_2 .
- (2) Due to a structural phase transition, the (100) reflection is allowed. Then $k = (\delta', 0, \delta'')$ and the other satellites are either 2nd or 3rd harmonics.

Returning to the line cuts made from the intensity maps in Fig. 6.19 we can compare the intensity of the (100) reflection between the three magnetic phases. As can be seen there is a very small increase in the intensity of the (100) reflection in the NSF channel between the HT and IT phase and a similarly small increase in the SF channel. The NSF intensity is approximately 20% the intensity of the SF peak, suggesting it is not arising due to leakage. There is no significant increase between the intensity of the (100) between the IT and LT in the NSF channel, despite the large increase in intensity for the SF intensity, lending strength that it may be a real peak. This suggests that the second option is the correct one. However the increase is very small and D7 is not well suited for intensity measurements, which means we cannot say definitively that this is the case based on a peak that is barely distinguishable from the background and further measurements will need to be made.

6.2.3 Zero Field Magnetic Structure Determination

In order to determine the magnetic structures of NdB₄ a good starting point on the structural parameters is needed. To do this we collected a set of 112 integer (hkl) at $T = 25$ K. As a starting point the parameters from the powder x-ray pattern were used and refined to best match the calculated and observed intensities. The structural parameters were determined from the fit ($R_{\text{Bragg}} = 9.17\%$) and are shown in table. 6.3. These parameters are in agreement with Ref. [124]

High Temperature Phase ($T_{\text{N}2} < T < T_{\text{N}1}$)

For the high temperature phase we found an antiferromagnetic $\mathbf{k} = 0$ commensurate magnetic structure. To determine the magnetic structure we have collected the intensities of a set of 112 integer (hkl) reflections and to find the magnetic intensity subtracted the nuclear intensity from each reflection. There are 12 irreducible representations for a $\mathbf{k} = 0$ structure [55], which are shown in Fig. 6.20. From measurements on D7, we can eliminate the ferromagnetic structures (F, H-1 and H-2) as there was no depolarisation of the neutron beam. In addition we can also eliminate any structures that predict the intensity on the (100) coming from an ab -component

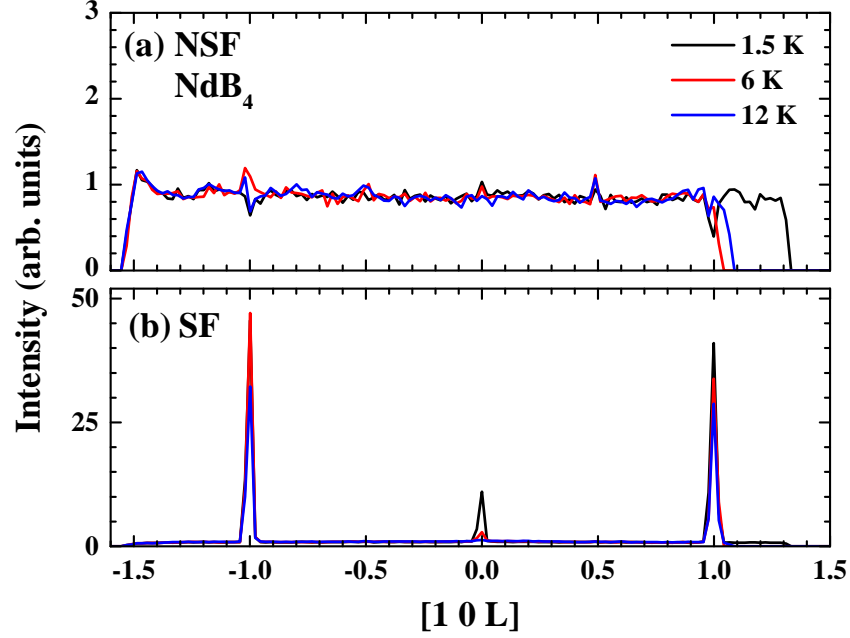


Figure 6.19: Line cuts from along the $[1\ 0\ L]$ direction for NdB_4 taken using the D7 polarised neutron diffractometer. Measurements were made for three temperatures, 1.5, 6 and 12 K using the two channels (a) non-spin-flip and (b) spin-flip.

Space Group: $P4/mbm$			
Lattice Parameters: $a = b = 7.21\ \text{\AA}$, $c = 4.10\ \text{\AA}$			
Ion	Wyckoff Position	Positions	Fractional Coordinates
Nd	$4g$	$(x, x + \frac{1}{2}, 0)$	$x = 0.184$
B1	$4e$	$(0, 0, z)$	$z = 0.205$
B2	$8j$	$(x, y, \frac{1}{2})$	$x = 0.039, y = 0.179$
B3	$4h$	$(x + \frac{1}{2}, x, \frac{1}{2})$	$x = 0.089$

Table 6.3: Fractional coordinates and Wyckoff Positions for each site in NdB_4 , determined through the magnetic refinement of NdB_4 single crystal neutron diffraction pattern.

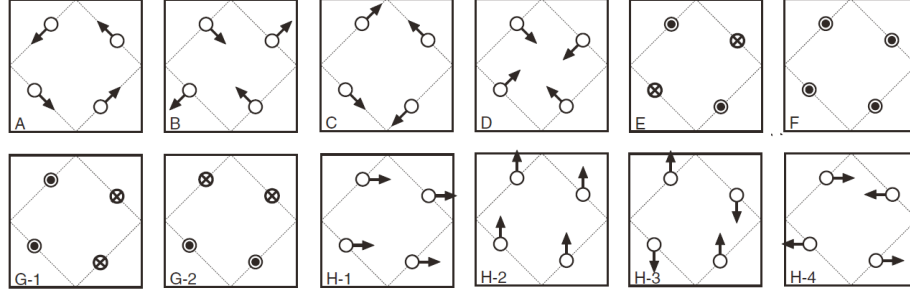


Figure 6.20: The irreducible representations of a $k = 0$ commensurate structure. The picture is taken from ref. [46].

(A, B, H-3 and H-4). This leaves the representations of C, D, E and G. We tried each of the remaining representations and mixture there within to find the best fit. In doing so we found the best fits arose from a combination of D and E or C and E, these are shown in Fig. 6.21(a) and (b) respectively. We have also tried the structure proposed in ref. [125]. This fit is very similar to the other two fits, however our refinements always returned zero tilt in the ab -plane and thus zero intensity on the (100)-reflection. While our ab -plane structure is the same we find the intensity on the (100) is not arising from a tilting of the moments in the ab -plane, but from a tilt of the moments towards the c -axis, which is consistent with what was observed on D7.

As can be seen, the magnetic refinements fail to predict the intensities of a number of different reflections. This was a problem in all the refinements, so in order to investigate this we performed ψ -scans (see section 4.3.1), that is we chose a reflection and rotated around ψ while measuring the intensity. This was to check for the presence of multiple scattering. If there is multiple scattering we would expect to observe a variation in the intensity with rotation around ψ . The ψ -scans for (010) and (050) are shown in Fig. 6.22(a) and (b) respectively. These reflection were chosen to determine if there was a Q dependence to the multiple scattering. As can be seen there is a huge variation in the intensity as a function of ψ , which appears to be random as well as no clear indication of any Q dependence. Further to determine whether this is arising due to the magnetic ordering we performed a small ψ scan at two different temperatures. These are shown in Fig. 6.22(c) and (d). There is no significant temperature dependence between the two suggesting it is due to the sample itself. We currently believe these fluctuations are arising due to significant multiple scattering in the crystal. Due to the large changes in intensity

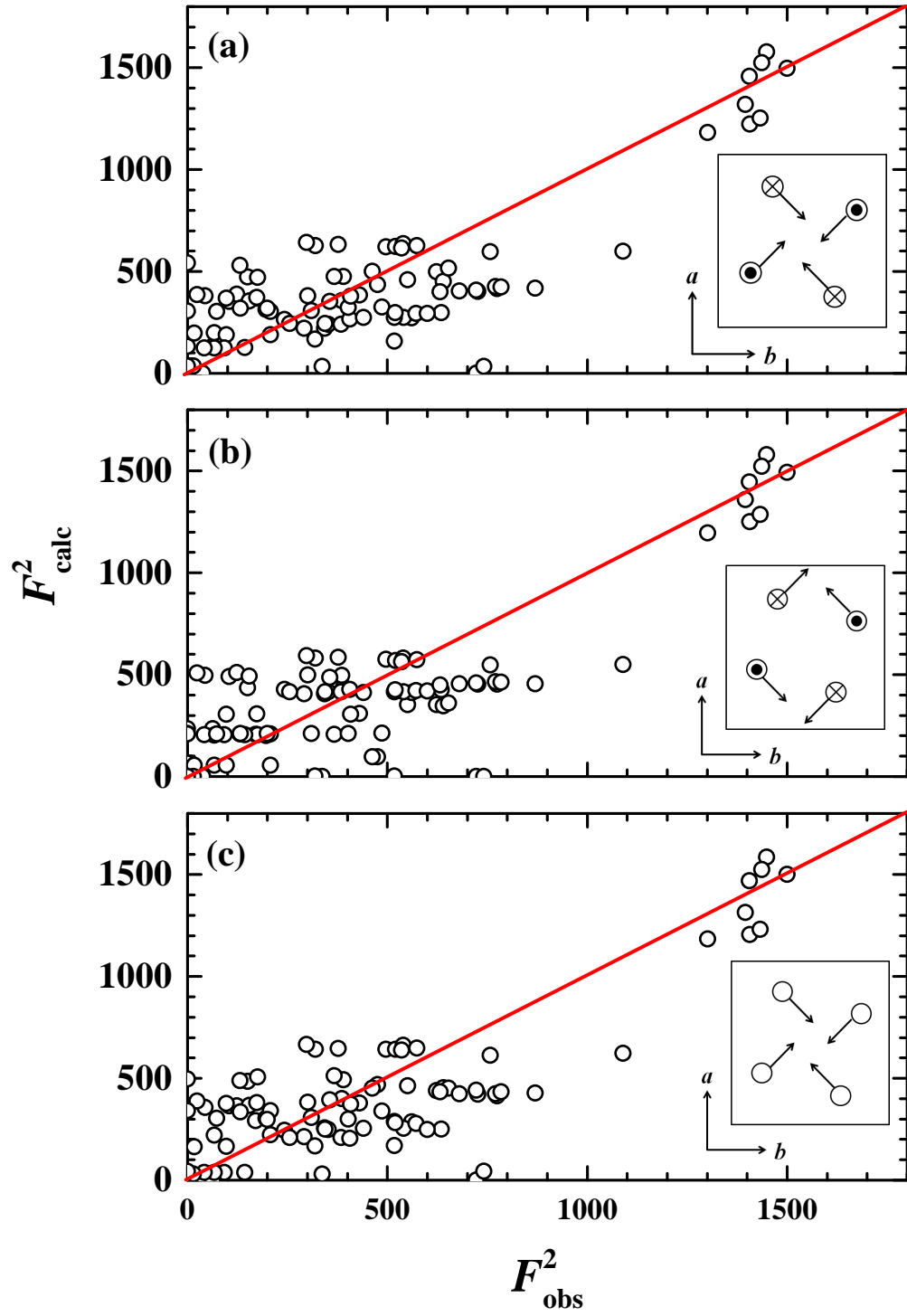


Figure 6.21: Magnetic refinements of 3 separate magnetic structures corresponding to a mixture of two irreducible representations (a) D+E, (b) C+E and (c) D+A. The inset shows the resultant magnetic structure.

at different ψ values, magnetic refinements have become a significant challenge.

Intermediate Temperature Phase ($T_{N3} < T < T_{N2}$)

The intensities of 363 incommensurate reflections corresponding to a propagation vector of $(\delta, \delta, \delta')$ were collected using the D10 diffractometer. From the experiment on D7 we know that the incommensurate reflections are arising from a significant c -axis component. From the irreducible representations calculated from Basireps [128, 129] only one was predominantly along the c -axis and compared the calculated and observed intensities. The best fit ($R_{\text{Bragg}} = 41.34\%$) is shown in Fig. 6.23(a). As can be seen the fit is not particularly good, there is a positive trend with the fit line central to all the points. As with the high temperature phase, multiple scattering and extinction effects are a significant problem in this system. This can be seen in Fig. 6.23(b), where the intensities for each reflection are plotted against $\sin \theta / \lambda$. Reflections and their Friedel pairs, which should nominally have the same intensity dramatically differ, which can be seen as lines of observed intensity at constant values of $\sin \theta / \lambda$. The proposed structure has an amplitude modulation, which propagates along the $[110]$ -direction at an angle of 66.4° to the c -axis. It is more clearly understood, by breaking it down into the three axis. Along the a and b -axis there is a repeating unit cell every 20 unit cells, while along the c -axis, there is a repeating unit cell every five cells. While this is the best fit and is consistent with the polarised neutron measurements. Due to the difficulty in fitting the data due to multiple scattering and extinction, we are unable to definitively say whether or not this is the true magnetic structure and further measurements are needed to clarify this.

Low Temperature Phase ($T < T_{N3}$)

For the low temperature phase we have two components, the commensurate and incommensurate reflections, which were treated separately. First of all considering the commensurate structure we collected a set of intensities of 95 integer (hkl) reflections and performed a magnetic refinement using a mixture of the irreducible representation. The best fit ($R_{\text{Bragg}} = 22.17\%$) shown in Fig. 6.24 was achieved by mixing irreducible representations D and E, comparing the low and high temperature commensurate phase we see that they are formed by the same irreducible representations, however there is a greater c -axis component explaining the increase in the intensity of the (100) reflection in the SF channel.

For the incommensurate structure we collected a set of 120 intensities of

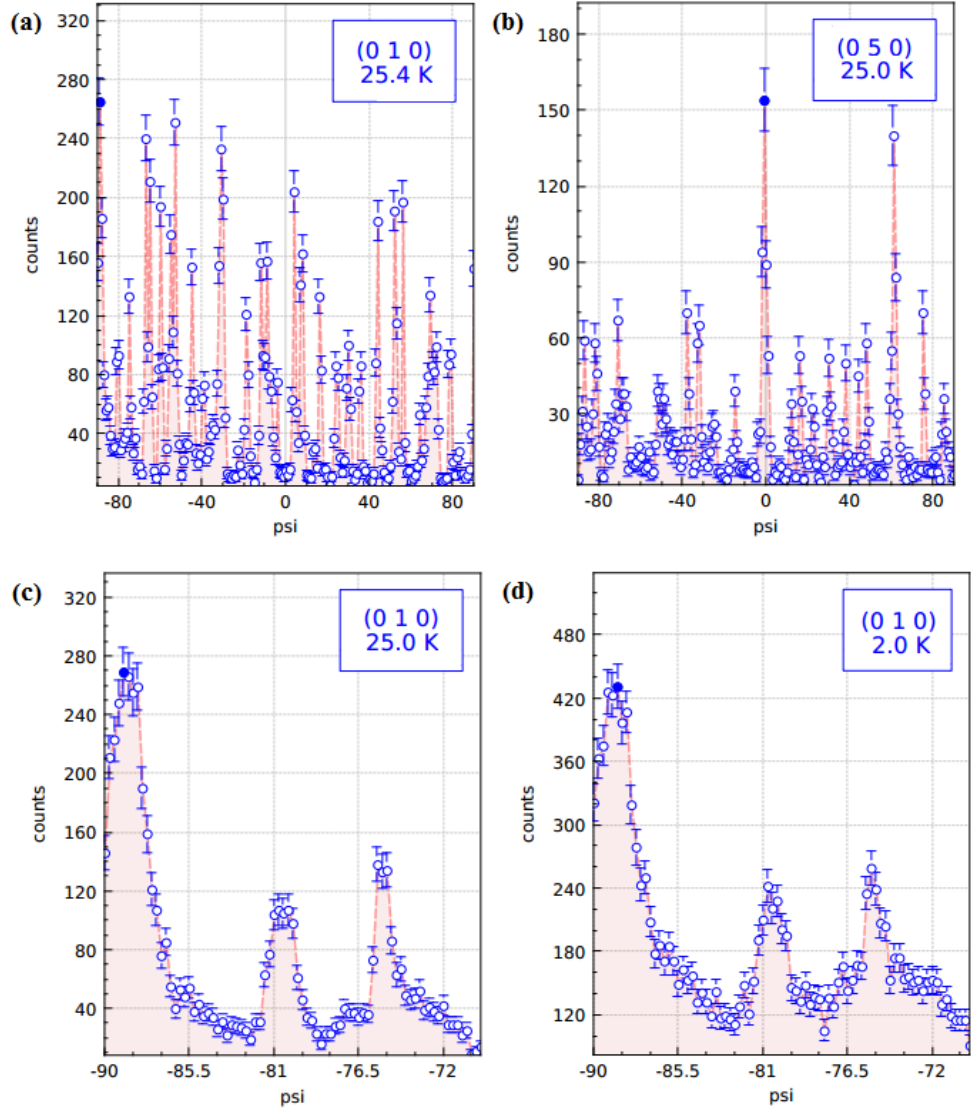


Figure 6.22: psi scans between $\psi = -90$ and 90° at $T = 25$ K for the (a) (010) and (b) (050) reflections. Smaller psi-scans between -90 and -70° were taken for the (010) reflection at (c) 25 K and (d) 2 K.

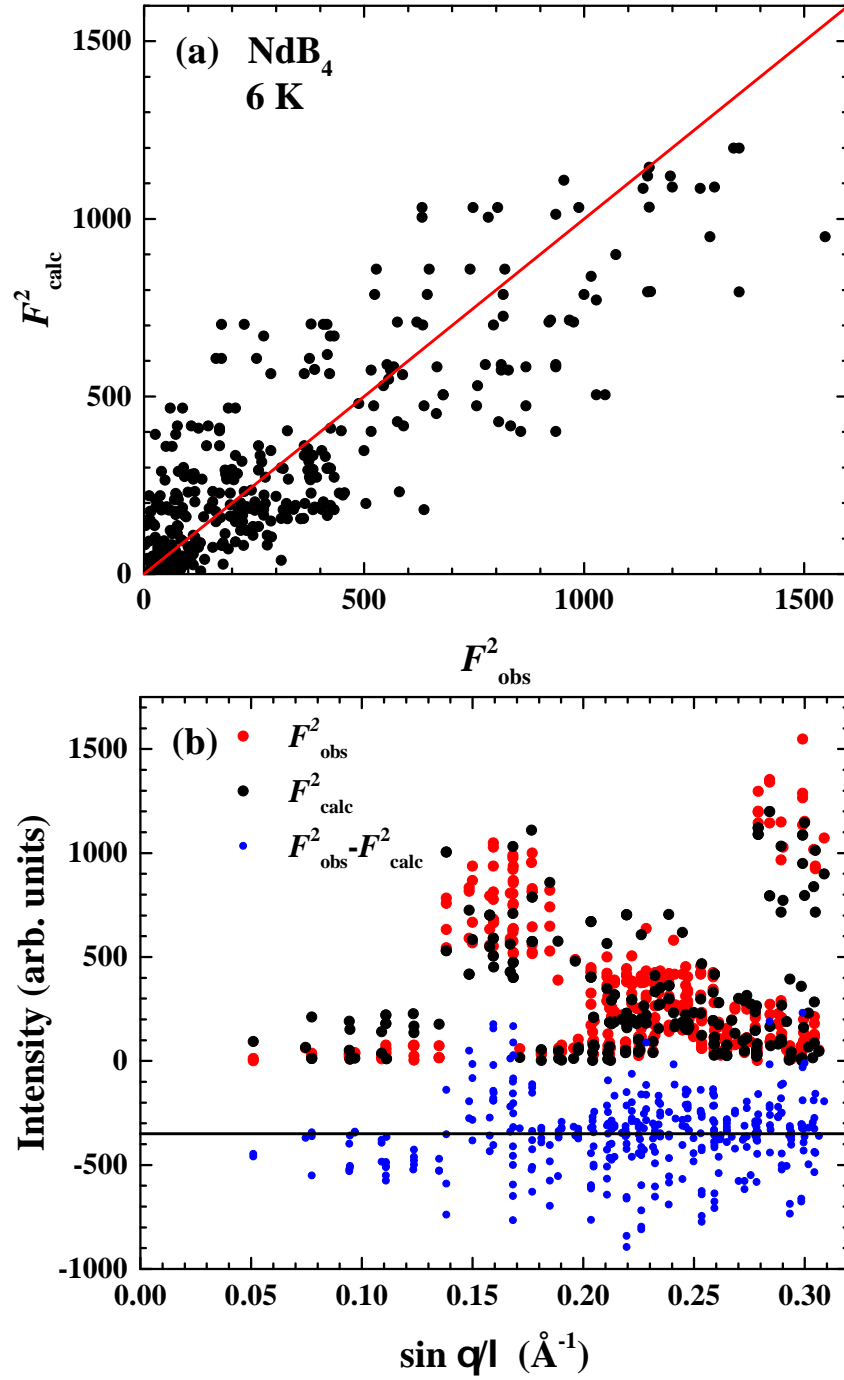


Figure 6.23: Comparison of the observed and calculated intensity for the magnetic refinement of the intermediate temperature phase. (a) is a direct comparison between the two intensity, while (b) plots the intensity of the reflections as a function of $\sin \theta / \lambda$.

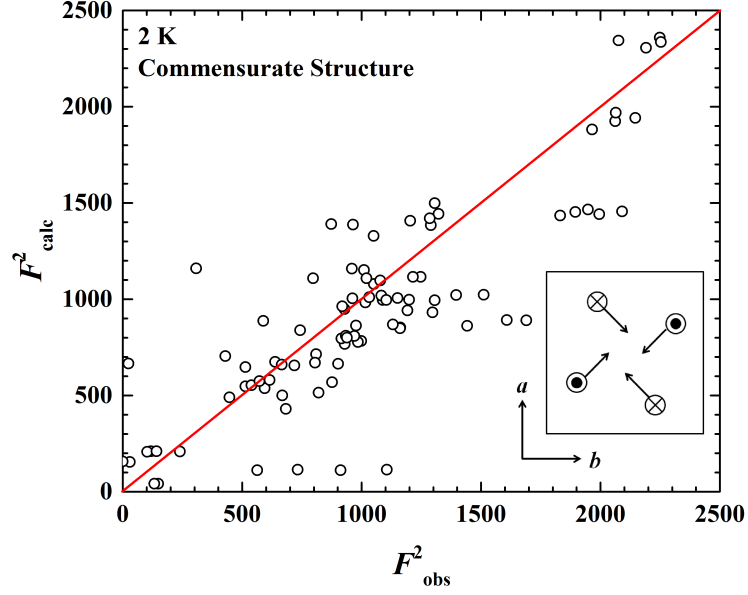


Figure 6.24: Comparison of the observe and calculated magnetic intensities at $T = 2$ K.

incommensurate reflections corresponding to a propagation vector of $(0, \delta'', \delta')$. The best fit ($R_{\text{Bragg}} = 15.62\%$) is shown in Fig. 6.25(a). The magnetic structure is shown in Fig. 6.25(b). The moments are aligned along the c -axis, consistent with the D7 measurements. There is an amplitude modulation along the c -axis, with the moments changing direction between layers. While there is a much broader modulation along the a or b -axis (depending on the propagation vector).

6.2.4 In Applied Magnetic Field

Fig. 6.26(a) shows the temperature dependence of the intensity of the antiferromagnetic (010) reflection and the Bragg (210) reflection in different magnetic fields. As can be seen there is an increase in the intensity at $T = 17$ K, which is present up to 50 kOe, with the transition temperature not changing significantly across this field range. There is a further transition in zero field at 4.9 K, where there is a dramatic increase in the intensity, most likely arising from a re-arrangement of the spins changing the commensurate phase. This phase is no longer present above 20 kOe.

The temperature dependence of the (210) reflection is shown in Fig. 6.26(b). As can be seen there is an increase in intensity at $T = 17$ K, with the onset of antiferromagnetic ordering, this gradually increases and levels off. There is then a

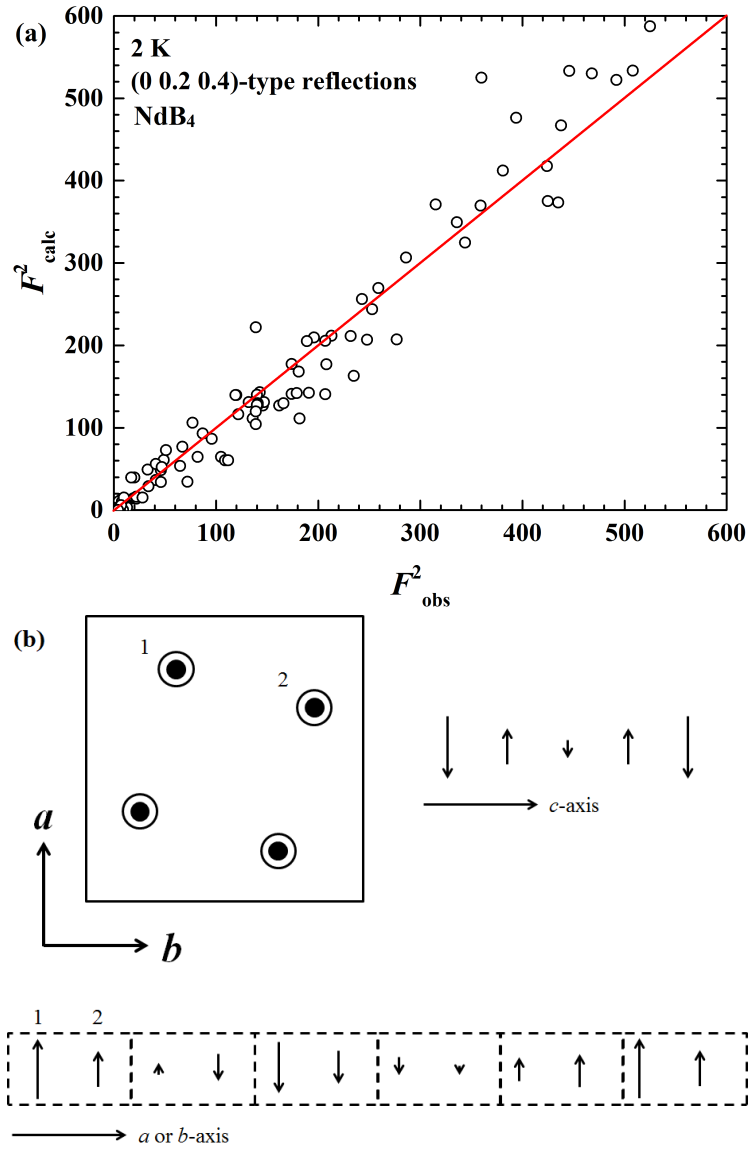


Figure 6.25: Comparison of the observe and calculated magnetic intensities at $T = 2$ K and the incommensurate magnetic structure.

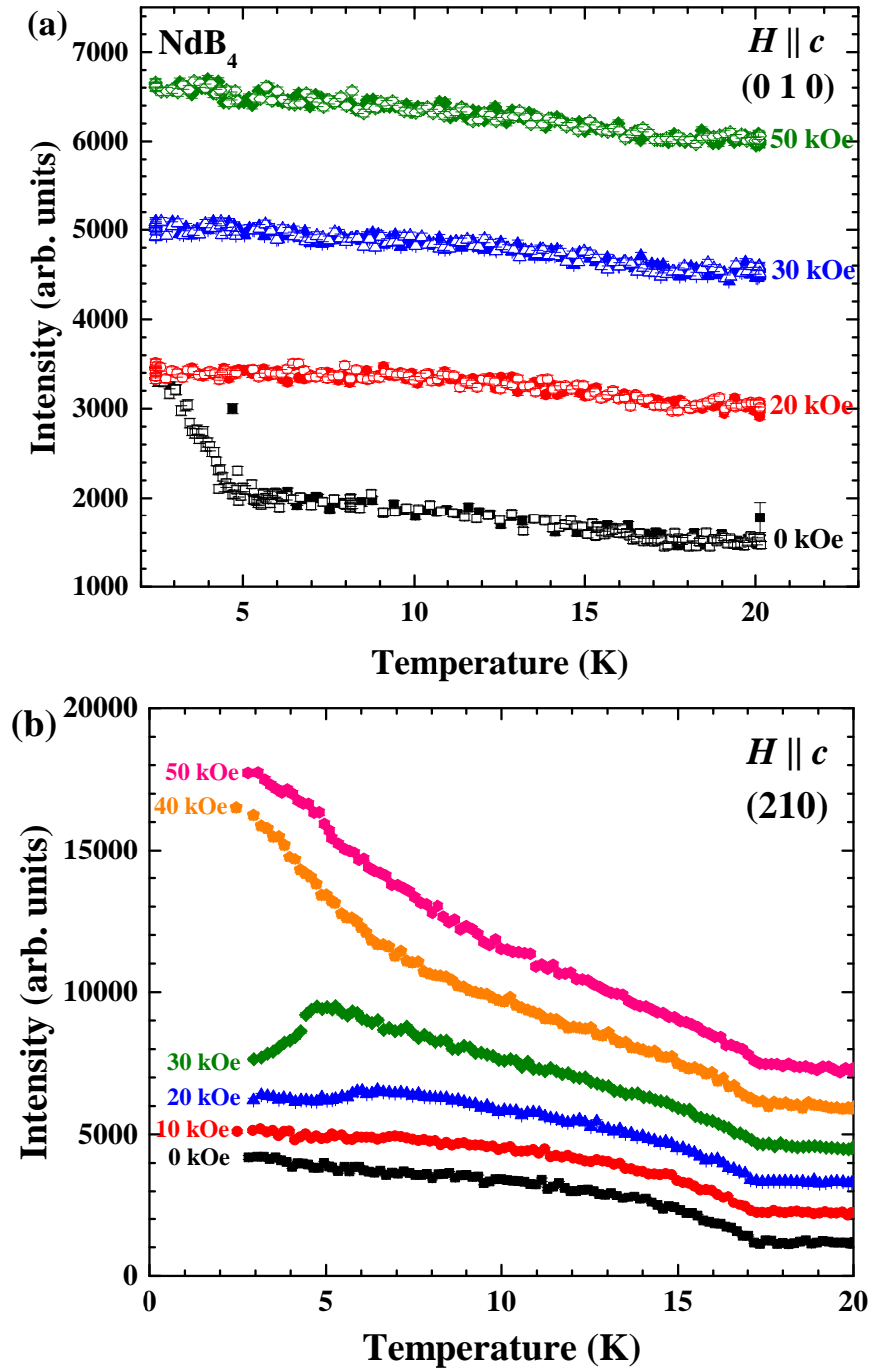


Figure 6.26: Temperature dependence of the intensity of (a) the antiferromagnetic (010) reflection each curve is subsequently offset by 1500 and (b) the Bragg (210) reflection in increasing fields each curve offset subsequently by 1000.

transition observed for 20 and 30 kOe corresponding to a transition to the $\frac{1}{5}$ -plateau, while above 30 kOe, the intensity just increases, suggesting a polarised state. The consistent increase in the intensity of the (210) and the (010) reflection at 17 K suggests the commensurate antiferromagnetic phase that is observed at zero field also permeates in all phases up to 50 kOe.

Fig. 6.27 shows the temperature and field scans of a number of incommensurate reflections. Fig. 6.27(a) shows the $(-1.85 \ 0.15 \ 0.4)$, which is associated with the propagation vector $(\delta, \delta, \delta')$, where $\delta = 0.15$ and $\delta' = 0.4$, this is present only in the intermediate temperature phase. In zero field, we can see the reflection is present between 4.2 and 6.8 K, consistent with the other measurements. Increasing the field to 10 kOe, the region shifts to lower temperature, with the reflections appearing between 4.1 and 6.2 K. Increasing the field to 20 kOe, again the transitions temperature are further suppressed to a temperature range of 3.6 and 5.8 K. Finally at $H = 50$ kOe, the intensity of the incommensurate reflection decreases and is suppressed to the temperature region between 3.1 and 4.1 K. The intensity of the incommensurate region decreases with increasing field, this implies that there is a soft transition where the incommensurate component of the phase gradually becomes polarised and shrinks.

Fig. 6.27(b) shows the intensity of incommensurate reflection corresponding to the low temperature phase. First of all the $(0 \ -1.8 \ -0.4)$ corresponds to the zero field low temperature phase with a propagation vector of $(0, \delta'', \delta')$, where $\delta'' = 0.2$. As can be seen it is present until approximately 13 kOe, giving way to the reflections $(1 \ -2 \ -0.4)$ and $(2 \ 1 \ 0.2)$. Whether these reflections correspond to two separate propagation vectors at $(0, 0, \delta')$ and $(0, 0, \delta'')$ or whether the reflection is a harmonic of the other is not known at present. Both reflection, however, correspond to the unit cell increasing by a factor of 5 along the c -axis. The reflections are present up until 30 kOe, where there is a dramatic decrease in the intensity of both reflections, interesting, there is a small plateau in the intensity, which lasts until 33 kOe, where the intensity decreases to zero. The small plateau corresponds to the small feature observed at $M/M_{\text{sat}} = 0.24$, further supporting that it is a real feature.

6.2.5 Magnetic Phase Diagrams

Figure 6.28 and 6.29 show the magnetic phase diagrams of NdB_4 constructed from magnetisation, heat capacity and resistivity measurements for $H \parallel c$ and $H \perp c$.

For $H \parallel c$, Fig. 6.28(a) the magnetic phase diagram contains five distinct magnetically ordered phases (labelled with roman numerals I to V) as well as a

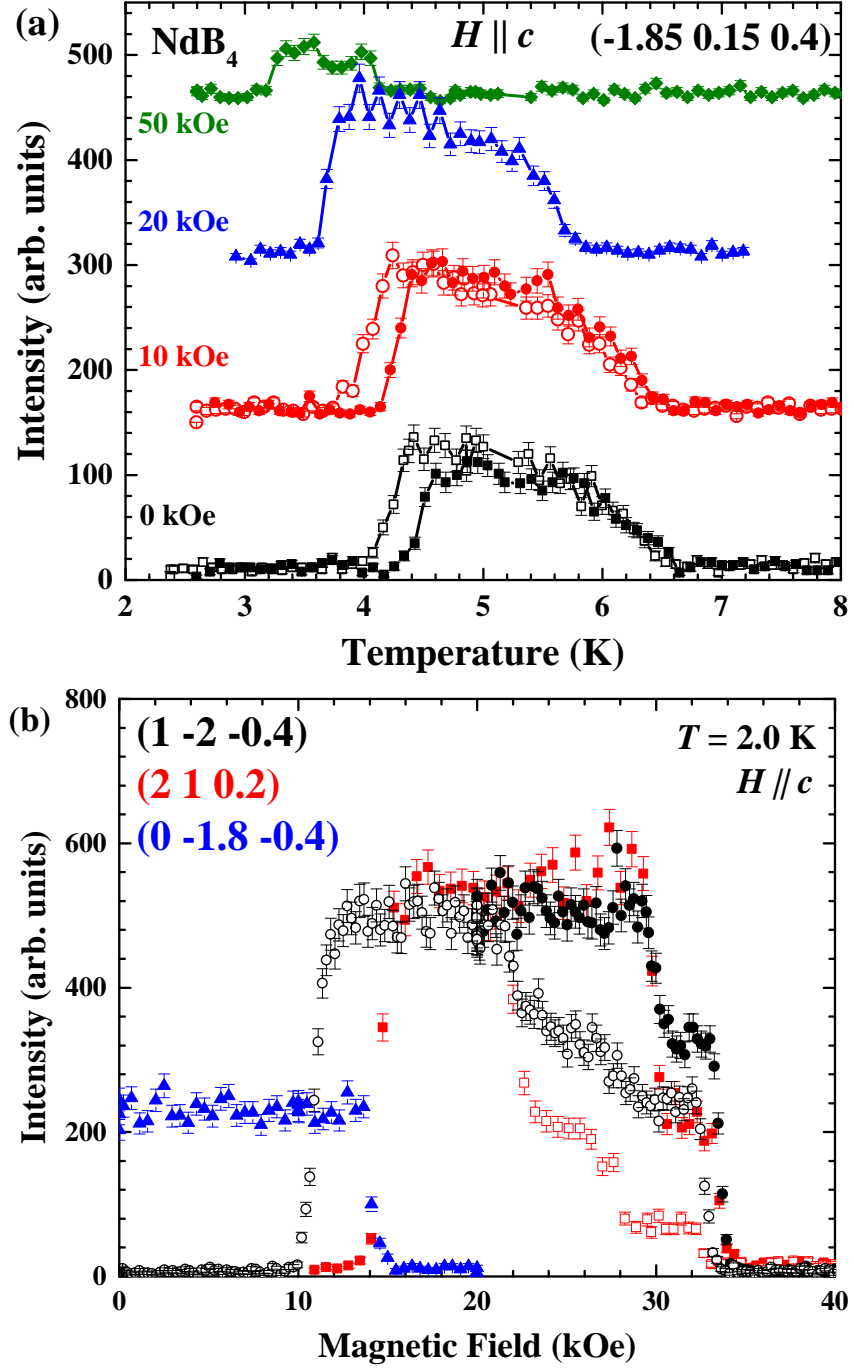


Figure 6.27: (a) Temperature dependence of the intensity of incommensurate $(-1.85 \ 0.15 \ 0.4)$ reflection present in the intermediate temperature phase. (b) Field dependence of the intensity of incommensurate reflections in the low temperature phase.

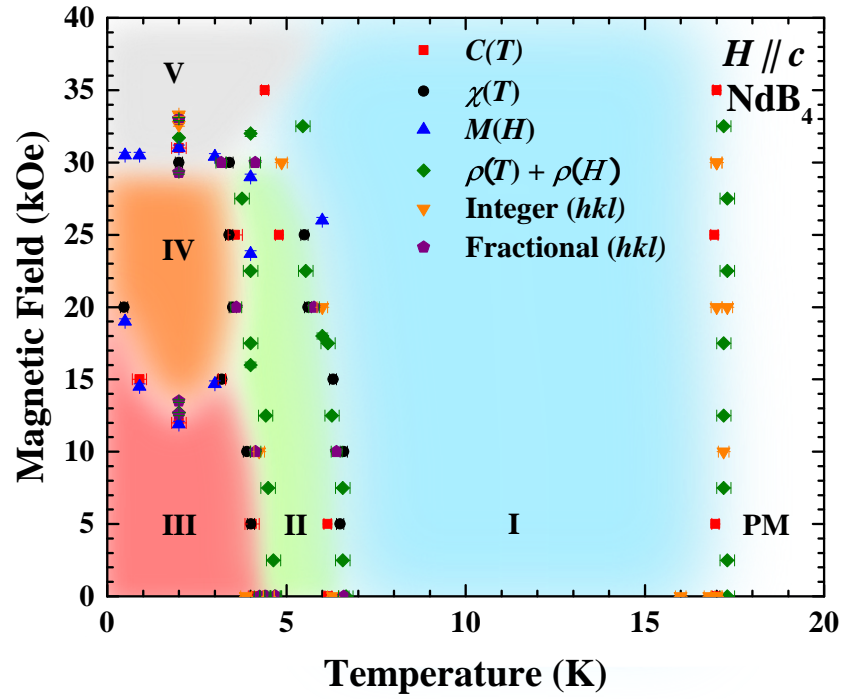


Figure 6.28: Magnetic phase diagram of NdB_4 for $H \parallel c$ constructed from neutron diffraction data for different reflections (inverted triangles and pentagons), and magnetisation (circles and triangles), resistivity (diamonds) and heat capacity (squares) measurements. All field dependent measurements were made by ramping the field up. The different magnetic structures is denoted with roman numerals.

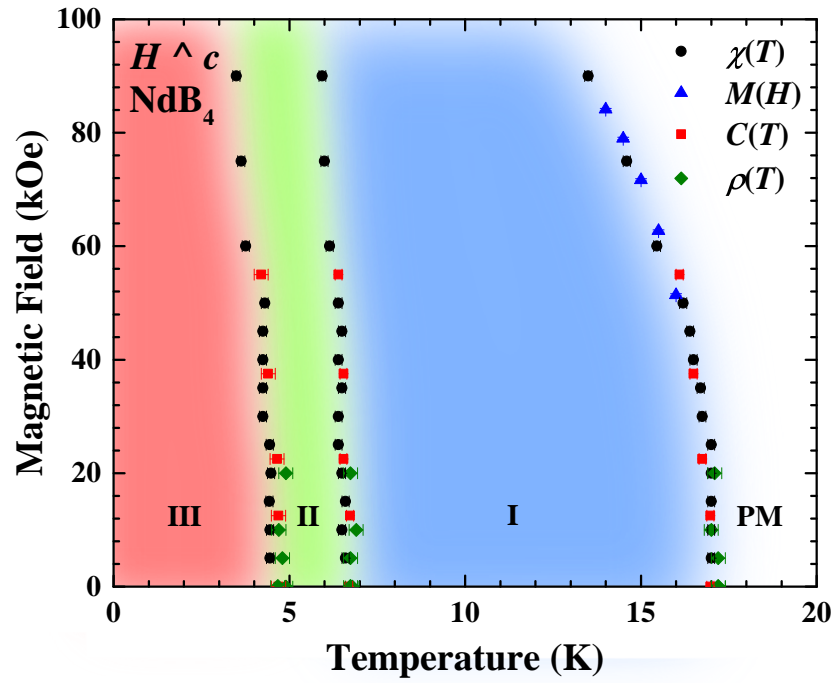


Figure 6.29: Magnetic phase diagram of NdB_4 for $H \perp c$ constructed from magnetisation (circles and triangles), resistivity (diamonds) and heat capacity (squares) measurements. All field dependent measurements were made by ramping the field up. The different magnetic structures is denoted with roman numerals.

paramagnetic (PM) phase. The high-temperature phase I remains largely unaffected by application of a magnetic field. The magnetisation curves suggest no sign of saturation up to 100 kOe. The incommensurate intermediate temperature phase II seems to disappear in fields above 30 kOe. The low-temperature zero-field phase III transforms to phases IV and V in an applied field with the unusually shaped magnetic transition line between phases III and IV showing a clear minimum at approximately 2 K. Phase V corresponds to the fully polarised phase.

For $H \perp c$, the phase diagram (Fig. 6.29) contains three distinct ordered states (labelled with roman numerals I to III) as well as the PM phase. Apart from a slight reduction of the transition temperatures (particularly for the PM to the phase I transition) on application of magnetic field, all three ordered phases remain largely unaffected by application of magnetic field. This is further re-enforced with by the high field measurements up to 500 kOe, which for the $H \perp c$ shows no indication of saturation in phases I and III. As the small “kink” is present in the high field magnetisation curves for both the low and high temperature phase, implies that the transition is associated with the commensurate structure and is not involved in loss of the incommensurate structure. It could be the case that that gradual transition observed in the high field measurements is the system gradually tending towards a purely commensurate phase. However without further measurements to determine the high field structure no concrete conclusion can be drawn.

6.3 Inelastic Neutron Scattering

6.3.1 $E_i = 12$ meV

Inelastic neutron scattering measurements were made on NdB₄ using MARI at ISIS. Figure 6.30 shows the colour intensity plots at 5, 10 and 20 K. These correspond to the IT, HT and paramagnetic phases. A CCR was used during the experiment and was unable to achieve temperatures below 5 K, so we were unable to investigate the LT phase at present. The three intensity plots show two main features, the first is the elastic line, the second is an energy level centred on approximately 4.5 meV at 5 K. Increasing the temperature, the energy level becomes less dispersive at 10 K and further 20 K. The final temperature sees a shift in the energy level to approximately 3 meV. The intensity of energy level present in all three temperatures remains constant with Q , suggesting they are crystal field levels.

In order to more accurately determine the energy of the crystal field as well as track the temperature dependence of the features we have taken line cuts at $Q = 1.5 \pm 0.5 \text{ \AA}^{-1}$. Figure 6.31 shows the energy transfer for NdB₄ at different

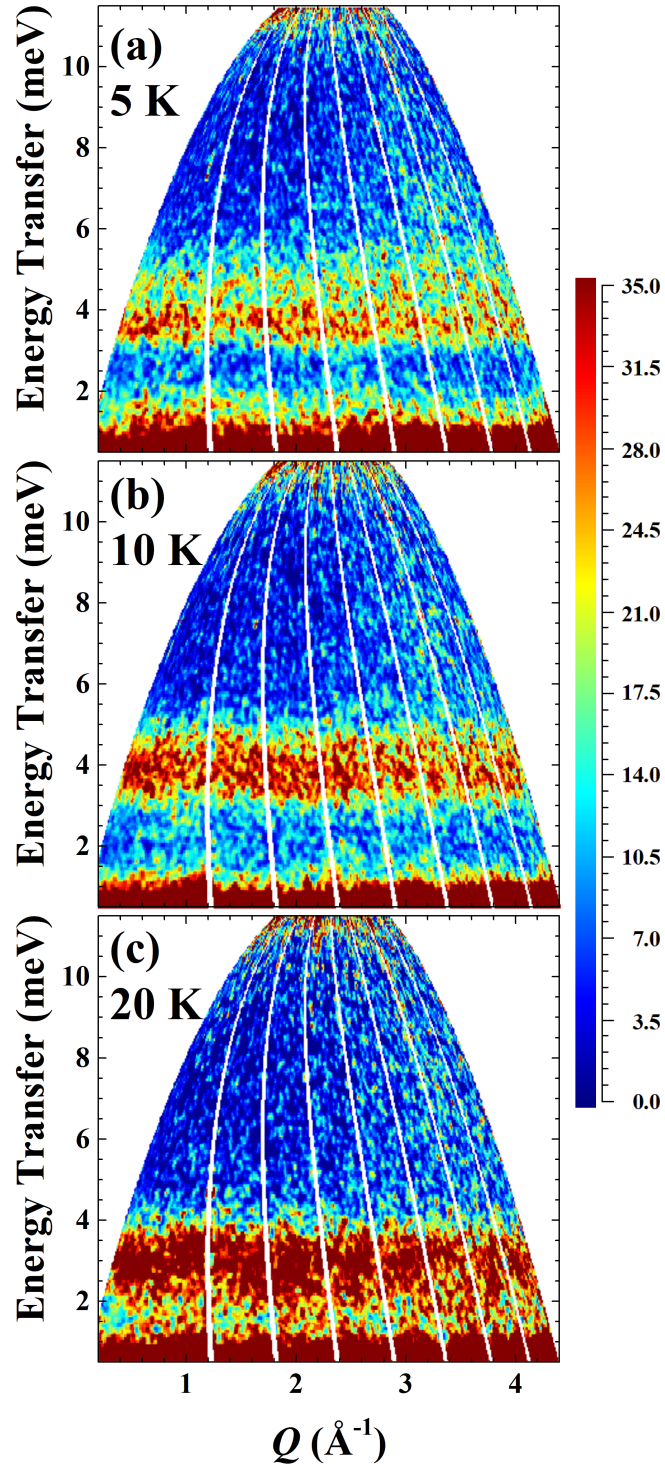


Figure 6.30: Colour intensity plots from inelastic neutron measurements on NdB₄. Each measurement was taken in a different magnetic phase (a) IT at 5 K, (b) HT at 10 K and (c) the paramagnetic regime at 20 K using an incident energy of 12 meV.

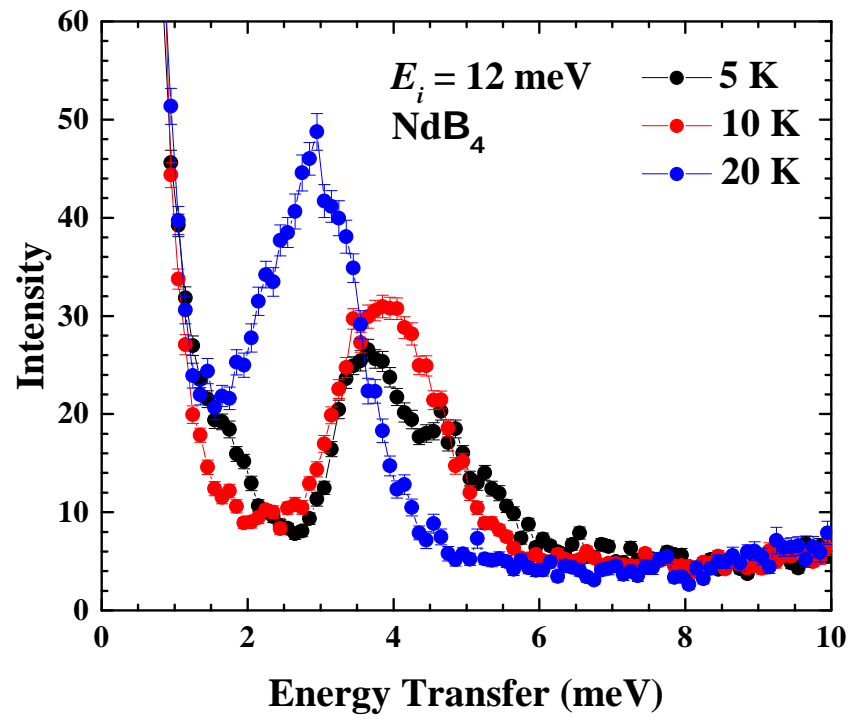


Figure 6.31: Dynamic susceptibility of NdB_4 taken at temperatures between 5–20 K using an incident energy of 12 meV.

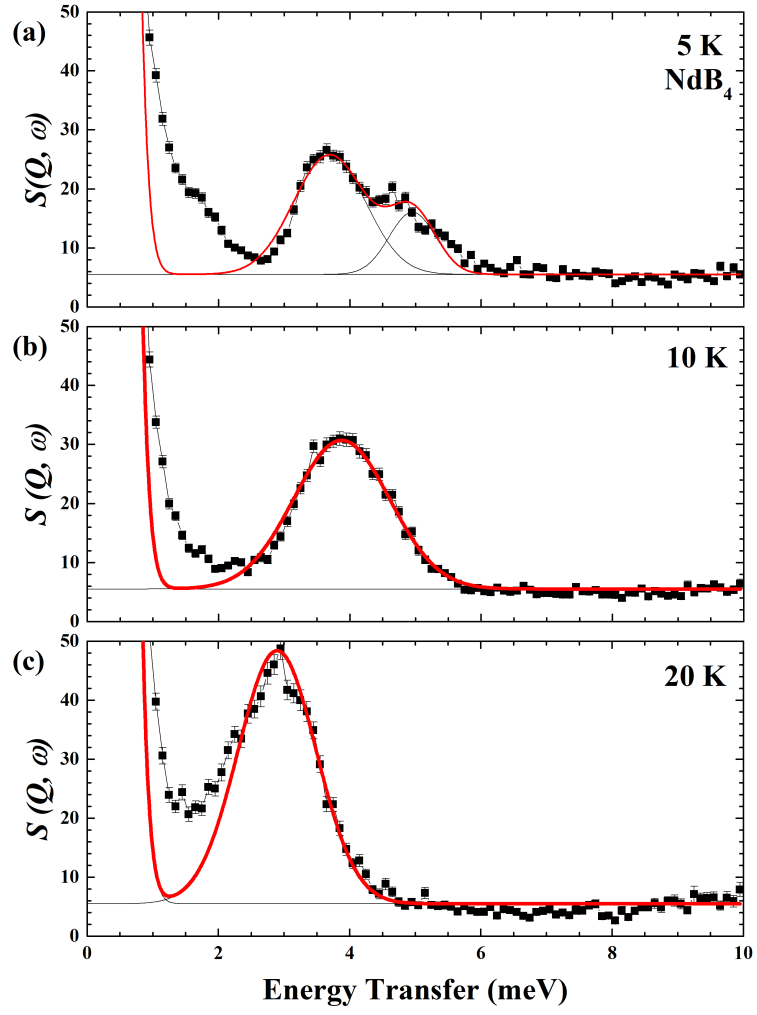


Figure 6.32: Gaussian fits of $S(Q, \omega)$ of NdB_4 in a range of temperatures with an incident energy of 12 meV. Blue peaks correspond to crystal field levels, while green peaks correspond to secondary transitions from thermally populated energy levels.

temperatures with an incident energy of 12 and 24 meV. As NdB_4 is a Kramer ion, we are expecting five doublet energy levels. Beginning with an incident energy of 12 meV, there are two energy levels with energies 3.6 and 5 meV at 5 K (Fig. 6.31(a)). These are most likely arising due to energy level splitting from the onset of magnetic order in the system. There is also a shoulder to the elastic line at around 1.5 meV. Increasing the temperature to 10 K, the splitting is no longer obvious and the shoulder has disappeared. Increasing the temperature further to 20 K into the paramagnetic phase the single peak shifts to lower energies of 2.9 meV. As can be seen the peak shape is a little unusual, possibly due to two overlapping energy levels.

6.3.2 $E_i = 24 \text{ meV}$

The incident energy was changed to 24 meV and the colour intensity maps are shown in Fig. 6.33. As for an incident energy of 12 meV, three of the magnetic regimes were investigated; The IT (5 K) and HT (10 K) and the paramagnetic regime (20–150 K). At 5 K (Fig. 6.33(a)) there are three main lines approximately situated at 4, 14 and 18 meV. These features are mirrored in the measurements taken at 6 K (Fig. 6.33(b)). Further warming into the paramagnetic phase, the crystal field level at 4 meV has become more dispersive, while the energy level at 14 meV has shifted to 12 meV. At 50 K a line is starting to appear at around 19 meV, which is like a secondary transition from the thermal population of lower energy crystal field level. There is then a “blob” of intensity at high Q at around 7 meV. This is generally characteristic of phonons. These features are also present for 100 and 150 K, which are shown in Fig. 6.33(e) and (f) respectively.

As before we have taken line cuts at $1.5 \pm 0.5 \text{ \AA}^{-1}$ to track the features more accurately. We can again see the peak at low energy, but there is also a well defined peak at 12.47 meV, which is most likely due to a second crystal field level. There is a third peak where the intensity increases up to 150 K, it is difficult to determine whether this is arising due to population of the either the first or second energy level so it could suggest a crystal level at either 17.72 or 27.57 meV. There is also an increase in the intensity of the background at around 5 meV, so it is more likely that there is a crystal field level at 17.72 meV, but with the present data we are unable to determine this for sure.

6.3.3 $E_i = 110 \text{ meV}$

Figure 6.36 shows the colour intensity maps using an incident energy of 110 meV at 5 and 20 K. Figure 6.36(a) shows the measurements taken in the magnetic IT phase.

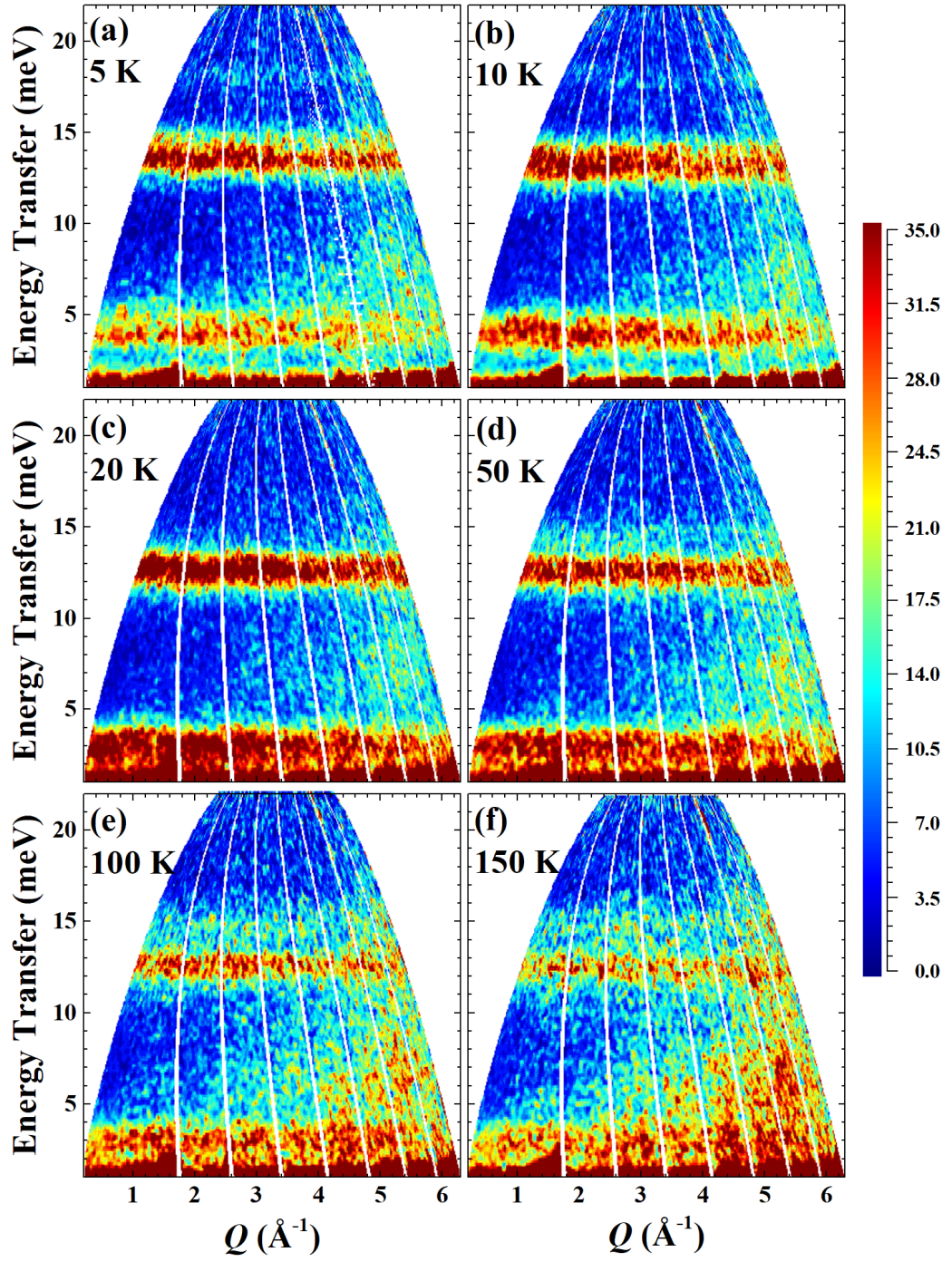


Figure 6.33: Colour intensity plots from inelastic neutron measurements on NdB_4 . Each measurement was taken in a different magnetic phase (a) IT at 5 K, (b) HT at 10 K and the paramagnetic regime at (c) 20 K, (d) 50 K, (e) 100 K and (f) 150 K using an incident energy of 24 meV.

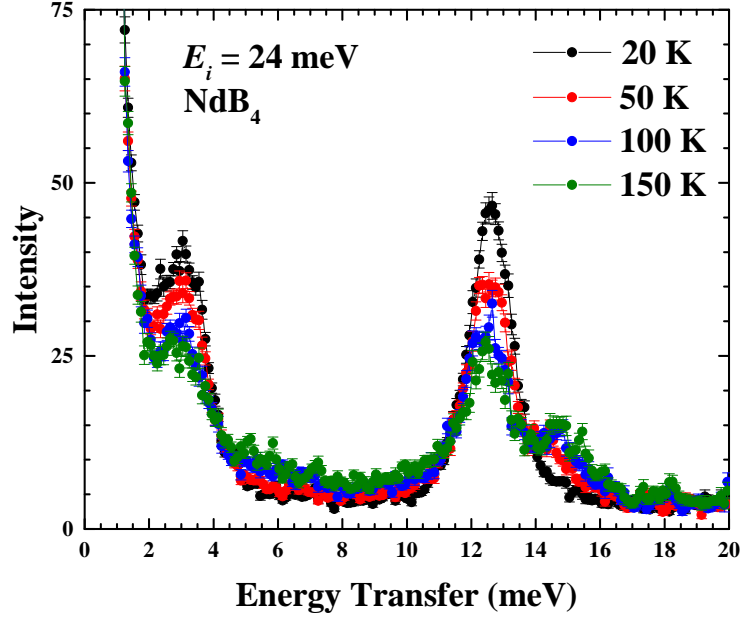


Figure 6.34: Dynamic susceptibility of NdB_4 for temperatures between 20–150 K using an incident energy of 24 meV.

There are a number of features in the plot. There is an energy level at approximately 17 meV, which was observed for an incident energy of 24 meV. There are further features at approximately 20, 40, 70 and 90 meV. The intensity of these latter features increases with Q , which is characteristic of phonons. The paramagnetic regime at 20 K is shown in Fig. 6.36(b). The features observed at 5 K are also present at 20 K, with no apparent changes to the intensity. There are no more apparent crystal field levels at higher energies. From the three incident used, we have found the presence of phonons at 20, 40, 70 and 90 meV. This would gives us 3 of the 4 transitions we are expecting, with energies $E = 2.9, 12.5$ and 17.7 meV. The Schottky anomaly observed in the heat capacity correspond to an energy of 10.3 meV, which we do not observe in the inelastic neutron scattering data. This gap is similar to that between the first and second energy level and could be arising due to a transition after the first energy level has become populated. With this energy level included we have a possibility of the 4 transitions we would expect to observe, however further modelling and refinement is needed.

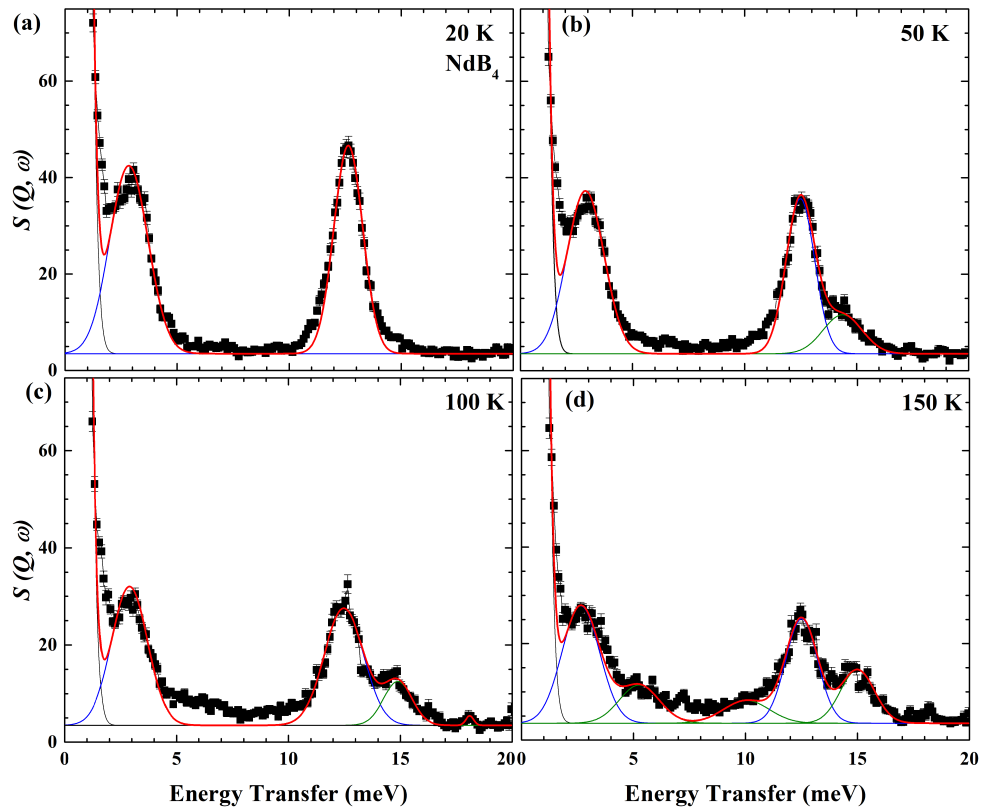


Figure 6.35: Gaussian fits of $S(Q, \omega)$ of NdB_4 in a range of temperatures with an incident energy of 12 meV. Blue peaks correspond to crystal field levels, while green peaks correspond to secondary transitions from thermally populated energy levels.

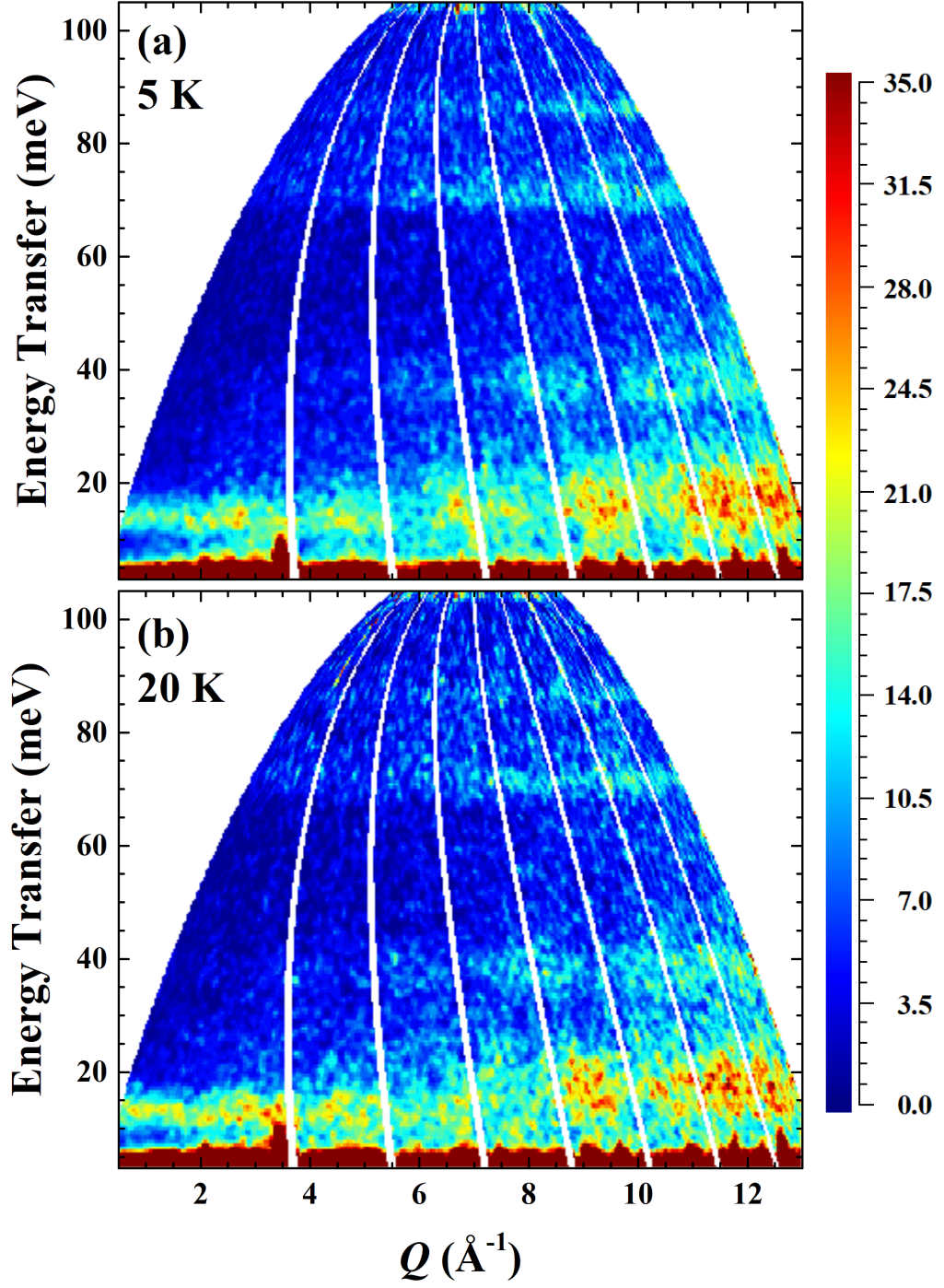


Figure 6.36: Colour intensity plots from inelastic neutron measurements on NdB₄. Each measurement was taken in a different magnetic phases (a) IT at 5 K and (b) the paramagnetic regime at 20 K using an incident energy of 110 meV.

6.4 Summary

An investigation into the magnetic properties on the frustrated antiferromagnet NdB_4 has been presented in this chapter. Magnetic susceptibility and heat capacity measurements have revealed the presence of three magnetic phase transitions at 17.0, 6.9 and 4.2 K respectively and are in line with those presented in ref. [44]. For both $H \parallel c$ and $H \perp c$ the inverse magnetic susceptibility shows Curie-Weiss behaviour at high temperatures and the effective moment was found to be $3.73\mu_B$ and $3.76\mu_B$ while the Curie-Weiss temperatures were -15.9 and -27.4 K strongly suggesting the presence of antiferromagnetic exchange, as is the case for most of the members of the RB_4 family.

Neutron diffraction measurements have revealed the appearance of the (100) reflection further supporting antiferromagnetic ordering. Magnetic refinements have suggested that the magnetic structure has an all-in structure where the moments point into the square formed by the Nd ions. The intensity of the (100) is arising due to an out of plane antiferromagnetic component which is at odds with the commensurate structure put forward by ref [125]. This commensurate structure is prevalent through all three magnetic phases, where the intermediate and low temperature phases also has an incommensurate component too. The ordering is in a single unit cell and can be described with a J_1 and J_2 exchange interaction and thus by the SSL. This structure is very similar to the other members of the RB_4 family, which in zero field tend to order in plane, with no expansion of the magnetic unit cell compared to the crystallographic unit cell [46, 61, 62, 66].

The intermediate temperature phase has a propagation vector of $(\delta, \delta, \delta')$, where $\delta = 0.15$ and $\delta' = 0.4$. Magnetic refinements revealed there was an amplitude modulation along the [110] direction at an angle of 66.7° to the c -axis with all the moments point parallel to the c -axis, which is supported by polarised neutron measurements on D7. Further experiments on the polarised neutron diffractometer, D3 performed by Navid Qureshi also support this, finding that the reflections arising from the propagation vector of $(\delta, \delta, \delta')$ had only a c -axis component.

In the low temperature phase we observe a separate set of reflections arising from the propagation vectors $(\delta'', 0, \delta')$ and $(\delta', 0, \delta'')$. There is still some uncertainty arising from the propagation vector for this incommensurate component in the low temperature phase. There are two possible options, first of all there is a multi- k structure with the two vectors list above, the second option is structural phase transition allows a nuclear component to the (100) reflection and all the reflections can be described with a propagation vector of $(\delta'', 0, \delta')$. There is evidence

for a structural phase transition due to an increase in the intensity of the (001) reflection, which due to symmetry arguments cannot have any magnetic intensity on it unless it is ferromagnetic. This is further supported by measurements on D7 and D3. Measurements on the (100) reflection using D3 have also been inconclusive, there appears to be magnetic and nuclear signal, but the nuclear component is small and could be arising due to multiple scattering. Treating the two propagation vectors separately the magnetic refinements revealed the incommensurate component is along the c -axis and has an amplitude modulation along the c -axis and a much broader modulation along the a -axis. This is supported by measurements on D7 and D3 and measurements on these instruments suggest the other set of incommensurate reflections has a very similar component, lending strength to the second option of the propagation vector. However, further measurements are needed for a conclusive answer. Magnetically induced lattice distortions have also been observed in HoB_4 [46], TbB_4 and ErB_4 [130].

Field dependent magnetisation measurements have revealed the presence of a magnetisation plateau at $\frac{1}{5}$ the saturation magnetisation. The nature of this field induced phase remains undetermined. However, neutron diffraction measurements revealed it had a propagation vector of $(0, 0, \delta'')$ and similar to HoB_4 there is an expansion of the magnetic unit cell along the c -axis. This again suggests the interplanar interactions are important and the SSL is not well suited to describing the physics of NdB_4 . NdB_4 is unusual in that it shares no other fractional plateaux with the other members of the RB_4 family, most having either a $\frac{1}{3}$ or $\frac{1}{2}$ plateau. In addition, to date, no theoretical study has predicted the presence of a $\frac{1}{5}$ -plateau. The nature of this field induced phase still remains undetermined and magnetic refinements have offered no insight into the magnetic structure.

Finally we have investigated the crystal field scheme of NdB_4 . Inelastic neutron scattering measurements have revealed the presence of three crystal field levels at 2.9, 12.5 and 17.7 meV, while heat capacity measurements show a Schottky anomaly, which implied a further transition at 4.5 meV. This would be in line with the five doublets we are expecting from the maximum entropy, but further determination of the crystal field parameters and modelling is needed before we can definitively confirm this is the crystal field scheme.

Chapter 7

Conclusion

Since the initial characterisation by Buschow *et al.* [47], the RB_4 family has offered a rich variety of magnetic phases, order and later a chance to study the physics of the Shastry-Sutherland lattice as it is a rare experimental realisation of the lattice. In this thesis, the results of an investigation into the magnetic properties of two geometrically frustrated compounds, HoB_4 and NdB_4 , has been presented. The structure of RB_4 compounds consists of a R^{3+} sublattice ions, which forms a network of squares and triangles. This network topologically maps to the Shastry-Sutherland lattice, however the applicability of the Shastry-Sutherland lattice has come into question with the neutron diffraction experiments on both HoB_4 and NdB_4 revealing interplanar interactions are important. To date HoB_4 and NdB_4 are the only members of the RB_4 family, where the field induced phases do not order in the ab -plane. HoB_4 and NdB_4 has a magnetic structure in field that propagates along the c -axis with propagation vectors of $(0, 0, \frac{1}{3})$ and $(0, 0, 0.2)$ respectively.

HoB_4 single crystal samples were grown and the crystals have been characterised by bulk property measurements and these have revealed a wealth of magnetic phases and anisotropic behaviour. The field dependent magnetisation measurements at low temperatures show the presence of plateaux at $\frac{1}{6}$, $\frac{1}{3}$, $\frac{3}{5}$ and the newly discovered $\frac{1}{2}$. Single crystal neutron diffraction measurements revealed that the $\frac{1}{6}$ corresponds to the re-establishment of the zero-field incommensurate magnetic structure with propagation vector of $(\delta, \delta, \delta')$ where $\delta = 0.02$ and $\delta' = 0.43$. The $\frac{1}{3}$ -plateau phase was found to have a propagation vector of $(0, 0, \frac{1}{3})$ and magnetic refinements revealed the structure to be ferrimagnetic with layers of ferromagnetic spins arranged in an up-up-down structure along the c -axis. The $\frac{3}{5}$ was found to be accompanied by a field induced structural phase transition, however the nature of this transition as well as the magnetic structure remain undetermined. We currently

have plans to perform powder x-ray diffraction measurements in an applied magnetic field to determine the nature of this phase transition and further single crystal x-ray diffraction measurements. Once these experiments have been performed, the structure can be accounted for and the magnetic structure of the $\frac{3}{5}$ plateau phase determined. Finally the magnetic structure of the $\frac{1}{2}$ remains a mystery and further neutron diffraction measurements to be performed. However due to the phases proximity of the $\frac{1}{2}$ phase to the $\frac{3}{5}$ phase, the field induced structural change may also be a problem.

NdB₄ single crystal samples were grown and the crystals have been characterised by bulk property measurements, and these have revealed a rich phase diagram with three distinct zero field phase and a single field induced phase which corresponds to $\frac{1}{5}$ the saturation magnetisation. The zero field phases were studied with single crystal neutron diffraction measurements revealed the high temperature phase has a $\mathbf{k} = 0$ structure, which is prevalent through all phases. The structure of which has an “all-in” arrangement where the spins point to into the square formed by the Nd ions in the basal plane, the antiferromagnetic reflections arising from a c -axis component. This and HoB₄ align very well with the other members of the RB_4 , where the predominant ordering is non-collinear in the ab -plane. The intermediate temperature phase was found to have a propagation vector of $(\delta, \delta, \delta')$, where $\delta = 0.15$ and $\delta' = 0.4$. While the propagation vector in the low temperature phase of NdB₄ remains an open question current evidence suggests that there is a structural phase transition and the propagation vector is $(\delta', 0, \delta'')$, where $\delta'' = 0.2$ and further reflection arising are due to higher order harmonics. There are a number of avenues open to confirming this. As the latter propagation vector depends chiefly on there being a nuclear component to the (100) reflection we can perform x-ray diffraction measurements on powder or single crystal samples. Alternatively we can expand upon the work by Navid Qureshi on the D3 diffractometer and arrange the sample such that the [100] direction is parallel to the x -direction. The x -axis is arrange such that it run parallel to the scattering vector, Q . Hence performing x -polarisation measurements will then only be sensitive to any nuclear component on the (100) reflection. Magnetic refinement for the intermediate temperatures phase find an amplitude modulation along the [110] direction at an angle of 66.7° to the c -axis with all the moments point parallel to the c -axis. While the low temperature phase refinements have shown the moments are aligned parallel to the c -axis with an amplitude modulation along the c -axis and a broader modulation along the a -axis. However, all the magnetic refinements have been plagued with multiple scattering with a significant spread of intensity for the same reflections. This has made refine-

ments challenging and an improvement to this fits could be achieved by performing further neutron diffraction experiments and accounting for the multiple-scattering.

Inelastic neutron scattering measurements on polycrystalline samples have revealed the positions of a selection of crystal field levels have been found at 1.4, 2.9, 5.3, 9.5 and 17 meV for HoB_4 . However single crystal inelastic neutron scattering measurements have suggested that the lowest observed energy level may not be a simple crystal field level as it shows significant dispersive behaviour, persisting the paramagnetic regime, well above the ordering temperature of HoB_4 giving a strong indication that there are strong correlations present even at 35 K in HoB_4 . The intermediate temperature phase shows a unusual spin wave dispersion, where a comparison of exchange interaction suggest the strength of the antiferromagnetic coupling between the a - and c -axis are identical, further suggesting the SSL is not ideal for HoB_4 . The next steps would be to attempt fitting the crystal field levels and excitation in an attempt to understand the interaction scheme. The crystal field levels in NdB_4 have been found to be 2.9, 12.5 and 17.7 meV. We are part of an on going collaboration to determine the crystal field scheme for the RB_4 family, with inelastic neutron scattering measurements for TmB_4 and ErB_4 also have been collected. Fitting and modelling the crystal field schemes will give us a greater understanding of the magnetic properties of these compounds. Single crystal inelastic neutron scattering measurements have been performed on NdB_4 (not shown in this thesis). Some initial analysis was perform but the was significant spurious signal, which coupled with the weak scattering from the NdB_4 made it difficult to draw any real conclusions and it would be interesting to repeat this experiment.

Whilst the work of this thesis has added to the current knowledge and understanding of the RB_4 it has equally highlighted the complexity of the magnetism and competing interactions in HoB_4 and NdB_4 and the need for further investigations to reach a more complete understanding of the system and the family as a whole.

Bibliography

- [1] S. Blundell, *Magnetism: A Very Short Introduction* (OUP, Oxford, 2012).
- [2] S. T. Bramwell, M. J. Harris, B. C. den Hertog, M. J. P. Gingras, J. S. Gardner, D. F. McMorrow, A. R. Wildes, A. L. Cornelius, J. D. M. Champion, R. G. Melko, et al., Phys. Rev. Lett. **87**, 047205 (2001).
- [3] C. Castelnovo, R. Moessner, and S. L. Sondhi, Nature **451**, 42 (2008).
- [4] S. Blundell, *Magnetism in Condensed Matter* (Oxford University Press, Oxford, 2001).
- [5] F. M. C. Lacroix, P. Mendels, *Introduction to Frustrated Magnetism* (Springer, Berlin, 2011).
- [6] H. T. Diep, *Frustrated Spin Systems* (World Scientific, New York, 2013).
- [7] A. I. M. Rae, *Quantum Mechanics* (CRC Press, London, 2007).
- [8] K. W. H. Stevens, Proceedings of the Physical Society. Section A **65**, 209 (1952).
- [9] P. Fulde and M. Loewenhaupt, Advances in Physics **34**, 589 (1985).
- [10] R. J. Birgeneau, J. K. Kjems, G. Shirane, and L. G. Van Uiter, Phys. Rev. B **10**, 2512 (1974).
- [11] M. Ries, *Fundamentals of magnetism* (Academic Press, Amsterdam, 2013).
- [12] M. den Nijs, Phys. Rev. B **31**, 266 (1985).
- [13] S. Hov, H. Bratsberg, and A. Skjeltorp, Journal of Magnetism and Magnetic Materials **15**, 455 (1980).
- [14] M. J. Harris, S. T. Bramwell, P. C. W. Holdsworth, and J. D. M. Champion, Phys. Rev. Lett. **81**, 4496 (1998).

- [15] T. H. Cheffings, M. R. Lees, G. Balakrishnan, and O. A. Petrenko, *Journal of Physics: Condensed Matter* **25**, 256001 (2013).
- [16] A. P. Ramirez, *Annual Review of Materials Science* **24**, 453 (1994).
- [17] K. Binder and A. P. Young, *Rev. Mod. Phys.* **58**, 801 (1986).
- [18] M. F. Collins and O. A. Petrenko, *Canadian Journal of Physics* **75**, 605 (1997).
- [19] J. E. Greedan, *J. Mater. Chem.* **11**, 37 (2001).
- [20] R. Moessner and A. P. Ramirez, *Physics Today* **59**, 24 (2006).
- [21] R. Moessner, *Canadian Journal of Physics* **79**, 1283 (2001).
- [22] Villain, J., Bidaux, R., Carton, J.-P., and Conte, R., *J. Phys. France* **41**, 1263 (1980).
- [23] J. T. Chalker and J. F. G. Eastmond, *Phys. Rev. B* **46**, 14201 (1992).
- [24] M. R. Norman, *Rev. Mod. Phys.* **88**, 041002 (2016).
- [25] R. Moessner, S. L. Sondhi, and P. Chandra, *Phys. Rev. B* **64**, 144416 (2001).
- [26] H. Karunadasa, Q. Huang, B. G. Ueland, P. Schiffer, and R. J. Cava, *Proceedings of the National Academy of Sciences* **100**, 8097 (2003).
- [27] J.-W. G. Bos and J. P. Attfield, *Phys. Rev. B* **70**, 174434 (2004).
- [28] J. S. Gardner, M. J. P. Gingras, and J. E. Greedan, *Rev. Mod. Phys.* **82**, 53 (2010).
- [29] S. T. Bramwell and M. J. P. Gingras, *Science* **294**, 1495 (2001).
- [30] T. Yoshioka, A. Koga, and N. Kawakami, *Journal of the Physical Society of Japan* **73**, 1805 (2004).
- [31] P. Schiffer, A. P. Ramirez, D. A. Huse, and A. J. Valentino, *Phys. Rev. Lett.* **73**, 2500 (1994).
- [32] N. Rogado, M. K. Haas, G. Lawes, D. A. Huse, A. P. Ramirez, and R. J. Cava, *Journal of Physics: Condensed Matter* **15**, 907 (2003).
- [33] M. Moliner, D. C. Cabra, A. Honecker, P. Pujol, and F. Stauffer, *Journal of Physics: Conference Series* **145**, 012053 (2009).

- [34] J. Dorier, K. P. Schmidt, and F. Mila, Phys. Rev. Lett. **101**, 250402 (2008).
- [35] S. Miyahara and K. Ueda, Phys. Rev. B **61**, 3417 (2000).
- [36] S. Shastry and B. Sutherland, PhysicaB+C **108**, 1069 (1981).
- [37] J. Rossat-Mignod, P. Burlet, J. Villain, H. Bartholin, W. Tcheng-Si, D. Florence, and O. Vogt, Phys. Rev. B **16**, 440 (1977).
- [38] P. Bak, Reports on Progress in Physics **45**, 587 (1982).
- [39] M. Takigawa, T. Waki, M. Horvati, and C. Berthier, Journal of the Physical Society of Japan **79**, 011005 (2010).
- [40] S. Miyahara and K. Ueda, Journal of Physics: Condensed Matter **15**, R327 (2003).
- [41] in *Boron and Refractory Borides*, edited by V. Matkovich (Springer-Verlag, Heidelberg, 1977).
- [42] S. Mat'a, K. Siemensmeyer, E. Wheeler, E. Wulf, R. Beyer, T. Hermannsdrfer, O. Ignatchik, M. Uhlarz, K. Flachbart, S. Gabni, et al., Journal of Physics: Conference Series **200**, 032041 (2010).
- [43] W. Schfer, G. Will, and K. Buschow, Journal of Magnetism and Magnetic Materials **3**, 61 (1976).
- [44] R. Watanuki, T. Kobayashi, R. Noguchi, and K. Suzuki, Journal of Physics: Conference Series **150**, 042229 (2009).
- [45] R. Watanuki, G. Sato, K. Suzuki, M. Ishihara, T. Yanagisawa, Y. Nemoto, and T. Goto, Journal of the Physical Society of Japan **74**, 2169 (2005).
- [46] D. Okuyama, T. Matsumura, T. Mouri, N. Ishikawa, K. Ohoyama, H. Hiraka, H. Nakao, K. Iwasa, and Y. Murakami, Journal of the Physical Society of Japan **77**, 044709 (2008).
- [47] K. H. J. Buschow and J. H. N. Creighton, The Journal of Chemical Physics **57**, 3910 (1972).
- [48] G. A. Wigger, E. Felder, R. Monnier, H. R. Ott, L. Pham, and Z. Fisk, Phys. Rev. B **72**, 014419 (2005).
- [49] B. Bressel, B. Chevalier, J. Etourneau, and P. Hagenmuller, Journal of Crystal Growth **47**, 429 (1979).

- [50] Z. Fisk, A. Cooper, P. Schmidt, and R. Castellano, *Materials Research Bulletin* **7**, 285 (1972).
- [51] S. Okada, K. Kudou, Y. Yu, and T. Lundstrm, *Japanese Journal of Applied Physics* **33**, 2663 (1994).
- [52] J. Etourneau, *Journal of the Less Common Metals* **110**, 267 (1985).
- [53] S. Michimura, A. Shigekawa, F. Iga, M. Sera, T. Takabatake, K. Ohoyama, and Y. Okabe, *Physica B: Condensed Matter* **378**, 596 (2006), proceedings of the International Conference on Strongly Correlated Electron Systems.
- [54] B. K. Cho, J.-S. Rhyee, J. Y. Kim, M. Emilia, and P. C. Canfield, *Journal of Applied Physics* **97**, 10A923 (2005).
- [55] W. Schfer, G. Will, and K. H. J. Buschow, *The Journal of Chemical Physics* **64**, 1994 (1976).
- [56] S. Ji, C. Song, J. Koo, K.-B. Lee, Y. J. Park, J. Y. Kim, J.-H. Park, H. J. Shin, J. S. Rhyee, B. H. Oh, et al., *Phys. Rev. Lett.* **91**, 257205 (2003).
- [57] S. W. Lovesey, J. F. Rodríguez, J. A. Blanco, and P. J. Brown, *Phys. Rev. B* **70**, 172414 (2004).
- [58] J. Fernández-Rodríguez, J. A. Blanco, P. J. Brown, K. Katsumata, A. Kikkawa, F. Iga, and S. Michimura, *Phys. Rev. B* **72**, 052407 (2005).
- [59] J. A. Blanco, P. J. Brown, A. Stunault, K. Katsumata, F. Iga, and S. Michimura, *Phys. Rev. B* **73**, 212411 (2006).
- [60] R. Watanuki, H. Mitamura, T. Sakakibara, G. Sato, and K. Suzuki, *Physica B: Condensed Matter* **378**, 594 (2006), proceedings of the International Conference on Strongly Correlated Electron Systems.
- [61] D. Okuyama, T. Matsumura, H. Nakao, and Y. Murakami, *Journal of the Physical Society of Japan* **74**, 2434 (2005).
- [62] J.-S. Rhyee, J. Y. Kim, and B. K. Cho, *Journal of Applied Physics* **101**, (2007).
- [63] F. Elf, W. Schfer, G. Will, and J. Etourneau, *Solid State Communications* **40**, 579 (1981).
- [64] T. Matsumura, D. Okuyama, and Y. Murakami, *Journal of the Physical Society of Japan* **76**, 015001 (2007).

- [65] F. Iga, A. Shigekawa, Y. Hasegawa, S. Michimura, T. Takabatake, S. Yoshii, T. Yamamoto, M. Hagiwara, and K. Kindo, *Journal of Magnetism and Magnetic Materials* **310**, e443 (2007), proceedings of the 17th International Conference on Magnetism.
- [66] S. Michimura, A. Shigekawa, F. Iga, T. Takabatake, and K. Ohoyama, *Journal of the Physical Society of Japan* **78**, 024707 (2009).
- [67] J. Etourneau, J. Mercurio, A. Berrada, P. Hagenmuller, R. Georges, R. Bourezg, and J. Gianduzzo, *Journal of the Less Common Metals* **67**, 531 (1979).
- [68] S. Yoshii, T. Yamamoto, M. Hagiwara, T. Takeuchi, A. Shigekawa, S. Michimura, F. Iga, T. Takabatake, and K. Kindo, *Journal of Magnetism and Magnetic Materials* **310**, 1282 (2007).
- [69] S. Yoshii, T. Yamamoto, M. Hagiwara, A. Shigekawa, S. Michimura, F. Iga, T. Takabatake, and K. Kindo, *Journal of Physics: Conference Series* **51**, 59 (2006).
- [70] F. Pfeiffer, W. Schfer, G. Will, J. Etourneau, and R. Georges, *Journal of Magnetism and Magnetic Materials* **14**, 306 (1979).
- [71] K. Siemensmeyer, E. Wulf, H.-J. Mikeska, K. Flachbart, S. Gabáni, S. Mat'aš, P. Priputen, A. Efdokimova, and N. Shitsevalova, *Phys. Rev. Lett.* **101**, 177201 (2008).
- [72] J. Y. Kim, N. H. Sung, B. Y. Kang, M. S. Kim, B. K. Cho, and J.-S. Rhyee, *Journal of Applied Physics* **107**, 09E111 (2010).
- [73] G. E. Bacon, *Neutron Diffraction* (Oxford University Press, Oxford, 1975).
- [74] C. Kittel, *Solid State Physics* (John Wiley and Sons Inc., London, 1976).
- [75] D. S. Sivia, *Elementary Scattering Theory: For x-ray and neutron users* (Oxford University Press, Oxford, 2011).
- [76] G. L. Squires, *Introduction to the Theory of Thermal Neutron Scattering* (Cambridge University Press, Cambridge, 1978).
- [77] S. H. Simon, *The Oxford Solid State Basics* (Oxford University Press, Oxford, 2013).
- [78] A. Wills, *J. Phys. IV France* **11**, Pr9 (2001).

- [79] M. T. Dove, *Structure and Dynamics: An atomic view of materials* (Oxford University Press, Oxford, 2003).
- [80] J. R. Stewart, P. P. Deen, K. H. Andersen, H. Schober, J.-F. Barthélémy, J. M. Hillier, A. P. Murani, T. Hayes, and B. Lindenau, *Journal of Applied Crystallography* **42**, 69 (2009).
- [81] J. R. Stewart, *Collection SFN* **7**, 173 (2007).
- [82] Y. Kakehashi, *Modern Theory of Magnetism in metals and alloys* (Springer, New York, 2012).
- [83] in *Handbook of Crystal Growth (Second Edition)*, edited by P. Rudolph (Elsevier, Boston, 2015), *Handbook of Crystal Growth*, pp. 281 – 329, second edition ed.
- [84] G. Dhanaraj, *Springer Handbook of Crystal Growth* (Springer, Heidelberg, 2010).
- [85] J. Rodriguez-Carvajal, *Physica B: Condensed Matter* **192**, 55 (1993).
- [86] H. M. Rietveld, *Acta Crystallographica* **22**, 151 (1967).
- [87] H. M. Rietveld, *Journal of Applied Crystallography* **2**, 65 (1969).
- [88] L. B. McCusker, R. B. Von Dreele, D. E. Cox, D. Louër, and P. Scardi, *Journal of Applied Crystallography* **32**, 36 (1999).
- [89] O. Halpern and M. H. Johnson, *Phys. Rev.* **55**, 898 (1939).
- [90] M. McElfresh, *Fundamentals of Magnetism and Magnetic Measurements* (Quantum Design, 1994).
- [91] N. Shirakawa, H. Horinouchi, and Y. Yoshida, *Journal of Magnetism and Magnetic Materials* **272-276, Supplement**, E149 (2004), proceedings of the International Conference on Magnetism (ICM 2003).
- [92] *Vibrating Sample Magnetometer (Superconducting magnet) – System Manual 1 of 4*, Oxford Instrument (1997).
- [93] J. S. Hwang, K. J. Lin, and C. Tien, *Review of Scientific Instruments* **68**, 94 (1997).
- [94] J. Lashley, M. Hundley, A. Migliori, J. Sarrao, P. Pagliuso, T. Darling, M. Jaime, J. Cooley, W. Hults, L. Morales, et al., *Cryogenics* **43**, 369 (2003).

- [95] *Specific Heat Physical Property Measurement System operation manual*, Quantum Design (2000).
- [96] G. Cicognani, *Guide to the Neutron Research Facilities at the ILL, The Yellow Book* (ILL, 2008).
- [97] K. Andersen, Nuclear Instruments and Methods in Physics Research Section A: Accelerators, Spectrometers, Detectors and Associated Equipment **371**, 472 (1996).
- [98] G. Cicognani, H. Mutka, and F. Sacchetti, Physica B: Condensed Matter **276-278**, 83 (2000).
- [99] H. Schober, A. Dianoux, J. Cook, and F. Mezei, Physica B: Condensed Matter **276-278**, 164 (2000).
- [100] Z. Fisk, M. Maple, D. Johnston, and L. Woolf, Solid State Communications **39**, 1189 (1981).
- [101] J. Gianduzzo, R. Georges, B. Chevalier, J. Etourneau, P. Hagenmuller, G. Will, and W. Schfer, Journal of the Less Common Metals **82**, 29 (1981).
- [102] J. Y. Kim, B. K. Cho, and S. H. Han, Journal of Applied Physics **105**, (2009).
- [103] Z. Fisk, A. Cooper, P. Schmidt, and R. Castellano, Materials Research Bulletin **7**, 285 (1972).
- [104] *OrientExpress*, part of the the LMGP Suite software, J. Laugier and B. Bochu <http://www.ccp14.ac.uk/tutorial/lmgp/index.html> (2003).
- [105] *OriginLab*, <http://www.originlab.com/doc/Origin-Help/Linear-Polynomial-Regression> ((last accessed 13/08/2017)).
- [106] A. Aharoni, Journal of Applied Physics **83**, 3432 (1998).
- [107] V. Novikov, N. Mitroshenkov, A. Matovnikov, D. Avdashchenko, A. Morozov, L. Pavlova, and V. Koltsov, Journal of Alloys and Compounds **613**, 170 (2014).
- [108] M. Bouvier, P. Lethuillier, and D. Schmitt, Phys. Rev. B **43**, 13137 (1991).
- [109] V. Hardy, S. Lambert, M. R. Lees, and D. McK. Paul, Phys. Rev. B **68**, 014424 (2003).

- [110] V. Novikov, V. rozov, V. atovnikov, N. itroshenkov, D. vdashchenko, S. Kuznetsov, B. Krnev, . rakhina, V. Novikova, and . Bordacheva, Journal of Alloys and Compounds **581**, 431 (2013).
- [111] V. V. Novikov, N. V. Mitroshenkov, A. V. Morozov, A. V. Matovnikov, and D. V. Avdashchenko, Journal of Applied Physics **111**, 063907 (2012).
- [112] V. V. Novikov, N. V. Mitroshenkov, A. V. Morozov, A. V. Matovnikov, and D. V. Avdashchenko, Journal of Thermal Analysis and Calorimetry **113**, 779 (2013).
- [113] V. V. Novikov, A. V. Morozov, A. V. Matovnikov, D. V. Avdashchenko, Y. N. Poleskaya, N. V. Sakhoshko, B. I. Kornev, V. D. Solomennik, and V. V. Novikova, Physics of the Solid State **53**, 1839 (2011).
- [114] E. S. R. Gopal, *Specific Heats at Low Temperatures* (Hetwood Books, London, 1966).
- [115] H. Blte, R. Wielinga, and W. Huiskamp, Physica **43**, 549 (1969).
- [116] L. Ye, T. Suzuki, and J. G. Checkelsky, Phys. Rev. B **95**, 174405 (2017).
- [117] A. Grechnev, Phys. Rev. B **87**, 144419 (2013).
- [118] S. Michimura, A. Shigekawa, F. Iga, M. Sera, T. Takabatake, A. Kikkawa, Y. Tanaka, and K. Katsumata, Journal of Magnetism and Magnetic Materials **310**, e446 (2007), proceedings of the 17th International Conference on Magnetism.
- [119] J. J. Feng, L. Huo, W. C. Huang, Y. Wang, M. H. Qin, J.-M. Liu, and Z. Ren, EPL (Europhysics Letters) **105**, 17009 (2014).
- [120] W. C. Huang, L. Huo, G. Tian, H. R. Qian, X. S. Gao, M. H. Qin, and J.-M. Liu, Journal of Physics: Condensed Matter **24**, 386003 (2012).
- [121] L. Huo, W. C. Huang, Z. B. Yan, X. T. Jia, X. S. Gao, M. H. Qin, and J.-M. Liu, Journal of Applied Physics **113**, 073908 (2013).
- [122] S. Yoshii, T. Yamamoto, M. Hagiwara, S. Michimura, A. Shigekawa, F. Iga, T. Takabatake, and K. Kindo, Phys. Rev. Lett. **101**, 087202 (2008).
- [123] S. Yoshii, K. Ohoyama, K. Kurosawa, H. Nojiri, M. Matsuda, P. Frings, F. Duc, B. Vignolle, G. L. J. A. Rikken, L.-P. Regnault, et al., Phys. Rev. Lett. **103**, 077203 (2009).

- [124] P. Salamakha, A. Goncalves, O. Sologub, and M. Almeida, *Journal of Alloys and Compounds* **316**, L4 (2001).
- [125] H. Yamauchi, N. Metoki, R. Watanuki, K. Suzuki, H. Fukazawa, S. Chi, and J. A. Fernandez-Baca, *Journal of the Physical Society of Japan* **86**, 044705 (2017).
- [126] H. A. Eick and P. W. Gilles, *Journal of the American Chemical Society* **81**, 5030 (1959).
- [127] D. Brunt, G. Balakrishnan, A. R. Wildes, B. Ouladdiaf, N. Qureshi, and O. A. Petrenko, *Phys. Rev. B* **95**, 024410 (2017).
- [128] *Basireps*, J. Rodriguez-Carvajal <http://www.ccp14.ac.uk/ccp/web-mirrors/plotr/Tutorials&Documents/basireps.pdf> (2007).
- [129] C. Ritter, in *Solid Compounds of Transition Elements* (Trans Tech Publications, 2011), vol. 170 of *Solid State Phenomena*, pp. 263–269.
- [130] Z. Heiba, W. Schfer, E. Jansen, and G. Will, *Journal of Physics and Chemistry of Solids* **47**, 651 (1986).